Role of Geometric Complexities and Off-Fault Damage in Dynamic Rupture Propagation

A dissertation presented
by

Harsha Suresh Bhat

to
The School of Engineering and Applied Sciences
in partial fulfillment of the requirements
for the degree of
Doctor of Philosophy
in the subject of

Engineering Sciences

Harvard University
Cambridge, Massachusetts
June 2007

Thesis advisor Author

Prof. James R. Rice **Harsha Suresh Bhat**

Role of Geometric Complexities and Off-Fault Damage in Dynamic Rupture Propagation

Abstract

To analyze the effect of fault branches on dynamic rupture propagation we numerically simulated the observed dynamic slip transfer from the Denali to Totschunda faults during the M_w 7.9, November 3, 2002, Denali fault earthquake, Alaska and show that the theory and methodology of *Poliakov et al.* [2002] and *Kame et al.* [2003] is valid for the 2002 Denali fault event. To understand the effect of fault branch length on dynamic rupture propagation we analyze earthquake ruptures propagating along a straight "main" fault and encountering a finite-length branch fault. We show finite branches have the tendency of stopping or re-nucleating rupture on the main fault depending on their length in addition to the parameters singled out by *Kame et al.* [2003]. We also illustrate branch-related complexities in rupture velocity and slip evolution. We illustrate the effect of backward branches (branches at obtuse angle to the main fault with the same sense of slip as the main fault) and propose a mechanism of backward branching. As a field example we simulate numerically, using a two-dimensional elastodynamic boundary integral equation formulation incorporating slip-weakening rupture, the backward branching phenomenon observed during the Landers 1992 earthquake.

To characterize the effect of supershear ruptures on off-fault materials we extend a model of a two-dimensional self-healing slip pulse, propagating dynamically in steady-state with slip-weakening failure criterion, to the supershear regime and show that there exists a non-attenuating stress field behind the Mach front which radiates high stresses arbitrarily far from the fault (practically this would be limited to distances comparable to the depth of the seismogenic zone). We apply this model to study damage features induced during the 2001 Kokoxili (Kunlun) event in Tibet. We also study the 3D effects of supershear ruptures by simulating bilateral ruptures on a finite-width vertical strike-slip fault breaking the surface of an elastic half-space, and focus on the wavefield in the near-source region. We provide numerical evidence for the existence of Rayleigh Mach fronts, in addition to shear Mach fronts. We conclude that radiating Mach waves of three-dimensional supershear ruptures do transmit large-amplitude ground motions and stresses far from the fault. The amplitudes along the shear Mach front would be moderated at distances greater than the fault width by decay with distance due to geometrical spreading. However, in an ideally elastic material, we do not expect any geometrical attenuation along the Rayleigh Mach front.

Contents

Citations to Previously Published Work

Large portions of Chapter 2 has appeared in the following paper:

> "Dynamic slip transfer from the Denali to Totschunda faults, Alaska: Testing theory for fault branching",
> Bhat, Harsha S., Renata Dmowska, James R. Rice, and Nobuki Kame, *Bull. Seismol. Soc. Amer.*, *94*, S202–S213, 2004.

Sections of Chapter 3 has been submitted to a journal

> "Role of fault branches in earthquake rupture dynamics",
> Bhat, Harsha S., Marion Olives, Renata Dmowska and James R. Rice, submitted to *J. Geophys. Res.*, 2007.

Sections of Chapter 4 appears in

> "Fault branching and rupture directivity",
> Fliss, Sonia, Harsha S. Bhat, Renata Dmowska, and James R. Rice, *J. Geophys. Res.*, *110*, B06312, doi:10.1029/2004JB003368, 2005.

Sections of Chapter 5 appears in

> "Off-fault damage patterns due to supershear ruptures with application to the 2001 M_w 8.1 Kokoxili (Kunlun) Tibet earthquake",
> Bhat, Harsha S., Renata Dmowska, Geoffrey C. P. King, Yann Klinger, and James R. Rice, *J. Geophys. Res., in press*

A manuscript based on Chapter 6, co-authored with Eric M. Dunham, is in preparation for submission.

Electronic reprints and preprints are available at the following URL:

> `http://people.deas.harvard.edu/~bhat/publications.html`

Acknowledgments

I would like to thank Jim and Renata for not only being my thesis advisors but also for the support, help and encouragement that they have provided over the years. Arriving in a new country at the age of 21 was equivalent to starting a new life all over and I thank all my friends who have tolerated and pampered me over the years. It would be unfair not to list all. Suffice to say that a substantial part of me is a sum total of all their wishes.

I would like to thank my colleagues for many a lively scientific debates, advice and encouragement. Specifically, I extend my gratitude to Prof. John W. Hutchinson and Prof. Zhigang Suo for all their encouragement. My gratitude also goes to Prof. Ares Rosakis and Prof. David D. Oglesby for their helpful comments and encouragement.

Last but not the least my greatest gratitude goes to my family. Thank you dad and mom for believing in me when I always chose the unconventional route and supporting me throughout my up and downs. Thank you Deepti, my sister, for your encouragement and your bubbling-with-life persona. Many a rough days have passed unnoticed because of you.

Chapter 1

Introduction

A fault system has in general geometric complexities, long known to geologists [*King and Nabelek*, 1985; *Sibson*, 1985; *King*, 1986; *Wesnousky*, 1988; *Knuepfer*, 1989; *Aydin and Schultz*, 1990; *Yule and Sieh*, 2003; *Brankman and Aydin*, 2004; *Wesnousky*, 2006, among others], like bends, branches, step-overs, and sub-parallel strands at different length scales (e.g. 1992 Landers earthquake, Figure 1.1). A long standing issue in geophysics is the role played by these geometric complexities in dynamic earthquake rupture propagation and generation/re-activation of off-fault damage.

Since one of the goals of seismic hazard analysis is predicting the rupture extent of future events it becomes even more relevant, from a practical standpoint, to understand the role of geometric complexities in dynamic earthquake rupture propagation. Recently, *Wesnousky* [2006] has compiled surface rupture maps of 20 large strike-slip surface rupture earthquakes and emphasized the role of geometric complexities, specifically step-overs, in stopping an earthquake rupture (Figure 1.2). One of the claims made in that work was that variations in earthquake rupture lengths are not necessarily controlled by the relative size of initial slip pulses or stress drops but rather by the geometrical complexity of fault traces and variations in accumulated stress levels along faults are due to the location of past earthquakes along the respective faults.

The interaction between geometric complexities like fault bends and jogs and rupture has been observed for various earthquakes. For example, the 1992 Landers event branched from the Johnson Valley Fault to the Kickapoo fault with part of the rupture continuing on the Johnson Valley fault for four kilometers beyond the branching junction [*Sowers et al.*, 1994; *Kame et al.*, 2003]. The rupture then transitioned, via a step-over, to Homestead Valley fault where part of the rupture seemed to branch “backwards” [*Fliss et al.*, 2005].

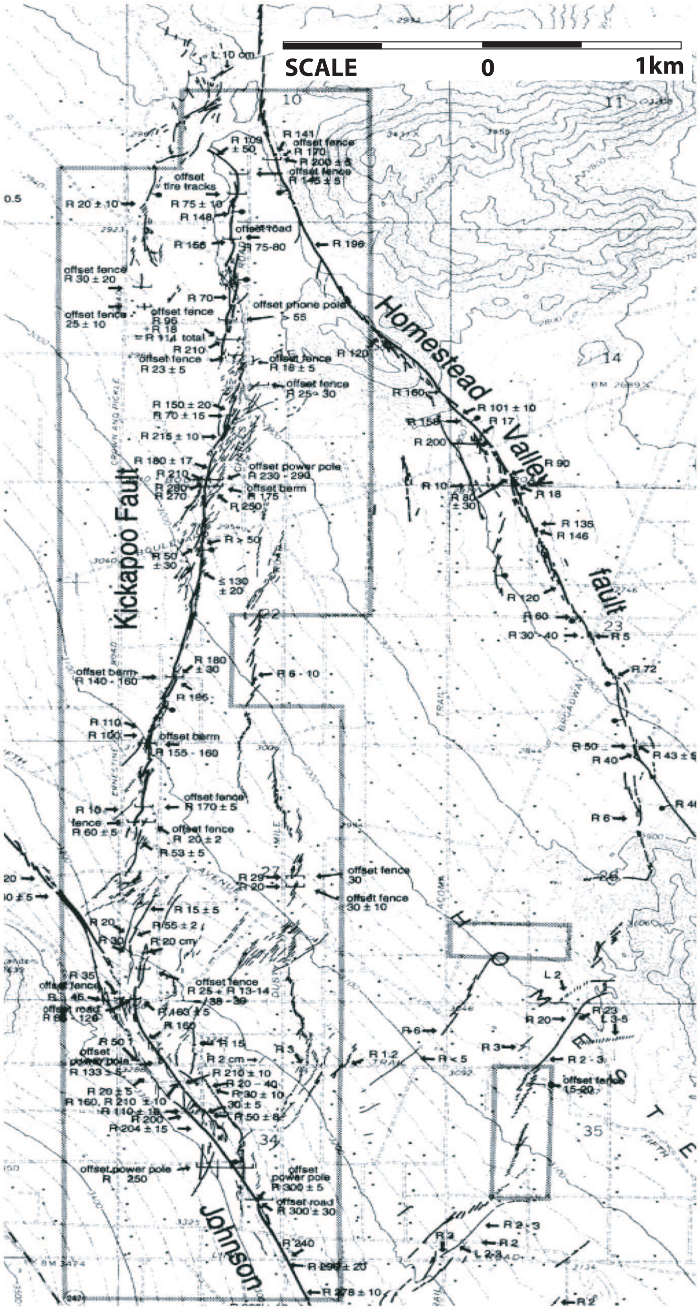

Figure 1.1: Map from *Sowers et al.* [1994] showing region of transition from the Johnson Valley to the Kickapoo and to the Homestead Valley faults during the 1992 Landers earthquake. The thickest lines show fault breaks with surface slip > 1 m, intermediate lines > 0.05 m, and thinnest lines > 0.01 m.

The 2002 Denali event branched off from the main Denali fault to the Totschunda fault with no observable surface slip on Denali fault beyond the branching junction [*Bhat et al.*, 2004]. Similar examples of branching from various other earthquakes are discussed in *Kame et al.* [2003]. For more examples on observations of earthquake rupture propagation through geometric complexities see *Wesnousky* [2006].

Theoretical modeling of a mode II rupture propagation on a planar fault, in an isotropic elastic medium, suggests two key points of relevance to this study [*Yoffe*, 1951; *Poliakov et al.*, 2002; *Rice et al.*, 2005, and references therein]. One is that a dynamic shear rupture, once nucleated on a planar fault with uniform frictional properties and stress distribution, accelerates to its limiting speed (c_R, the Rayleigh wave speed for Mode II and c_s, the shear wave speed for mode III), sometimes even transitioning to the supershear (rupture speed exceeding c_s) regime for mode II ruptures. Thus to explain observations of a variety of earthquake event sizes, the event size being a proxy for rupture length, on a given fault one has to appeal to some kind of heterogeneity introduced into the fault frictional properties and stress distribution. The second point is that as the rupture accelerates to its limiting speed the stress perturbation in the medium is larger on off-fault planes than on the plane directly ahead of the rupture front [e.g. *Poliakov et al.*, 2002]. These two theoretical observations suggest that off-fault structures, such as branches, step-overs etc., can get stress perturbations that could be large enough sometimes to activate them. This could then lead to inhomogeneous changes in stress distribution (arising chiefly from geometric complexities), and fault frictional behavior, which could in turn significantly perturb the rupture propagation characteristics on a fault.

The consensus, so far, in the area of earthquake source physics is that spatial hetero-

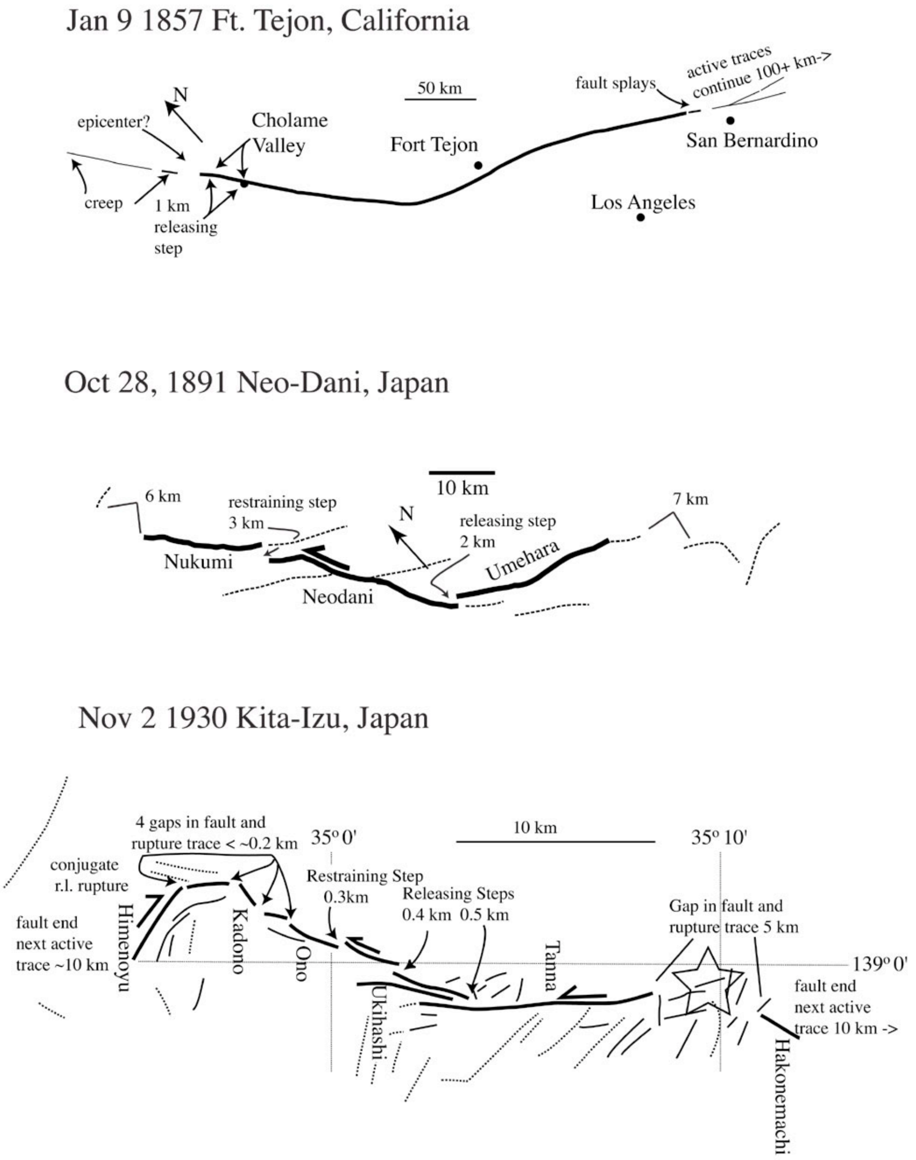

Figure 1.2: Maps of various earthquake rupture surface traces. Adjacent and continuing traces of active faults that did not rupture during the earthquake are shown as dotted lines. Also annotated are the dimensions of fault steps measured approximately perpendicular to fault strike. The star is the earthquake epicenter [from *Wesnousky*, 2006].

geneity in the strength/stress distribution along the fault could lead to the stoppage of an earthquake rupture. One should however note that this consensus is derived mainly from the fact that most of the modeling of earthquake ruptures is done via kinematic or dynamic inversion of events on planar faults to match seismological observations.

Hence the question of the source of heterogeneities in the fault stress and frictional properties is still not addressed definitively. To fully address that issue two ingredients are vital. One is the numerical ability to perform multi-earthquake cycle studies on a geometrically complex fault system and the other is to incorporate a fault friction law that allows for an evolution in the strength of a fault system in the inter-seismic period. The latter is achieved quite effectively through a rate-and-state type frictional behavior where the strength of the fault could depend on the sliding velocity, the contact time between fault asperities, the total amount of slip accumulated by the fault (or some other measure of history of sliding between the faults) and various other hydro-thermo-poro-mechanical properties of the fault [*Segall and Rice*, 2006; *Rice*, 2006; *Rempel and Rice*, 2006, and references therein]. Because of computational limitations no studies have been done yet that fully incorporate the above two ingredients. It should however be noted that these issues have been addressed in the context of a planar fault by *Lapusta et al.* [2000] and *Lapusta and Rice* [2003]. More recently *Liu and Rice* [2005] have shown that small perturbations in the fault frictional properties can lead to a very inhomogeneous stress state on the fault altering the seismic cycle significantly enough to make the small frictional perturbations irreversible. *Duan and Oglesby* [2005] were the first to conduct multi-cycle dynamics study of an earthquake rupture through a branched fault geometry (with a visco-elastic constitutive response of the medium to mimic the inter-seismic loading period rather than the one mentioned above) and have shown that the stress field left in the wake of an earthquake event did alter the general rupture propagation direction during the subsequent earthquake events. In the light of the questions mentioned above the importance of understanding the relevance of geometric complexities of a fault in dynamic earthquake rupture becomes a pertinent one.

However, that does not mean that the issue of complex fault geometries has not been addressed in the past. For example, *Harris et al.* [1991] and *Harris and Day* [1993] have numerically investigated the conditions under which rupture transitions from one planar segment of a step-over to another. There has been a surge of activity recently in the numerical modeling of rupture propagation through geometric complexities. Numerical modeling of geometric complexities and their interaction with the rupture process has been done by *Tada and Yamashita* [1997], *Kame et al.* [2003] and *Bhat et al.* [2004], among others, for a rupture branching through a fault system in 2D using the Boundary Integral Equation (BIE) method (see Appendix A), and by *Duan and Oglesby* [2005] using the Finite Element (FE) method. *Aochi et al.* [2000a,b, 2002, 2005] and *Aochi and Fukuyama* [2002] addressed similar problems in 3D using the BIE method, and *Oglesby et al.* [2003a], *Dreger et al.* [2004] and *Oglesby* [2005] using the FE method.

The theoretical framework for dynamic off-fault processes due to an earthquake rupture on a fault was laid out by *Poliakov et al.* [2002], in the context of a dynamic steady state semi-infinite shear rupture. The authors noted that off-fault slip systems could get activated due to an earthquake rupture with the extent and location of such activated zones depending on the large scale stress field and the rupture velocity. *Rice et al.* [2005] extended this framework to a slip pulse propagating in a medium, on a prescribed fault plane. Following the concepts introduced by *Poliakov et al.* [2002] on factors governing fault branching, *Kame et al.* [2003] performed an extensive set of numerical simulations of branching. Those were done in 2D, for a mode II, rupture model with a linear slip-weakening friction coefficient, with strength during slip-weakening proportional to the instantaneous local normal stress. The simulations involved a range of branching fault angles (φ) with the primary fault, rupture velocities (v_r) approaching the branching location, and maximum horizontal pre-stress inclinations (Ψ) with the main fault. These parameters were crucial in rupture taking or not taking a branch, and continuing or not along the main fault as well. The simulations were compared with field cases of branching earthquakes, namely the 1944 Tonankai event, the 1971 San Fernando event, the 1979 Imperial Valley event, the 1985 Kettleman Hills event and the 1992 Landers event for the rupture branching from the Johnson Valley fault to the Kickapoo fault [Figure 1.1].

In chapter 2 we further validate the theory of fault branching developed by *Poliakov et al.* [2002] and *Kame et al.* [2003] with another field branching event during the 2002 Denali fault earthquake, where the rupture branched, by about 15^0 to the extensional side, abruptly from the Denali fault to the Totschunda fault (Figure 1.3). We show that a relatively simple 2D theory of fault branching can quite satisfactorily explain this phenomenon.

The above model, however, does not address a key issue which is the role of the length of the fault branch. A cursory glance at the map of surface rupture trace after the 1992 Landers event (Figure 1.1) reveals branch segments at various length scales ranging from few tens of meters to a few kilometers. The question then is can we ignore the small scale geometrical features when, say, modeling this event. Theoretical work by *Eshelby* [1969] for mode III and *Fossum and Freund* [1975] for mode II emphasizes that when a

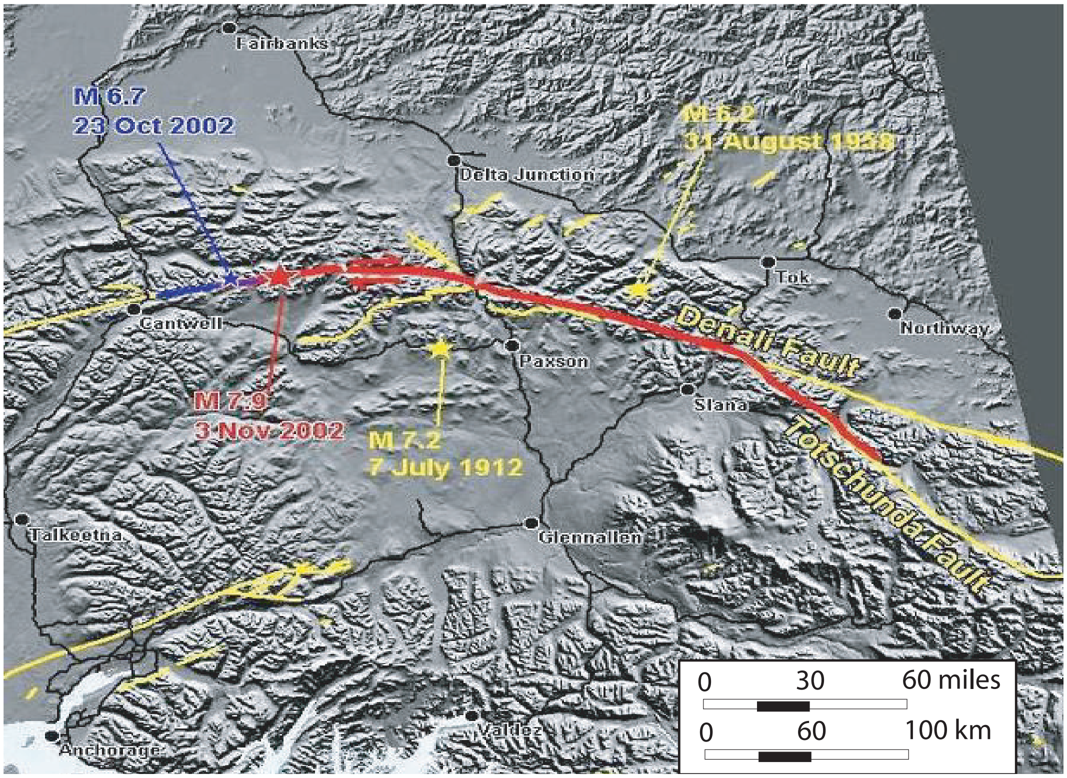

Figure 1.3: Rupture path, solid line, of the M_w 7.9 Denali fault earthquake. A star towards the left of center of the figure marks the epicenter of the 3 November 2002 event. [Figure courtesy: Alaska Division of Geological and Geophysical Surveys.]

dynamic rupture is suddenly stopped it radiates large stress perturbations into the medium from the rupture termination point. In fact *Harris et al.* [1991] and *Fliss et al.* [2005] use this as a mechanism for the rupture to dynamically jump from one fault segment to another. Thus a termination of a rupture on a short branch segment could significantly alter rupture propagation characteristics on the main fault. This leads us to a hypothesis that short branch segments could indeed be significantly important in modeling an earthquake event. We address this issue of “finite” branches in chapter 3.

Another interesting question that is posed, recently, in the area of geometrical fault complexity is: Is it possible to judge the directivity of a large earthquake from the rupture pattern it left? The answer to that question would be very useful for risk assessment of future earthquakes, even if it is currently unknown if large earthquakes do systematically repeat their rupture direction (while not necessarily the entire rupture pattern). A narrower version of that question is, could we associate the directivity of a major earthquake with the pattern of branches that it left?

That question has been posed by *Nakata et al.* [1998], who proposed to relate the observed surface branching of fault systems with directivity. Their work assumed that all branches were through acute angles, in the direction of rupture propagation. However *Dmowska et al.* [2002] pointed out that, for at least some field observations, the rupture paths seemed to branch through highly obtuse angles, as if to propagate “backwards” along the branch. Mechanically such branching is forbidden, it is rather more probable that some obtuse branches are due to early aftershocks. However during the 1992 Landers, California, earthquake, *Poliakov et al.* [2002] showed that the pattern of damage off the southern Homestead Valley fault, which lies mainly on the western side of the fault, and the relatively steep direction of maximum compressive stress with respect to the fault ($\Psi \approx 65^0$) clearly indicates such a backward direction of propagation (NNW to SSE) on that branch (Figure 1.1). In chapter 4 we analyze and numerically simulate the mechanics of such backward branching, and relate the results to understanding rupture directivity.

The velocity at which a rupture propagates influences the amplitude and character of the radiated ground motion and stresses. A distinct manifestation of this occurs when ruptures exceed the S-wave speed and generate shear Mach fronts that coherently transmit ground motion and stresses far from the fault. The earliest inference of supershear earthquake rupture was during the 1979 Imperial Valley earthquake for which *Archuleta* [1984] noticed that for a better fit of near-fault strong motion records, the rupture speed had to exceed the shear wave speed. More recent inferences were made during the 1999 Izmit and Düzce events [*Bouchon et al.*, 2000, 2001] the 2001 Kokoxili (Kunlun) event [*Bouchon and Vallee*, 2003] and the 2002 Denali event [*Ellsworth et al.*, 2004; *Dunham and Archuleta*, 2005]. Laboratory verification of supershear rupture was provided by *Rosakis et al.* [1999] and *Xia et al.* [2004].

The aim of chapter 5 is to point out some unique features of supershear ruptures that manifest themselves as patterns of off-fault damage which should be, in favorable circumstances, directly observed in the field. Earlier work by *Poliakov et al.* [2002] and *Rice et al.* [2005] for 2D steady sub-Rayleigh rupture speeds has revealed expected off-fault damage patterns. Those were dependent on rupture speed, orientation of the pre-stress field among other parameters, and were shown to have some consistency with field observations. Adopting the *Dunham and Archuleta* [2005] extension of the speed regime of the *Rice et al.* [2005] solution for a steady self-healing slip pulse to the supershear regime we study the off-fault damage created during rupture propagation.

The combined assumptions of two dimensions (i.e., an infinite extent of the slipping region parallel to the rupture front), steady-state propagation, and a homogeneous linear-elastic medium cause the Mach fronts to extend infinitely far from the fault and for the amplitude of fields associated with the Mach front to remain undiminished with distance from the fault. To understand the effect of bounding the lateral extent of the slipping region, consider two limiting cases of a rupture on a finite-width fault (with width $2W$ and ignoring, for the present, the free surface). At locations close to the fault and away from its edges (specifically, those much closer that W), the finite fault width is unimportant and two-dimensional models provide an accurate description of the fields. In this extremely near-source region, the Mach front assumes the form of a wedge (Figure 1.4a) and Mach front amplitudes will not diminish with distance from the fault. Of course, this region is further complicated by the presence of dilatational fields of comparable amplitude. At the opposite extreme, consider points far removed from the fault (specifically, at distances greatly exceeding W). From these distant points, the finite-width fault appears as a line source, and S-wave radiation now forms a Mach cone (Figure 1.4b). Since the cross-section of the cone is a circle, geometrical spreading dictates that displacement amplitudes will diminish as the inverse square-root of radial distance from the fault. It is of critical importance to hazard calculations to understand exactly how the transition between these two extremes occurs. Specifically, to what distances are large ground motion and stresses transported for realistic fault geometries? *Bhat et al.* [2007a] hypothesized that the transition between the two limits ought to occur at distances close to W based on the argument that once the rupture saturates in depth the dominant length scale in the problem is related to this depth

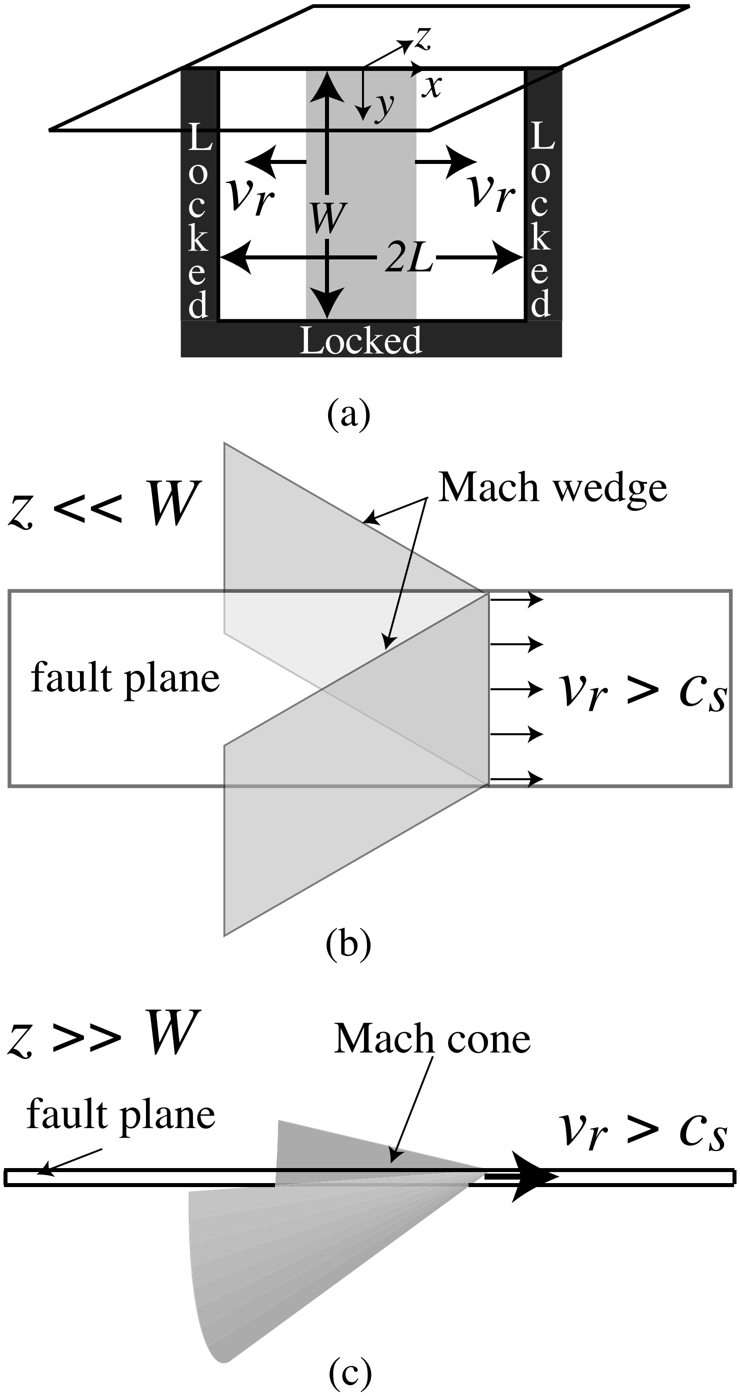

Figure 1.4: (a) & (b) Conceptual models of Mach fronts experienced by two extreme points in a medium hosting supershear ruptures. z is the fault normal distance. Here v_r is the rupture speed and c_s is the shear wave speed of the medium. W is the width of the slipping region also referred to as the width of the seismogenic zone. (c) Model geometry adopted in numerical simulations.

and 3D effects can no longer be ignored.

While investigations have been carried out in the context of 3D kinematic supershear ruptures [*Savage*, 1971; *Ben-Menahem and Singh*, 1987; *Aagaard and Heaton*, 2004; *Bernard and Baumont*, 2005] no such systematic analysis has been done for dynamic supershear ruptures. The aim of chapter 6 is to address the questions raised earlier by considering ruptures in three dimensions, specifically ruptures on a finite-width surface-breaking fault in an elastic half-space.

Chapter 2

Dynamic slip transfer from the Denali to Totschunda Faults, Alaska: Testing theory for fault branching

2.1 Abstract

We analyze the observed dynamic slip transfer from the Denali to Totschunda faults during the M_w 7.9, November 3, 2002, Denali fault earthquake, Alaska. This study adopts the theory and methodology of *Poliakov et al.* [2002] and *Kame et al.* [2003], in which it was shown that the propensity of the rupture path to follow a fault branch is determined by the preexisting stress state, branch angle and incoming rupture velocity at the branch location. Here we check that theory on the Denali-Totschunda rupture process using 2D numerical simulations of processes in the vicinity of the branch junction.

The maximum compression direction with respect to the strike of the Denali fault near the junction has been estimated to range from approximately 73^o to 80^o. We use the values of 70^o and 80^o in our numerical simulations.

The rupture velocity at branching is not well constrained but has been estimated to average about $0.80c_s$ throughout the event. We use $0.60c_s$, $0.80c_s$, $0.90c_s$ and even $1.40c_s$ as parameters in our simulations.

We simulate slip transfer by a 2D elastodynamic boundary integral equation model of mode II slip-weakening rupture with self-chosen path along the branched fault system. All our simulations except for 70^o and $0.90c_s$ predict that the rupture path branches off along the Totschunda fault without continuation along the Denali fault. In that exceptional case there is also continuation of rupture along the Denali fault at a speed slower than that along the Totschunda fault and with smaller slip.

2.2 Introduction

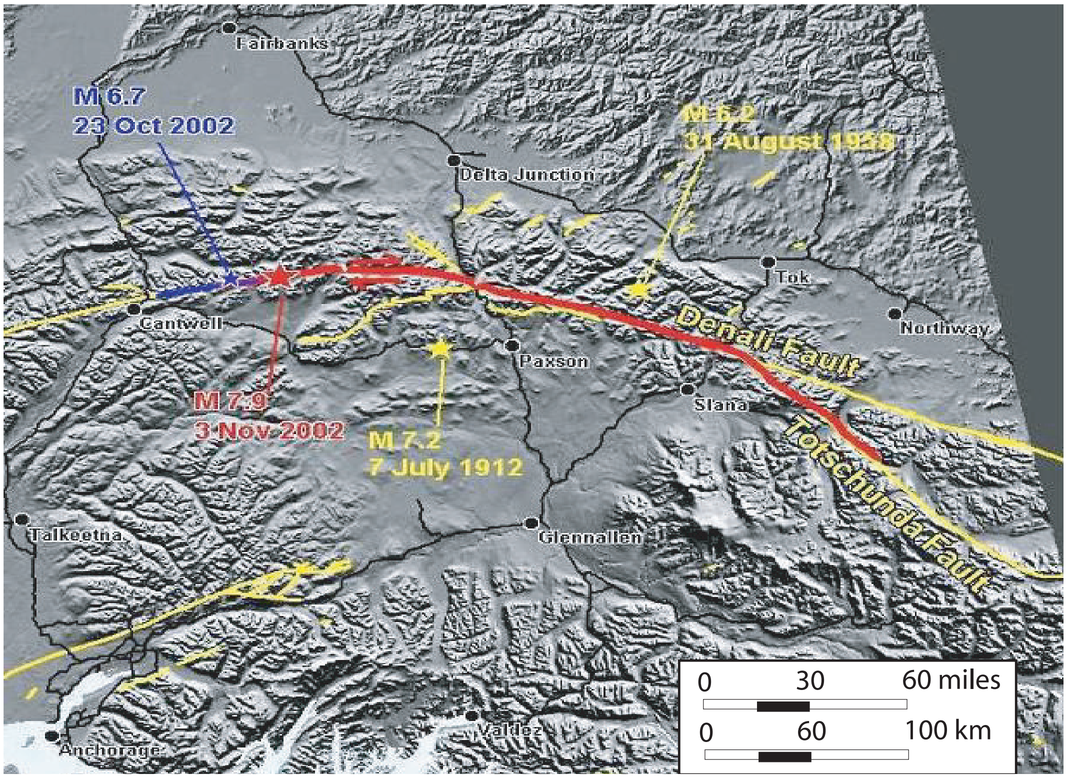

Figure 2.1: Rupture path, solid line, of the M_w 7.9 Denali fault earthquake. A star towards the left of center of the figure marks the epicenter of the 3 November 2002 event. [Figure courtesy: Alaska Division of Geological and Geophysical Surveys.]

A M_w 7.9 earthquake struck central Alaska on November 3, 2002. The Denali fault earthquake (DFE) occurred along the Denali fault system and ruptured a total length of approximately 350 km. The last segment of rupture was along the Totschunda fault, which branches off from the Denali fault, with 68 km of observed surface rupture [Peter Haeussler, USGS, Anchorage; private communication, 2002]; see Figure 2.1 (epicenter: star in center left of the figure). Beyond the branching location there was no surface rupture visible on the Denali fault for at least 25 km [Peter Haeussler, USGS, Anchorage; private communication,

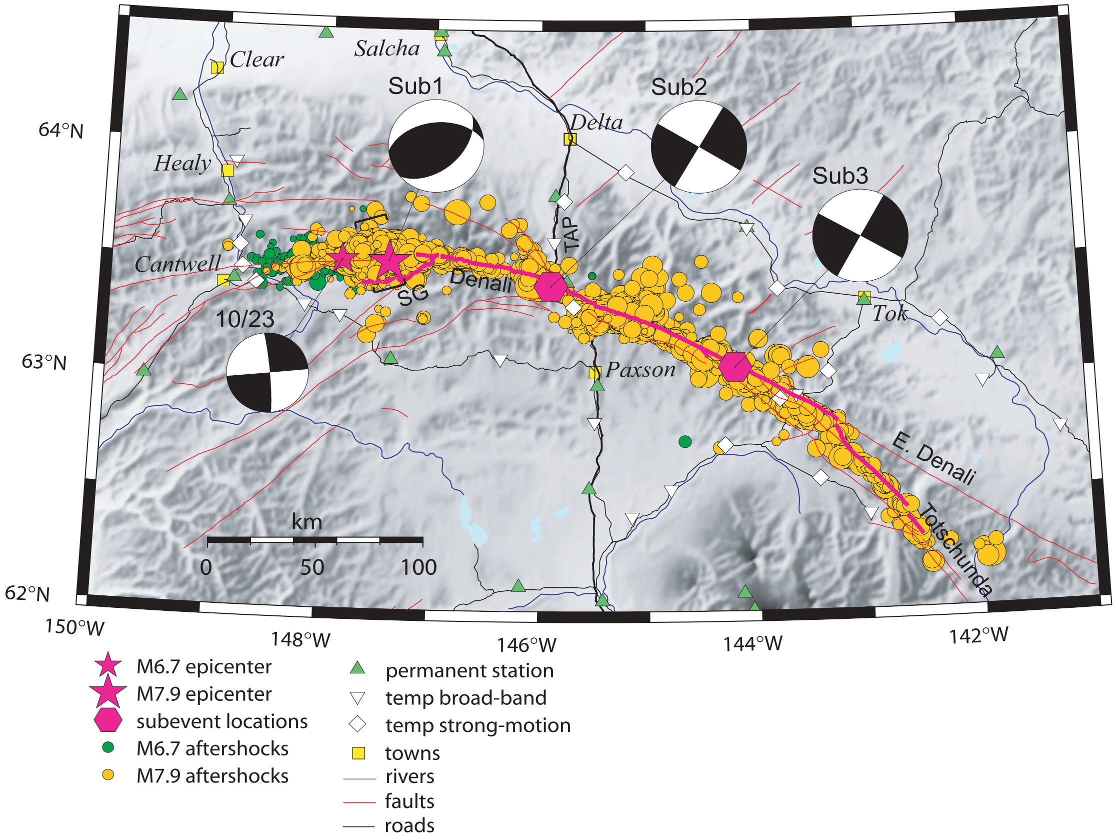

Figure 2.2: Aftershocks of the M_w 7.9 Denali fault event, from *Eberhart-Phillips et al.* [2003], also showing three sub events during the rupture.

2002].

Beyond the Denali-Totschunda branching location the aftershocks of the M_w 7.9 event occurred predominantly along the Totschunda fault segment; Figure 2.2 [*Eberhart-Phillips et al.*, 2003]. Together with the lack of surface rupture along the continuation of the Denali fault, this indicates that after branching the rupture progressed exclusively along the Totschunda fault.

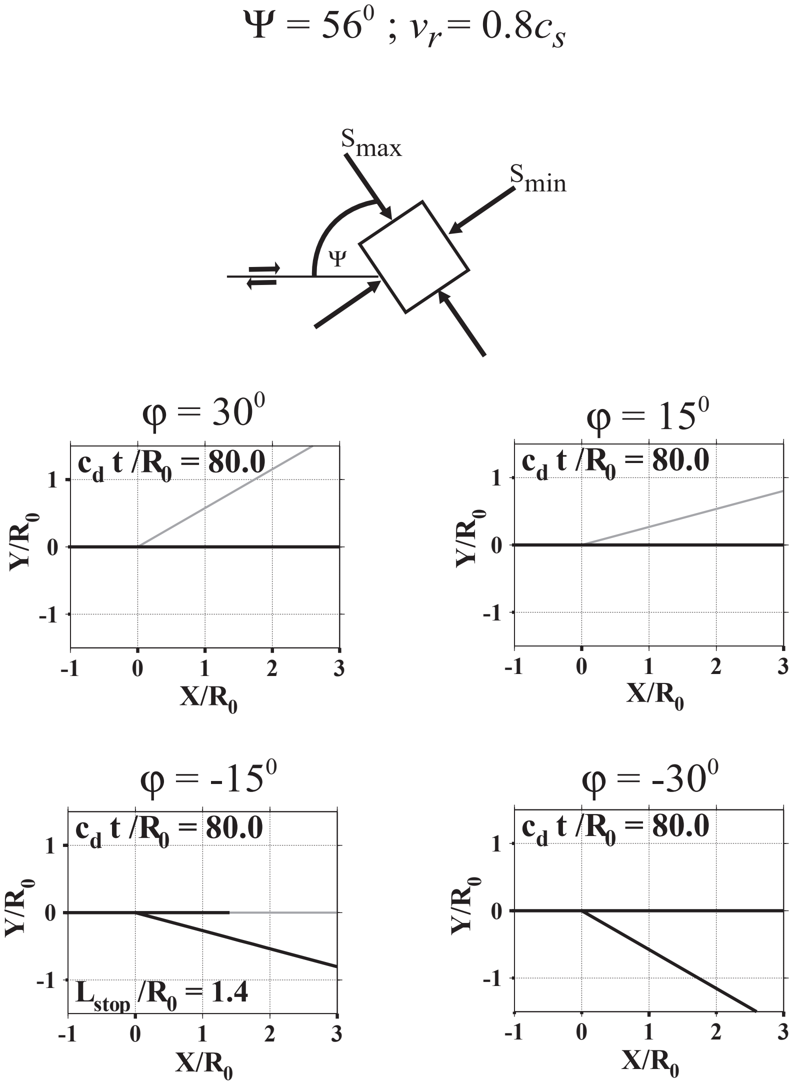

Figure 2.3: Results of 2D numerical simulations from *Kame et al.* [2003] showing the influence of branching angle (φ) on a right-laterally propagating rupture at a velocity (v_r) of $0.8c_s$ near the branching location. The orientation angle Ψ of the principal maximum stress with respect to the main fault is 56^o. The solid black line shows the path of the rupture; fault regions are shown in gray; c_s is the shear wave speed of the medium

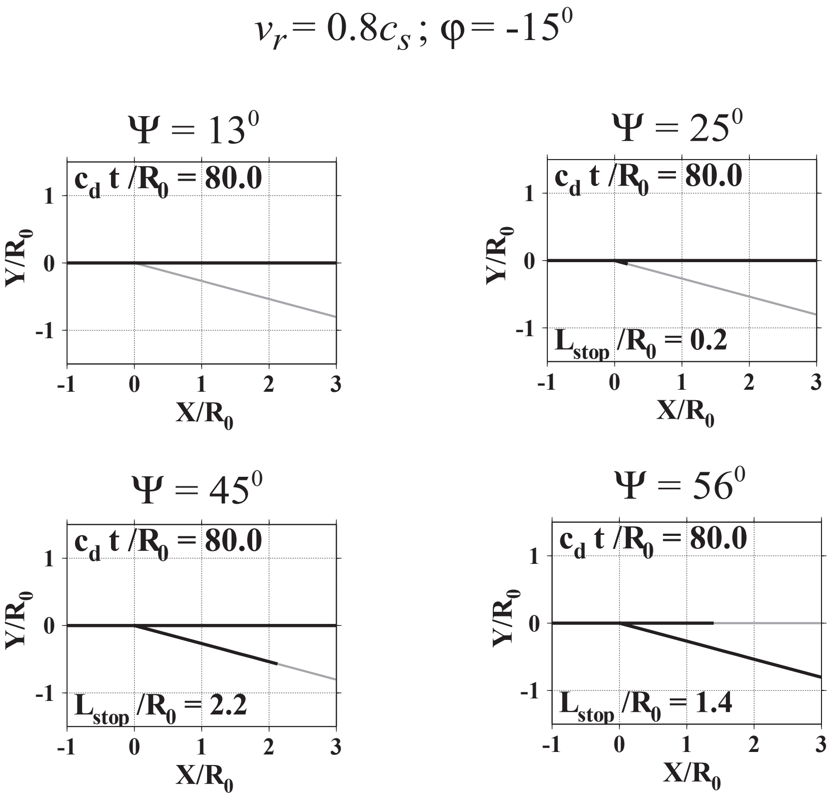

Figure 2.4: Results of 2D numerical simulations from *Kame et al.* [2003] showing the influence of the orientation of the principal maximum stress with respect to the main fault (Ψ) on a right-laterally propagating rupture at a velocity (v_r) of $0.8c_s$ near the branching location. The fault geometry is fixed with the branching angle $\varphi = -15^o$.

2.3 Summary of theory of fault branching

Following the concepts introduced by *Poliakov et al.* [2002] on factors governing fault branching, *Kame et al.* [2003] performed an extensive set of numerical simulations of branching. Those were done in the context of a 2D, mode II, rupture model with a linear slip-weakening friction coefficient, with strength during slip-weakening proportional to the instantaneous local normal stress. They involved a range of branching fault angles (φ) with the primary fault, rupture velocities (v_r) approaching the branching location, and maximum horizontal pre-stress inclinations (Ψ) with the main fault. See Figures 2.3-2.5 for their results which are most relevant for the present discussion; all results are shown for right-lateral rupture.

The results can be summarized as follows. For a given rupture velocity the most vulnerable branch orientations change from those on the compressional side ($\varphi > 0$) to those on the extensional side ($\varphi < 0$) with increasing orientation of the maximum horizontal stress with the main fault (as partly illustrated in Figures 2.3 and 2.4).

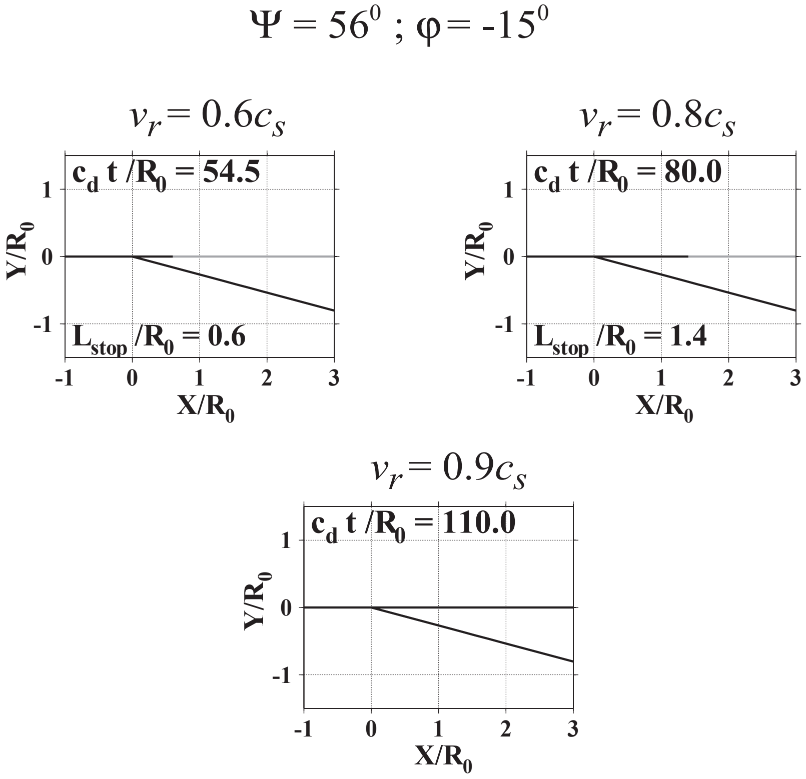

Figure 2.5: Results of 2D numerical simulations from *Kame et al.* [2003] showing the influence of the rupture velocity at the branching location (v_r) on a right-laterally propagating rupture approaching a branched fault segment at $\varphi = -15^o$. The orientation of the principal maximum stress with respect to the main fault (Ψ) is 56^o. The solid line shows the path of the rupture; c_s is the shear wave speed of the medium.

The tendency of the rupture path to proceed exclusively on the branch also increases (and becomes increasingly independent of rupture velocity) as one approaches the limits of maximum stress inclinations with respect to the main fault (0^o or 90^o for exclusive propagation on compressional or extensional branches respectively). With increasing rupture velocity (keeping Ψ constant) the stress shadow effect of one fault on another, which is important for small branching angles, decreases; this makes the rupture path lie less exclusively either along the main fault or along the branched one (Figure 2.5). The parameter L_{stop} /R_0 in the figures refers to the distance, L_{stop}, beyond the branch junction at which propagation has stopped on either the branch or the main fault. L_{stop} is normalized by R_0, which is the length that the slip-weakening zone would occupy along the main fault in low speed propagation [*Kame et al.*, 2003].

2.4 Determination of parameters influencing branching for the Denali fault earthquake

2.4.1 Maximum principal stress direction (Ψ)

Nakamura et al. [1980], have estimated the late Quaternary tectonic stress trajectories in the Aleutians and Alaska, using geologic indicators along continental Alaska. Their results show averaged directions of maximum horizontal compression. The principal stress direction near to the Denali-Totschunda branching region is estimated from their results as approximately 75^o with respect to the main fault. *Estabrook and Jacob* [1991] later provided a map of maximum horizontal compression-determined stress trajectories from a variety of sources, including seismic focal mechanisms, volcanic, geologic fault and bore-

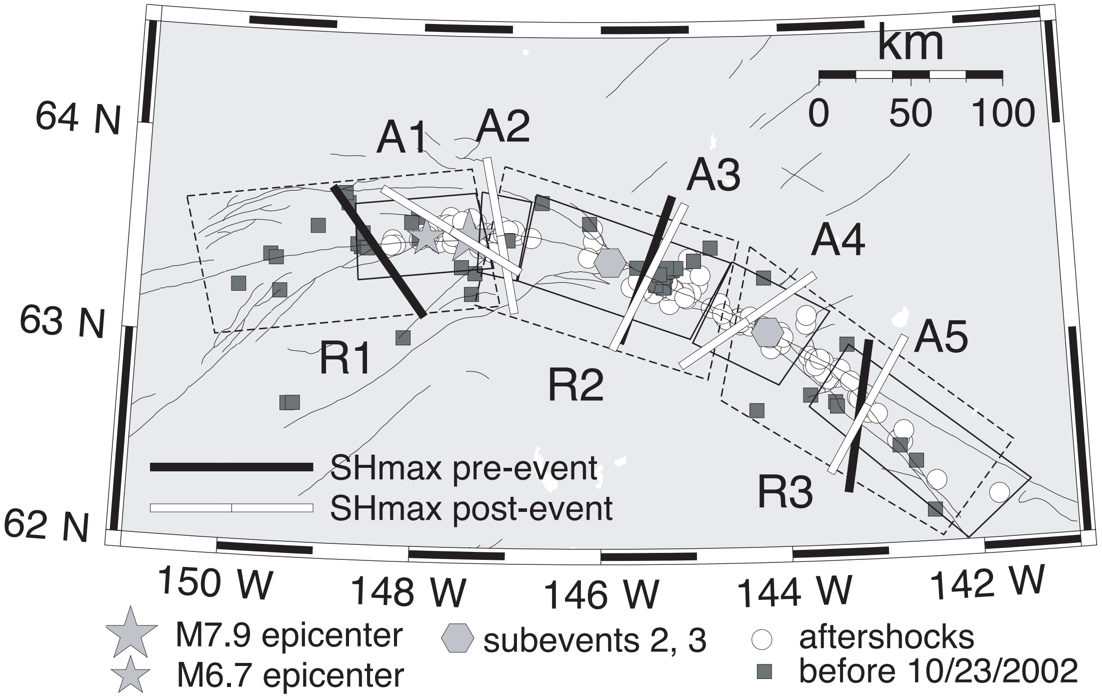

Figure 2.6: Maximum principal stress orientations prior to the 2002 Denali fault earthquake sequence (black bars) and for the 2002 Denali fault earthquake sequence aftershocks (white bars), from [*Ratchkovski*, 2003]. Dashed polygons outline inversion blocks for events prior to October 2002. Solid polygons are the inversion regions using the aftershocks. Solid lines are the mapped fault traces. Subevent locations [*Eberhart-Phillips et al.*, 2003] of the magnitude 7.9 earthquake are shown as hexagons.

hole breakout data, for Alaska, the Aleutians, and the Bering Sea. This was based on the results of *Nakamura et al.* [1980] and *Estabrook et al.* [1988]. The principal stress direction nearest to the Denali-Totschunda branching region was again reported to be at approximately 75^o with respect to the strike of the Denali fault just before branching.

Azimuths of maximum and minimum horizontal compression, obtained using stress tensor inversion from focal mechanisms, were determined along different fault systems in central Alaska by *Ratchkovski and Hansen* [2002]. All of their regions were on the order 100 to 400 km west of the branching location, and most also to the north. The principal stress direction nearest to the Denali-Totschunda branching region was found to be approximately 73^o (by extrapolating results from closest locations) with respect to the strike of the Denali fault just before branching.

Based on the more recent focal mechanism inversions of *Ratchkovski* [2003] it can be seen that as one traverses along the Denali fault eastward, from the epicenter, the direction of principal maximum stress, before the earthquake, rotates slightly in a clockwise sense from R1 to R2 and counter-clockwise from R2 to R3 (Figure 2.6). The direction of principal maximum compressive stress close to the Denali-Totschunda branching location was therefore inclined at about 80^o with respect to the Denali fault prior to the DFE.

We choose two values of Ψ, 70^o and 80^o, to cover the range of observations. The latter better represents measurements near the branching junction; the former is an approximate lower bound based on regional stress studies. Based on the results of *Kame et al.* [2003], Ψ=70^o is a conservative estimate for our simulations because, as it was noted earlier, the likelihood of the rupture taking the branch exclusively increases with increasing Ψ and becomes increasingly independent of the rupture velocity when approaching the branching location. We will show that the rupture path is predicted to be captured exclusively by the branch in nearly all cases studied when Ψ=70^o and in all cases when Ψ=80^o.

2.4.2 Rupture velocity (v_r)

The average rupture velocity during the DFE seems to be about 80% of the shear wave speed [*Kikuchi and Yamanaka*, 2002], although the velocity as the branch was approached is not yet constrained very well. Inversion of strong motion records by *Eberhart-Phillips* *et al.* [2003] revealed three sub-events (Figure 1b) during the DFE with the second and the third subevent occurring at about 125 km and 50 km to the west of the Denali-Totschunda branching location respectively. Best fitting inversion required a high rupture velocity of about 3.5 km/s between sub events 2 and 3. *Ellsworth et al.* [2004] note that the rupture actually went supershear near Pump Station 10 (PS10), whose location is much further to the west of the branching location and is very close to subevent 2. They also mention that the rupture velocity is around $0.80c_s$ for about 20 km east of PS10. We therefore carry out our numerical simulations for different values of rupture velocity when approaching the branching location, including supershear rupture velocity. *Rousseau and Rosakis* [2003] have extended branching concepts like in *Poliakov et al.* [2002] to the supershear regime.

2.4.3 Branching angle (φ)

The Totschunda fault branches away from the Denali fault, to the extensional side, at an angle of approximately 15^o. The angle was measured from a fault map of central Alaska provided by *Savage and Lisowski* [1991].

Wallace et al. [2002] suggested that the northern part of the Totschunda fault system may consist of multiple discontinuous southeast striking strands and are locally connected by south-striking step-over faults. This may reflect the immaturity of the northern Totschunda system. The aim of our study is to do a first order analysis of the branching process by simplifying the geometry. This approach to a simpler model is supported by examination of an aerial photo (Peter Haeussler, personal communication) of the branch location, which suggests a simple branching geometry.

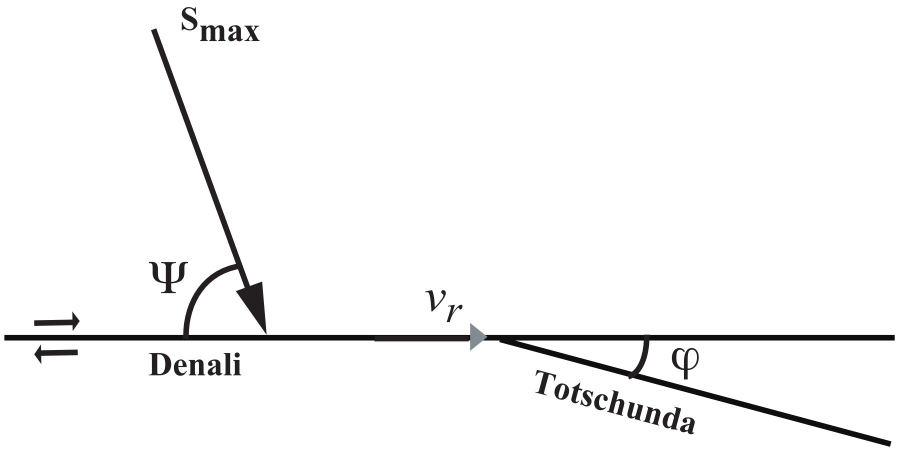

Figure 2.7: Fault geometry used in the model along with the associated parameters.

2.5 Slip-weakening coulomb friction law

To describe the failure criterion on the faults, we use the slip-weakening friction law [*Ida*, 1972, *Palmer and Rice*, 1973, *Andrews*, 1976]. As shown in Figure 2.8, for the simple linear-weakening version, when the normal stress is constant, the shear strength, τ, decreases linearly in this model with ongoing fault slip, Δu, from a peak strength, τ_p to a residual strength,τ_r , and then remains constant after the slip has reached a critical value D_c.

$$\tau = \tau_r + (\tau_p - \tau_r)(1 - \Delta u/D_c)H(1 - \Delta u/D_c) \tag{2.1}$$

where $H(.)$ is the Heaviside function.

We add to this model the Coulomb friction law that describes the shear stress as a linear function of the instantaneous normal stress, $\tau = -f\sigma_n$. The friction coefficient, f, decreases from an initial value, f_s, the static friction coefficient, to f_d, the dynamic friction coefficient, with ongoing fault slip and then remains constant. Thus, $\tau_p = -f_s\sigma_n$ and $\tau_r =$

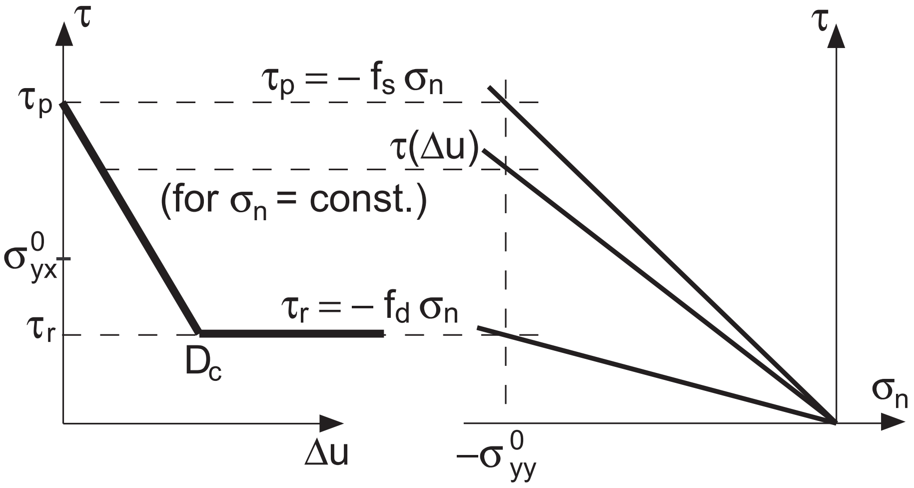

Figure 2.8: slip-weakening Coulomb friction law [*Kame et al.*, 2003]. The peak and residual strength (τ_p, τ_r), and strength (τ) at any particular amount of slip (Δu), is proportional to normal compressive stress ($-\sigma_n$).

$-f_d\sigma_n$ in equation (2.1). *Andrews* [1976] defined a parameter S $[= (\tau_p - \sigma^0_{yx})/(\sigma^0_{yx} - \tau_r)]$ associated with the slip-weakening law where σ^0_{yx} is the initial shear stress on the fault. This parameter has a critical value (approximately 1.77) below which the rupture would propagates with a speed that ultimately transitions to supershear for propagation paths that are sufficiently long compared to the size of the nucleation zone.

This model (slip-weakening Coulomb friction law) has been widely used as a failure criterion in describing earthquake rupture processes because of its simplicity and its ease to implement in numerical methodology. In spite of its simplicity the slip-weakening Coulomb friction law allows the explanation of many complex dynamic rupture processes.

2.6 Summary of results

Numerical studies were conducted using the boundary integral equation method elaborated in Appendix A. A long running rupture, which is depth limited, as for the DFE event, cannot be modeled in a 2D framework. However, following the theoretical concepts outlined in *Poliakov et al.* [2002], *Kame et al.* [2003] and *Rousseau and Rosakis* [2003], we can argue that the critical factor, other than the geometry and pre-stress, is the rupture speed as the branch is approached. This can be suitably simulated in 2D, with far greater grid refinement than in 3D simulations, by nucleating a 2D rupture at various distances from the branching location. Given the present computing capabilities, the 2D formulation allows adequate grid refinement to fully resolve the slip-weakening process, a feature which is not generally achieved in 3D simulations. Nevertheless, the rupture phenomenon is clearly a 3D one, and much has been learned about branching from such simulations by *Aochi et al.* [2000a,b], *Aochi and Fukuyama* [2002], *Oglesby et al.* [2000a,b] and *Oglesby and Day* [2001].Figure 2.7 shows the fault geometry adopted for our simulations, of which preliminary results were reported in *Bhat et al.* [2002].

Since the S ratio governs the nature of rupture (supershear or sub-Rayleigh), a desired value is first chosen. This would then give the initial shear stress acting on the fault (as a fraction of $-\sigma_{yy}^{o}$) if values of f_s and f_d are assumed. If the pre-stress field is normalized by the fault normal pre-stress then the normalized fault parallel pre-stress can be obtained by using the desired value of Ψ, the orientation of the principal maximum compressive stress with the primary fault. The pre-stress parameters thus obtained must be checked so that the Mohr-Coulomb failure criterion based on f_s is not violated either on the primary or the branched fault.

Dreger et al. [2004] noted, in their dynamic source modeling of the DFE using a 3-D finite element method, that the rupture actually jumps ahead of the primary rupture front by 14 km, triggering slip on the Totschunda fault. We do not observe such a phenomenon in our simulations.

Our calculations were done for various values of v_r and Ψ at the Denali-Totschunda branching location.

$$\boxed{\boldsymbol{v_r = 0.60c_s\ ;\ \Psi = 70^o\ ;\ f_s = 0.60\ ;\ f_d = 0.12\ ;\ S_{Den} = 3\ ;\ S_{Tot} = 0.6}}$$

When the velocity of the rupture approaching the branching location at the Totschunda fault was $0.60c_s$, it was observed that the rupture branches completely onto the Totschunda fault. Figure 2.9 shows the combined plots of slip velocity along both the Denali and Totschunda faults. It is clearly observed that once the rupture on the Denali fault crosses the branching location the slip velocity decreases rapidly with time. This is a clear indication of the fact that the main fault can no longer accommodate slip beyond the branching location.

At time step 365 the rupture has reached the branching point. We observe in our simulations at this time step that the slip velocity at the right end of the rupture front accelerates briefly before slowing down. This may be a result of numerical oscillations in our calculations.

$$\boxed{\boldsymbol{v_r = 0.80c_s\ ;\ \Psi = 70^o\ ;\ f_s = 0.60\ ;\ f_d = 0.12\ ;\ S_{Den} = 3\ ;\ S_{Tot} = 0.6}}$$

For this case, the rupture again branches along the Totschunda fault with no further continuation on the Denali fault. Figure 2.10 shows slip velocity along both the Denali and Totschunda faults. It is clear, as in the previous case, that beyond the branch, the slip

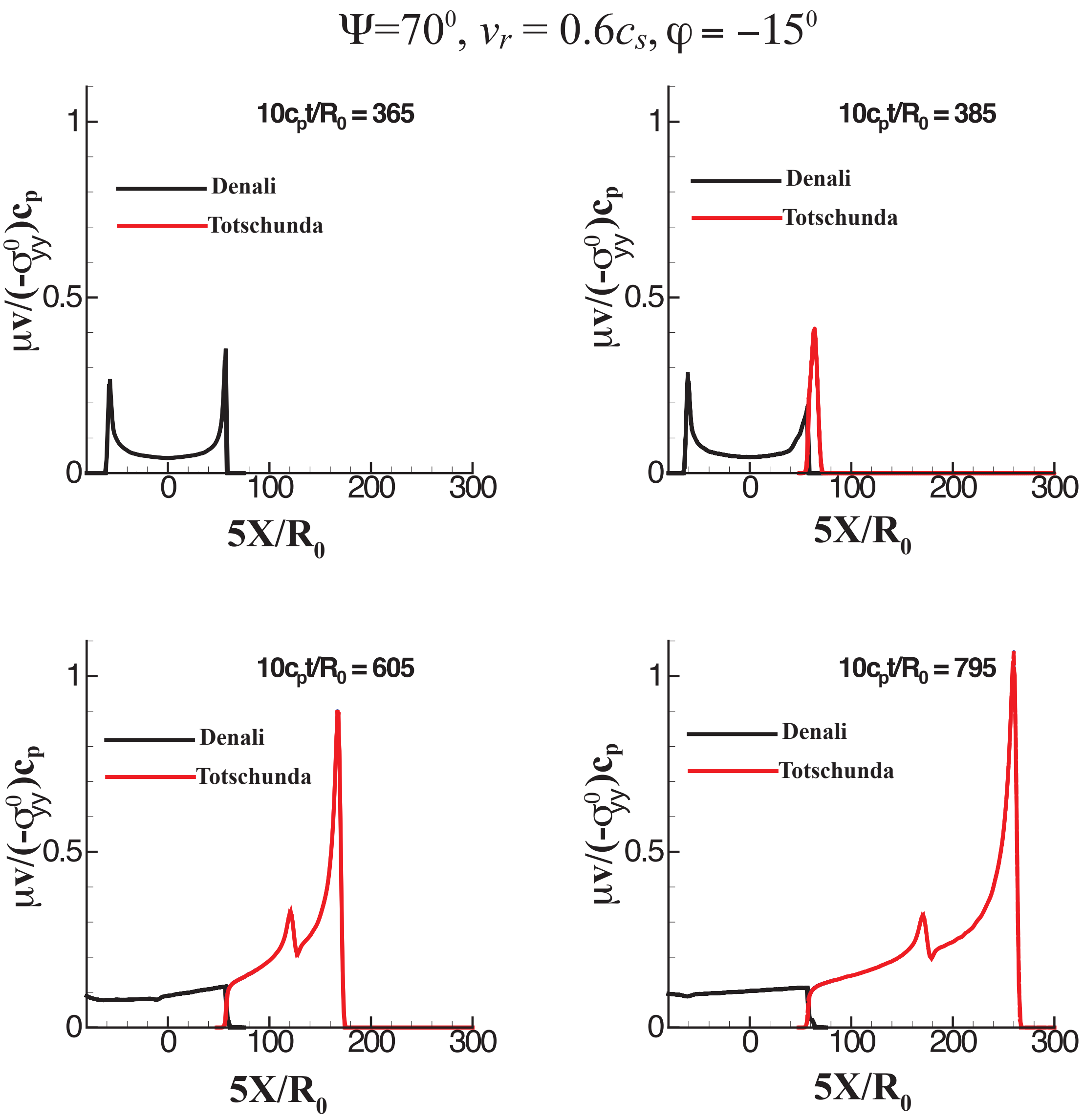

Figure 2.9: Plot of slip velocity along the Denali and Totschunda fault segments for $\Psi = 70^o$;$v_r = 0.60c_s$. Slip velocity variation along the Totschunda fault is projected onto the Denali fault. The Totschunda fault begins at $5X/R_0$ = 58. v_r, c_s, R_0, μ, ν and c_p represent the rupture velocity near the branching point, the S-wave speed of the medium, the size of the slip-weakening zone, the shear modulus of the medium, the slip velocity, the initial normal compressive stress and the P-wave velocity of the medium respectively.

velocity diminishes rapidly on the Denali fault.

$\boxed{\boldsymbol{v_r = 0.90c_s \; ; \; \Psi = 70^o \; ; \; f_s = 0.60 \; ; \; f_d = 0.12 \; ; \; S_{Den} = 3; S_{Tot} = 0.6}}$

Earlier studies by *Kame et al.* [2003] showed that for this value of rupture velocity and for Ψ = 56^o, the rupture would tend to propagate both along the main and the branched fault in the extensional side with a small branching angle of 15^o. The same happens in this case with Ψ = 70^o but not, as we shall see next, when Ψ = 80^o. Figure 2.11 shows the variation of slip velocity along the Denali and Totschunda faults. As can be seen in this figure, the slip velocity on the Denali fault beyond the Totschunda fault is significant resulting in simultaneous propagation of rupture along both faults beyond the branching location albeit at a slower rate and with less slip on the Denali fault than on the Totschunda fault.

$\boxed{\boldsymbol{v_r = 0.87c_s \; ; \; \Psi = 80^o \; ; \; f_s = 0.40 \; ; \; f_d = 0.05 \; ; \; S_{Den} = 4 \; ; \; S_{Tot} = 0.4}}$

As stated earlier, the likelihood of the rupture propagating exclusively along the extensional branch increases with increasing inclination of Ψ. In this case we increase Ψ to 80^o and maintain the rupture velocity at$0.87c_s$ while approaching the Totschunda fault. In this model, we changed the friction coefficients because with the earlier values of friction coefficients the pre-stress field violated the Mohr-Coulomb failure criterion outside the fault zones.

Our results show that, for the above case, the rupture proceeds rapidly along the Totschunda fault with almost no continuation on the Denali fault. Figure 2.12 shows slip velocity along both the Denali and Totschunda faults. Again, beyond the Totschunda fault, the slip velocity diminishes quickly on the Denali fault. There is some continuation of rupture on the

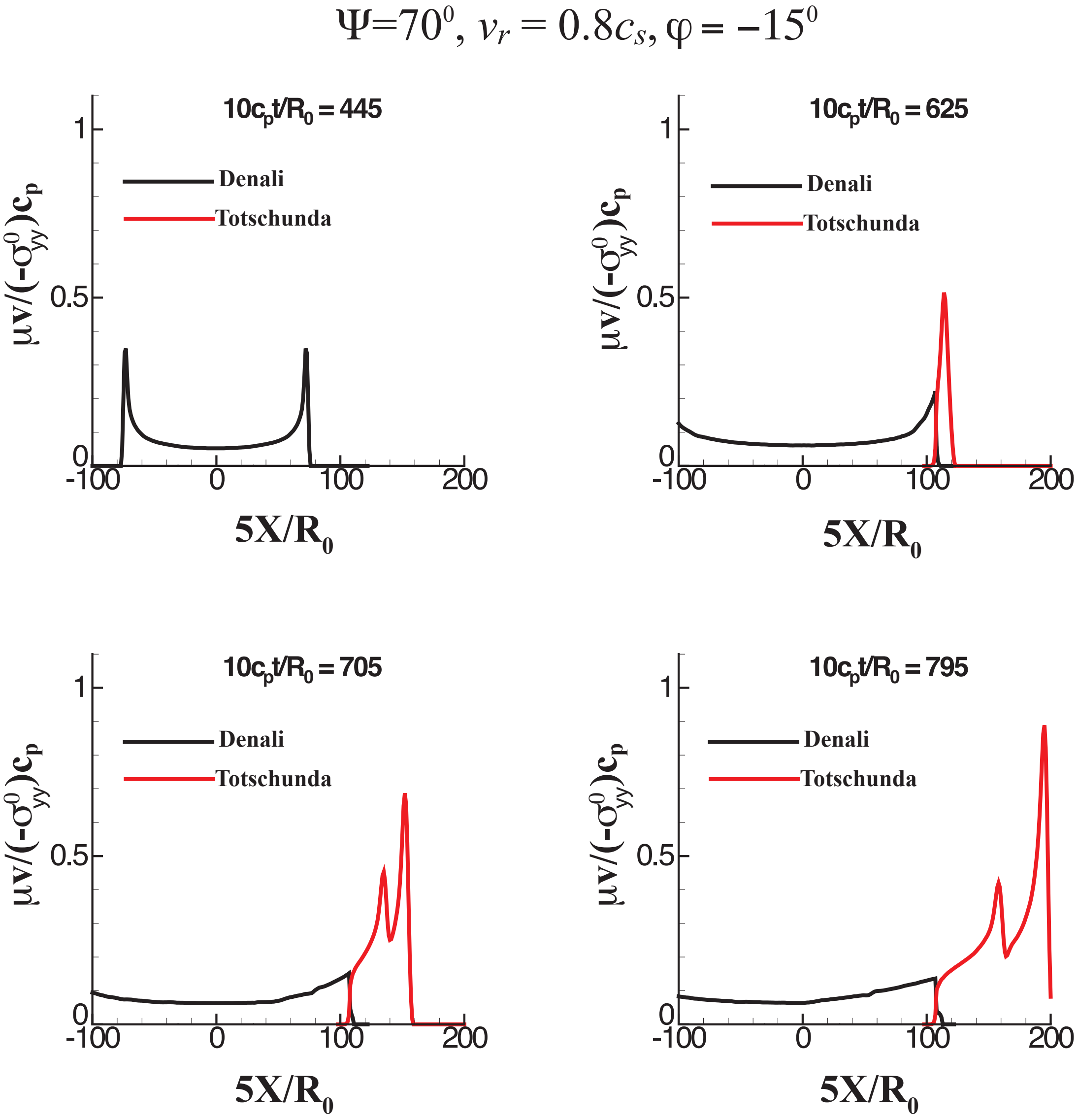

Figure 2.10: Slip velocity along the Denali and Totschunda fault segments for $\Psi = 70^o$;$v_r = 0.80c_s$. Slip velocity variation along the Totschunda fault is projected on the Denali fault. Totschunda fault begins at $5X/R_0$ = 108.

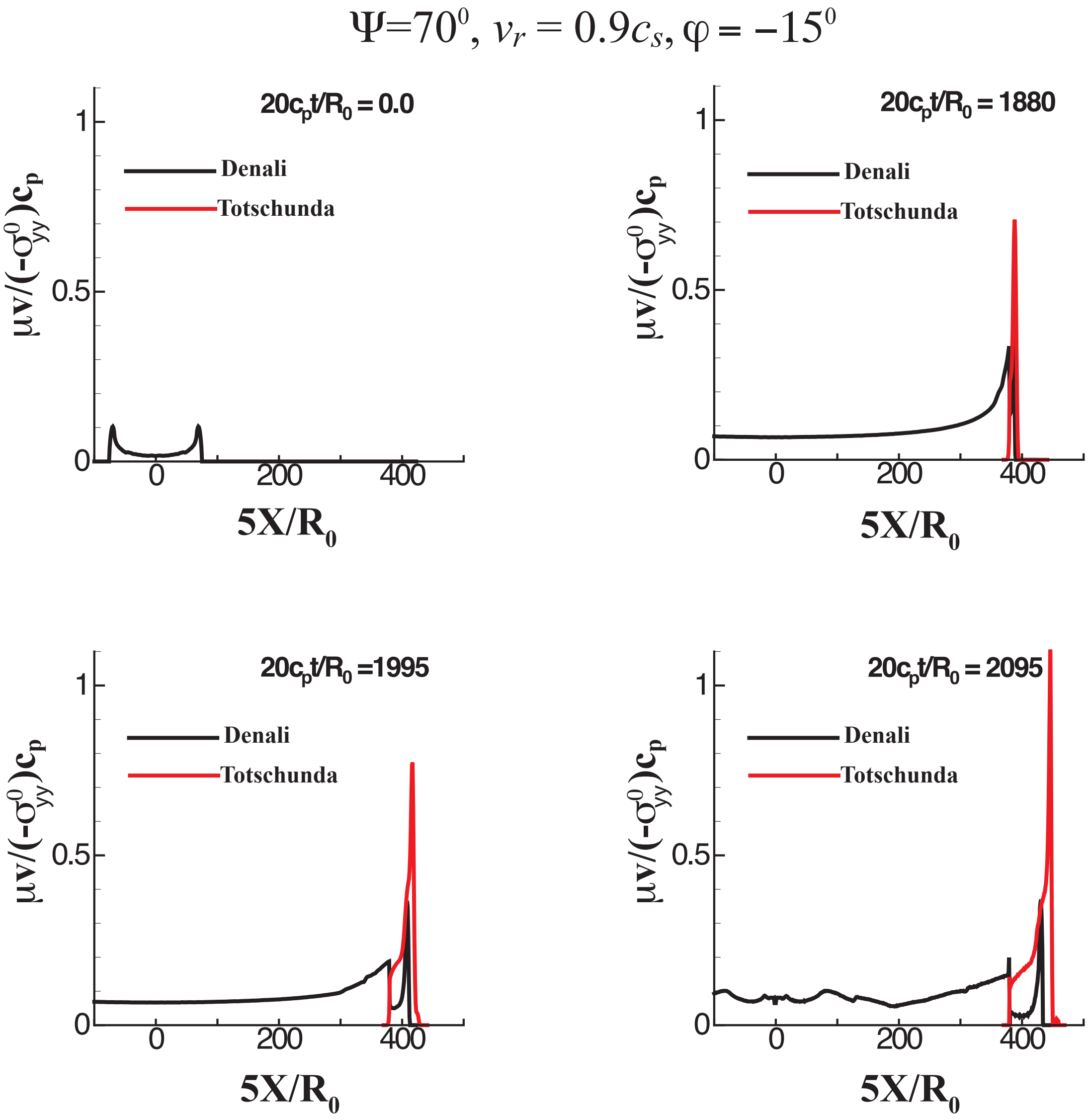

Figure 2.11: Slip velocity along the Denali and Totschunda fault segments for $\Psi = 70^o$;$v_r = 0.90c_s$. Slip velocity variation along the Totschunda fault is projected onto the Denali fault. The Totschunda fault begins at $10X/R_0$ = 380.

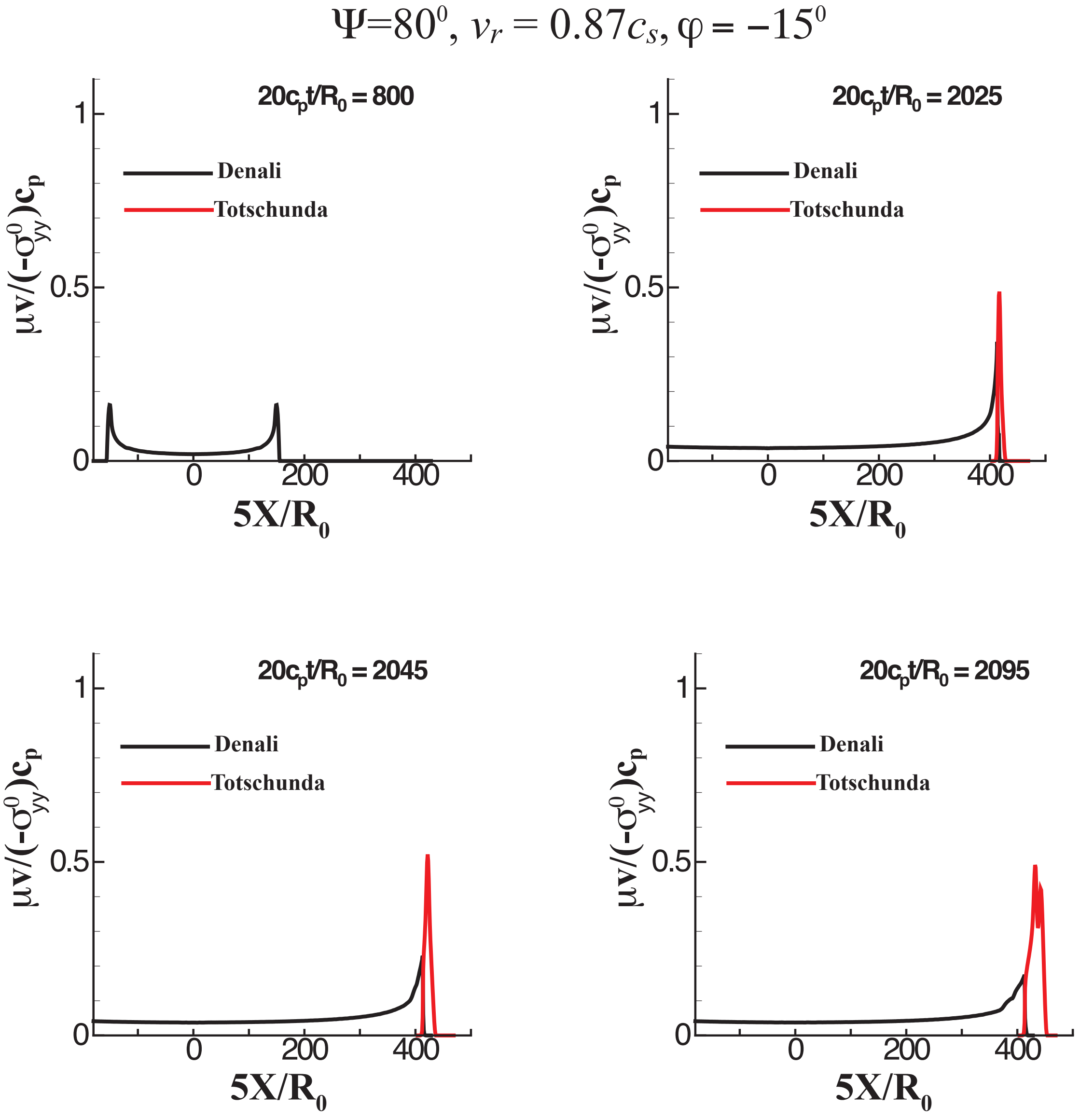

Figure 2.12: Slip velocity along the Denali and Totschunda fault segments for $\Psi = 80^o$;$v_r = 0.87c_s$ case. Slip velocity variation along the Totschunda fault is projected onto the Denali fault. The Totschunda fault begins at $10X/R_0 = 414$.

Denali fault beyond the Totschunda fault, although this length is of the order of R_0, the size of the slip-weakening zone. This is negligible in comparison with the progress of rupture on the Totschunda fault. Hence, we can conclude here that the rupture takes the Totschunda fault exclusively.

$\boxed{\boldsymbol{v_r = 1.40c_s \ ; \ \Psi = 70^o \ ; \ f_s = 0.50 \ ; \ f_d = 0.10; S_{Den} = 1 \ ; \ S_{Tot} = 0.09}}$

While we have no reason at present to think that the rupture velocity was supershear near the branch junction, we also performed a simulation in which the rupture velocity when approaching the Denali-Totschunda branching location was $1.40c_s$. To make an appropriate choice for the S ratio so that the rupture velocity was supershear and the Mohr-Coulomb failure criteria were not violated by the pre-stress field, we were required to choose the above values for dynamic and static coefficients of friction.

Slip velocity, Figure 2.13, on the Denali and Totschunda faults shows that on the part of the Denali fault beyond the junction, the slip velocity decays rapidly, suggesting that segment of the Denali fault beyond the Totschunda intersection will ultimately stop slipping. On the Totschunda fault the speed briefly reduced to sub-Rayleigh then went supershear again, exhibiting a pattern similar to those observed in other cases of sub-Rayleigh to supershear transitions, leaving pulses that move as Rayleigh waves on what was the crack surface before the intersonic transition, and provide a multi-pulse character to the slip-rate distribution.

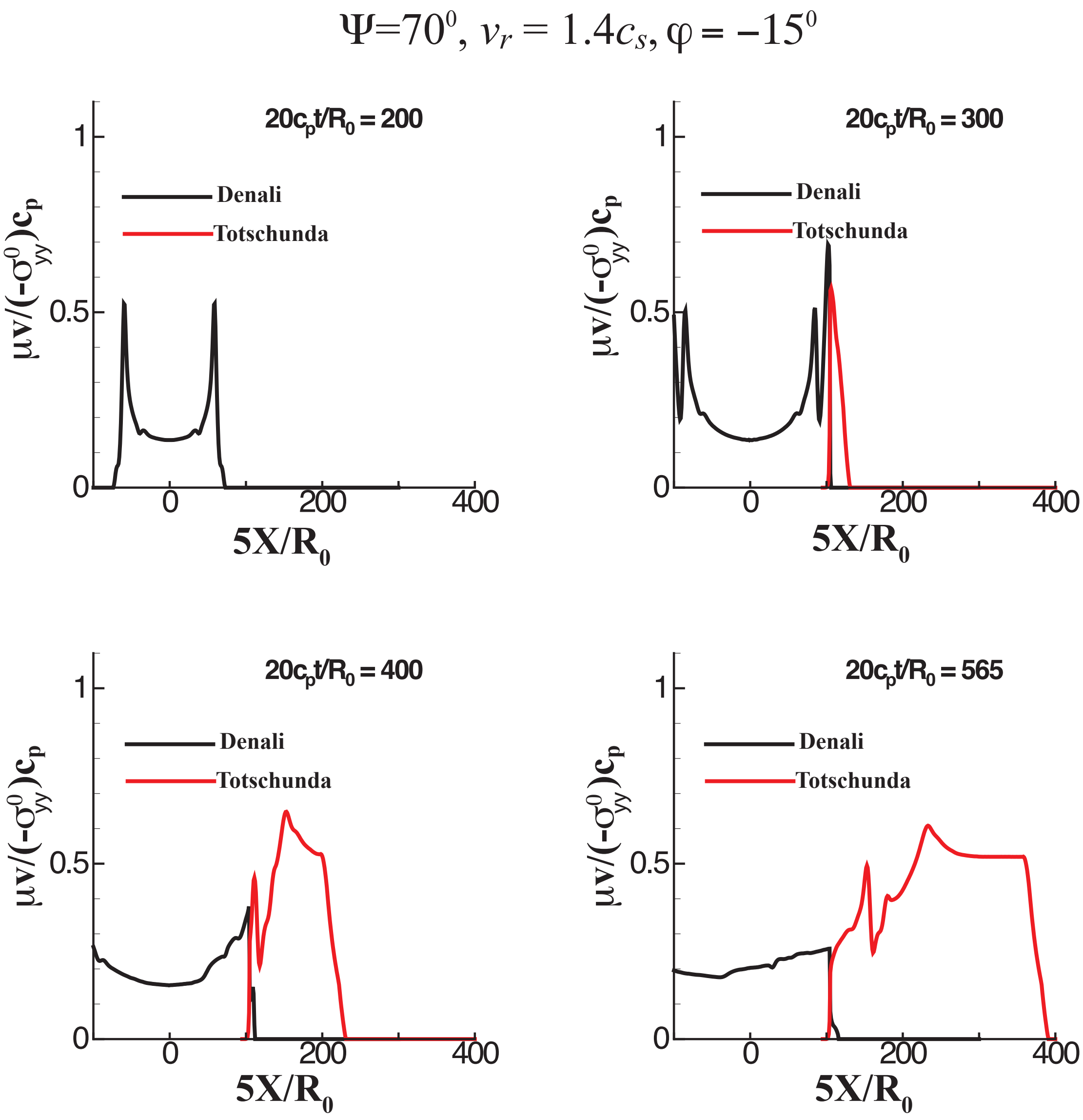

Figure 2.13: Slip velocity along the Denali and Totschunda fault segments for $\Psi = 70^o$; $v_r = 1.40c_s$. Slip velocity variation along the Totschunda fault is projected onto the Denali fault. The Totschunda fault begins at $10X/R_0$ = 104.

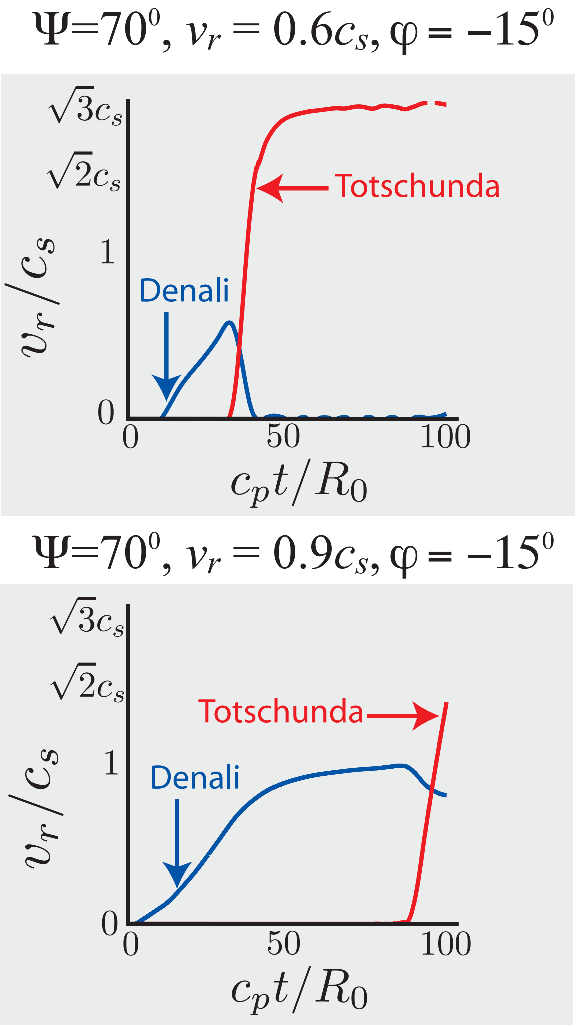

Figure 2.14: Variation of the rupture velocity along the Denali and the Totschunda fault segments for $\Psi = 70^o$;$v_r = 0.60c_s$ and $\Psi = 70^o$;$v_r = 0.90c_s$ cases. v_r, c_s, R_0, and $c_p = \sqrt{3}c_s$ represent the rupture velocity near the branching point, the S-wave speed of the medium, the size of the slip-weakening zone, and the P-wave velocity of the medium respectively. The rupture velocity is determined using a smoothing procedure described in Appendix B.

2.7 Summary and conclusions

The theory of fault branching developed by *Poliakov et al.* [2002] and *Kame et al.* [2003] was tested on the recent Denali fault earthquake using the numerical method developed by *Kame et al.* [2003]. The theoretical stress analysis of a propagating mode II rupture suggests that the tendency to follow a branch is influenced by rupture velocity v_r approaching the branch, preexisting maximum compressive stress inclination Ψ, and prospective branching angle φ. This study provides another comparison of the rules of branching with a field case; five other such field cases were discussed by *Kame et al.* [2003].

We numerically simulated the observed slip transfer from the Denali to Totschunda faults by the methodology of *Kame et al.* [2003] which uses a 2D elastodynamic boundary integral equation model of mode II rupture with self-chosen path along a branched fault system. The strength of the faults was assumed to follow a Coulomb law with a friction coefficient that slip-weakens from its static to dynamic value. Figure 2.14 shows the rupture velocity variation on the Denali and Totschunda faults for cases Ψ = 70^o; v_r = $0.60c_s$ and Ψ = 70^o; v_r = $0.90c_s$ respectively. All but one of our simulations for incoming sub-Rayleigh rupture velocities predict that the rupture path will branch off along the Totschunda fault without continuation along the Denali fault. The exception is the case when the prestress inclination is 70^o, a lower limit to the plausible range, and incoming rupture speed at the branching point is $0.90c_s$. In this case rupture follows the branch but there is also a continuation of rupture along the Denali fault beyond the branching location, at a lower speed than that along the Totschunda fault. However when the prestress inclination is steeper, at 80^o, the rupture chooses Totschunda exclusively when its velocity near the branching location is around $0.90c_s$. We also see exclusive continuation of rupture on the Totschunda fault when the rupture is supershear, $1.40c_s$.

Chapter 3

Role of Finite Branches in Dynamic Rupture Propagation

3.1 Abstract

We analyze earthquake ruptures propagating along a straight “main” fault and encountering a finite-length branch fault. Such intersections are often observed in natural fault systems. The predicted effects of the interaction with the branch that we report can be remarkable; they can strongly perturb the propagation velocity on the main fault and, in some cases, even arrest that propagation. Earlier work [*Kame et al.*, 2003; *Bhat et al.*, 2004] emphasized the role of the fault pre-stress state, branch geometry (i.e., branching angle), and the incoming rupture velocity at the branching junction in determining whether the rupture would follow the branch or continue on the main fault or both, through simulations which did not let a rupture on the branch encounter a barrier or a fault end (called “infinite” branch cases henceforth). In this study we look at “finite” branch cases, and study the effect also of branch length, with rupture being blocked from propagation beyond the branch end. We show that in general rupture termination on a compressional branch little affects propagation on the main fault compared to the infinite branch cases. For branches on the extensional side, we show in some cases, that whereas an infinite’ branch would have allowed (or stopped) rupture propagation on the main fault, a finite branch stops (or allows) propagation on the main fault. Such results have a dependence on branch length that we document. We also illustrate branch-related complexities in rupture velocity evolution which could be one of the sources of the high-frequency content of strong ground motion record. Complexities in the slip distribution, often associated with a presumed heterogeneous strength distribution along the fault, can also be observed when rupture is terminated on a branch.

3.2 Introduction

Large earthquake events are complex processes. These complexities show up in the form of short bursts of high-frequency ground motion, branches and offsets in the rupture path, and asymmetry in the inferred slip pattern, to name a few. The source of seismic complexities is normally thought to be associated with heterogeneity in the stress and/or strength distribution along the fault. The other important question of how an earthquake stops is also often attributed to spatial heterogeneity in the strength/stress distribution along the fault. The aim of this study is to explore another mechanism to explain seismic complexities, namely, a class of geometric complexities in the form of branches.

A fault system has in general geometric complexities, long known to geologists [*King and Nabelek*, 1985; *Sibson*, 1985; *King*, 1986; *Wesnousky*, 1988; *Knuepfer*, 1989; *Aydin and Schultz*, 1990; *Yule and Sieh*, 2003; *Brankman and Aydin*, 2004; *Wesnousky*, 2006, among others], like bends, branches, step-overs, and sub-parallel strands at different length scales (eg. 1992 Landers earthquake, Figure 3.1). The interaction between these geometric complexities like fault bends and jogs and rupture has been observed for various earthquakes. For example, the 1992 Landers event branched from the Johnson Valley Fault to the Kickapoo fault with part of the rupture continuing on the Johnson Valley fault for four kilometers beyond the branching junction [*Sowers et al.*, 1994; *Kame et al.*, 2003]. The 2002 Denali event branched off from the main Denali fault to the Totschunda fault with no observable surface slip on Denali fault beyond the branching junction [*Bhat et al.*, 2004]. Similar examples of branching from various other earthquakes are discussed in *Kame et al.* [2003].

Numerical modeling of geometric complexities and their interaction with the rupture process has been done by *Tada and Yamashita* [1997], *Kame et al.* [2003] and *Bhat et al.* [2004], among others, for a rupture branching through a fault system in 2D using the Boundary Integral Equation method (see Appendix A), and by *Duan and Oglesby* [2005] using the Finite Element method. *Aochi et al.* [2000a,b, 2002, 2005] and *Aochi and Fukuyama* [2002] addressed similar problems in 3D using the BIE method, and *Oglesby et al.* [2003a], *Dreger et al.* [2004] and *Oglesby* [2005] using the FE method.

In this work we emphasize the role of small finite branches off the main fault in explaining certain complexities associated with the whole rupture process like large scale asymmetry in the slip pattern and even arrest of rupture propagation on the main fault due to the branch.

3.3 Dynamic rupture model

3.3.1 Model geometry and properties

We consider a two dimensional mode II rupture propagating in a medium that is unbounded, homogeneous, isotropic and linear elastic. The rupture propagates right-laterally as in *Kame et al.* [2003]. We also assume that the slip along the fault is purely tangential and hence do not allow any opening.

The aim is to understand the influence of a finite branch fault [Figure 3.2] on rupture propagation along a main fault. We compare results with those established by *Kame et al.* [2003] and *Bhat et al.* [2004] who analyzed an “infinite” branch, in the sense that their branch fault had no end, or other imposed barrier-like feature, that was encountered during the time of simulation and hence that would would stop the rupture along it.

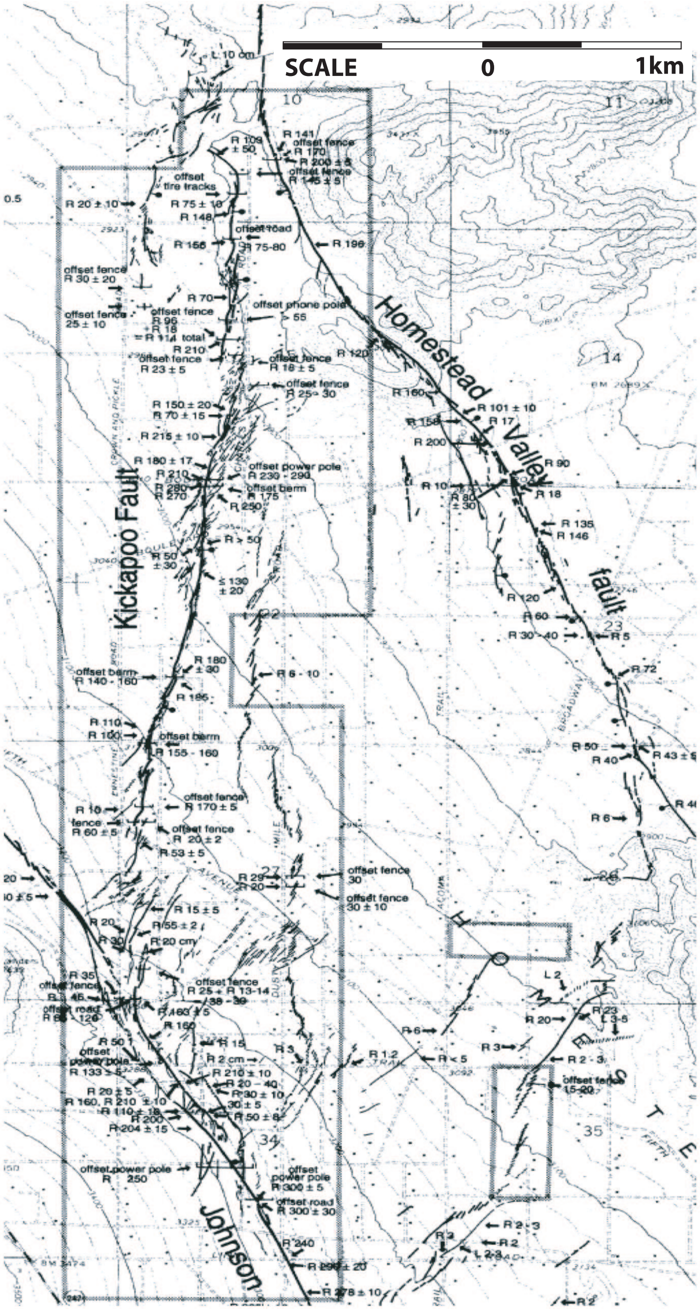

Figure 3.1: Map from *Sowers et al.* [1994] showing region of transition from the Johnson Valley to the Kickapoo and to the Homestead Valley faults during the 1992 Landers earthquake. The thickest lines show fault breaks with surface slip > 1 m, intermediate lines > 0.05 m, and thinnest lines > 0.01 m.

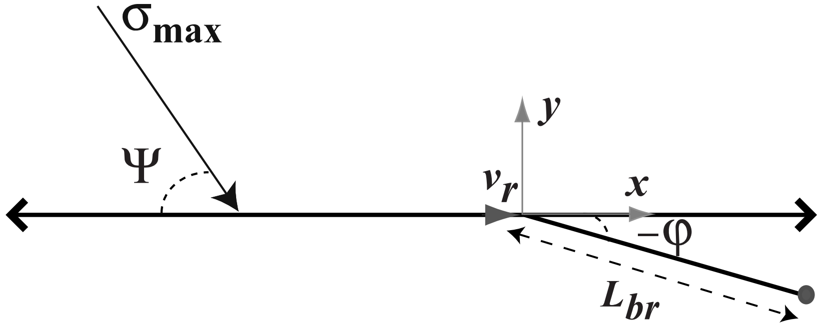

Figure 3.2: Model geometry and parameters used in the numerical simulations. Here Ψ is the orientation of the maximum principal compressive stress with the main fault, v_r is the incoming rupture velocity at the branching junction, φ is the inclination of the branch with the main fault and L_{br} is the length of the finite branch fault.

As proposed in *Poliakov et al.* [2002], and verified by detailed simulations and refined in *Kame et al.* [2003] and *Bhat et al.* [2004], the three key parameters that determine rupture path selection at an infinite branch junction are:

1. Inclination of the maximum principal compressive stress with the fault, Ψ
2. Rupture velocity when approaching a branching junction, v_r
3. Fault geometry, the inclination of the branch fault with the main fault, φ

Kame et al. [2003] have shown that types of faults most susceptiple to branch activation are those for which the maximum principal compressive pre-stress direction of the regional stress field is at a steep or shallow angle Ψ relative to what might be regarded as an optimal Coulomb direction, namely $\Psi = 45^o - \phi_{Coulomb}/2 \approx 29.5^o$ for $tan(\phi_{Coulomb}) = f_s = 0.6$. It was shown in their simulations that when $\Psi = 25^o$, the rupture always continued on the main fault and rupture on a branch, if it began at all, soon arrested on it. Thus branch activation is principally a feature of faults which are not near to Coulomb-optimal orientations in their regional pre-stress fields.

Some aspects of the results may also be controlled by the magnitude of the shear pre-stress, e.g., as measured by the seismic S ratio [*Andrews*, 1976]. In addition to these parameters, we must now, for finite branches, also introduce the new parameter, L_{br}, which describes the length of the branch. We non-dimensionalize this length by the size of the slip-weakening zone at low rupture speeds, R_0. *Rice et al.* [2005] have estimated the value of R_0 to be in the range $1-70$m, with typical sizes of $10-30$m, at mid-seismogenic depth, from their slip pulse model, assuming a peak friction coefficient of 0.6 for a fault with high peak strength and low dynamic strength, and fitting the model to seismic slip inversions by *Heaton* [1990].

3.3.2 Slip-weakening coulomb friction law

To describe the failure criterion on the faults, we use the slip-weakening friction law [*Ida*, 1972; *Palmer and Rice*, 1973; *Andrews*, 1976]. This is discussed earlier in section 2.5.

3.3.3 Rupture nucleation

There are different ways of nucleating a rupture. We could have imposed a very high initial shear stress along the nucleation zone, greater than the failure stress, so that the crack would have been statically unstable or imposed a reduction of normal stress there. The other way of nucleating rupture is to impose a slip distribution, compatible with the slip-weakening law along the total crack length equal to the nucleation size, L_{nucl}, and zero everywhere else. This will produce stress concentration, higher than the failure criterion, near the crack tips if $L_{nucl} > L_c$. This minimal nucleation size (which refers here to the total crack length), L_c, is derived from the fracture mechanics energy balance and has a simple expression when using the slip-weakening Coulomb friction law, if we assume as in *Palmer and Rice* [1973] and *Rice* [1968] that the slip-weakening zone size, R_0, for low rupture velocities is small compared to all geometric dimensions of the model. Further if, as in *Palmer and Rice* [1973], we consider that in the slip-weakening zone the shear stress varies linearly with distance along the crack within the end zone, then with a Poisson ratio equal to 0.25 ($\lambda = \mu$), we get

$$L_c = \frac{16\mu G}{3\pi(\sigma^o_{yx} - \tau_r)}; \quad R_0 = \frac{9\mu G}{4\pi(\tau_p - \tau_r)^2} \tag{3.1}$$

where $G = \int_o^\infty (\tau(\Delta u) - \tau_r) d(\Delta u)$ is the fracture energy for the slip-weakening model, μ is the shear modulus of the medium and σ^o_{yx} is the initial shear stress in the medium.

The size of the slip-weakening zone, R, depends on the rupture velocity [*Rice*, 1980; *Poliakov et al.*, 2002; *Rice et al.*, 2005; *Bhat et al.*, 2007a], at least for essentially steady state dynamic rupture configurations with v_r nearly uniform over a transit time R/v_r. In the range $v_r <$ Rayleigh wave speed c_R of the medium, of primary interest here, it diminishes with increasing rupture velocity to reach the value of zero at the limiting speed c_R, as

$$R = \frac{R_0}{F(v_r)} \tag{3.2}$$

where $F(v_r)$ increases from one to infinity when v_r increases from 0 to c_R. To obtain correct results, the slip-weakening zone should be adequately represented in any numerical model. As in *Kame et al.* [2003] we will take the cell size, Δs, equal to $R_0/5$ for low and intermediate rupture velocities ($v_r = 0.60c_s$ and $0.80c_s$ respectively) and $\Delta s = R_0/10$, and for the high velocity $v_r = 0.90c_s$.

3.3.4 Rupture propagation

Assuming that the normal stress is compressive ($\sigma_n < 0$), the rupture will propagate the following way. If $\tau > -f_d\sigma_n$ the rupture will slip right-laterally; else, if $\tau < f_d\sigma_n$ the rupture will slip left-laterally. Here, we focus on right-lateral rupture. If the slip-velocity is predicted to be negative we then set it to zero. We do not allow any backward slipping, i.e., we do not allow left-lateral slip.

3.4 Choice of parameters

Different parameters play a major role when explaining the propagation of an earthquake, such as the state of stress in the region before the earthquake nucleates, the rupture velocity, the direction of propagation of the fault and the length of the fault [*Poliakov et al.*, 2002; *Kame et al.*, 2003].

3.4.1 Influence of rupture velocity

Some earthquakes are observed to be very slow and others propagate very quickly. In their two dimensional steady state slip pulse model, *Rice et al.* [2005], building on the semi-infinite mode II crack model of *Poliakov et al.* [2002], have shown that the closer is the rupture velocity v_r to the Rayleigh wave speed of the medium, the larger is the off-fault stress concentration, around the rupture tip and extending away from the fault to distances of the order of the size of the slip-weakening zone in the low rupture velocity, low stress drop limit, as shown in Figure 3.3.

Thus different rupture velocities, when approaching the branching point, may or may

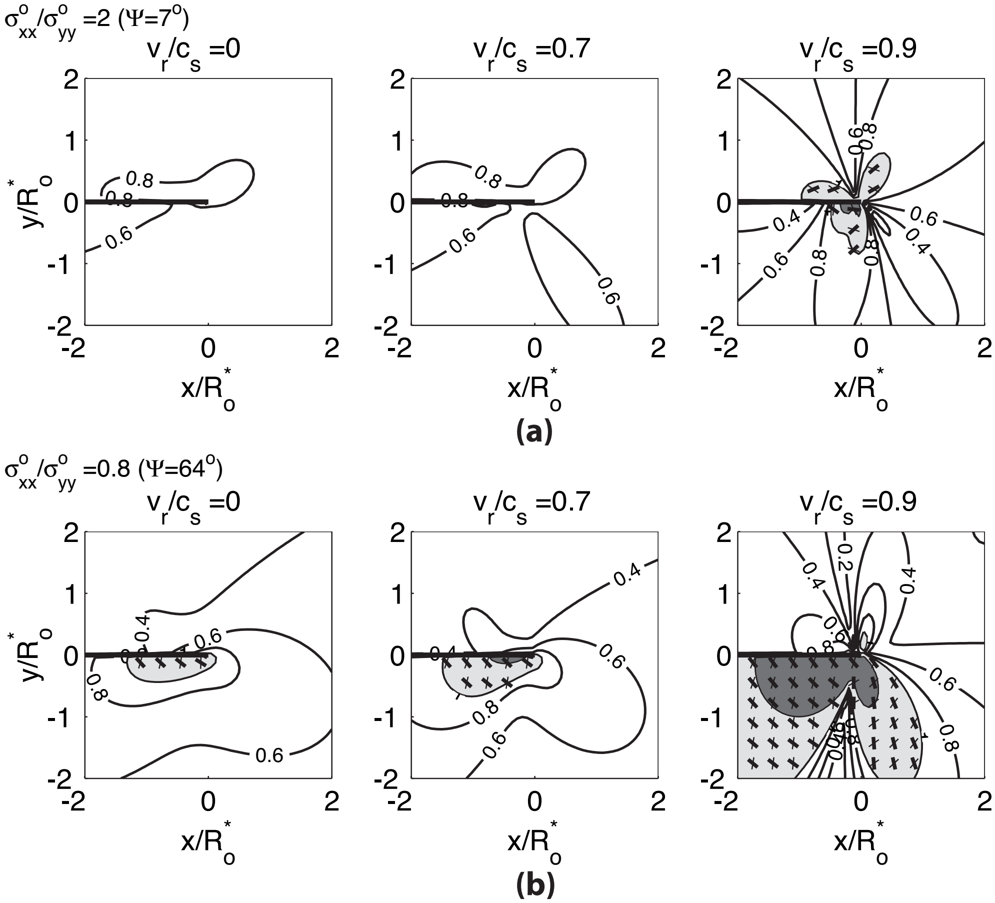

Figure 3.3: (a) Elastically predicted regions of cohesionless Mohr-Coulomb failure around a slip pulse propagating with a steady speed of v_r, scaled by the shear wave speed, c_s. Fault constitutive behavior characterized by spatially linear strength weakening criterion with the peak strength, $\tau_p = -0.6\sigma^o_{yy}$ and the residual strength, $\tau_r = 0.2\tau_p$ at pre-stress ratio $\sigma^o_{xx}/\sigma^o_{yy} = 2.0$. The size of the slip-weakening zone, R, is 0.001 times the length of the slip pulse, L. R^*_0 is the value of R in the low rupture velocity, low stress drop, limit. The light gray region represents the zone of potential Mohr-Coulomb failure and the failure planes are shown. The dark line represents the main fault. The dark gray region represents the region where one of the principal stress components turns tensile. (b) Same as (a) except $\sigma^o_{xx}/\sigma^o_{yy} = 0.8$. [*Rice et al.*, 2005]

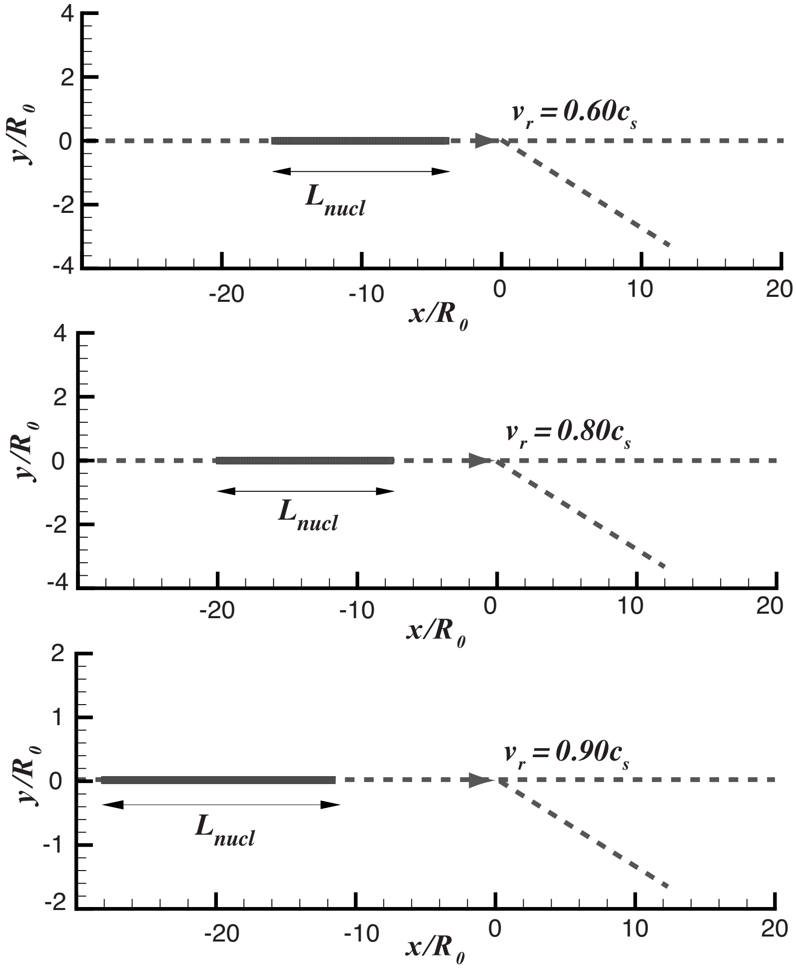

Figure 3.4: Position of the branch with respect to the nucleation zone in order to achieve different rupture velocities at the branching junction.

not nucleate rupture on the branched fault. We choose three values for the rupture velocity near the branching region, $0.60c_s$, $0.80c_s$ and $0.90c_s$, low, medium and high rupture velocity respectively, characterized in *Kame et al.* [2003]. We control the rupture velocity, when approaching the branching junction, by nucleating rupture at various distances from the branching junction as shown in Figure 3.4.

3.4.2 Friction coefficient and fracture energy

The slip-weakening law depends on the values of f_d and f_s, the friction coefficients, and on D_c, the critical slip. In *Poliakov et al.* [2002] and *Rice et al.* [2005] it is shown that the ratio f_d/f_s has a large influence on the shape of the high-stress region. For our study we take the same values as those in *Kame et al.* [2003], which are f_s = 0.60 and f_d = 0.12.

3.4.3 Influence of initial stress

From *Poliakov et al.* [2002] and *Kame et al.* [2003] we know that although rupture velocity plays a key role in triggering high off-fault stresses, the sustenance of rupture on a branch is controlled by the inclination of the principal maximum compressive stress with respect to the main fault. All stresses can be normalized by the initial compressive normal stress, $-\sigma^o_{yy}$ (σ^o_{yy} is positive in tension), on the main fault. The normalized shear stress was fixed at 0.24 to set the seismic S ratio, $(\tau_p - \sigma^o_{xy})/(\sigma^o_{xy} - \tau_r)$,*Andrews* [1976], to be equal to 3 (which leads to sub-Rayleigh rupture). $\sigma^o_{xx}/\sigma^o_{yy}$ was then chosen to fix the inclination of the principal maximum compressive stress on the main fault.

For a given value of rupture velocity *Poliakov et al.* [2002] and *Rice et al.* [2005] showed that the size and the shape of off-fault high-stress region depended on the value of the initial stresses, and especially on the inclination of principal maximum compressive stress along the main fault. *Poliakov et al.* [2002] concluded that generally for low principal maximum compressive stress inclination, Ψ, with respect to the main fault, the high stress region would be on either side of the fault as in Figure 3.3a. For large values of Ψ, especially angles greater than 45^o, the damage would be mainly on the extensional side. *Kame et al.* [2003] showed in their numerical simulations that similar results held for the side of the fault plane on which branches would be activated. They fixed the friction coefficient values as discussed before and also fixed $\sigma_{xy}^o/\sigma_{yy}^o = 0.24$.

The only initial value of pre-stress that was varied was $\sigma_{xx}^o/\sigma_{yy}^o$, which fixes the orientation of the principal maximum compressive stress inclination. They then considered four different angles of inclination, φ, for the branch with respect to the main fault, 15^o and 30^o (compressional side) and -15^o and -30^o (extensional side).

Kame et al. [2003] showed that with increasing orientation angle Ψ of the maximum principal compressive stress with respect to the main fault, the favored branch for rupture propagation changes from the one on the compressional side to the one on extensional side. Also, the rupture path becomes more and more exclusively along the branch when the extreme values (0^o and 90^o) of the maximum principal compressive stress orientation are approached. This exclusivity is lost with increasing rupture velocity but once again, as the limits of Ψ are reached, the exclusivity becomes more and more independent of rupture velocity. So branches on the compressional side are taken, with or without exclusivity, when $\Psi = 13^o$ and branches on the extensional side are taken, with or without exclusivity, when $\Psi = 56^o$. In addition to this, *Bhat et al.* [2004] also have studied rupture propagation through a branched fault system with $\Psi = 70^o, \varphi = -15^o$ and for different rupture velocities at the branching region. They observed that the branch is taken exclusively for low and intermediate values of rupture velocity but this exclusivity is lost at a high value of rupture velocity, very close to c_R. However, when Ψ is increased to 80^o, even for the high rupture velocity case the branch was taken exclusively.

We hence choose $\Psi = 13^o, 56^o$ and 70^o in our simulations and compare our results with those for infinite branches of *Kame et al.* [2003] and *Bhat et al.* [2004], for different branch angles and rupture velocities near the branching junction.

3.4.4 Influence of the branch orientation with respect to the main fault

The extensional and the compressional sides of a fault are stressed asymmetrically. The final rupture pattern depends on the orientation of the branch fault with the main fault (i.e., with the x-axis) as shown in *Kame et al.* [2003]. For instance if we look at Figure 3.5 we see that for a given rupture velocity, $0.60c_s$, and a maximum stress inclination of 13^o the rupture will not propagate on a branch after it has been nucleated on a main fault if the branch makes an angle of 30^o with the main fault, but will propagate if the angle is 15^o. We will, hence, consider different inclinations of the branch with respect to the main fault. We will consider for Ψ equal to 13^o, φ equal to 15^o and 30^o (compressional side), and for Ψ equal to 56^o and 70^o, φ equal to -15^o and -30^o (extensional side).

3.4.5 Influence of the length of the branch

Maps of surface slip of large earthquakes [e. g. *Sowers et al.*, 1994] reveal many minor branches, along and beyond the damage zone of a fault structure, and that these branches are of varying lengths with mapped lengths extending from one hundred to a few hundreds of meters. For example, during the 1992 Landers event, one can hypothesize that the main rupture made several attempts to branch on the extensional side of the Johnson Valley fault before finally branching off to the Kickapoo fault. The influence of these features has not been studied precisely yet. The small ones have always been neglected until now while the larger ones were considered to be infinite, effectively, for purposes of analyzing whether the branch path was followed. In this work we will try to explain the role of branches, specifically their length, L_{br}, on rupture propagation along the main fault.

3.5 Discussion of results

3.5.1 Role of finite branches as compared to 'infinite' branches

A very detailed study of rupture propagation along a branched fault system had been conducted by *Kame et al.* [2003] for the case where rupture was never terminated on the branch ('infinite' branch case). The three main parameters delineated by them, based on the earlier work by *Poliakov et al.* [2002], were the orientation angle Ψ of the maximum principal compressive direction of the pre-stress field with respect to the main fault, the incoming rupture velocity v_r at the branching junction, and the orientation angle φ of the branch fault with respect to the main fault. *Bhat et al.* [2004], making use of the Boundary Integral Equation Method for the same set of parameters mentioned above, tried to explain the exclusivity of the branching phenomenon observed during the 2002 Denali Fault earthquake in Alaska.

We would like to categorize the results of *Kame et al.* [2003] and *Bhat et al.* [2004], where branching was observed, into two cases, as follows:

1. The rupture took the branch exclusively and stopped on the main fault.
2. The rupture propagated on both the main and the branch fault.

The goal here is then to study the effect of finite short and long branches on the rupture propagation characteristics along the main fault, as compared to the infinite branches of *Kame et al.* [2003] and *Bhat et al.* [2004].

Kame et al. [2003] observed that for extreme inclinations of Ψ (=13^o and 56^o), the rupture almost always propagated, exclusively, on the compressional ($\varphi > 0$) or the extensional branch ($\varphi < 0$), respectively. This exclusiveness was no longer observed when either the branch angle was high ($\varphi = 30^o$ or -30^o) or when the rupture velocity was close to the limiting speed, the Rayleigh wave speed. In both these cases, the authors hypothesized that the stress-shadow effect was less dominant (due to high rupture velocity or high inclination of the branch) making the two propagating ruptures, on the main and the branch fault, almost independent of each other. *Bhat et al.* [2004] observed exclusivity of branching with the 2002 Denali fault earthquake, where $\Psi = 70^o$ with $\varphi = -15^o$, for low and intermediate values of rupture velocities.

We hence chose the above-mentioned values for Ψ (=13^o, 56^o and 70^o) and considered branch angles for which rupture was taken along the branch in the infinite branch case. These are φ = 15^o and 30^o for Ψ =13^o and φ = -15^o and -30^o for Ψ =56^o and φ = -15^o (the only case studied in *Bhat et al.* [2004]) for Ψ = 70^o. We also consider all incoming rupture velocities at the branching region, namely v_r = $0.60c_s$, $0.80c_s$ and $0.90c_s$ as in *Kame et al.* [2003] and *Bhat et al.* [2004].

3.5.2 Case with exclusive branching

When Ψ = 13^o and when the branch was inclined at an angle of 15^o to the main fault, the *Kame et al.* [2003] infinite branch analysis showed that irrespective of the incoming rupture velocity at the branching junction, the rupture always stopped on the main fault almost immediately beyond the branching junction. There was also stoppage of rupture on the main fault when the branch angle was 30^o but only at the lowest speed studied,

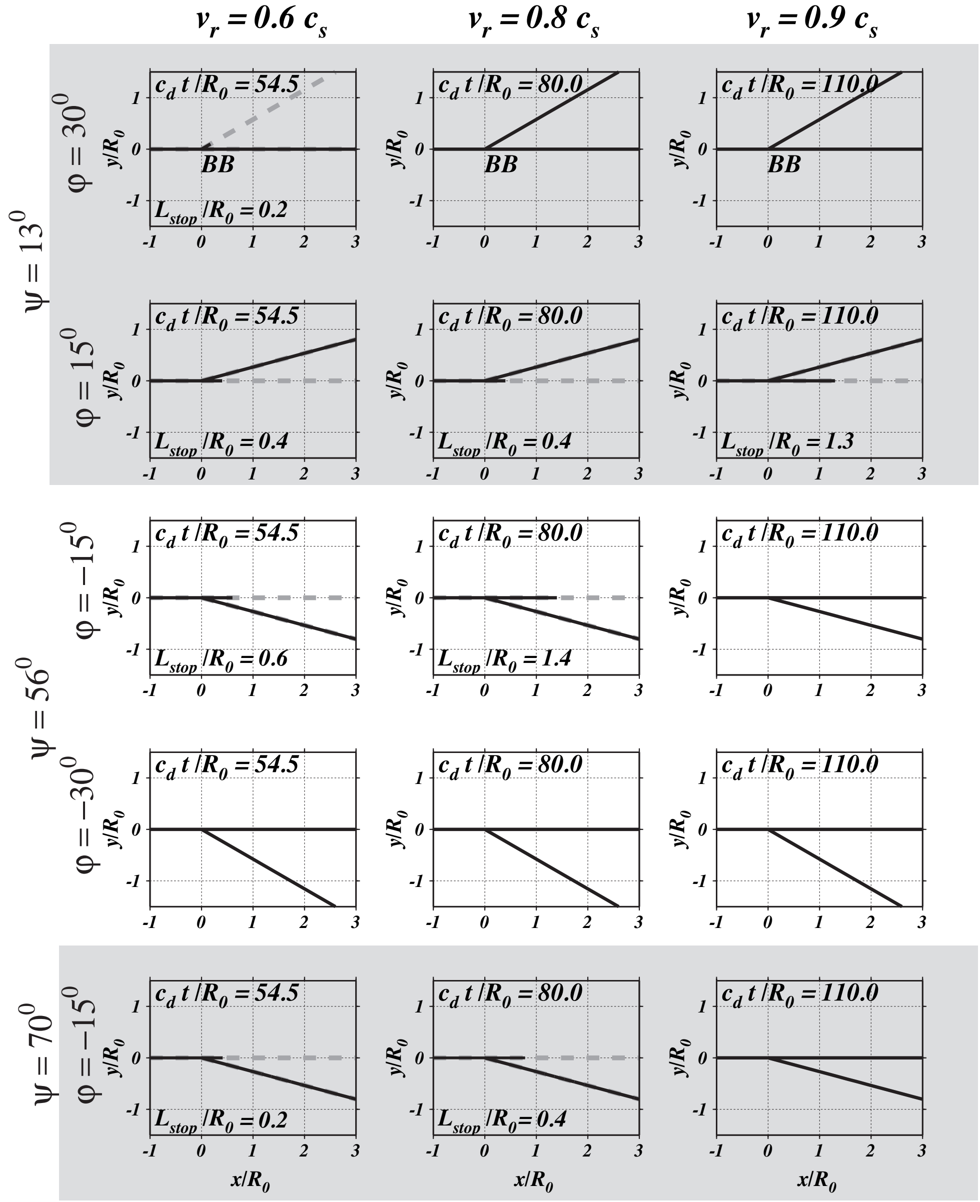

Figure 3.5: Summary of the results from *Kame et al.* [2003] and *Bhat et al.* [2004] “infinte” branch analyses. L_{stop} indicates the length of stopped rupture front from the branching junction. BB indicates cases with *Branching Behind*; i.e., the rupture front on the main fault had propagated somewhat beyond the junction before slip initiated on the branch fault. Solid line shows the ruptured part of the fault and the dashed lines represent the unbroken section of the fault.

$v_r = 0.60c_s$.

When the rupture on the branch is terminated due to finite branch length, in simulations analogous to those discussed in the previous paragraph, we observe some very interesting dynamical behavior of rupture on the main fault. For the case when $\Psi = 13^o, \varphi = 15^o$, the perturbation of the stress field on the main fault during rupture propagation on the branch was sufficient to terminate propagation on the main fault, irrespective of the incoming rupture speed, for both short ($L_{br} = 6R_0$) and long branches ($L_{br} = 30R_0$ for $v_r = 0.60c_s, 0.80c_s$ and $L_{br} = 20R_0$ for $v_r = 0.90c_s$). For the above case, when $v_r = 0.80c_s$, we studied the precise sensitivity of rupture to branch length and noticed that only when the branch is extremely short, $L_{br} = 1R_0$, rupture continues to propagate on the main fault. This shows that short branches, in general, can cause earthquake ruptures to renucleate on the main fault, at least on faults like this one which are in a regional stress field which is poorly aligned relative to the optimal alignment for Coulomb rupture on the main fault ($\Psi = 13^o$ vs. $\Psi_{Coulomb} = 29.5^o$ based on $f_s = 0.60$). This result for the finite branch case could have been suspected from the infinite branch case [Figure 3.5], in which rupture chose to follow the branch and soon abandoned the main fault.

For branches on the extensional side, exclusive branching was observed by *Kame et al.* [2003] in the infinite branch case when $\Psi = 56^o$ and $\varphi = -15^o$ when $v_r = 0.60c_s$ and $v_r = 0.80c_s$ [Figure 3.5]. For the above cases, the rupture once again stops on the main fault beyond the branching point for both short ($L_{br} = 6R_0$) and long branches ($L_{br} = 30R_0$) for $v_r = 0.60c_s$ and for long branch ($L_{br} = 30R_0$) when $v_r = 0.80c_s$.

When the length of the branch was reduced from $30R_0$ to $10R_0$ and when the incoming rupture velocity was $0.80c_s$, the rupture slowed down and stopped temporarily on the main

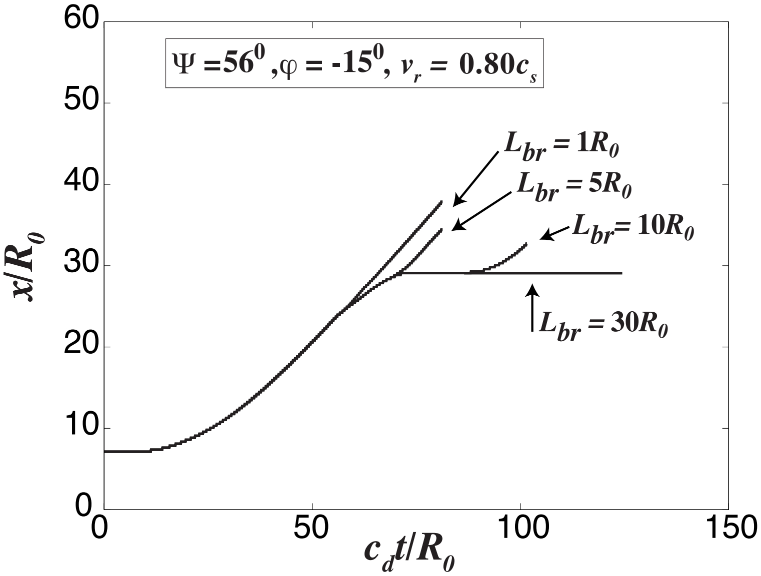

Figure 3.6: Effect of increasing branch length on the state of rupture front on the main fault (its length is x), plotted as a function of normalized time, for the case when $v_r = 0.80c_s$. L_{br} is the length of the branch, c_d and c_s are the dilatational and shear wave speeds of the medium respectively.

fault until the large perturbation in the stress field, due to the stoppage of rupture on the branch, reached the main fault to kick-start the rupture again on the main fault. Thus a short enough branch (with a length up to $10R_0$, Figure 3.6) , with an intermediate rupture velocity like $0.80c_s$ on the main fault, was sufficient to renucleate the rupture on the main fault. Figure 3.7 shows this phenomenon quite clearly. When the branch length was $6R_0$, the scaled shear stress evolution on the main fault around the branching junction shows clear propagation of the rupture front, corresponding to the peaks in the figure. The time steps shown in the plots correspond to the time when the rupture front on the main fault was approaching the branching junction to the time when the rupture has completely stopped on the branch. When the branch length was increased to $30R_0$ we see the peaks in the shear stress never reaching the peak strength ($\tau_p = 0.6\sigma_{yy}$) resulting in no further rupture propagation.

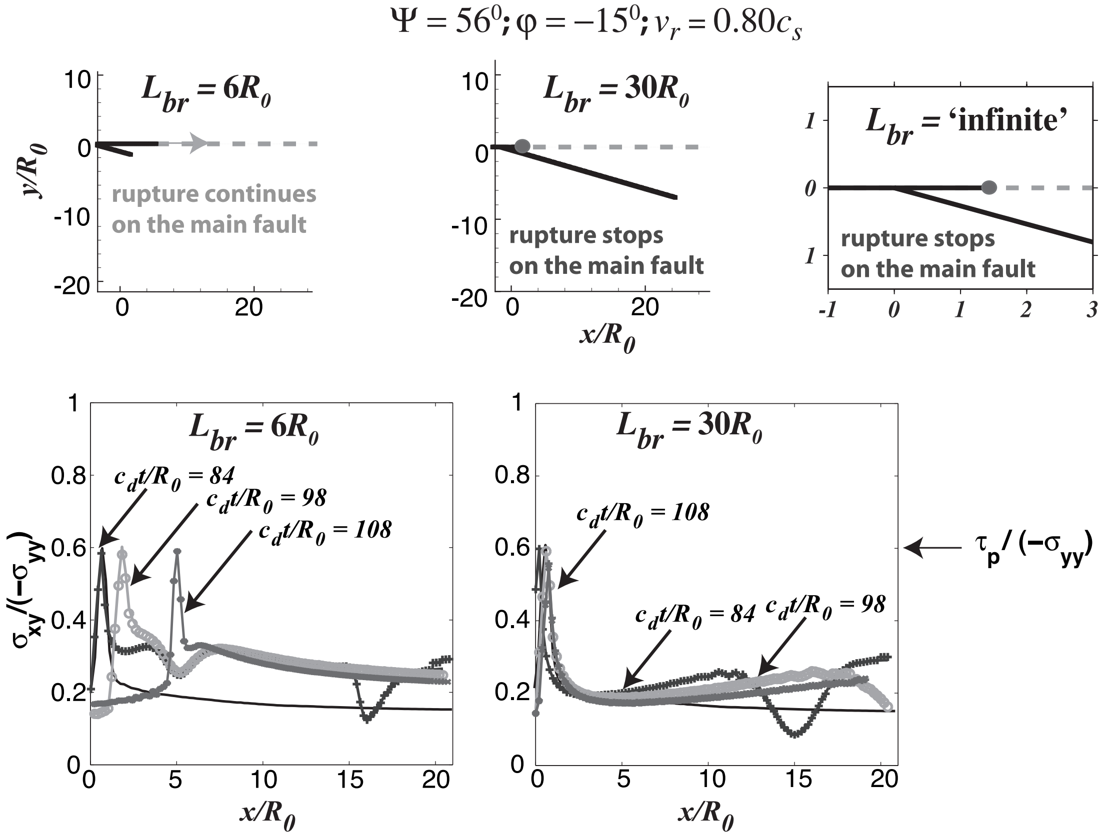

Figure 3.7: Effect of increasing branch length on the final state of rupture and the corresponding evolution of scaled shear stress distribution on the main fault around the branching junction (stress scaled by fault normal stress, $-\sigma_{yy}$) for various time steps (non-dimensionalized as $c_d t/R_0$) for the case when $\Psi = 56^o$, $\varphi = -15^o$ and $v_r = 0.80c_s$. The time steps correspond to time from when the rupture on the main fault is approaching the branching junction to the time when the rupture has completely stopped on the main fault. τ_p is the peak strength of the fault in the slip-weakening relationship. Here $\tau_r/\sigma_{yy} = 0.12$ and L_{br} is the length of the branch.

When $\Psi = 70^o$ and $\varphi = -15^o$ *Bhat et al.* [2004] observed in the infinite branch case that the rupture stops on the main fault for low and intermediate rupture velocities ($v_r = 0.60c_s$ and $v_r = 0.80c_s$) [Figure 3.5].

For branch lengths greater than $6R_0$ our simulations show that a finite branch has the same effect on the rupture on the main fault, i. e. the rupture terminates on the main fault, although the distance covered by the rupture, before stopping, on the main fault depended on the branch length. We also studied sensitivity to branch length for the particular case when the incoming rupture velocity was $0.80c_s$. We introduced branches of length $1, 2, 3, 4, 5$ and $6R_0$ and studied their effect of rupture propagation characteristics on the main fault. We observe a transition length of the branch, at $6R_0$, where the rupture on the main fault transitions from a continuously propagating state to a state in which it arrests [Figure 3.8].

Bhat et al. [2004] also studied a case, for the Denali event, in which the approaching rupture velocity at the branching junction was supershear at $v_r = 1.41c_s$ and they observed exclusive branching. Our simulations of the above case with branch lengths of $6R_0$ and $30R_0$ show that the shorter branch slows the rupture temporarily on the main fault before accelerating it whereas the longer branch halts the rupture on the main fault.

3.5.3 Case with rupture propagation on both the main and the branch fault

For certain orientations of the maximum principal compressive stress with respect to the main fault, branch angles and incoming rupture velocities at the branching junction, *Kame et al.* [2003] (and *Bhat et al.* [2004]) observed, for the infinite branch case, no stoppage of rupture on the main fault once the branch is taken [Figure 3.5].

For the case when $\Psi = 13^o, \varphi = 30^o$ the termination of rupture on the branch did not alter, from the infinite branch case, in any way the final state of rupture on the main fault for all incoming rupture speeds ($v_r = 0.60c_s, 0.80c_s$ and $0.90c_s$) and branch lengths

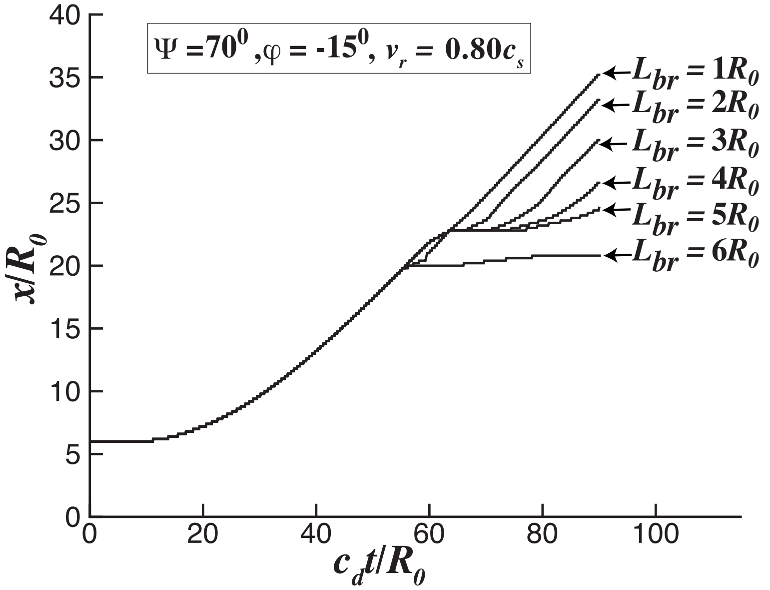

Figure 3.8: Effect of increasing branch length on the state of rupture front, plotted as a function of normalized time, for the case when $v_r = 0.80c_s$. L_{br} is the length of the branch, c_d and c_s are the dilatational and shear wave speeds of the medium respectively.

($L_{br} = 6, 30R_0$ for $v_r = 0.60c_s$, $L_{br} = 6, 8, 10, 20, 25R_0$ for $v_r = 0.80c_s$ and $L_{br} = 6, 20R_0$ for $v_r = 0.90c_s$) except for the case when $L_{br} = 30R_0$ and $v_r = 0.80c_s$. Figure 3.9 shows the evolution of scaled shear stress on the main fault around the branching junction starting from the time when the rupture is approaching the branching junction to the time when the rupture has completely terminated on the branch for this case. The peaks in the shear stress distribution correspond to the rupture front. When the stress at the peak is less than the shear strength, clearly the rupture front is not able to progress. For $L_{br} = 6R_0$ case we see that for a brief period of time, the rupture front fails to progress before picking up speed again. When $L_{br} = 30R_0$ the magnitude of the peak decreases with time, even after the rupture has stopped on the branch, indicating the termination of rupture on the main fault. The transition length appears to be between 25 and $30R_0$ [Figure 3.10].

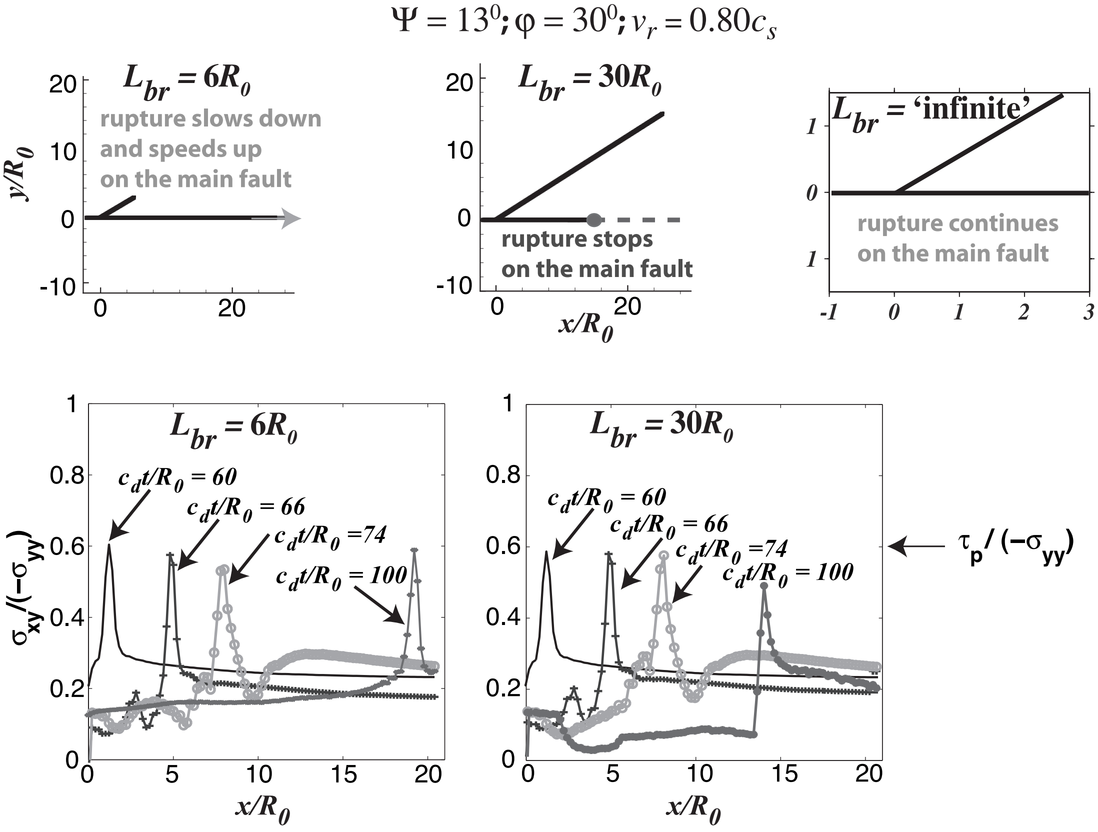

Figure 3.9: Effect of increasing branch length on the final state of rupture and the corresponding evolution of scaled shear stress distribution on the main fault around the branching junction (stress scaled by fault normal stress, $-\sigma_{yy}$) for various time steps (non-dimensionalized as $c_d t/R_0$) for the case when $\Psi = 13^o$, $\varphi = 30^o$ and $v_r = 0.80c_s$. The time steps correspond to time from when the rupture on the main fault is approaching the branching junction to the time when the rupture has completely stopped on the main fault. τ_p is the peak strength of the fault in the slip-weakening relationship. Here $\tau_r/\sigma_{yy} = 0.12$ and L_{br} is the length of the branch. In the $L_{br} = 6R_0$ case, the slow down is extreme and involves a brief cessation of rupture propagation on the main fault.

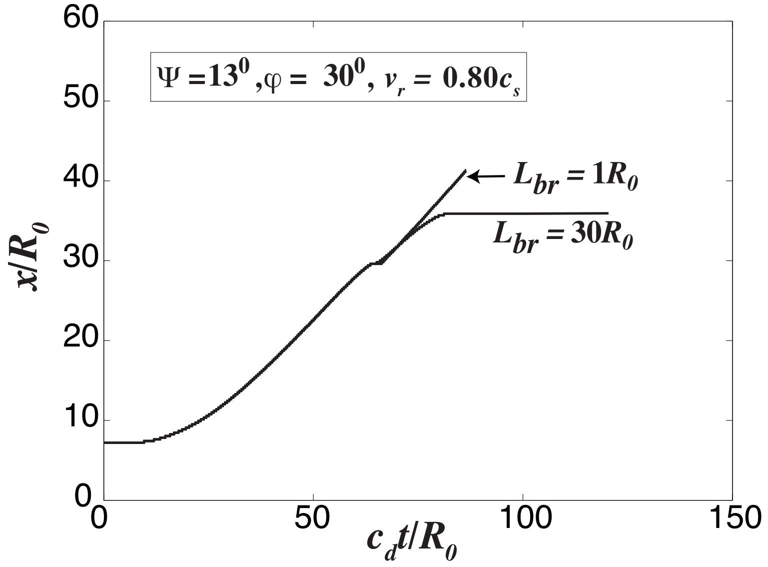

Figure 3.10: Effect of increasing branch length on the state of rupture front, plotted as a function of normalized time, for the case when $v_r = 0.80c_s$. L_{br} is the length of the branch, c_d and c_s are the dilatational and shear wave speeds of the medium respectively.

We suspect this to happen due to the interaction between the rupture front on the main fault and the large stress perturbation emanating from the branch end when rupture stops there. In the short branch case, the rupture on the main fault had already accelerated past the branching junction to a distance where the effect of the branch termination is barely felt. Hence the brief slow down and acceleration of the rupture. For long branch length, $L_{br} > 25R_0$, the rupture on the main fault did not accelerate fast enough to outpace the effect of the large stress perturbation, emanating due to branch termination, which led ultimately to its stoppage.

When $\Psi = 56^o$ and $\varphi = -15^o$ and when $v_r = 0.90c_s$ the rupture propagated both on the main and the branch fault in the *Kame et al.* [2003] infinite branch simulations. This was attributed by the authors to the reduction in the stress-shadow effect with increasing rupture velocity. Another case where the rupture always continued on the main fault, irrespective of v_r, after branching was when the branch angle in the above case was increased to -30^o. The relatively high branch angle in this case made the ruptures on the main and the branch fault almost independent of each other irrespective of the incoming rupture velocity at the branch junction [Figure 3.5].

We notice no significant change in rupture propagation characteristics for the above case when the rupture was terminated on the branch.

Bhat et al. [2004] observed, when trying to numerically simulate the branching phenomenon for the 2002 Denali fault earthquake, that when $\Psi = 70^o$ and $\varphi = -15^o$ and for extremely high but sub-Rayleigh incoming rupture velocity near the branching junction ($0.90c_s$) the rupture propagated on both the main and the branch faults in the infinite branch analysis. [Figure 3.5].

When the rupture is terminated on the branch then both the short ($6R_0$) and long branch ($20R_0$) have the effect of stopping the rupture completely on the main fault unlike the infinite branch case where the rupture propagates on the main fault [Figure 3.11].

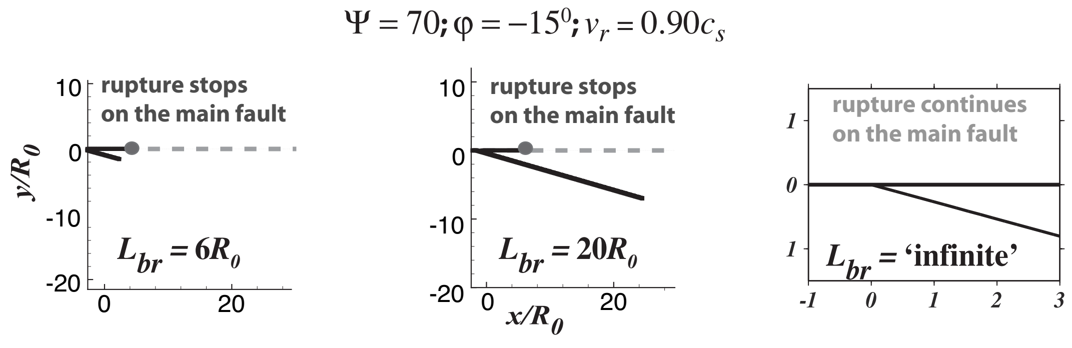

$\Psi = 70; \varphi = -15^0; v_r = 0.90c_s$

Figure 3.11: Effect of increasing branch length on the final state of rupture for the case when $\Psi = 70^o$, $\varphi = -15^o$ and $v_r = 0.90c_s$. L_{br} is the length of the branch.

3.5.4 Seismic complexities due to a finite branch

A dynamically propagating rupture when stopped radiates stress perturbations as it tries to establish a static stress field. The zone of influence of this static-like field depends on many parameters including the length of the rupture. *Harris and Day* [1993]; *Harris et al.* [2002] and *Fliss et al.* [2005] have studied the phenomenon of rupture jumping to an adjacent fault due to stoppage on the main fault. In our studies, with finite branched systems, we thus expect some complexity in the rupture propagation process on the main fault due to the stoppage of rupture on the branch.

As outlined in section 3.5.1, a dynamic shear rupture propagating through a branched fault system behaves quite differently depending on whether the rupture is terminated on the branch or not. It was also noted that the length of the branch plays a key role in influencing the rupture on the main fault. The presence of a finite branch alters the rupture propagation characteristics along the main fault, near the branching junction, as observed in our simulations. In this section we delineate resulting complexities in rupture velocity patterns on the main fault, and on slip patterns, based on the parameters of our model (will therefore be expected to have a bearing on high-frequency ground acceleration).

Two key observations were made regarding the complexities in rupture velocity induced by fault branches. One, there was a general slow down and then a speed up in the rupture velocity and the temporal duration and the spatial extent of this complexity decreased with increasing rupture velocity. Two, there could be a complete slow down and stoppage of rupture propagation on the main fault; that is, the branch could arrest the earthquake.

In the case where the orientation of the maximum principal compressive stress with the main fault, Ψ, is 56^o and the inclination of the branch with respect to the main fault, φ, is -15^o we observe a general slow down and speed up of rupture on the main fault. The duration of this slow down period, before speed up, is longer with increasing length of the branch. When the branch angle is increased to $\varphi = -30^o$ the effect of the branch in the slowdown-speedup process is also significantly reduced. For the case when $\Psi = 13^o, \varphi = -15^o$ when the length of the branch is $6R_0$ we see complete stoppage of the rupture on the main fault. We in-fact see, for this case, that the rupture stops on the main fault for branch lengths between $2R_0$ and $30R_0$.

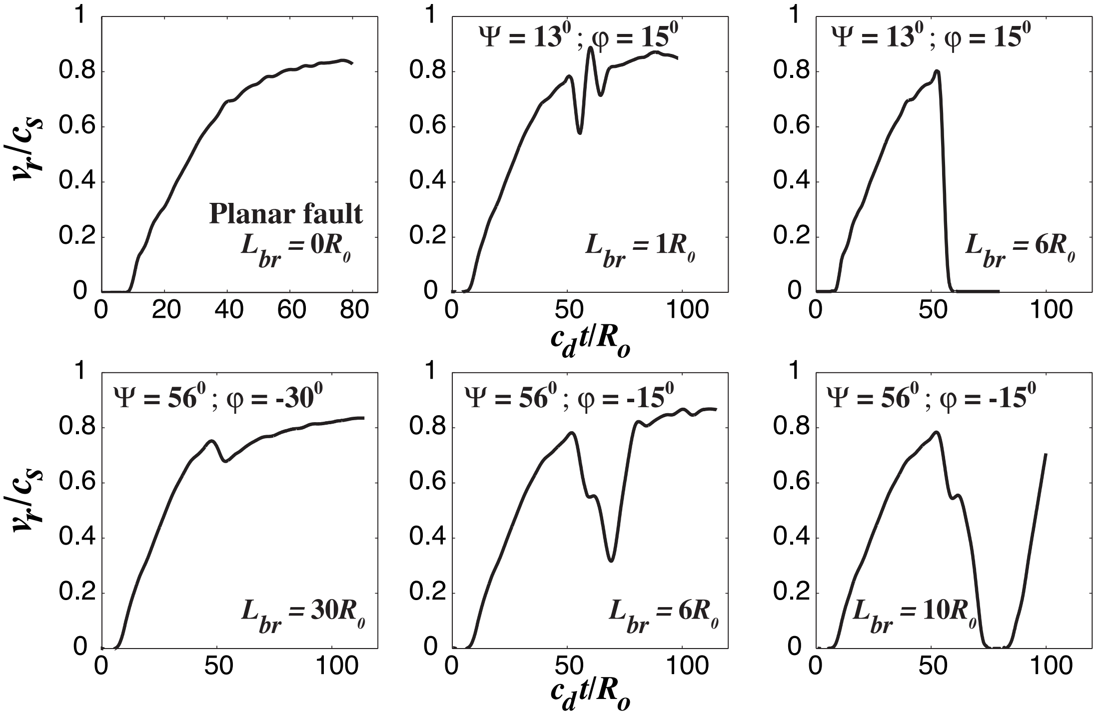

Figure 3.12: Complexities in the evolution with time of rupture velocity v_r (normalized by the shear wave speed c_s) on the main fault, for various configurations. Rupture velocity v_r when approaching the branching junction is $0.80c_s$ for all cases.

The rupture slow down and speed up process decreases both in spatial and temporal extent with increasing rupture velocity near the branching junction. This could be attributed to the fact that as the rupture velocity increases, the stress shadow effect of one fault on the other decreases and the two ruptures behave more and more independently of each other. With increasing rupture velocity near the branching junction two phenomena can be observed.

First, the stress shadow effect of the branch fault on the main fault diminishes. Second, because of the high rupture velocity on the main fault, any factor promoting slow down causes a higher energy flux into the rupture tip, thus mitigating against slow down; that makes it easier for a fast moving rupture to overcome the stress shadow effect of the branch than would its slow moving counterpart, and results in shorter duration of rupture complexities [Figure 3.12].

Some interesting features can be observed in the slip distribution along the main fault as well. Firstly, on average, the slip deficit on the main fault beyond the branching junction is compensated by the slip on the branch. Secondly, the gradient in slip near the branching junction is higher for longer branches than the same for short branches, for cases where finite branches significantly perturbed the rupture process on the main fault. We could attribute this to the strength of the arresting pulse arriving from the end of the branch. From a singular elastic fracture mechanics perspective, the strength of this pulse depends on the rest stress intensity factor, K_{II}, of the branch, which could be expected to increase with L_{br} and hence be stronger for the long branch than the shorter one. Figures 3.13 and 3.14 provide some illustrative slip distribution plots.

In general, sudden gradients in slip distribution on the main fault could be observed when a geometric complexity like a branch is introduced to the main fault. Depending on wether the rupture on the main fault is terminated or not various complexities are introduced in the slip distribution. A sudden drop in the slip accumulation around the branching junction is indicative of rupture termination on the main fault. Small gradients in the slip accumulation process indicate possible slow down and speed up of rupture propagation on the main fault. Figure 3.15 shows a summary slip distribution on the main fault for all values of Ψ, φ considered when $v_r = 0.80c_s$ and $L_{br} = 6R_0$.

In the above cases ($\Psi = 56^o$ and 70^o) when the branch angle was increased to -30^o the slow down and speed up process on the main fault is remarkably reduced than the same for a smaller branching angle of -15^o. Also, interestingly, the length of the branch does not then seem to change remarkably the rupture slow down and speed up process on the main fault. This could be because the increased branch angle has already decreased the interaction between the main and the branch fault to such an extent that the length of the branch is then immaterial.

For a branch on the compressional side, $\varphi = 15^o$, and low pre-stress inclination, $\Psi = 13^o$, the slow down and speed up process seems to be more gradual than the same for branches on the extensional side. Of course, the rupture on the main fault slows down for a shorter period of time with increasing rupture velocity. When the branch angle is increased to 30^o the behavior of rupture on the main fault is very interesting. When $v_r = 0.60c_s$ the slow down in rupture velocity is almost negligible as is the case when $v_r = 0.90c_s$. However, when $v_r = 0.80c_s$ there is short period where the rupture slows down before picking up when the branch length is $6R_0$. The same is observed when the branch length is increased to $30R_0$ there is a similar slow down and speed up in rupture velocity before the rupture completely stops on the main fault at a distance of $13R_0$ from the branching junction.

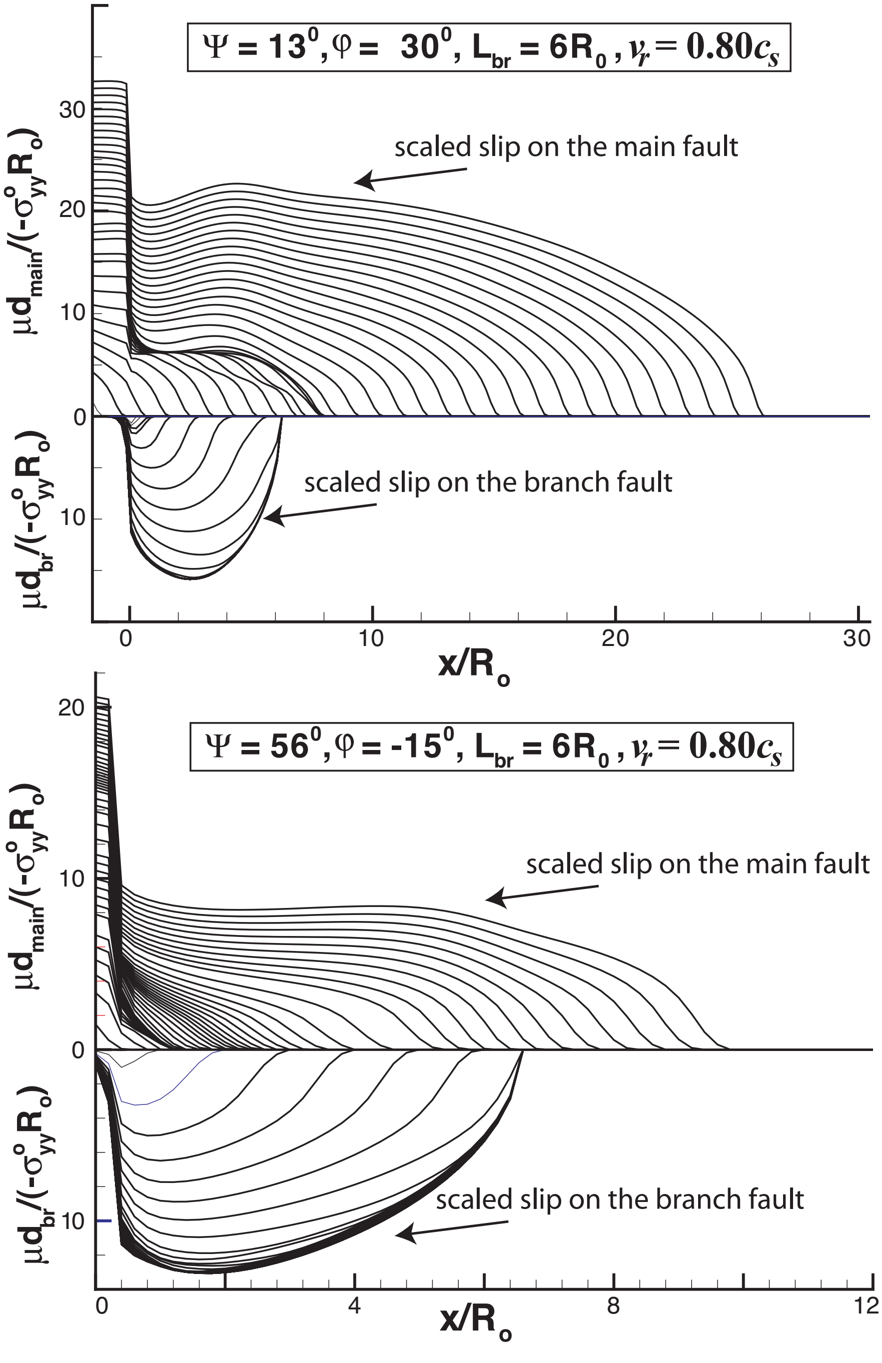

Figure 3.13: Complexities in normalized slip, around the branching junction, for both the main and the branch fault. Here d is the slip, μ, σ^o_{yy}, L_{br} are the shear modulus, initial fault normal stress and the length of the branch respectively.

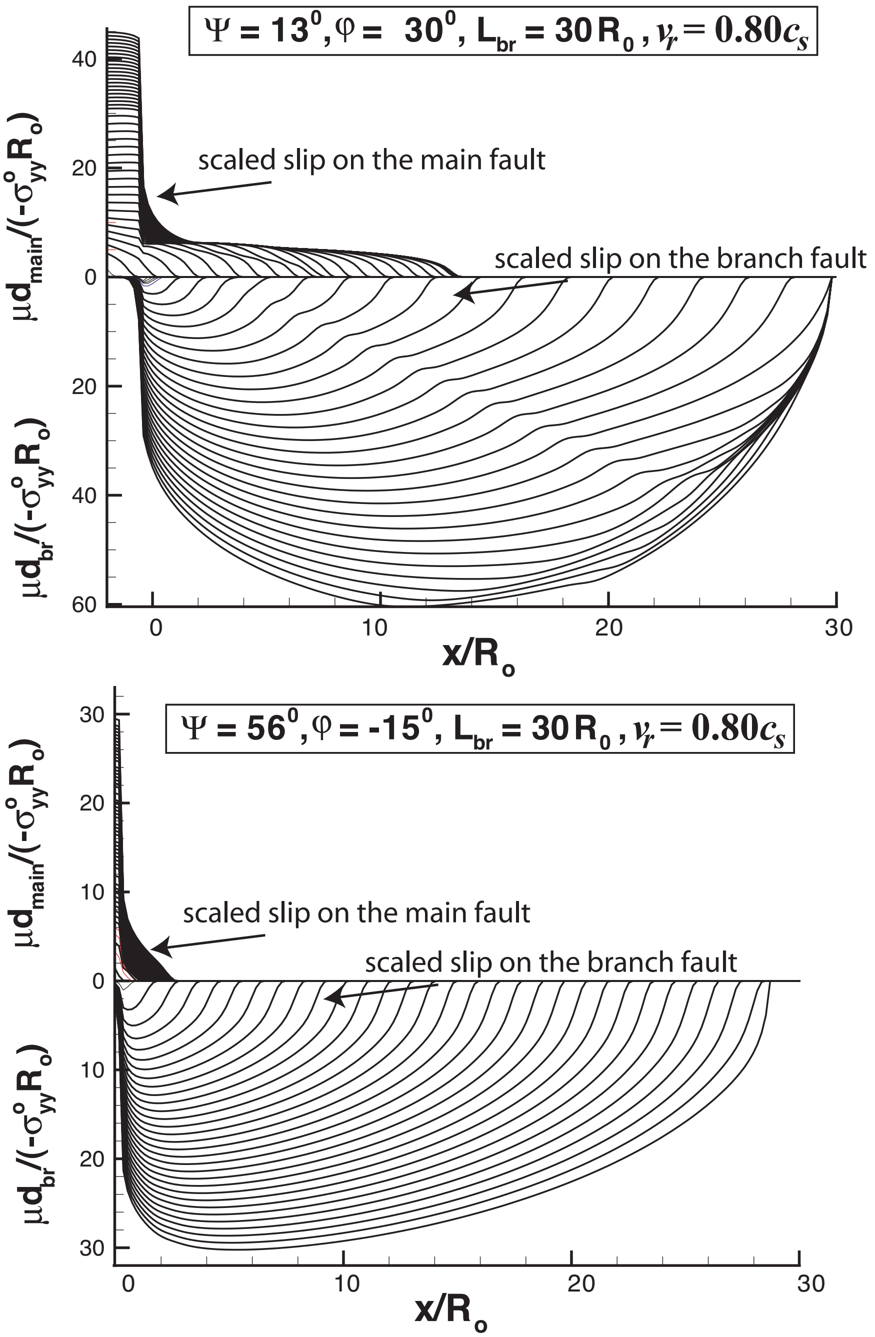

Figure 3.14: Complexities in normalized slip, around the branching junction, for both the main and the branch fault. Here d is the slip, μ, σ^o_{yy}, L_{br} are the shear modulus, initial fault normal stress and the length of the branch respectively.

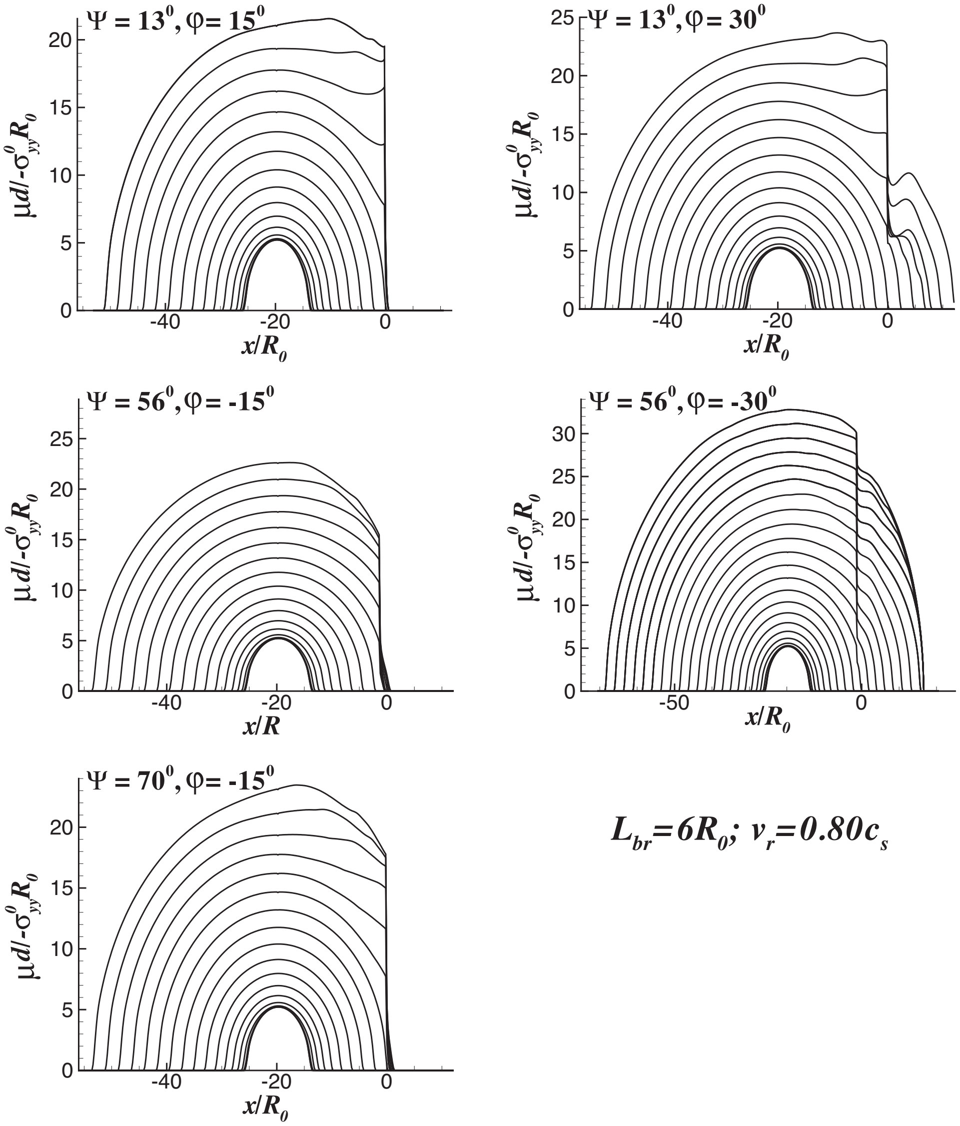

Figure 3.15: Complexities in normalized slip on the main fault. Here d is the slip, $\mu, \sigma_{yy}^{o}, L_{br}$ are the shear modulus, initial fault normal stress and the length of the branch respectively.

3.6 Summary and conclusions

We have studied the effect of fault branches on dynamic rupture propagation characteristics along a main fault. This adds to the work of *Kame et al.* [2003] and *Bhat et al.* [2004] which focussed on the role of pre-stress state, rupture velocity at the branching junction, and the branch angle in controlling rupture path selection on branched fault systems, without terminating the rupture on the branch (referred to as "infinite" branch cases in this study). In brief, their results showed that a shallow branching angle ($\varphi = \pm 15^o$) and a pre-stress state conducive for branching ($\Psi = 13^o$ for $\varphi = 15^o$ and $\Psi = 56^o, 70^o$ for $\varphi = -15^o$) resulted in rupture termination on the main fault for all rupture velocities, when approaching the branch junction, except high valued ones ($v_r = 0.90 c_s$) because of reduced interaction between the main and the branched faults. However, when the orientation of the principal maximum compressive stress, Ψ, approached its extremum, $\Psi = 0^o$ or 90^o, even the high rupture velocity cases led to exclusive branching.

In this body of work we considered the role of the length of the branches on rupture propagation characteristics on the main fault. We studied the cases by *Kame et al.* [2003] and *Bhat et al.* [2004] where branching was observed and terminated rupture on the branched fault at various distances from the branching junction. A dynamically propagating rupture when stopped radiates stress perturbations as it tries to establish a static stress field. The zone of influence of this static-like field depends on many parameters including the length of the rupture. *Harris and Day* [1993]; *Harris et al.* [2002] and *Fliss et al.* [2005] have studied the phenomenon of rupture jumping to an adjacent fault due to stoppage on the main fault. In our studies, with finite branched systems, we thus expect some complexity in the rupture propagation process due to the stoppage of rupture on the branch.

We have noticed that for branches on the compressional side termination of rupture on the same barely affects the rupture on the main fault except for the case when $\Psi = 13^o, v_r = 0.80c_s, \varphi = 30^o$ and $L_{br} = 30R_0$. For the above case we pointed out that a propitious combination of parameters led to the direct interaction between the rupture front on the main fault and the large stress perturbation from the branch end led to the termination of rupture on the main fault. A short or an infinite branch would have allowed for the rupture to continue on the main fault [Figure 3.10].

For branches on the extensional side, while an infinite branch would have allowed continuation of rupture on the main fault for high incoming rupture velocity and shallow branch angle, termination of rupture on the branch led to its continuation on the main fault for and $\Psi = 70^o, L_{br} = 6, 20R_0$. We also showed that, for the above cases, when v_r was reduced to $0.80c_s$ terminating the rupture on the branch closer to the main fault led to re-nucleation of rupture on the main fault.

We observed complexities in slip distribution and rupture velocity evolution on the main fault. The complexities in the slip distribution process, which might normally have been attributed to a rupture encountering a barrier or an asperity were the result of rupture propagation and termination on the main fault. Complexities in rupture velocity evolution, like deceleration and acceleration of rupture, are directly associated with the finiteness of the branch and could be the source of the high-frequency content of strong ground motion.

Chapter 4

Fault Branching and Rupture Directivity

4.1 Abstract

Could the directivity of a complex earthquake be inferred from the ruptured fault branches it created? Typically, branches develop in forward orientation, making acute angles relative to the propagation direction. Direct backward branching of the same style as the main rupture (e.g., both right lateral) is disallowed by the stress field at the rupture front. Here we propose another mechanism of backward branching. In that mechanism, rupture stops along one fault strand, radiates stress to a neighboring strand, nucleates there, and develops bilaterally, generating a backward branch. Such makes diagnosing directivity of a past earthquake difficult without detailed knowledge of the branching process. As a field example, in the Landers 1992 earthquake, rupture stopped at the northern end of the Kickapoo fault, jumped onto the Homestead Valley fault, and developed bilaterally there, NNW to continue the main rupture but also SSE for 4 km forming a backward branch. We develop theoretical principles underlying such rupture transitions, partly from elastostatic stress analysis, and then simulate the Landers example numerically using a two-dimensional elastodynamic boundary integral equation formulation incorporating slip-weakening rupture. This reproduces the proposed backward branching mechanism based on realistic if simplified fault geometries, prestress orientation corresponding to the region, standard lab friction values for peak strength, and fracture energies characteristic of the Landers event. We also show that the seismic S ratio controls the jumpable distance and that curving of a fault toward its compressional side, like locally along the southeastern Homestead Valley fault, induces near-tip increase of compressive normal stress that slows rupture propagation.

4.2 Introduction

The rupture zones of major earthquakes often involve geometric complexities including fault bends, branches and step-overs. Recently some understanding of the mechanics underlying dynamic processes of fault branching and jumping has started to emerge. A new question has emerged as well: Is it possible to judge the directivity of a large earthquake from the rupture pattern it left? The answer to that question would be very useful for risk assessment of future earthquakes, even if it is currently unknown if large earthquakes do systematically repeat their rupture direction (while not necessarily the entire rupture pattern). Here we address a particular, narrower version of that question, namely: Could we associate the directivity of a major earthquake with the pattern of branches that it left?

That question has been posed by *Nakata et al.* [1998], who proposed to relate the observed surface branching of fault systems with directivity. Their work assumed that all branches were through acute angles, in the direction of rupture propagation. However *Dmowska et al.* [2002] pointed out that, for at least some field observations, the rupture paths seemed to branch through highly obtuse angles, as if to propagate “backwards” along the branch. In general there are no observational proofs that this is what really happened in these cases. It is even possible that some obtuse branches are due to early aftershocks. However, in the case examined here involving a particular backward branch in the 1992 Landers, California, earthquake, *Poliakov et al.* [2002] showed that the pattern of damage to a single side of the fault clearly indicates such a backward direction of propagation on that branch. Here we analyze and numerically simulate the mechanics of such backward branching, and relate the results to understanding rupture directivity.

4.2.1 Diagnosing rupture directivity

The basic mechanical questions when relating fault branching to rupture directivity are summarized in Figure 4.1. Figure 4.1(a) presents the typical fault branching through acute angle, readily observed in the field and recently analyzed by *Poliakov et al.* [2002] and *Kame et al.* [2003]. The propensity of the fault to branch in that way depends on the orientation of the local pre-stress field relative to that of the main fault, the rupture velocity at branching junction and the geometry of the branch (the angle between the main and branching faults). The turn of rupture path through an obtuse angle while continuing on main fault is illustrated in Figure 4.1(b) and is never favored by the stress field; see below. What is proposed here as the mechanism of creation of a backward branch is presented in Figure 4.1(c) and consists of arrest of rupture propagation along an initial fault strand, radiating stress increase and hence jump of the rupture to a subsidiary fault [*Harris et al.*, 1991; *Harris and Day*, 1993] on which it nucleates and then propagates bilaterally. Part of the rupture along the neighboring fault creates the backward branch.

Figure 4.1(d) presents the mechanical dilemma of backward branching: Did the rupture arrive from the right and branch through an acute angle, as illustrated in the top panel? Or, did it arrive from the left, stop, jump, and nucleate on a neighboring fault, then develop bilaterally, as illustrated in the lower panel of Figure 4.1(d)? The jump here is exaggerated, in real field cases the observation of surface ruptures might not at once provide the right answer. The purpose of the present paper is to document a field example of the latter case as well as to develop theoretical understanding and numerical simulation of the process.

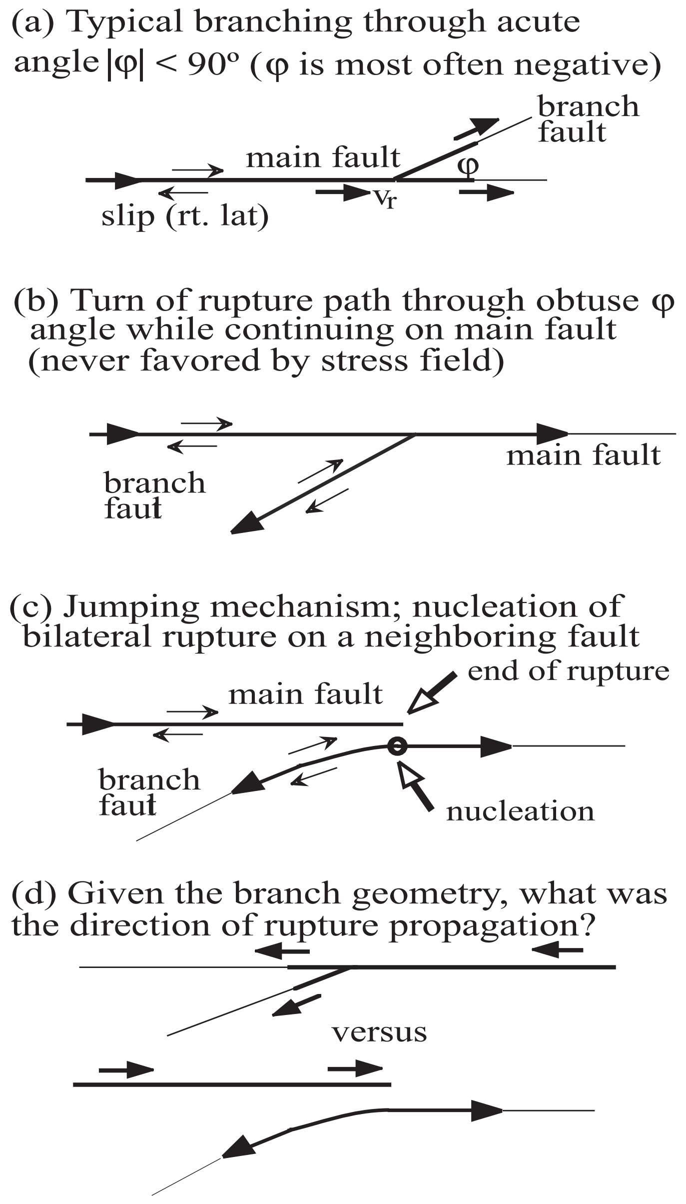

(a) Typical branching through acute angle |φ| < 90º (φ is most often negative)

(b) Turn of rupture path through obtuse φ angle while continuing on main fault (never favored by stress field)

(c) Jumping mechanism; nucleation of bilateral rupture on a neighboring fault

(d) Given the branch geometry, what was the direction of rupture propagation?

Figure 4.1: Issues in fault branching (see text).

4.2.2 Field examples of backward branching

We study the transition of the rupture path from the Kickapoo to the Homestead Valley faults, Figure 4.2, during the 1992 Landers earthquake, so as to leave a backward branch in the rupture path along the southern end of Homestead Valley fault. The rupture started to the SSE of the area covered by the map, along the Johnson Valley fault, and continued far to the NNW, first along the Homestead Valley fault and then the Emerson and Camp Rock faults [*Rockwell et al.*, 2000; *Sowers et al.*, 1994; *Spotila and Sieh*, 1995; *Zachariasen and Sieh*, 1995].

In the 1992 Landers earthquake [*Sowers et al.*, 1994], right-lateral slip on the Johnson Valley Fault propagated first along that fault but then, after several aborted attempts signaled by the short surface breaks shown, it branched to the dilational side onto the Kickapoo fault, at an angle $\varphi \approx -30^o$. The rupture also continued a few kilometers to the NNW on the main (Johnson Valley) fault. That exemplifies the type of branching typically considered, through an acute angle relative to the direction of propagation along the primary fault. (The Johnson Valley and Kickapoo branch has been analyzed as a field case in support of recent theoretical work [*Poliakov et al.*, 2002; *Kame et al.*, 2003], explaining how such typical branching depends on pre-stress state, branch geometry, and rupture propagation speed as the branch junction is approached.)

What is of interest here, however, is that the rupture, after propagating along the Kickapoo segment, transitioned to the Homestead Valley fault and progressed not just to the north on that fault, in continuation of the main Landers rupture, but also backwards along the Homestead Valley fault where it curves to the SSE. That forms the backward branch (backward relative to the main direction of rupture propagation) that we consider, a promi-

Figure 4.2: Map from *Sowers et al.* [1994] showing region of transition from the Johnson Valley to the Kickapoo and to the Homestead Valley faults during the 1992 Landers earthquake. The thickest lines show fault breaks with surface slip > 1 m, intermediate lines > 0.05 m, and thinnest lines > 0.01 m.

nent feature of 4 km length. Measurements of surface slip along that backward branch [*Sowers et al.*, 1994], show right-lateral slip, decreasing towards the SSE. Prominent surface breaks were also observed along the western side of the Homestead Valley fault (Figure 4.2). From those it can be argued [*Poliakov et al.*, 2002; *Kame et al.*, 2003] that, given the local principal pre-stress orientation [*Hardebeck and Hauksson*, 2001], the western side of the southern Homestead Valley fault should have been the dilational side of the rupture. That, along with the slip pattern, suggests that rupture initiated on the Homestead Valley fault in the region where it is closely approached by the Kickapoo fault, near the northern termination of the latter, and then propagated bilaterally, both N and SSE along the Homestead Valley fault.

The following are other cases, also from the Eastern California Shear Zone, of rupture transitions that leave backward-branched rupture patterns: As rupture continued along the Homestead Valley fault, NNW of the region mapped in Figure 4.2, there was a transition of the rupture path to the Emerson fault but, while primarily propagating to the NW, the rupture also progressed backwards along different SSE splays of the Emerson fault [*Zachariasen and Sieh*, 1995]. The rupture path next transitioned from the Emerson to the Camp Rock fault, and in doing so again generated a backward branch to the SSE on the Camp Rock fault. Another case is in the 1999 Hector Mine earthquake. Rupture originated on a buried fault without surface trace [*Li et al.*, 2002; *Hauksson et al.*, 2002; *Oglesby et al.*, 2003a] and progressed bilaterally south and north. In the south it met the Lavic Lake fault and progressed a large distance south on it, but also progressed backward, i.e. NNW, along the northern stretch of the Lavic Lake fault. The angle between the buried fault and the northern Lavic Lake fault is $\varphi \approx -160^o$, and that NNW stretch extends around 15 km, defining a major backward branch.

4.2.3 Backward branching mechanisms

Such examples with highly obtuse branch angles (backward branching) suggest that there may be no simple correlation between fault geometry and directivity. An important question is whether those obtuse branches actually involved a rupture path which directly turned through an obtuse angle (while continuing also on the main fault) like in Figure 4.1(b), or rather involved arrest by a barrier on the original fault and jumping to a neighboring fault, on which rupture propagated bilaterally (Figure 4.1(c)). The importance of stopping on the main fault to making the jumping mechanism possible will be discussed later.

Stress fields around a dynamically moving mode II crack tip with right-lateral slip have been reported by *Poliakov et al.* [2002]. At the obtuse angles considered, they predict strongly left-lateral shear stress, and hence are inconsistent with having the rupture path directly turn through highly obtuse angles like in Figure 4.1(b), if slip is to remain right-lateral on the branch. Thus we discount that mechanism. Note, that there is no inhibition to obtuse-angle branching with *left*-lateral slip on the branch; that situation was observed in lab experiments under impact loading [*Rousseau and Rosakis*, 2003]. In that work, small tensile fracture arrays along the extensional side of the rupture diagnosed where the slip was right- vs. left-lateral.

On the other hand, there is evidence that the Kickapoo and Homestead Valley faults are disjoint from one another, so that the transition fits the stopping and jumping scenario of Figure 4.1(c). First, mapping of observable fault slip (> 10 mm) in the vicinity of the transition ([*Sowers et al.*, 1994]; see Figure 4.2 here) suggests that the faults do not actually intersect one another at the surface. Second, *Li et al.* [1994] used studies of fault zone trapped waves to show that there was transmission in a channel along the southern Johnson Valley and Kickapoo faults and in another channel along the Homestead Valley fault, but no communication between those channels. Those results suggest that the Kickapoo and Homestead Valley faults do not join, at least at the possibly shallow depths controlling the observations. Finally, precise relative relocations of Landers aftershocks have been used to image the fault strands at depth [*Felzer and Beroza*, 1999], and suggest that they form two discrete structures throughout the seismogenic depth range.

4.2.4 Branching and rupture directivity

If such a jumping mechanism turns out to be a reasonably general mechanism of backward branching, then an implication for the *Nakata et al.* [1998] aim of inferring rupture directivity from branch geometry is that such will be possible only when rather detailed characterization of fault connectivity (by surface geology, microearthquakes relocation, trapped waves) can be carried out in the vicinity of the branching junction. Such studies must ascertain whether direct turning of the rupture path through an angle, or jumping and then propagating bilaterally, were involved in prior events. Those two possibilities have opposite implications (Figure 4.1(d)) for how to associate directivity with a (nominally) branched fault geometry.

In the following sections of the paper, we analyze the mechanics of rupture propagation and slip transfer for faults with complex geometries similar to those near the Kickapoo to Homestead Valley transition. We show that these considerations strongly support the possibility that the backward branch formed by the jumping and bilateral propagation mechanism of Figure 4.1(c). (Further, we note that *Aochi and Fukuyama* [2002] tried to simulate the Kickapoo to Homestead Valley rupture transition by assuming that the faults were actually connected in an inverted "y" type of branch junction, rather than forming the stepover configuration that we assume here. They could then achieve rupture continuation from Kickapoo onto the northern Homestead Valley fault, but not onto the southeastern part of the Homestead Valley fault which is the object of our study here, and which hosted the backward branch of rupture observed.)

4.3 Choice of prestress and modeling parameters

For convenience, we treat the Kickapoo fault near its northern termination as being straight and coincident with the x axis, which runs south to north (like the fault itself does approximately in that region; Figure 4.2). The fault plane is $y = 0$, with the y axis positive to the west, and we perform 2D modeling in that x, y plane. Here and later, all faults are considered to undergo right-lateral strike-slip.

The prestress, i.e., the tectonic stress in the region, has the form

$$\sigma^0_{ij} = \begin{pmatrix} \sigma^0_{xx} & \sigma^0_{xy} \\ \sigma^0_{yx} & \sigma^0_{yy} \end{pmatrix}. \tag{4.1}$$

as regards in-plane components, where normal stresses are positive if tensile. We should actually think of these as effective stresses $(\sigma^0_{ij})^{tot} + p^0\delta_{ij}$, where p^0 denotes initial fluid pore pressure. Like in [*Kame et al.*, 2003] where the branching from the Johnson Valley to Kickapoo faults during this earthquake is studied, the static friction coefficient $tan(\Phi_s) = f_s$ is taken as 0.6, generally consistent with laboratory values, and cohesion is neglected.

It is less clear what to take for the dynamic coefficient $\tan(\Phi_d) = f_d$ after slip-weakening, or how reasonable it is to regard it as actually constant at large earthquake slip, especially when thermal weakening and possible fluidization is considered. Values of $f_d/f_s = 0.8$ and 0.2 have been tested and the results do not show significant differences. Only the results for $f_d/f_s = 0.2$ will be shown here. We choose the shear modulus $\mu = 30$ GPa and the Poisson ratio $\nu = 0.25$ ($\lambda = \mu$).

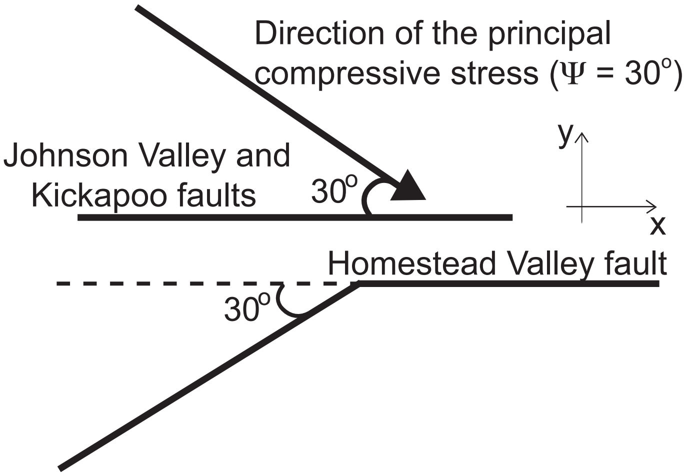

Figure 4.3: Simple modeling of the faults involved in the 1992 Landers earthquake.

Most of our results can be expressed in non-dimensional form but when necessary for numerical illustrations here, we have used $G = 1$ MJ/m^2 for the crack energy release rate and $\sigma^0_{yy} = -50$ MPa. For the corresponding σ^0_{xx}, to be discussed subsequently, the in-plane invariant $(\sigma^0_{xx} + \sigma^0_{yy})/2 = -59.5$ MPa. Assuming ideal strike-slip rupture (i.e., vanishing intermediate deviatoric stress), that invariant is equal to the effective overburden, and assuming hydrostatic pore pressure, that corresponds to a depth of 3.3 km. Given the nondimensionalization of our problem, features of the solution such as the speed of rupture propagation and its time evolution, and details of if, where and how slip transfers between faults, would be unchanged for the choice of parameters $G = 4$ MJ/m^2 and $\sigma^0_{yy} = -100$ MPa. That change, which keeps the slip-weakening zone length R at the same (time dependent) size throughout the rupture as for the above case, would correspond to a depth of 6.6 km. Such depth is a reasonable estimate of the centroidal depth of rupture during the Landers event, and the fracture energy is close to the 5 MJ/m^2 inferred for it by seismic slip inversions, fitted to 3D analyses of slip-weakening rupture [*Olsen et al.*, 1997; *Peyrat et al.*, 2001].

To properly determine the in plane prestress field around the faults, if all the stresses are normalized by $-\sigma^0_{yy}$, two further quantities have to be specified. First, on the basis of inference of principal stress directions from microseismicity by *Hardebeck and Hauksson* [2001], the maximum principal compressive stress direction around the faults is approximately 30^o east of north. Because the tangent direction to the Kickapoo fault is about north. Thus there is an angle $\Psi \approx 30^o$ between the most compressive stress and that fault (Figure 4.3).

We have to specify one more value, for example the shear stress ratio, $\sigma^0_{yx}/(-\sigma^0_{yy})$. There is no rigorous way to specify that. We choose it according to considerations of rupture propagation velocity v_r. Supershear v_r is sometimes, but only relatively rarely, inferred for natural events. Thus we choose parameters so that v_r remains sub-Rayleigh. *Andrews* [1976] shows the influence on v_r of the ratio

$$S = (\tau_p - \sigma^0_{yx})/(\sigma^0_{yx} - \tau_r) \tag{4.2}$$

where $\tau_p = -f_s\sigma^0_{yy}$ is the peak strength and $\tau_r = -f_d\sigma^0_{yy}$ is the residual strength after slip-weakening. When S is small enough, a transition from sub-Rayleigh to supershear propagation will occur, so we do not want S to be so small as to allow that in our modeling.

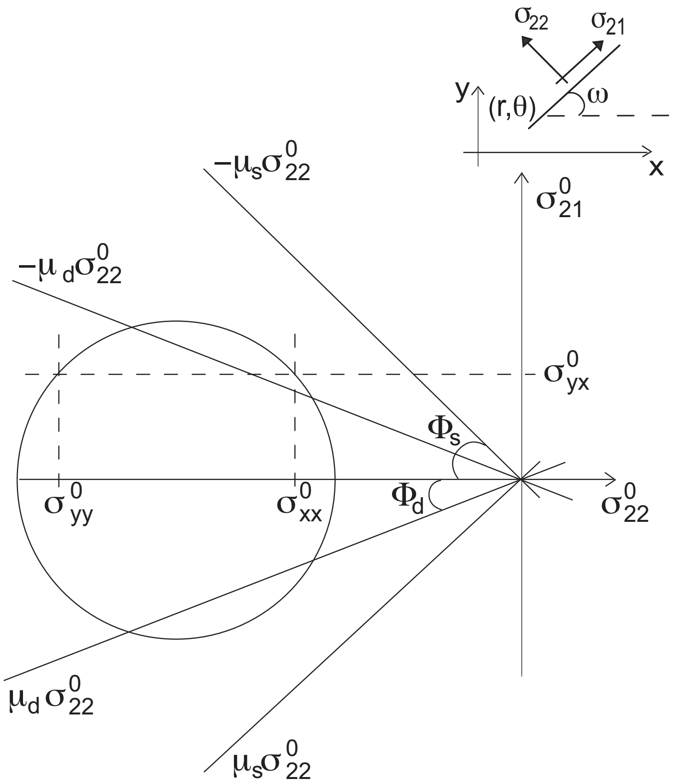

Figure 4.4: Mohr circle of the pre-stress: conditions required to not violate the failure conditions in any orientation and to favor the propagation of the rupture for some orientations.

However, in a simple static study to follow, we show that the smaller is the value of S, the larger is the the maximum distance that can be jumped, and vice-versa. So it won't do to make S too large, and a compromise has to be reached. Using Figure 9 of *Andrews* [1976] (which shows the v_r achieved as a function of S and the ratio of the length L of the ruptured zone to the minimum unstable crack length L_c), and the static study, we have chosen $S = 1.3$. For that, v_r remains sub-Rayleigh in our configuration. It leads to $\sigma^0_{yx}/(-\sigma^0_{yy}) = 0.33$.

Given the principal direction at $\Psi = 30^o$, we can then calculate, the remaining in-plane stress ratio as $\sigma^0_{xx}/\sigma^0_{yy} = 1.38$. That corresponds to the in-plane invariant $(\sigma^0_{xx} + \sigma^0_{yy})/2 =$

$1.19\sigma^0_{yy}$.

4.3.1 Strength constraints on prestress

In order to make the prestress field realistic we have to satisfy some mechanical conditions. Since large regions of earth cannot sustain tensile stresses, no principal stress should be tensile. Also, the prestress field should not violate the Mohr-Coulomb criterion for onset of frictional rupture.

With the two parameters, Ψ and $\sigma^0_{yx}/(-\sigma^0_{yy})$, the condition to avoid tension is:

$$\frac{\sigma^0_{yx}}{-\sigma^0_{yy}}\tan(\Psi) < 1, \tag{4.3}$$

which is respected with our parameters. Secondly, to make sure that the prestress does not violate the Coulomb failure condition, i.e., that $|\sigma^0_{21}| < -f_s\sigma^0_{22}$, for any orientation of the faults (Figure 4.4), $\sigma^0_{yx}/\sigma^0_{yy}$ has to satisfy:

$$\frac{\sigma^0_{yx}}{-\sigma^0_{yy}} < \frac{\sin(\Phi_s)\sin(2\Psi)}{1-\sin(\Phi_s)\cos(2\Psi)} \tag{4.4}$$

In this case, the condition is $\sigma^0_{yx}/(-\sigma^0_{yy}) < 0.60$ which is also respected.

4.4 Elastostatic singular crack modeling

The goal of this section is to give a general idea of stressing near the end of an arrested rupture, to begin to determine conditions so that a rupture can jump to another fault, parallel [*Harris and Day*, 1993] or not. For simplicity, we start with the study of an elastostatic singular crack model of a mode II rupture.

We suppose that the two ends of a finite rupture have finished their motion and that all along the crack there is sustained a stress equal to the residual shear strength, $\sigma_{yx} =$

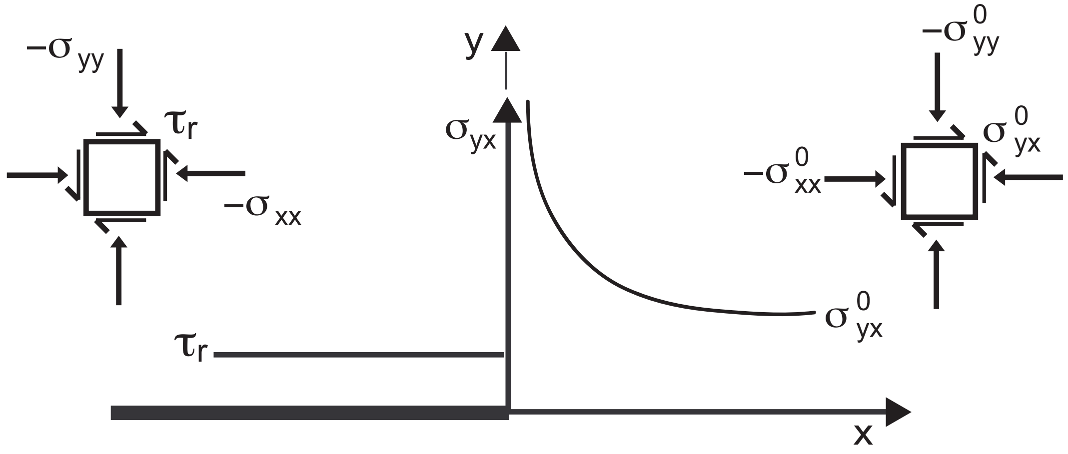

Figure 4.5: Singular elastic crack model (mode II shear) for static rupture. Stress state shown (left) behind the tip, near the fault surface, and (right) far ahead, where it coincides with the prestress.

$\tau_r = -f_d\sigma^0_{yy}$ (as represented in Figure 4.5). This static study can be understood as a study after the motion. It is suggestive only, because we cannot preclude the possibility that dynamic stresses very close to the stopped rupture tip were higher than in the final static field; they cannot be on the crack plane itself, from basic results on unsteady crack dynamics [*Fossum and Freund*, 1975], but the situation is more complex in the near tip field at other orientations relative to the rupture, as well as at more distant locations.

4.4.1 The faults

In the branching transition from the Johnson Valley to the Kickapoo faults, we will neglect the few km continuation along the former, and consider it and the Kickapoo fault as one, and only one, main fault, whose length is 15 km. (Of course the actual length is longer, but we do not want to allow crack lengths in a 2D model which are much greater than the seismogenic thickness of the crust. From 3D considerations that thickness sets a limit, which is not contained in 2D models, on how much further increase of crack length along strike can increase the stress concentration at the crack ends.) To determine the stress distribution due to the crack for the singular static model, the Johnson Valley and Kickapoo faults are represented, just here but not in the elastodynamic study to follow, as a straight fault of 15 km length. Figure 4.3 gives one simple modeling of the faults, with the Homestead Valley fault at orientation angles $\omega = 0^o$ and 30^o, in pieces, relative to the straight fault. Actually, the smallest distance between the Kickapoo and Homestead Valley fault is a few hundred meters (between 200 and 300 m) [*Sowers et al.*, 1994], and the orientation angle ω of the closest parts of the latter fault, relative to Kickapoo is between 0^o and 10^o.

4.4.2 Static stress distribution

Consider a single straight crack extending from $x = -X$ to 0 on the x-axis, with $X = 15$ km, in the infinite x, y plane, in a mode II configuration. We study the stress distribution near the crack tip $x = 0$. As explained by *Rice* [1980] and *Poliakov et al.* [2002], the final stress σ_{ij} is the sum of the initial stress σ^0_{ij} and stress change $\Delta\sigma_{ij}$ due to introduction of the crack, and is given by

$$\sigma_{ij} = \frac{K_{II}}{\sqrt{2\pi r}}\Sigma_{ij}(\theta) + \begin{pmatrix} \sigma^0_{xx} & \tau_r \\ \tau_r & \sigma^0_{yy} \end{pmatrix} + O(\sqrt{r}) \qquad (4.5)$$

where (r, θ) are the polar coordinates (the origin is the crack tip), the $\Sigma_{ij}(\theta)$ are certain universal functions normalized to $\Sigma_{yx}(0) = 1$ (see, e.g.,[*Lawn and Wilshaw*, 1993] or

[*Rice*, 1968] or other sources on elastic crack theory) ... and $\tau_r = -f_d\sigma^0_{yy}$ the residual shear strength .... In the present case the stress intensity factor is

$$K_{II} = (\sigma^0_{xy} - \tau_r)\sqrt{\pi X/2}, \tag{4.6}$$

and $O(\sqrt{r})$ denotes term which vanish in proportion to $\sqrt{r}$ or faster as $r \to 0$.

The full representation of the stress field, effectively identifying explicitly all terms in equation (4.5) including those denoted $O(\sqrt{r})$, may be done using standard techniques in the 2D elasticity analysis of cracked solids (e.g., [*Rice*, 1968]) to solve for $\Delta\sigma_{ij}$. Thus letting the complex position be denoted by $z = X/2 + x + iy$,

$$\begin{aligned} \sigma_{xx} + \sigma_{yy} &= \sigma^0_{xx} + \sigma^0_{yy} + 4\mathrm{Re}[\phi'(\mathrm{z})] \\ \sigma_{yy} - \sigma_{xx} + 2i\sigma_{yx} &= \sigma^0_{yy} - \sigma^0_{xx} + 2i\sigma^0_{yx} + 2[\bar{z}\phi''(z) + \psi'(z)] \end{aligned} \tag{4.7}$$

where for our mode II problem

$$\phi'(z) = \frac{\sigma^0_{yx} - \tau_r}{2i}\left[\frac{z}{(z^2 - X^2/4)^{1/2}} - 1\right], \ \ \psi'(z) = -2\phi'(z) - z\phi''(z) \tag{4.8}$$

Representation of the stress field for purposes of our plots in Figure 4.6 is done using the full equations (4.7) and (4.8), although the plots are very similar in appearance when we use equation (4.5) and simply neglect the terms denoted $O(\sqrt{r})$.

4.4.3 Conditions for rupture nucleation on a nearby fault

In the Coulomb friction model, rupture can nucleate at any point if the shear stress is higher that the static friction strength. So, it is relevant to consider the normal and shear stresses $(\sigma_{22}, \sigma_{21})$ at a point on a potential fault, whose polar coordinates are (r, θ). Different orientation angles ω given to the second fault are analyzed, and different situations of nucleation may arise as follows:

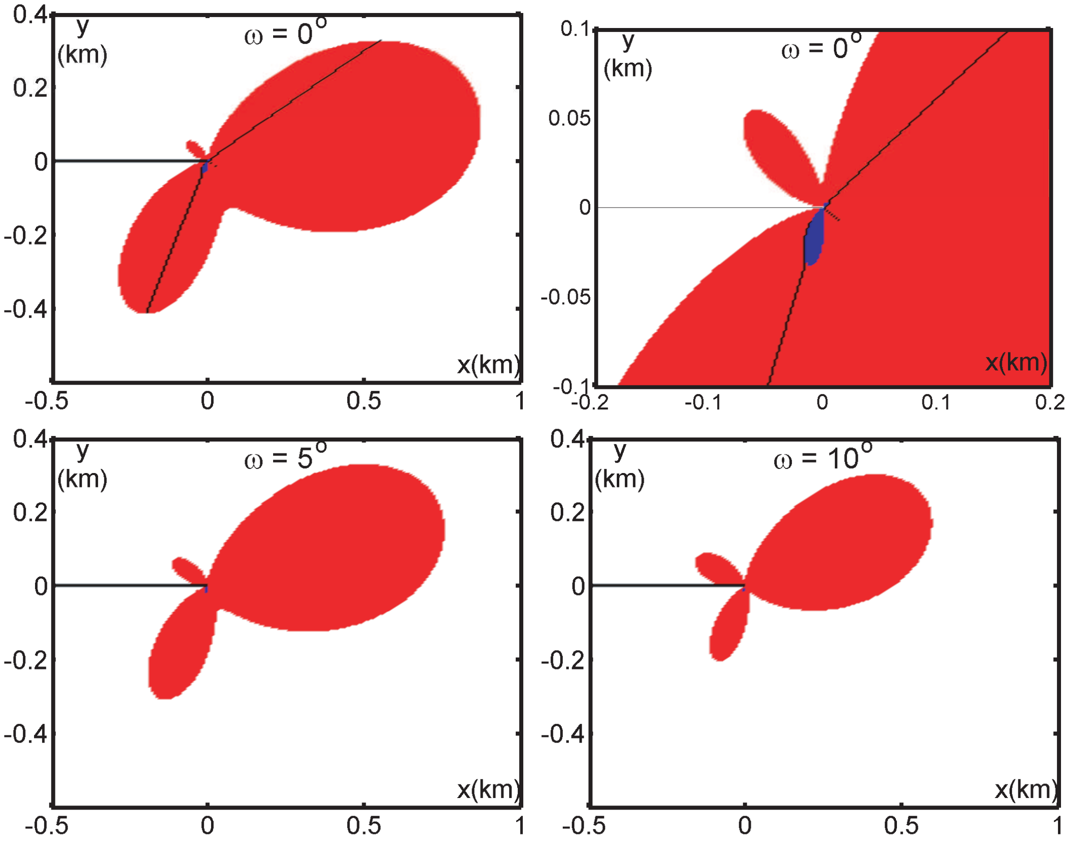

Figure 4.6: Areas where nucleation of a rupture is possible, for various orientation angles ω of the second fault. Angles $\omega = 0^o, 5^o$ and 10^o, are chosen with reference to the geometry of the Homestead Valley fault. The medium grey regions (bright red in color version) are those for which $\sigma_{coul} = \sigma_{21} + f_s\sigma_{22} > 0$ on a fault trace with orientation ω (i.e., areas where right-lateral failure nucleation is possible). Small, dark grey regions (dark blue in color version) near the crack tip are areas where the elastically calculated normal stress on the second fault is tensile ($\sigma_{22} > 0$); see enlarged view of region, for the $\omega = 0^o$ case, in upper right panel. The black lines in the upper two panels, for the $\omega = 0^o$ case, represent the points where, for each fixed y, σ_{coul} attains its maximum with respect to x.

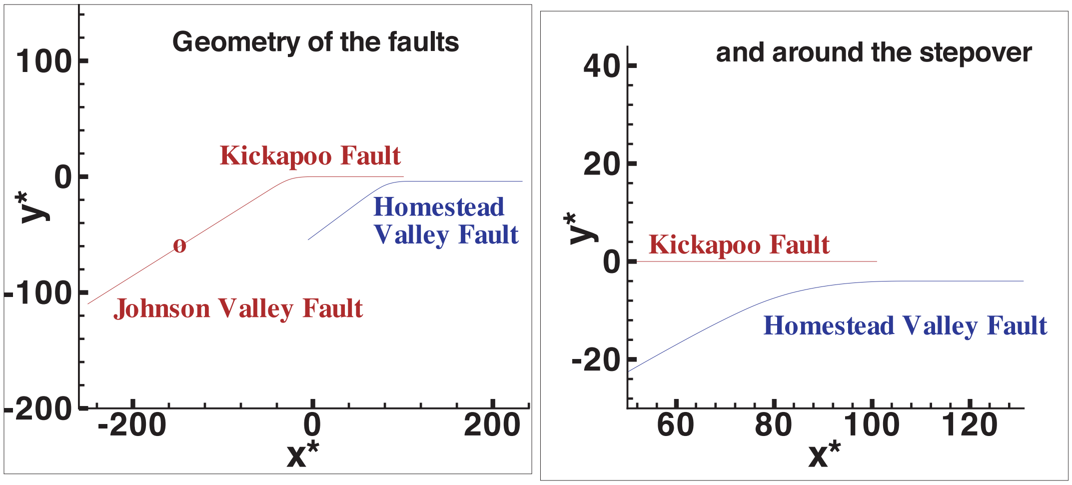

Figure 4.7: Geometry of faults in the x, y plane, $x^* = 3x/R_0^o$, $y^* = 3y/R_0^o$. The x-axis corresponds to the orientation of the portion of the Kickapoo fault that is modeled straight NS. The orientation of the Johnson Valley fault decreases from 0^o to 26^o. The orientation of left half of Homestead Valley fault decreases from 0^o to 30^o.

1. If $\sigma_{22} < 0$ and $\sigma_{21} > f_s(-\sigma_{22})$, right-lateral slip nucleates. The area where this condition is met is represented in medium grey (bright red in color version).
2. If $\sigma_{22} < 0$ and $\sigma_{21} < -f_s(-\sigma_{22})$, left-lateral slip nucleates. The area where the condition is met is represented in light grey (light green). In fact, we'll find none such for our ω range studied..
3. If $\sigma_{22} > 0$, the area is represented in dark grey (dark blue). Compressional remote stress fields only are studied so that the faults remained closed but it is interesting to test if there are local areas where the normal stress is predicted to be extensional.

With these different representations, we analyze where a nearby nucleation on a second fault could occur, at least as based on the static field. This allows a preliminary estimate of the influence of different parameters: characteristics of the stepover (width and overlap of the second fault, its local orientation ω), prestress, stress drop $\sigma_{yx}^0 - \tau_r$, and ratio $S = (\tau_p - \sigma_{yx}^0)/(\sigma_{yx}^0 - \tau_r)$.

4.4.4 Results for some second-fault orientations

Results based on our model parameters as above are shown in Figure 4.6 for local $\omega = 0^o$, 5^o and 10^o. We see that this simple static analysis is consistent with some conclusions of the *Harris and Day* [1993] dynamic study of stepovers between parallel fault strands (case $\omega = 0^o$). First is the difference between the compressional and the dilational sides. Indeed, there is no symmetry, and the areas of possible nucleation and the maximum “jumpable” distance are very different according to the overlap.

Moreover, for these orientations only right-lateral slip is possible; there are no light grey (light green) regions signaling left-lateral. The higher is the orientation of the second fault the smaller are the maximum jumpable distance and the area where the nucleation is possible.

There are very small regions adjoining the crack tip on the dilational side where the normal stress is positive, signaled by dark grey (dark blue) shading. That means a possible opening of the secondary fault, but strong conclusions cannot be drawn because this is particularly near the crack tip (where the simple model adopted has a singularity of the stress), and also because we have not analyzed effects on the stress field of plastic yielding in the Coulomb failure regions shown to envelop those zones.

Comparing the stress distribution calculations for several orientations which represent where the nucleation of a rupture is possible, given the position of the curved Homestead Valley fault and its orientations, we can anticipate that the rupture should jump from Kickapoo fault and might nucleate in several positions along the Homestead Valley fault, Figure 4.6, although this analysis cannot tell us which one will nucleate first.

4.4.5 Some analytical results

We can use our representation of the stress field to make simple estimates of the maximally stressed offset location (x coordinate) for a given stepover width (y coordinate), and of the scaling of maximum vulnerable width with other parameters, especially S. First note that the upper two panels of Figure 4.6 correspond to the case of two parallel faults ($\omega = 0^o$). They show that the loci of maximal Coulomb stress $\sigma_{coul} = \sigma_{21} + f_s\sigma_{22}$, for various y, define a pair of nearly straight lines emanating from the crack tip. Considering points where the normal stress is compressive and the slip is right lateral, that geometry and other features of the stressing can be understood when stresses are written like in equation 4.5 and we neglect the $O(\sqrt{r})$ terms to simplify (as commented above, they have little effect on the shapes shown in Figure 4.6). Using x, y variables instead of r, θ, equation 4.5 leads to

$$\sigma_{coul} = (\sigma^0_{21} + f_s\sigma^0_{22}) + [\sqrt{\frac{X}{|y|}}F(\frac{x}{y}) + C](\sigma^0_{yx} + f_d\sigma^0_{yy}) \tag{4.9}$$

Here the first pair of terms give the Coulomb prestress; they are dependent on ω and are linear in the σ^0_{ij}. In the remaining terms $F(x/y)$ is a dimensionless function proportional to $\sqrt{|\sin(\theta)|}[\Sigma_{21}(\theta) + f_s\Sigma_{22}(\theta)]$ and having different forms in $y > 0$ and $y < 0$, whereas C is a constant; both F and C depend on ω and vary linearly with f_s.

That expression makes it clear that σ_{coul} is maximum relative to x, at any given y, when F is a maximum relative to its dimensionless argument x/y. That defines loci $x/y =$ constant in $y > 0$ and $y < 0$, thus predicting that the heavy lines in the upper panels of

Figure 4.6 should be precisely straight, to the neglect of the $O(\sqrt{r})$ terms in equation 4.5. As noted, they are indeed nearly straight, when we include all terms like in equations (4.7) and (4.8).

Finally, for the $\omega = 0^o$ case of parallel faults [*Harris and Day*, 1993] we can estimate the influence of the S ratio on the maximum jumpable distance H_{max}. Writing $\tau_r = -f_d\sigma^0_{yy}$ in equation 4.5, and making C explicit in equation 4.9 leads to

$$\sigma_{coul} = (-f_d\sigma^0_{yy} + f_s\sigma^0_{yy}) + \sqrt{\frac{X}{|y|}}F(\frac{x}{y})(\sigma^0_{yx} + f_d\sigma^0_{yy}) \tag{4.10}$$

where $F(x/y)$ is linear in f_s. Identifying the terms corresponding to τ_p and τ_r, and setting the argument x/y of F to correspond to the maximal value, say F_m (> 0, but different on the two sides of the fault), and using the definition of S, this becomes

$$\frac{\sigma_{coul}}{\sigma^0_{yx} - \tau_r} = F_m\sqrt{\frac{X}{|y|}} - (1 + S) \tag{4.11}$$

Hence the maximum jumpable distance H_{max} is the largest value of $|y|$ for which the right side is positive, and that yields

$$\frac{H_{max}}{X} = (\frac{F_m}{1+S})^2 = F_m^2(\frac{\sigma^o_{yx} - \tau_r}{\tau_p - \tau_r})^2 \tag{4.12}$$

in which the coefficient of proportionality (F_m^2) depends on f_s. Thus H_{max} increases when S decreases (i.e., when prestress σ^0_{yx} is larger); Figure 4.6 is for $S = 1.3$ but the results can thereby be scaled to other S.

4.4.6 Long-range dynamic rupture propagation

If the rupture has nucleated along a suitable direction, will the prestress be consistent with an arbitrary amount of propagation along that direction? This condition will be met for at least some orientations if some part of the Mohr Circle lies outside the wedge of angle $2\Phi_d$, as represented in Figure 4.4.

Typically, $\sigma_{yx}^0/(-\sigma_{yy}^0) > f_d$ makes long range dynamic rupture possible along the part of Homestead Valley fault parallel to the x-axis. The condition to make it possible along the other part of the fault, with a maximum misorientation $\omega = 30^o$, is that $\sigma_{12}^0 > -f_d\sigma_{22}^0$, which is satisfied if $\sigma_{yx}^0/(-\sigma_{yy}^0) > 0.122$.

Thus the prestress field allows dynamic rupture along the Homestead Valley fault. Such has been inferred, to the N and at least for about 4 km to the SSE, in the earthquake.

From this simple static analysis, we have guidelines for knowing if a fault is near enough to the tip of another one for slip to be nucleated. But we do not know if the rupture can propagate and if it does so bilaterally. A dynamic study is required, and that analysis follows. It includes the time dependence of fault rupture, stress waves, and time dependent stress concentrations generated during the rupture process (e.g., we will show important dynamic normal stress changes on curved parts of the fault along which ω is changing).

4.5 Elastodynamic slip-weakening rupture modeling

4.5.1 Geometric modeling of the faults

We again choose the x axis parallel to the northern part of the Kickapoo fault, treating its last 4 km as straight. We do not consider the short rupture along the Johnson Valley fault north of its branch with Kickapoo, and treat that pair of faults as a single fault, curved before reaching the straight Kickapoo segment. Because the 2-D model is not sensible for crack lengths greater than the seismogenic thickness of the crust, we have to reduce the rupturing length of the Johnson Valley fault to 10km, but we keep the actual length of the Kickapoo fault, about 5 km. The angle φ between the two faults is $\approx 30^o$. The origin of the x, y system is taken at the beginning of the straight part of the Kickapoo fault. That is also the origin for the curvilinear distance s along the fault, so that $s > 0$ on the 4 km straight part.

The geometrical modeling is shown in Figure 4.7 in the x-y plane.

For the boundary integral equation (BIE) numerical analysis, we cover all potentially rupturing faults with uniformly sized cells of length Δs. Our parameter choices allow us to choose $\Delta s = 40$ m (25 cells over 1 km length), and still reasonably meet requirements [*Kame et al.*, 2003] for discretized numerical BIE solutions to suitably represent the continuum limit of the slip-weakening rupture model.

Thus, the straight northern segment of the Kickapoo fault has length 4 km $= 100\Delta s$. In the $s < 0$ region the Johsonn Valley-Kickapoo fault begins to curve progressively SSE along 2 km ($50\Delta s$) and then keeps the same orientation at 26^o east of south along 9 km ($225\Delta s$).

For the modeling of the Homestead Valley fault, we know that the stepover with the Kickapoo fault is between 200 and 300 m) at closest approach. From *Sowers et al.* [1994], the backward propagation seems to stop at about 4 km SSE from that closest region. Thus we choose to represent the entire part of the fault modeled with a length of 10 km ($250\Delta s$). Although rupture continues along Homestead Valley well to the north, in our model slip propagation is blocked on it 6 km north of the nucleation. We have verified that all of the action as regards forming the backward branch is over before waves from that artificial northern blockage of rupture propagate back into the region of interest.

The northern terminus of Kickapoo is offset in a direction perpendicular to Kickapoo by 200 m from the Homestead Valley fault. Thus for the simulation, the center of the 10 km long Homestead Valley fault is chosen to be at 160 m east ($y = -4\Delta s$) and 280 m north ($x = 107\Delta s$) of the terminus of Kickapoo. The northern half of the Homestead Valley fault ($125\Delta s$) is straight and parallel to Kickapoo. Along the curved SSE half, the orientation of the fault varies from 0^o to 30^o along 2 km ($50\Delta s$) to reach the value of 30^o and finally keeps it along the last 3 km ($75\Delta s$).

4.5.2 Slip-weakening Coulomb friction law

In our modeling, the rupture was allowed to propagate spontaneously using a slip-weakening friction law [*Ida*, 1972; *Palmer and Rice*, 1973]. The fault strength τ, once reaching the peak strength τ_p, decreases linearly (in the most commonly adopted variant of slip-weakening) with the slip, to the residual strength τ_r, and becomes constant when the slip Δu exceeds an amount D_c, the critical slip. D_c is considered to be a parameter inherent in the rupture process. Moreover, the Coulomb friction concept is added to the slip-weakening law so that τ is proportional to the normal stress $-\sigma_n$ at any particular amount of slip, as in Figure 2.8. That is,

$$\tau = \tau_r + (\tau_p - \tau_r)(1 - \frac{\Delta u}{D_c})H(1 - \frac{\Delta u}{D_c}) \tag{4.13}$$

where

$$\tau_p = f_s \times (-\sigma_n) \qquad \tau_r = f_d \times (-\sigma_n) \tag{4.14}$$

This criterion, contrary to the critical stress intensity factor criterion, does not suffer the unphysical infinite stresses at the edges: there is a continuous stress distribution at the crack tip. (see Figure 4.8). The notation R denotes the length of the slip-weakening zone, i.e. the zone in which $0 < \Delta u < D_c$ and $\sigma_{21} > \tau_r$.

Palmer and Rice [1973] and *Rice* [1968] showed that if the length of the slip weakening zone, R_0, of a static crack is small compared to all geometric dimensions of the model, such as overall crack size, then we can estimate from the energy balance of elastic-singular crack theory, with fracture energy G expressed in terms of the slip-weakening law, the minimum nucleation size of an initial crack so that the rupture can propagate. For $\lambda = \mu$ that is

$$L_c = \frac{16}{3\pi} \frac{\mu G}{(\sigma_{xy}^0 - \tau_r)^2} = \frac{8}{3\pi} \frac{\mu(\tau_p - \tau_r)}{(\sigma_{xy}^0 - \tau_r)^2} D_c \tag{4.15}$$

Here, following the notation of *Kame et al.* [2003], L_c is the total length of the nucleating crack (not half-length like in *Andrews* [1976]).

The initial crack has to be long enough to permit the rupture to propagate along the fault but should be small compared to the fault length to not affect the dynamic results.

In order to simply estimate R_0, *Palmer and Rice* [1973] use another slip weakening law chosen to make τ vary linearly with x within the end zone. For the case when the end zone size is small in comparison to the other lengths such as the crack length and the minimum nucleation size, they determine

$$R_0 = \frac{3\pi}{8} \frac{\mu}{\tau_p - \tau_r} D_c \tag{4.16}$$

Rice [1980] pointed out that for the same slip weakening law, during dynamic propagation under locally steady-state conditions on the scale of the end zone, the dynamic end zone size R is a function of the rupture velocity and diminishes with the velocity in particular way. That is:

$$R = \frac{R_0}{f(v_r)} \tag{4.17}$$

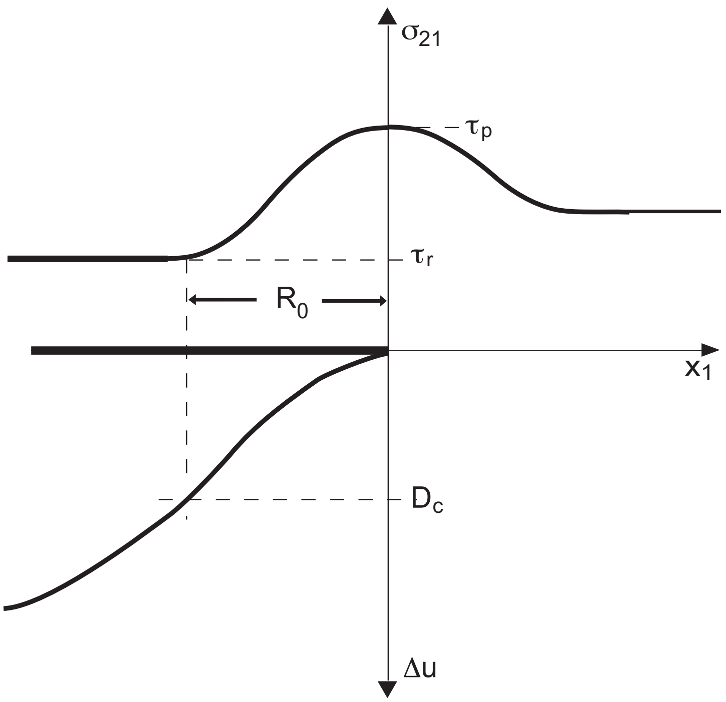

Figure 4.8: Fault and distribution of shear stress σ_{21} and slip displacement Δu.

where $f = 1$ when $v_r = 0^+$ and $f(v_r)$ increase with v_r, without limit as $v_r \to c_R$, where $c_R = 0.9194c_s$ (for $\lambda = \mu$) is the Rayleigh wave speed. In our model, we cannot calculate in closed form an exact value of the end zone length R. The results of equations 4.16 and 4.17 are quite realistic, according to mode II simulations by *Kame et al.* [2003] and our own results, and can often used as estimation of the end zone size.

Characteristics of the rupture velocity v_r attained during spontaneous dynamic propagation depend on S of equation 4.2 [*Andrews*, 1976; *Das and Aki*, 1977]: $v_r < c_R$ always if S is above a threshold (1.7-1.8), but given enough propagation distance L when S is below that threshold, v_r will ultimately transition to the range $c_s < v_r < c_p$; L/L_c diverges at the threshold. In natural earthquake studied until now, the rupture velocity seems usually to be below the shear wave velocity. We have chosen $S = 1.3$ on the straight segment of the Kickapoo fault, which has the property that the maximal jumpable distance calculated in the static study is large enough but also that $v_r < c_R$ during the entire propagation along our representation of the Johnson Valley and Kickapoo faults.

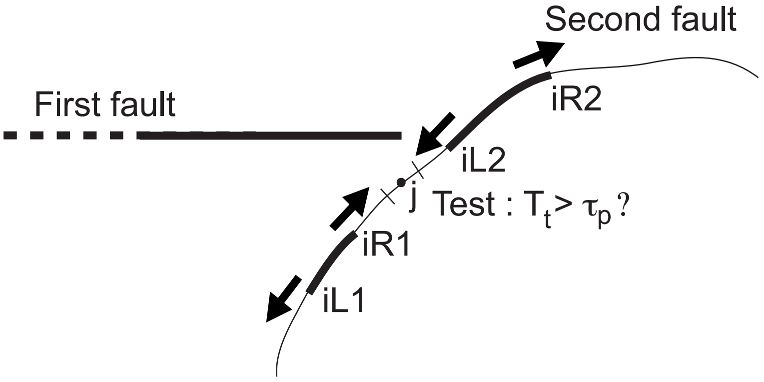

Figure 4.9: Multiple nucleations: the first fault has ruptured. iL and iR represent respectively the left and the right tip of each ruptured region.

Procedures for rupture transfer to the second fault

We will apply our procedures to study rupture along the Johnson Valley-Kickapoo fault and then address whether and how rupture could jump to the second fault, the Homestead Valley fault. As shown by *Harris and Day* [1993], three scenarios are possible, depending on the geometrical characteristics of the faults: (*i*) The rupture dies at the end of the first fault segment. (*ii*) The rupture triggers on the second fault segment but cannot absorb enough energy to propagate. (*iii*) The rupture triggers the second fault segment and then continues propagating.

With the slip rate history of the first fault given from a prior calculation, we study the possibility for the rupture to jump, considering time steps when the rupture has not yet completed on the first fault. We calculate the tangential and normal tractions all along the second fault for each time step, understanding that slip, if not a propagating rupture, can nucleate when in one cell the tangential traction is higher than the local peak strength. If this happens we later apply the algorithm explained above for the calculation of slip velocity in the ruptured region and the propagation of the rupture. To reduce computation time we suppose that the rupture on the second fault has no influence on the first; that means that we do not calculate the change of the stress on the first fault due to the rupture on the second one. This is sensible because slip on the first fault has stopped or nearly stopped by the time waves would reach it from the second fault. By the time waves from any small further slip on the first fault made their way back to the second, the rupture front would have moved much further along the second fault.

Depending on the geometry of the second fault, multiple nucleation sites may exist, as showed in the static study. A rupture can nucleate in different time steps and at different isolated locations. So, if a rupture has already nucleated, we continue to test along the region which has not ruptured if a nucleation is possible (Figure 4.9). If two nucleations are possible for example, we just must take care to join the tips (iL(i) and iR(j) represented in Figure 4.9) of the two ruptured regions when it is possible.

For the propagation of the rupture and the calculation of slip velocities for each region, the same algorithm as above is used.

4.6 Rupture along the Johnson Valley and Kickapoo faults

The nucleation is simulated near the center of the Johnson Valley segment of the fault around cell -150 (represented by a circle in Figure 4.7). According to the prestress σ_{ij}^0 and the 26^o orientation of the fault around this location, equation 4.15 determines the minimum nucleation size as $L_c = 5\Delta s$. That is about $2R_0$, which does not fully respect the assumption needed to validate equation 4.15 (R_0 should be much smaller than L_c). To enable the initiation of the rupture, the length of the initial crack is taken as $L_{nucl} = 20\Delta s$.

The rupture propagates bilaterally along the Johnson Valley segment, and continues along the curved part and along the Kickapoo fault. That is shown in Figures 4.10 and 4.11, which represent respectively the slip Δu (as $D^* = 3\mu\Delta u/(-\sigma_{yy}^0 R_0^o)$ for each 0.18s (that is $9R_0^o/c_p$) and the slip velocity V (as $V^* = \mu V/(-\sigma_{yy}^0 c_p)$) for several time steps ($N = 6c_p t/R_0^o$), all along the fault (as $s^* = 3s/R_0^o$ where s is the curvilinear coordinate). Here the scale length R_0^o refers to the static end zone size R_0 as calculated from the normal prestress on the straight part of the Landers fault; R_0 depends on the orientation considered. Note that the slight decrease in slip at the nucleation location is an artifact of the nucleation process.

Actually the rupture reaches the SSE end of the region of Johnson Valley fault modeled at $N = 531$ (1.77 s). Going NNW, it reaches the curved part (at cell -50) at time step $N = 437$ (1.47 s), the straight part of Kickapoo fault at $N = 629$ (2.1 s) and its end at $N = 1011$ (3.37 s).

The slip velocity increases slighly along the curved part and it is higher along the Kickapoo than along the Johnson Valley fault. This is partly because of the decrease of the normal stress along the fault and because the ruptured zone is getting longer. We notice too that, as we wanted at the beginning, reaching the SSE end of Johnson Valley seems to have no influence on the propagation of the rupture at the other end. After slipping, the end of the Kickapoo fault seems to lock very rapidly and stop slipping, which is represented

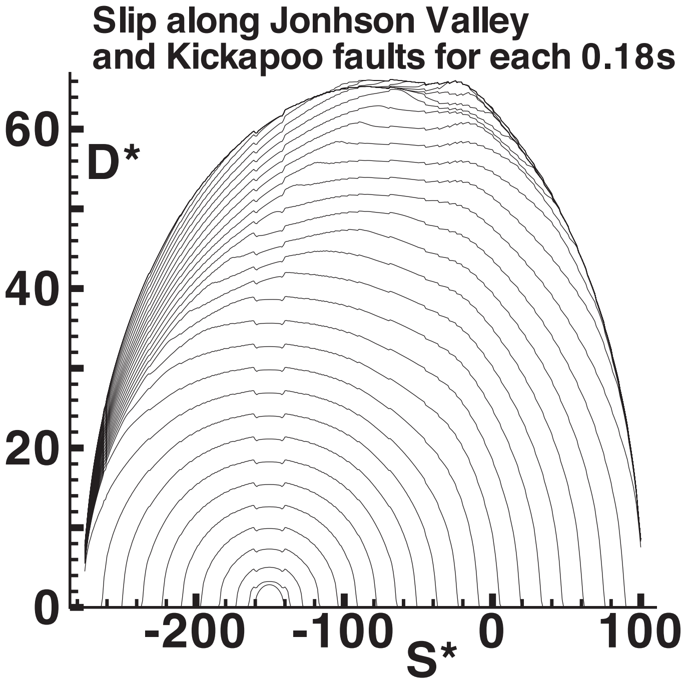

Figure 4.10: Along Johnson Valley and Kickapoo faults, slip Δu (as $D^* = 3\mu\Delta u/(-\sigma_{yy}^0 R_0^o)$ vs. $s^* = 3s/R_0^o$ where s is the curvilinear coordinate) for each 0.18s (that is $9R_0^o/c_p$).

between the time N=1060 and N=1200 but continues after.

According to the representation of slip, Figure 4.10, the maximum of slip is approximately 4.4m. The average along Johnson Valley is approximately 3.3m whereas in *Hardebeck and Hauksson* [2001] it is reported as 2.0 ± 0.5m. The difference is likely because of the assumptions of the slip weakening model and perhaps because of the simplicity of the pre-stress field and the 2D approximation itself. The average predicted along Kickapoo is about 3.6m.

As shown in Figures 4.10 and 4.11, the rupture is not inhibited by the curvature of the fault towards its extensional side (an inhibiting effect of curving away from the extensional side will be seen later for the SSE Homestead Valley fault). This is consistent with the

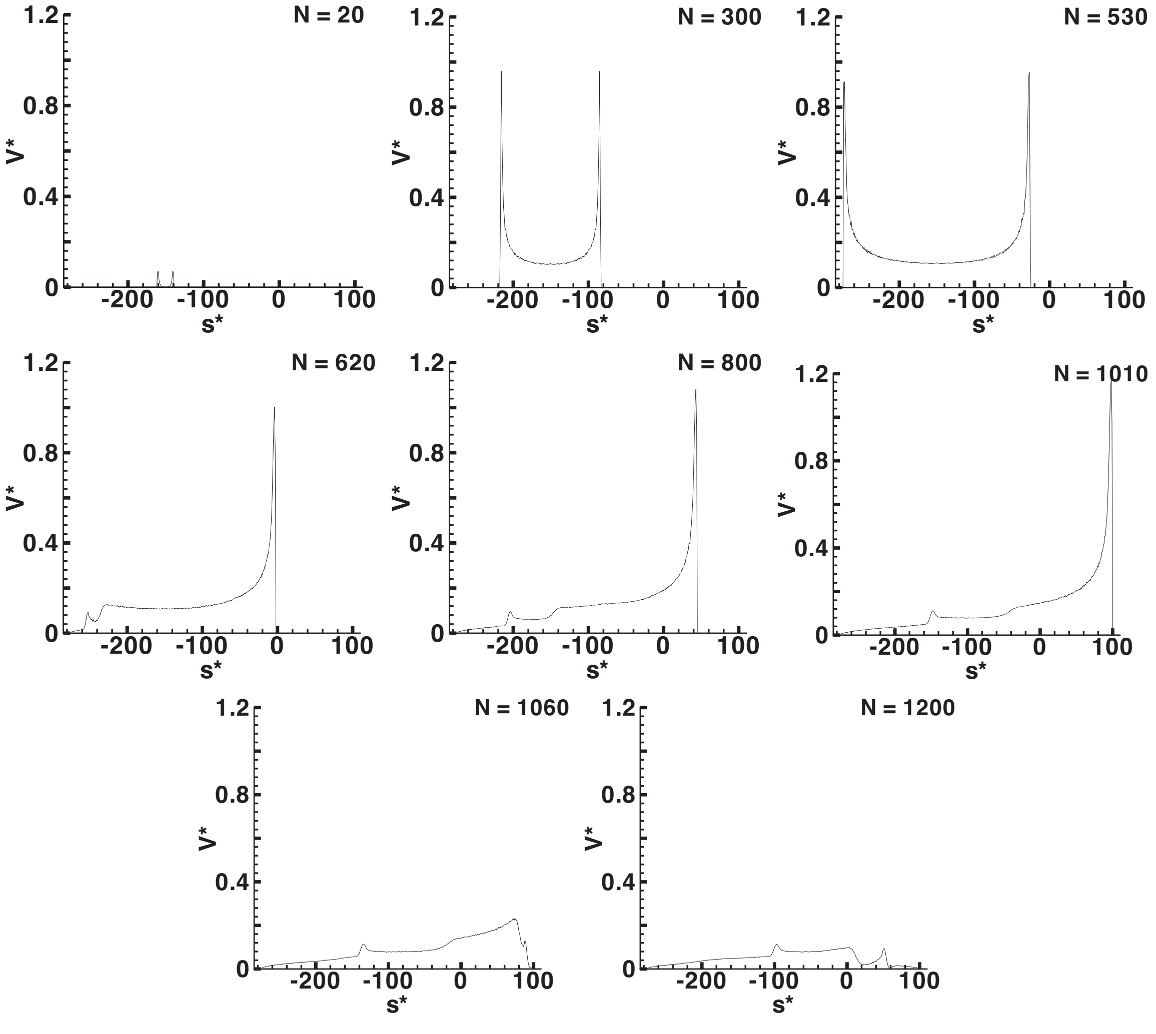

Figure 4.11: Along Johnson Valley and Kickapoo faults. Slip velocity V (as $V^* = \mu V/(-\sigma_{yy}^0 c_p)$ vs. $s^* = 3s/R_0^o$ where s is the curvilinear coordinate) for several time steps $N = 6c_p t/R_0^o$.

results of *Kame et al.* [2003] which suggest that for this orientation of the compressive principal stress, rupture along the branch (Kickapoo fault) is favored.

Figure 4.12 represents the propagation of each tip of the ruptured zone. The velocity of the right tip does not change when it reaches the curved part ($s^* = -50$) or the straight part parallel to the x axis ($s^* = 0$). The rupture velocity v_r, represented in Figure 4.13 (as v_r/c_s) increases and keeps a roughly constant value along the curved and the straight parts. That is around $0.9c_s$, i.e., very close to c_R. The v_r reported by our procedures is in the form $3\Delta s/n\Delta t$ where n is the number of time steps for the rupture to advance by 3 cell sizes; hence v_r is always quantized, as in the figure.

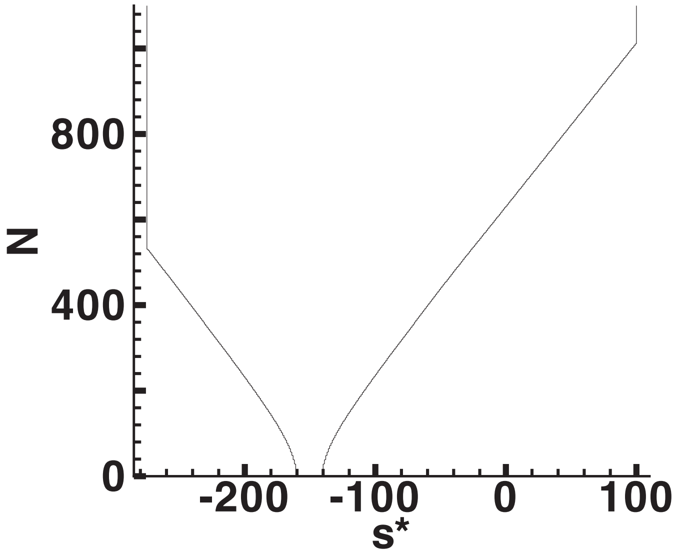

Figure 4.12: Position of the left and right ends of the ruptured zone along Johnson Valley and Kickapoo (as $s^* = 3s/R_0^o$ where s is the curvilinear coordinate, the origin is the beginning of the part of the fault parallel to the x-axis) for each time step (as $N = 6c_pt/R_0^o$). The two lines at each edge indicate the length of the ruptured zone.The length of the right part of the fault is about 4 km ($s^* = 100$) the length of the left part is 11km ($s^* = -275$).

4.7 Does the rupture jump from the Kickapoo fault to the Homestead Valley fault?

Using the slip history rate of the Johnson Valley-Kickapoo fault, we want to know now if a rupture, or more than one, can nucleate along the Homestead Valley fault and if it does, if it propagates bilaterally or not and finally what is the influence of the geometry on the propagation.

4.7.1 Stress distribution near the Homestead Valley fault

We first ignore rupture on that latter fault, and simply evaluate the stresses radiated from the first one, and if and where they are large enough to initiate slip-weakening elsewhere. For that we have considered a region (contoured in Figure 4.14) with the same local orientation as the Homestead Valley fault, with the same length and a thickness of 320 m (8 cells). The Homestead Valley fault is in the center of the region. For purposes of defining stress components on the $1, 2$ system, the 2 direction at any point in the region is the local perpendicular direction to the Homestead Valley fault. The quantity $\sigma_{21}/(-f_s\sigma_{22})$ is contoured for several time steps in Figure 4.14.

First, we notice something which does not happen in the stress distribution around the straight fault for parallel elements described in the static study: this is the region which moves from the time step N=800 to N=1200 and which represents a negative ratio $\sigma_{21}/(-f_s\sigma_{22})$. (The static study in the first part suggests that a tensile domain ($\sigma_{22} > 0$¿) will not exist in the region now studied.) Indeed, the calculations shows that for these regions the shear stress is negative which would imply a left-lateral slip if the ratio ever

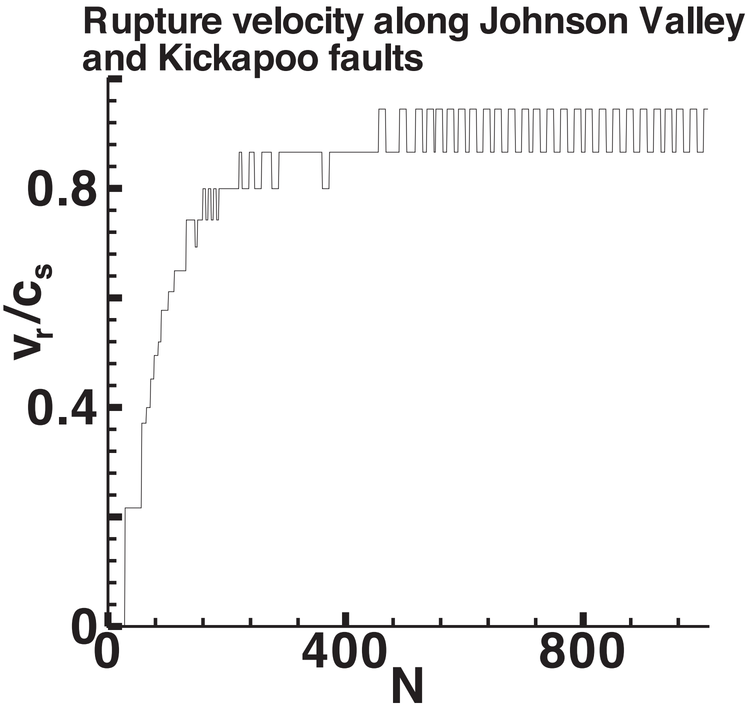

Figure 4.13: Rupture velocity v_r (as v_r/c_s) between the initiation of the rupture and the moment when it reaches the end of Kickapoo fault (in terms of time step $N = 6c_pt/R_0^o$) along first the Johnson Valley fault and afterwards Kickapoo fault. [No smoothing procedures applied here.]

becomes more negative than -1. Only right-lateral slip was allowed in our calculation.

The critical value of 1 for the ratio $\sigma_{21}/(-f_s\sigma_{22})$ (which means that a rupture is possible) is first reached in the curved part around the time step $N = 1040$. The region where the rupture is possible expands especially in the straight part and keeps a constant shape after the time step $N = 1300$ which is shown in the last picture. Note that there is reasonable correspondence, at the longer times shown here, of the region $\sigma_{21}/(-f_s\sigma_{22}) > 1$ and the static prediction of that region in Figure 4.6.

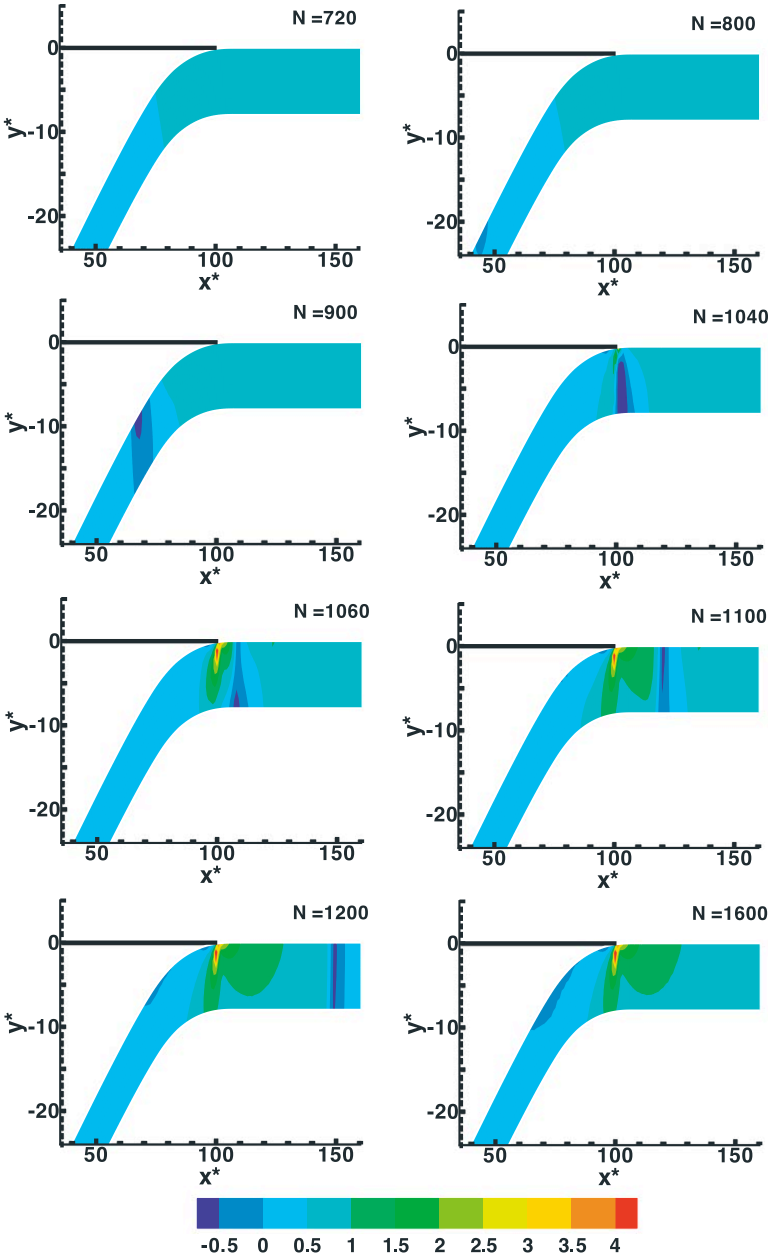

Figure 4.14: Stress distribution around Homestead Valley fault for elements locally parallel to it. The contoured quantity is $\sigma_{21}/(-f_s\sigma_{22})$, where (x_1, x_2) are the tangential and the normal directions relative to the Homestead Valley fault (see text). Here $x^* = 3x/R_0^o$ and $y^* = 3y/R_0^o$. Representation for several time steps: $N = 2c_pt/R_0$.

4.7.2 Stopping as an aid to jumping

We can see in Figure 4.14 that a rapidly propagating rupture is much more effective at generating high stresses on parallel, or roughly parallel, nearby faults once its propagation has been abruptly stopped by a barrier than it was just before that blockage. For example, the rupture reaches the barrier formed by the northern termination of Kickapoo, moving at high speed, at time step $N \approx 1000$. As Figure 4.14 shows, it is only some time later, as something resembling the static field of Figure 4.6 starts to develop, that a large region near the fault experiences failure-level stressing near the rupture tip.

Thus, it is much more likely for rupture to jump from a first to a roughly parallel second fault if its propagation has been abruptly stopped on the first. Jumps not associated with sudden slowing of propagation on the first fault are expected to be rare in nature. These observations are in accord with a basic result of dynamic crack theory for the singular model [*Fossum and Freund*, 1975], namely, that the stress intensity factor at a rapidly propagating crack tip increases significantly when that propagation is suddenly stopped. A case of rupture jumping when rupture velocity slows (rather than stops) is examined in *Oglesby et al.* [2003a], and other cases of rupture jumping between faults are examined in *Harris et al.* [1991] and *Harris and Day* [1993, 1999] as mentioned earlier, as well as in *Yamashita and Umeda* [1994], *Kase and Kuge* [1998, 2001], *Harris et al.* [2002] and *Oglesby et al.* [2003b].

We can conclude from this analysis that a rupture is likely to nucleate along the Homestead Valley fault and perhaps in several location. Further, stresses large enough to initiate right-lateral slip-weakening ultimately extend over the entire region between the Kickapoo and Homestead Valley faults.

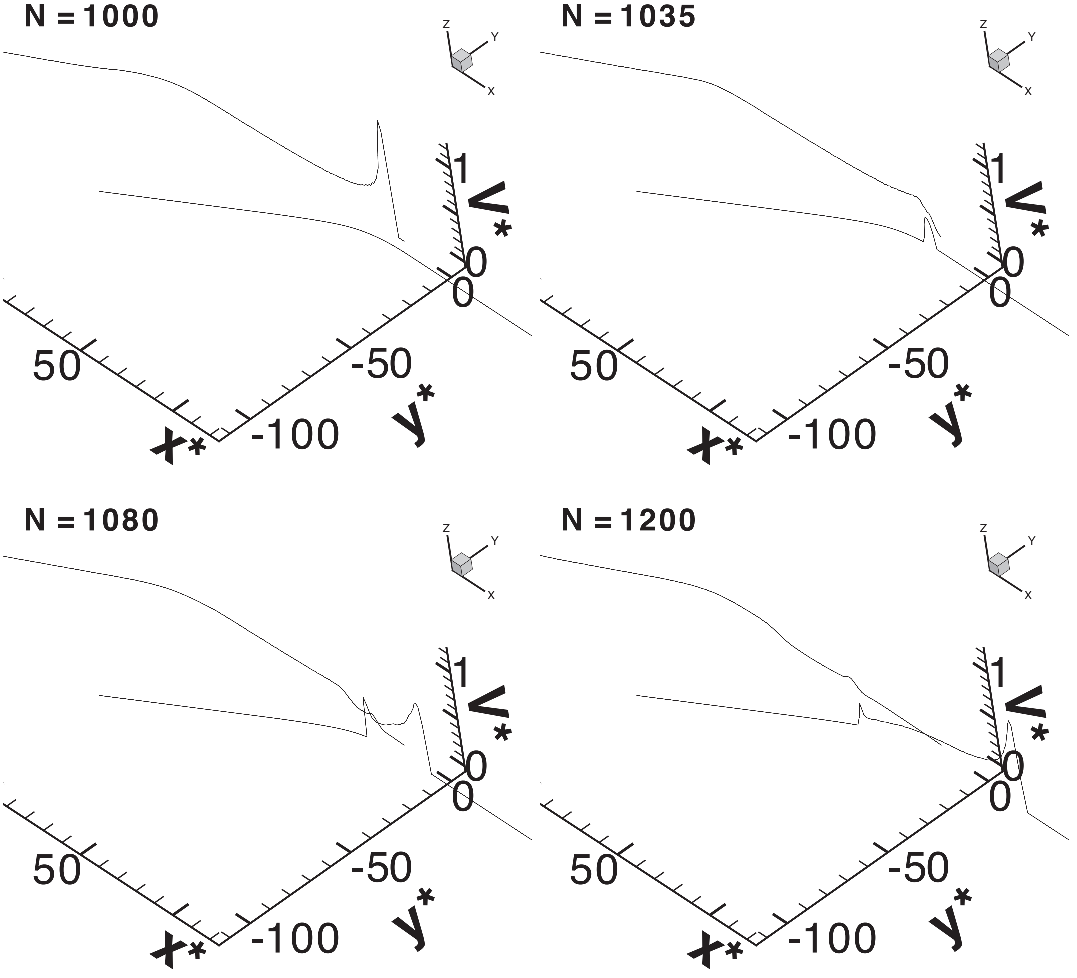

Figure 4.15: Slip velocity V (as $V^* = \mu V/(-\sigma^0_{yy} c_p)$ vs. $x^* = 3x/R^o_0$ and $y^* = 3y/R^o_0$) for several time steps $N = 4c_p t/R^o_0$,along the faults, around the step-over.

4.7.3 Jump of the rupture and bilateral propagation

The last calculations lead to the possibility of multiple nucleation along the second fault. However, as a matter of fact, a detailed calculation of the rupture shows that it nucleates at a *single location*: along the curved part at cell -8 ($x^* = 99$ and $y^* = -4.18$), which is just below the termination of Kickapoo (in terms of x^*, y^*, the end of the Kickapoo fault is at $x^* = 100$ and $y^* = 0$) and which has an orientation of $\omega = 2.8^o$. The initiation of slip occurs at $N = 1022$ (3.4s) and rupture starts *propagating bilaterally*, almost instantaneously, at $N = 1028$ (3.43s). Figure 4.15 represents the slip velocity V (as $V^* = \mu V/(-\sigma^0_{yy} c_p)$) along the Kickapoo and Homestead Valley faults represented in the x-y plane around the step-over before and after the jump. Figure 4.16 represents the slip velocity and so the rupture propagation at larger scale, along Johnson Valley and Kickapoo, and finally Homestead Valley, showing all the region modeled.

The rupture propagates bilaterally on the Homestead Valley fault: *forward* along the straight part parallel to the Kickapoo fault and *backward* along the curved part and then the straight part at orientation $\omega = 30^o$.

The rupture velocity slows down noticeably along the curved part of the Homestead Valley fault, as Figure 4.17 shows. The northern end of the ruptured zone moves forward more quickly than the SSE end, which has to contend with the curvature, which in this case is away from the extensional side. The effect is to increase normal stress along that curved part. *Bouchon and Streiff* [1997] have investigated rupture of a curved fault similar to the Homestead Valley fault, and also found a reduction in rupture velocity and slip. In more severe cases it is clear that such adverse curvature could arrest rupture propagation, although that does not happen in this case.

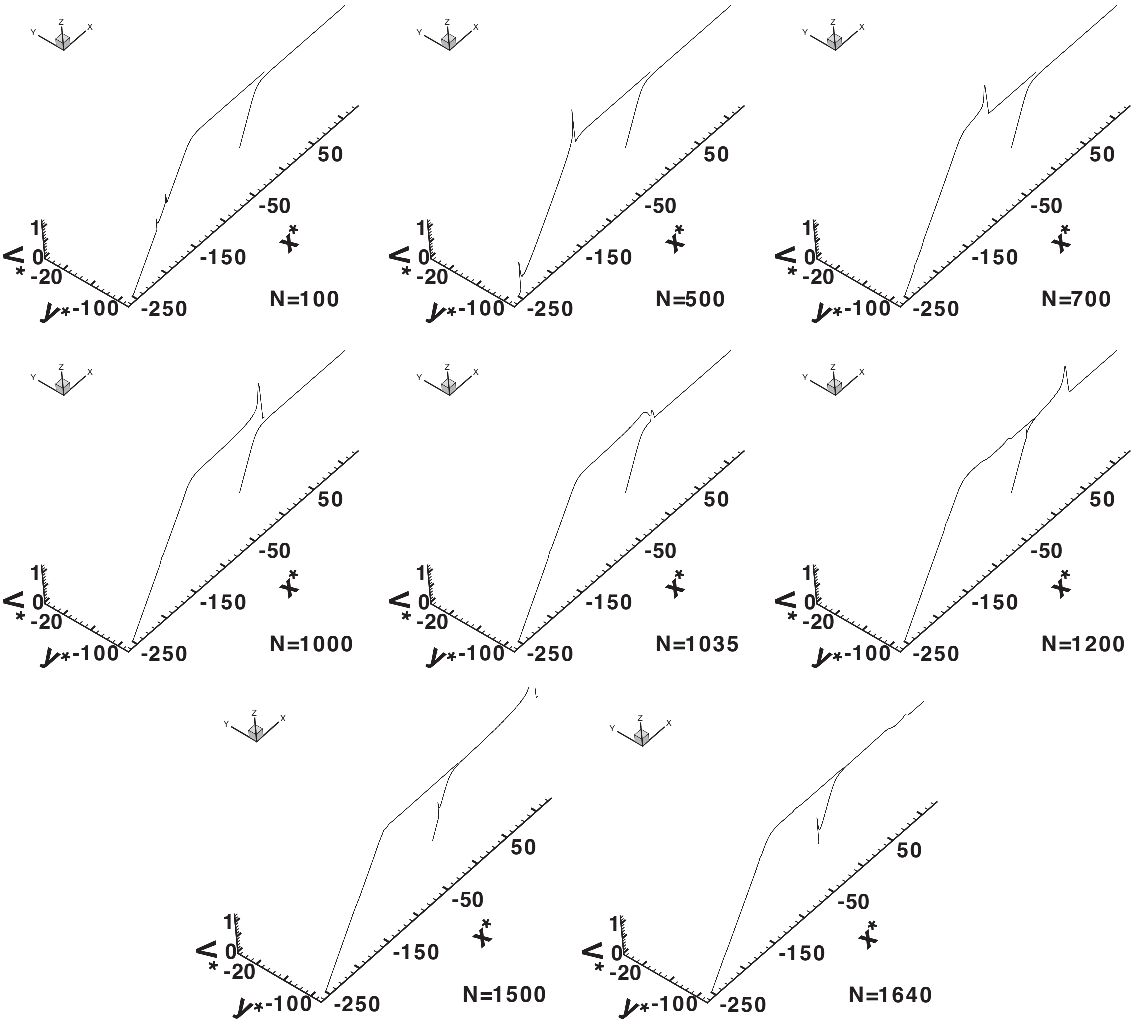

Figure 4.16: Slip velocity V (as $V^* = \mu V/(-\sigma_{yy}^0 c_p)$ vs. $x^* = 3x/R_0^o$ and $y^* = 3y/R_0^o$) for several time steps $N = 4c_p t/R_0^o$,along the faults.

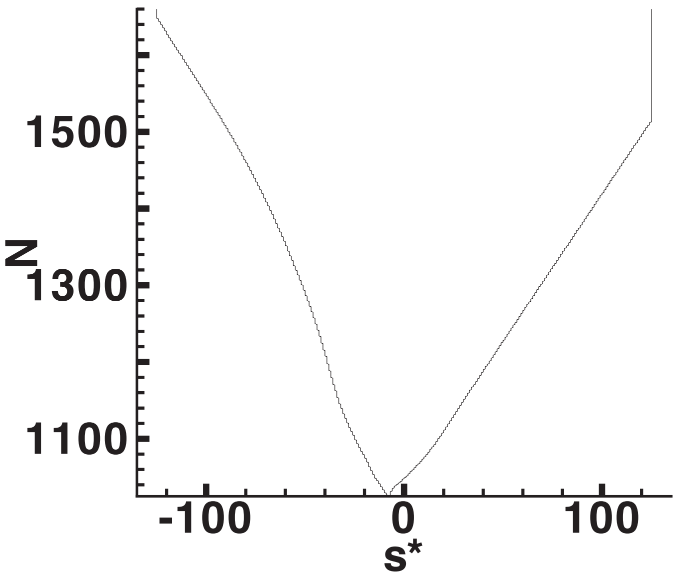

Figure 4.17: Position of the left and right ends of the ruptured zone (as $s^* = 3s/R_0^o$ where s is the curvilinear coordinate, the origin is the center of Homestead Valley fault) for each time step (as $N = 6c_pt/R_0^o$). The two lines at each edge indicate the length of the ruptured zone. The half length of the fault is fixed to about 5km ($s^* = 125$).

Forward, the rupture reaches the end at $N = 1513$ (5.04 s) of the northern portion of the Homestead Valley fault modeled. The actual rupture did not end there (instead continuing well to the NNW), but its stoppage in the simulation is too late for waves from that to compromise the modeling of the propagation to the SSE. Backward, it finishes crossing the curved part at $N = 1287$ (4.29 s). Its velocity increases again (as the discontinuity of the line at the cell -50 suggests) and then remains roughly constant along the oblique straight part. It reaches the end of the SSE zone at $N = 1648$ (5.49 s), leaving in its wake the backward branch which motivated our study.

In Figure 4.18 we compare the slip velocity along the different part of the fault. It is higher along the straight part than along the curved part where it decreases dramatically. However when the rupture reaches the oblique straight part, the slip velocity increases again, but remains lower than the section with an orientation parallel to the x-axis. Besides, as remarked, the end of the rupture forward has no influence for the rupture backward.

Finally, the Figure 4.19 represents the slip Δu (as $D^* = 3\mu\Delta u/(-\sigma_{yy}^0 R_0^o)$) all along the fault (in terms of cells $s^* = 3s/R_0^o$). It is not the location of nucleation which corresponds to the maximum slip (approximately 4m), but rather the region around cell -10. That corresponds to the beginning of the straight north-directed segment which is close to the nucleation site and on which high shear stress is applied, as the stress distribution around the fault (Figure 4.14) suggests. The average of slip is approximately 2.4m. We observe thus the high drop of slip along the adversely curved part. The rupture would stop if the fault did not stop curving, both because of the induced compressional normal stress discussed and because of increasingly unfavorable orientation relative to the prestress field.

4.8 Discussion and conclusions

Our work has addressed the relation between fault branches left after a large, complex earthquake and rupture directivity in the event. For that we investigated a new dynamic mechanism which leaves behind a feature that looks like a backward fault branch, that is, a branch directed opposite to the primary direction of rupture propagation. The mechanism consists of the stopping of the rupture on one fault strand and jumping to a neighboring strand, by stress radiation to it and nucleation of rupture on it which propagates bilaterally. Rare as such a feature might be, it could mislead observers attempting to understand the directivity of a past complex earthquake [*Nakata et al.*, 1998]. We conclude that it is difficult to judge the directivity of the main event from the pattern of branches it left, and that additional understanding of the structure near the fault junction is needed to reach

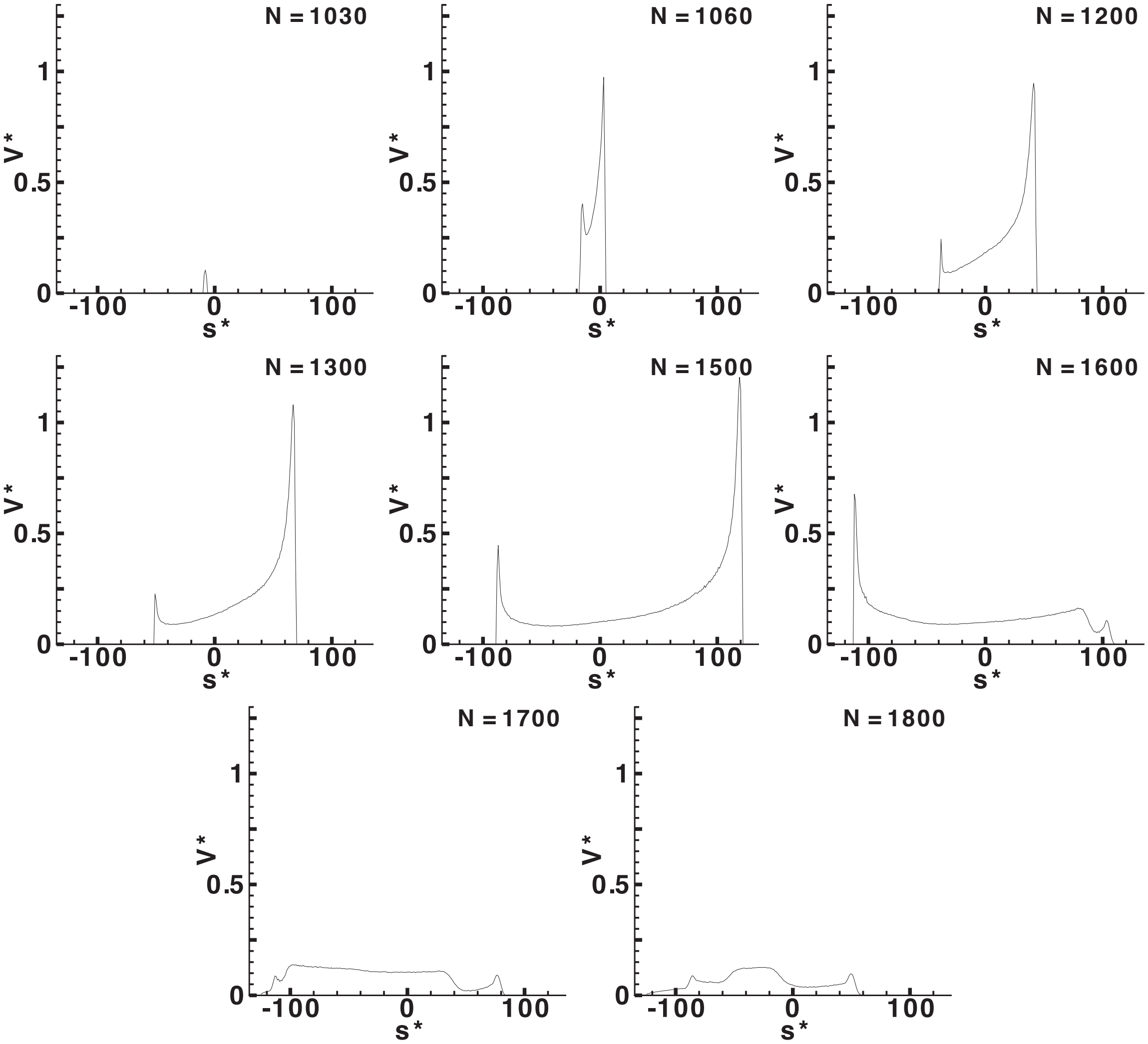

Figure 4.18: Along the Homestead Valley fault, slip velocity V (as $V^* = \mu V/(-\sigma^0_{yy} c_p)$ vs. $s^* = 3s/R^o_0$ where s is the curvilinear coordinate) for several time steps $N = 6c_p t/R^o_0$.

definitive conclusions.

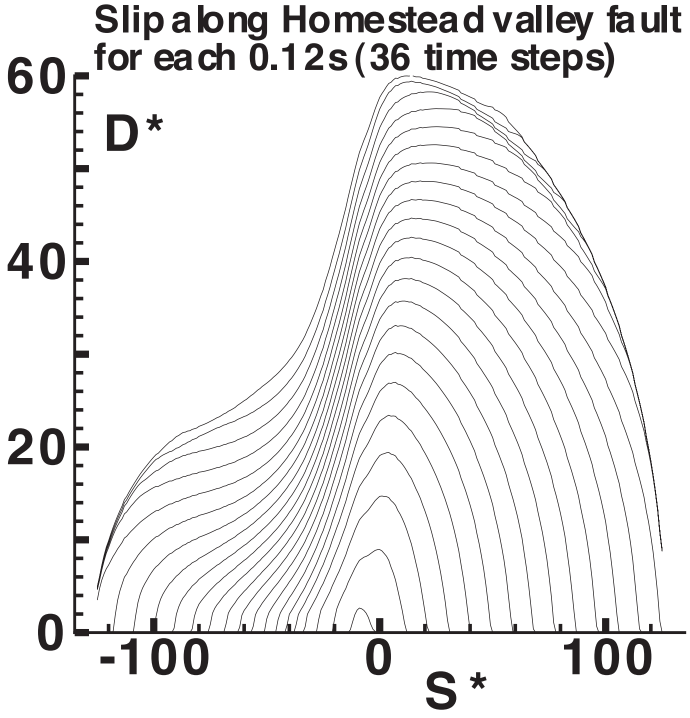

Figure 4.19: Along the Homestead Valley fault, slip Δu (as $D^* = 3\mu\Delta u/(-\sigma^0_{yy}R^o_0)$ vs. $s^* = 3s/R^o_0$ where s is the curvilinear coordinate) for each 0.18s (that is $9R^o_0/c_p$).

We analyze a field example of a backward fault branch formed during the Landers 1992 earthquake, when rupture propagating along the Kickapoo fault stopped at the end of that strand and then jumped to the Homestead Valley fault, where it developed bilaterally. The southern end of the Homestead Valley rupture formed a backward branch, while the main rupture continued NNW. We have no observational proof, other than the clear patterns of damage to a particular side of the Southern Homestead Valley fault (see Figure 4.2 and *Poliakov et al.* [2002]), that this is what really happened; existing analysis of co-seismic observations have not clarified that picture. It is even possible to assume that the southern end of the Homestead Valley fault broke in an early aftershock. However we have developed relevant theory for rupture transfer, and have simulated such a mechanism numerically, with a simplified geometry of the region under discussion.

We conclude that what we describe is definitely possible mechanically, that it very plausibly was the rupture mechanism in the Kickapoo to Homestead Valley transition, and that it could act more generally in other large earthquakes which rupture through complex fault systems. This means that caution is needed when relating fault branches of past earthquakes with their directivity. Simple forward branching, even if probably most common, might not be the only branching mechanism.

Our work has broadened the mechanical analysis of fault jumping, the basis of which is due to *Harris et al.* [1991], *Harris and Day* [1993] and*Harris and Day* [1999] who numerically analyzed ruptures jumping between parallel faults. Here we analyzed ruptures jumping onto possibly non-parallel faults, and subsequent propagation along gradually curving faults, using the elastodynamic boundary equation (BIE) method with a Coulomb type of slip-weakening. A fully systematic analysis of such jumps has to be left for future work. However we can offer some insights into the mechanics of such jumps.

First, it seems important that the rupture on the main fault stops or at least slows down if successful transfer of rupture to the neighboring, non-parallel fault is to be accomplished. This is because the stress concentration carried by the rupturing front diminishes with rupture velocity [*Fossum and Freund*, 1975] and is largest when propagation stops.

We showed that stresses radiated to the curved Homestead Valley fault, while the rupture tip was still propagating along the Johnson Valley-Kickapoo fault system, would be unlikely to nucleate rupture on the Homestead Valley fault. Rather, the jump was made possible by the much higher stresses radiated when the rupture stopped at the northern termination of the Kickapoo fault. Those stresses succeeded in nucleating on the Homestead Valley fault because the two fault traces are close to parallel there; the less parallel orientation of the curved Homestead Valley fault further to the southeast would not have allowed jumping.

When rupture stops at the termination of one fault strand, like on the Kickapoo fault here, the Coulomb stresses radiated to neighboring strands which are either parallel or only slightly misoriented relative to the first strand will increase in an approximately monotonic manner with time, and approach the final static stress distribution associated with the stopped rupture ([*Harris and Day*, 1993]; also, compare dynamic stressing in Figure 4.14 with the static results of Figure 4.6).

Thus, to simply estimate maximum jumpable distances, we have provided an analysis here of the static stress field also. We find that there is a strong sensitivity to the orientation of the target fault, even for misorientations as small as 5^o to 10^o (Figure 4.6). Focusing on parallel faults, we show that the maximum jumpable distance scales as a function of the seismic S ratio, being proportional to $1/(1+S)^2$. Thus lower S values (i.e., pre-stress σ^0_{yx} closer to the static friction strength $-f_s\sigma^0_{yy}$) favor jumping a greater distance from a blocked rupture tip.

Low S values also favor transition to supershear propagation speed v_r [*Andrews*, 1976]. We chose $S = 1.3$ for the simulation presented here, which was large enough to keep v_r sub-Rayleigh on our representation of a part of the Johnson Valley fault and the Kickapoo fault. The jumpable distance was then, nevertheless, still great enough to enable nucleation of propagating rupture on the Homestead Valley fault. While not shown here, we have also done a version of the same analysis with a lower S ratio, which allowed supershear v_r

along the Kickapoo fault. As would be expected because the maximum jumpable distance, scaling as $1/(1+S)^2$, was greater in that case, it too showed a jump of rupture to the Homestead Valley fault. The case presented here provides a more stringent test because of the larger S (i.e., because of the lower shear pre-stress).

Of course, there will exist a range of sufficiently larger S values for which rupture could not jump from the Kickapoo fault, then under yet lower pre-stress, to the Homestead Valley fault. In those cases the Landers earthquake could not extend beyond the northern termination of the Kickapoo fault. Such differences in the jumpable distance, depending on prestress along the main fault, might be responsible, among other mechanical reasons, for repeat earthquakes behaving in a variety of ways, sometimes rupturing single fault structures, and sometimes being able to continue, via multiple jumps, to other fault systems.

A phenomenon revealed in our simulations is how adverse curvature of a fault, like for the southern Homestead Valley fault in this modeling, can slow (and surely, sometimes stop) rupture propagation. By adverse curvature, we mean curvature towards the compressional side of a fault, like seen for the southern Homestead Valley fault in Figure 4.2 [*Sowers et al.*, 1994], just south of the presumed jump site, and Figure 4.7. Rupture is right lateral and propagates to the SSE on that segment, so the compressional side, towards which the fault curves, is the eastern side. With such curvature, nonuniform slip like that occurring near the rupture tip induces locally increased normal stress, and assuming as we have here that friction strength is proportional to effective normal compression, that locally increases the resistance to slip-weakening failure compared to that which coud be estimated based on the fault-normal component of the pre-stress field. While the curvature sugnificantly slowed, but did not stop, the rupture propagation in our simulations (Figures

4.15, 4.17 and 4.19), it is clear that stronger curvature could stop propagation.

Our analyses here have been based on 2D modeling. Such modeling has obvious limitations since we address 3D phenomena. For example, in a 3D study of the backward branch left by the rupture path in the 1999 Hector Mine earthquake, discussed previously,*Oglesby et al.* [2003b] found that the branch could not be produced if they allowed, in their simulation, for slip to extend all the way to the Earth's surface along the fault on which rupture nucleated and propagated into the branch junction. They could, however, produce that backward branch if they assumed that rupture on the first fault was blocked at shallow depths by a strong barrier, thus radiating stress increases to the second fault; that is, in fact, consistent with lack of observed surface slip on the first fault. These results suggest that 3D dynamic effects may be quite important in determining the rupture path through some complex fault junctions.

Nevertheless, given current computer limitations, it is possible in 2D modeling, but often not in 3D, to choose sufficiently small numerical cell sizes as to reasonably resolve the underlying continuum solution (e.g., by having several cells within the region of the fault undergoing slip weakening, a region which contracts in size as rupture speed increases [*Rice*, 1980; *Kame et al.*, 2003]. Also, the 2D representation may often be justified when length scales of phenomena modeled are small compared to the thickness of the seismogenic zone, as in this case for the small jump distance involved in the transition from the Kickapoo to Homestead Valley faults.

Such a process as we have investigated, of stopping on one fault strand but thereby radiating stresses to nucleate bilateral propagation on a nearby strand, may provide a general mechanism of backward branching.

Chapter 5

Off-fault damage patterns due to supershear ruptures with application to the 2001 M_w 8.1 Kokoxili (Kunlun) Tibet earthquake

5.1 Abstract

We extend a model of a two-dimensional self-healing slip pulse, propagating dynamically in steady-state with slip-weakening failure criterion, to the supershear regime, in order to study the off-fault stressing induced by such a slip pulse and investigate features unique to the supershear range. Specifically, we show that there exists a non-attenuating stress field behind the Mach front which radiates high stresses arbitrarily far from the fault (practically this would be limited to distances comparable to the depth of the seismogenic zone), thus being capable of creating fresh damage or inducing Coulomb failure in known structures at large distances away from the main fault. We allow for both strike-slip and dip-slip failure induced by such a slip pulse. We show that off-fault damage is controlled by the speed of the slip-pulse, scaled stress drop and principal stress orientation of the pre-stress field. We apply this model to study damage features induced during the 2001 Kokoxili (Kunlun) event in Tibet, for which it has been suggested that much of the rupture was supershear. We argue that an interval of simultaneous induced normal faulting is more likely due to a slip partitioning mechanism suggested previously than to the special features of supershear rupture. However, those features do provide an explanation for otherwise anomalous ground cracking at several kilometers from the main fault. We also make some estimates of fracture energy which, for a given net slip and dynamic stress drop, is lower than for a sub-Rayleigh slip pulse, because part of the energy fed by the far-field stress is radiated back along the Mach fronts.

5.2 Introduction

There have been increased recent reports of supershear earthquake ruptures (for which the propagation speed lies between the shear and the dilatational wave speed of the surrounding medium). The earliest inference of supershear was during the 1979 Imperial Valley earthquake for which *Archuleta* [1984] noticed that for a better fit of near-fault strong motion records, the rupture speed had to exceed the shear wave speed. More recent inferences were made during the 1999 Izmit and Düzce events [*Bouchon et al.*, 2000, 2001] the 2001 Kokoxili (Kunlun) event [*Bouchon and Vallee*, 2003] and the 2002 Denali event [*Ellsworth et al.*, 2004; *Dunham and Archuleta*, 2005]. Laboratory verification of supershear rupture was provided for the first time by *Rosakis et al.* [1999]. However, the theoretical work on these ruptures dates back to the early 1970's when *Burridge* [1973] studied the growth of a self-similar mode-II crack with a critical stress fracture criterion. His work suggested a possible mechanism for the transition of rupture from sub-Rayleigh to supershear regime by formation of daughter cracks ahead of the main crack and their subsequent coalescence. *Andrews* [1976, 1985] subsequently confirmed this in his numerical simulations with a linear slip-weakening failure criterion. *Andrews* [1976] also showed that for a sufficiently low seismic S ratio [= $(\sigma_{yx}^0 - \tau_r)/(\tau_p - \sigma_{yx}^0)$ where σ_{yx}^0, τ_p and τ_r are the initial shear stress, peak failure and residual failure strengths of the medium, respectively], supershear transition of rupture may occur after a propagation distance which scales with the size of the nucleation zone for that σ_{yx}^0. *Burridge et al.* [1979] showed that supershear ruptures whose speed were less than $\sqrt{2}c_s$ (c_s being the shear wave speed of the medium), the Eshelby speed [*Eshelby*, 1949] at which the shear wave contribution (also the Mach front) vanishes, had features suggesting that steady propagation would be unstable, although no complete stability analysis has been done of a steady state rupture. However, the small set of supershear earthquakes, laboratory and numerical studies do seem to confirm their analysis. *Bhat et al.* [2004] do find a numerical solution that appears stable at speed $< \sqrt{2}c_s$, but for a supershear rupture emanating from a fault branch that is interacting with a sub-Rayleigh crack from the other arm of the branch.

There remains still, however, much uncertainty about the observation of supershear ruptures in large crustal earthquakes because of the lack of sufficient strong ground motion records. For example, the 2002 Denali event is hypothesized to have propagated at supershear speed for about 40 km [*Ellsworth et al.*, 2004] based on a single ground motion record. Other claims of supershear rupture propagation come mainly from trying to fit a rupture speed for inversion of ground motion data, although recently *Dunham and Archuleta* [2005] have identified specific features of the near-fault waveform that indicate supershear rupture and have shown that a record written near the Denali rupture has that form.

The aim of this work is to point out some unique features of supershear ruptures that manifest themselves as patterns of off-fault damage which should be, in favorable circumstances, directly observed in the field. Earlier work by *Poliakov et al.* [2002] and *Rice et al.* [2005] for steady sub-Rayleigh rupture speeds has revealed expected off-fault damage patterns. Those were dependent on rupture speed, orientation of the pre-stress field among other parameters, and were shown to have some consistency with field observations. We thus adopt the *Dunham and Archuleta* [2005] extension of the speed regime of the *Rice et al.* [2005] solution for a steady self-healing slip pulse (right-lateral in nature to be consistent with *Poliakov et al.* [2002], *Kame et al.* [2003], *Bhat et al.* [2004], *Rice et al.* [2005]

and *Dunham and Archuleta* [2005]), to the supershear regime, and study the off-fault damage created during rupture propagation. *Dunham and Archuleta* [2005] focused on radiated ground motions.

5.3 Off-fault stress field due to an elastodynamic slip pulse

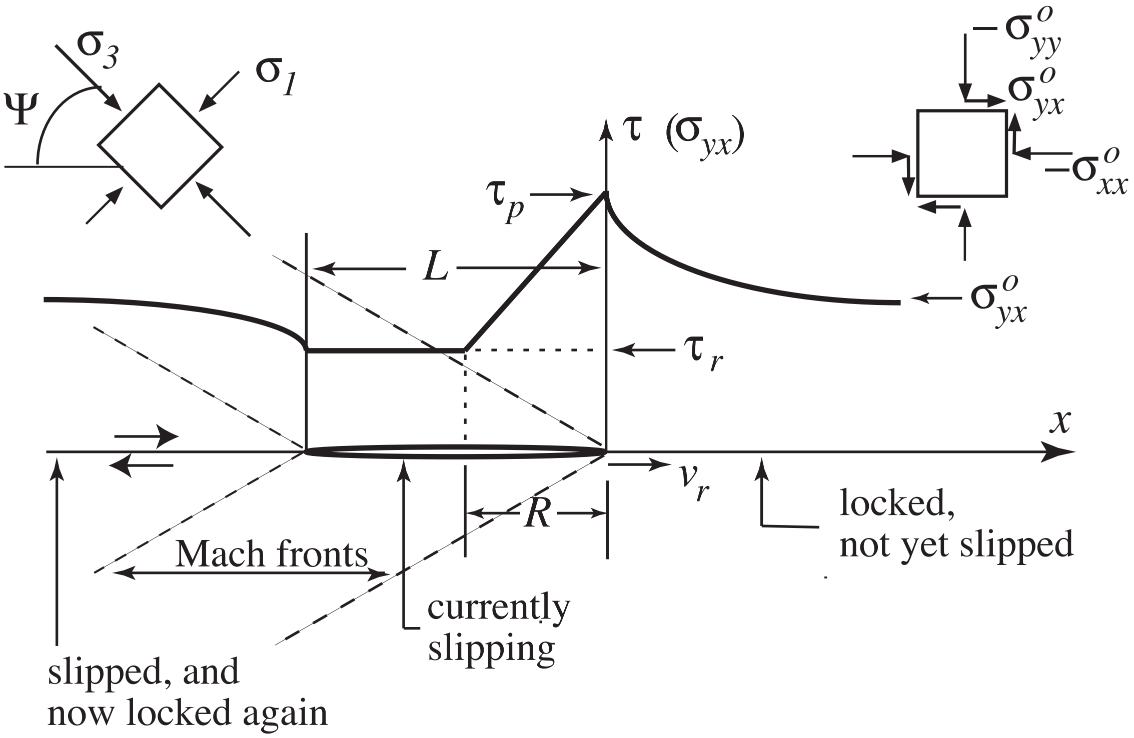

Figure 5.1: Supershear slip pulse of length L propagating at steady state in a two-dimensional homogeneous elastic medium under plane strain conditions. v_r is the rupture speed limited between the shear wave speed (c_s) and the P wave speed ($c_p = \sqrt{3}c_s$ for Poisson ratio, $\nu = 0.25$) of the medium. The shear strength of the pulse degrades linearly, with distance, from a peak value, τ_p to a residual value, τ_r over a distance R, the size of the slip weakening zone. σ^0_{ij} is the pre-stress in the medium. σ_1 and σ_3 are the minimum and maximum principal compressive stresses, of the pre-stress field, in the medium and Ψ is the angle of inclination of σ_3 with the slip pulse. [*Rice et al.*, 2005]

Following the work of *Poliakov et al.* [2002], and building on earlier studies of *Broberg*

[1978, 1989, 1999], *Freund* [1979], *Rice* [1980] and *Heaton* [1990], *Rice et al.* [2005] calculated the stress field near an elastodynamic slip pulse of length L propagating in steady state at the rupture speed v_r (the speed of the pulse) when v_r was in the sub-Rayleigh wave speed regime (The Rayleigh wave speed is the limiting speed for Mode-II ruptures, when the supershear transition can be avoided.). They used a non-singular slip-weakening model [*Ida*, 1972; *Palmer and Rice*, 1973], in a special simplified form introduced by *Palmer and Rice* [1973] in which stress is assumed to vary linearly with spatial position. Weakening begins when shear stress on the fault, τ, first reaches a finite peak strength τ_p on an unslipped part of the fault. When slip begins, τ decreases with slip, approaching τ_r at large slip, as illustrated in Figure 5.1; the simplified model assumes linear degradation of strength with distance over the slip-weakening zone length, R, and then a constant strength value over the remaing part of the pulse. The decrease of τ with slip δ is then not linear in δ, but is moderately different from linear and, in the sub-Rayleigh range, it is independent of v_r for a given R/L, and is only weakly dependent on R/L [*Rice et al.*, 2005]. We show later here that a similar feature holds for the supershear range, but with a small dependence on v_r. The peak strength τ_p is generally assumed to be proportional to the compressive normal stress acting on the fault and is set equal to $-f_s(\sigma_{yy})$. We take the static friction coefficient $f_s = 0.6$ based on lab values for typical rocks. The residual strength $\tau_r = -f_d(\sigma_{yy})$ is determined by the dynamic coefficient of friction, f_d. We choose $f_d/f_s = \tau_r/\tau_p = 0.2$ as in *Poliakov et al.* [2002] and *Rice et al.* [2005] but note that this number cannot be ascertained precisely. However, some results with appropriately scaled measures of stress changes (scaled with $\sigma^0_{yx} - \tau_r$ or $\tau_p - \tau_r$) do not depend on τ_r/τ_p.

The complete solution for the stress and particle velocity fields associated with the extension of the model to supershear has been derived in work by *Dunham and Archuleta* [2005].

Let the total stress tensor during the propagation of the slip-pulse be given by $\sigma_{ij} = \sigma^0_{ij} + \Delta\sigma_{ij}$ where σ^0_{ij} and $\Delta\sigma_{ij}$ are, respectively, the tensors of pre-stress and perturbation of stress. The perturbation of the stress field in a homogeneous, isotropic, elastic medium due to a slip pulse propagating at supershear speeds (under plane strain conditions in an unbounded solid) must have a form in terms of a single analytic function $S(z)$ [*Freund*, 1979], such that the stress perturbations are given by

$$\begin{aligned}
\Delta\sigma_{xx} &= \frac{1+\hat{\alpha}_s^2+2\alpha_d^2}{2\alpha_d}\Im S(z_d) + \frac{\hat{\alpha}_s^2-1}{2\alpha_d}\Im S(z_s) \\
\Delta\sigma_{xy} &= \Re S(z_d) + \frac{(\hat{\alpha}_s^2-1)^2}{4\alpha_d\hat{\alpha}_s}\Im S(z_s) \\
\Delta\sigma_{yy} &= \frac{\hat{\alpha}_s^2-1}{2\alpha_d}\Im[S(z_d)-S(z_s)] \\
\Delta\sigma_{zz} &= \nu(\Delta\sigma_{xx}+\Delta\sigma_{yy}) \qquad (5.1)
\end{aligned}$$

where $\hat{\alpha}_s = \sqrt{v_r^2/c_s^2-1}$; $\alpha_d = \sqrt{1-v_r^2/c_d^2}$; $z_s = x - v_r t + \hat{\alpha}_s|y|$ and $z_d = x - v_r t + i\alpha_d y; i = \sqrt{-1}$; we show results here at time $t = 0$. ν is the Poisson ratio for the medium and is chosen later to be 0.25, so that $c_d = \sqrt{3}c_s$, in our numerical evaluations. c_d and c_s are the P (dilatational) and S (shear) wave speeds of the medium respectively. $S(z)$, with different arguments, expresses the contributions of the P (dilatational) and the S (shear) waves propagating through the medium; it must be chosen so that the stresses follow the linear strength degradation boundary conditions like in Fig. 1. $\Re S(z)$ and $\Im S(z)$ are the real and imaginary parts of $S(z)$, respectively, and following the development of *Dunham and Archuleta* [2005], $S(z)$ is given by

$$\begin{aligned} S(z) \;&=\; -\frac{\sin(\pi q)}{\pi} z^{1-q}(z+L)^q \times \\ & \int_{-L}^{0} \frac{(\tau(\xi)-\sigma_{yx}^0)}{(-\xi)^{1-q}(\xi+L)^q(\xi-z)} d\xi \end{aligned} \tag{5.2}$$

Here

$$q(v_r) = \frac{1}{\pi}\tan^{-1}\left[\frac{4\hat{\alpha}_s\alpha_d}{(\hat{\alpha_s^2}-1)^2}\right] \qquad (0 \le q \le 1/2) \tag{5.3}$$

$$\tau(x) = \begin{cases} \tau_r + \left(1+\frac{x}{R}\right)(\tau_p-\tau_r) & \text{for} -R < x < 0 \\ \tau_r \quad \text{for} -L < x < -R \end{cases} \tag{5.4}$$

and σ_{yx}^0 is the initial shear stress (pre-stress) in the medium. A condition for such a solution to exist, giving bounded stresses at the leading and trailing edges of the pulse, is that $S(z) \to 0$ as $|z| \to \infty$ [*Muskhelishvili*, 1953]. This results in a constraint equation on the shear pre-stress level which is consistent with a given R/L and v_r. That can be determined as follows. Define

$$\sigma_{drop} = \frac{\sigma_{yx}^0 - \tau_r}{\tau_p - \tau_r} \tag{5.5}$$

Then

$$\sigma_{drop} = \frac{I_1}{I_2} \tag{5.6}$$

where

$$I_1 = \int_0^1 \frac{(1-t)dt}{(t)^{1-q}(L/R-t)^q}\ ; I_2 = \int_0^1 \frac{dt}{(t)^{1-q}(1-t)^q}$$

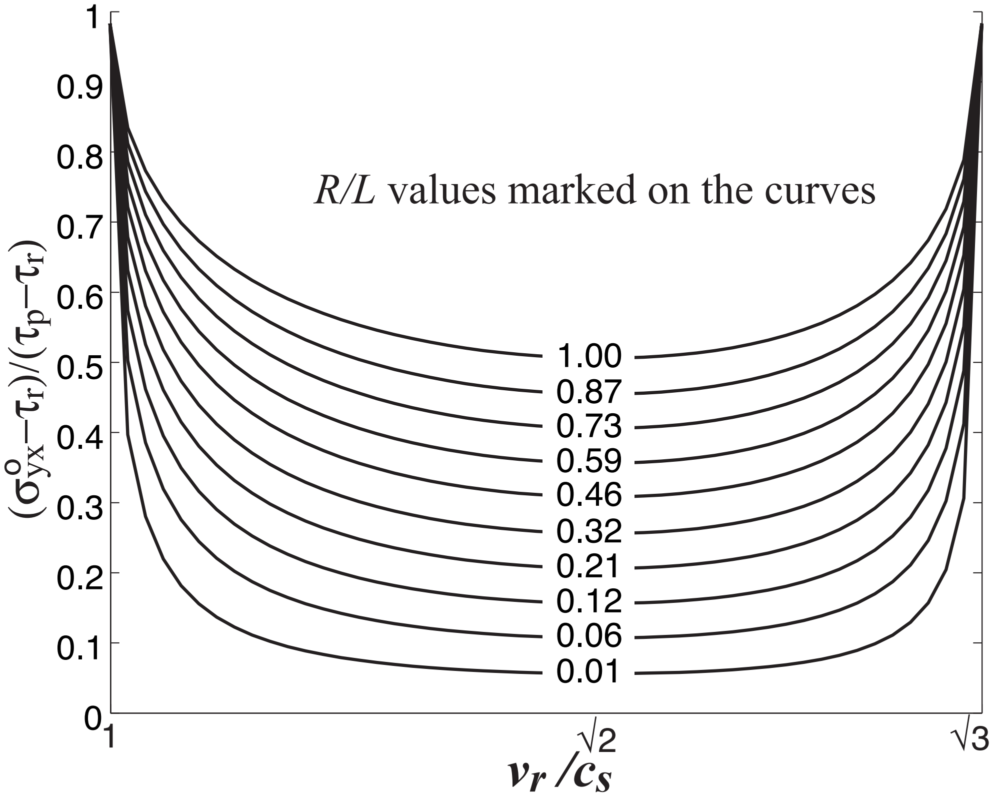

Figure 5.2: Variation of scaled dynamic stress drop $(\sigma^0_{yx} - \tau_r)/(\tau_p - \tau_r)$ with rupture speed v_r and R/L where R and L are the size of the slip weakening zone and the length of the slip pulse respectively. τ_p and τ_r are the peak and residual strengths respectively and σ^0_{yx} is the initial shear stress.

in non-dimensionalized form. Note that since $q = q(v_r)$ is involved, the scaled dynamic stress drop, $(\sigma^0_{yx} - \tau_r)/(\tau_p - \tau_r)$ depends on both R/L and v_r/c_s (Figure 5.2), unlike for its sub-Rayleigh analogue in which case the dependence was only on R/L [*Rice et al.*, 2005]. Similarly $S(z)$ can be non-dimensionalized as follows

$$\frac{S(\hat{z})}{\sigma^0_{yx} - \tau_r} = -\frac{\sin(\pi q)}{\pi}\hat{z}^{1-q}\left(\hat{z} + \frac{L}{R}\right)^q \times \left[\frac{R}{L}I_3 - \left(\frac{\tau_p - \tau_r}{\sigma^0_{yx} - \tau_r}\right)I_4\right] \tag{5.7}$$

where

$$\begin{aligned} I_3 &= \int_0^1 \frac{dt}{(t)^{1-q}(1-t)^q(t+\hat{z}\frac{R}{L})}\ ; \\ I_4 &= \int_0^1 \frac{(1-t)dt}{(t)^{1-q}(\frac{L}{R}-t)^q(t+\hat{z})} \text{ and } \hat{z} = \frac{z}{R} \end{aligned}$$

5.4 Non-dimensional parameters in the model

We now have the perturbation $\Delta\sigma_{ij}$ from the pre-stress field, if normalized by the dynamic stress drop $\sigma^0_{yx} - \tau_r$, or by the strength drop $\tau_p - \tau_r$, expressed in terms of non-dimensionalized parameters, namely z/R, R/L and v_r/c_s. Refer to section 7 for estimates of the physical size of R. The in-plane pre-stress is characterized by a non-dimensional parameter, $\sigma^0_{xx}/\sigma^0_{yy}$ which is a proxy for the angle of inclination of the maximum in-plane principal stress (compressive) with the slip-pulse, Ψ, measured clock-wise from the top of the slip pulse [Figure 5.1]. The in-plane stress components are then given by

$$\begin{aligned} \frac{\sigma^0_{yy}}{\sigma^0_{yx} - \tau_r} &= \frac{-1/f_s}{\sigma_{drop}(1 - f_d/f_s)} \\ \frac{\sigma^0_{yx}}{\sigma^0_{yx} - \tau_r} &= 1 + \frac{f_d/f_s}{\sigma_{drop}(1 - f_d/f_s)} \end{aligned} \tag{5.8}$$

To examine out-of-plane failure modes (reverse or normal faults) we must also assign a value for $\sigma^0_{zz}/\sigma^0_{yy}$. We choose various values for σ^0_{zz} lying between, or equal to one of, the maximum (σ_3) and minimum (σ_1) in-plane compressive principal stresses, determined from the initial in-plane stresses. That is, we consider pre-stress states which are at least as favorable to strike-slip as to normal or to thrust failure (Refer to Appendix C).

Thus the model has six non-dimensional parameters that need to be declared *a priori* (if the total stress tensor is to be evaluated), namely v_r/c_s, R/L, f_s, f_d/f_s, $\sigma^0_{xx}/\sigma^0_{yy}$ and $\sigma^0_{zz}/\sigma^0_{yy}$. On this list, σ_{drop} can replace R/L (Figure 5.2).

5.5 Off-fault stressing due to a supershear slip pulse

Supershear ruptures differ from their sub-Rayleigh analogues in many different ways. The stressing due to the P and the S waves in the medium is almost decoupled. The S wave field stresses the region only behind the Mach-front emanating from the rupture front. In case of a slip pulse, as studied here, two Mach fronts develop at the leading and the trailing edge of the slip pulse and the band between these fronts defines the S wave stressing region (Figure 5.1). Within the band, the stress field is non-attenuating with distance and is constant (neglecting the modest, attenuating, contributions of the P wave field) along lines parallel to the leading Mach front. The non-attenuation feature in the band is a unique signature of supershear pulses which could potentially lead to damage at distances far away from the slip pulse. The three-dimensional nature of the actual problem presumably restricts this distance to be of the order of the depth of the seismogenic zone (once the rupture saturates in depth the dominant length scale in the problem is related to this depth and 3D effects can no longer be ignored), usually around 10-15 km. However this distance is still substantial and of the order of a few tens of kilometers.

Outside the Mach band, the stressing is only due to the P waves and attenuates with distance. However, as the rupture speed approaches the upper limiting speed, i.e., the P wave speed of the surrounding medium, the Lorentz-like contraction of the stressing region in the fault parallel direction (with a corresponding extension in the fault normal direction) also increases significantly leading to a greater extent

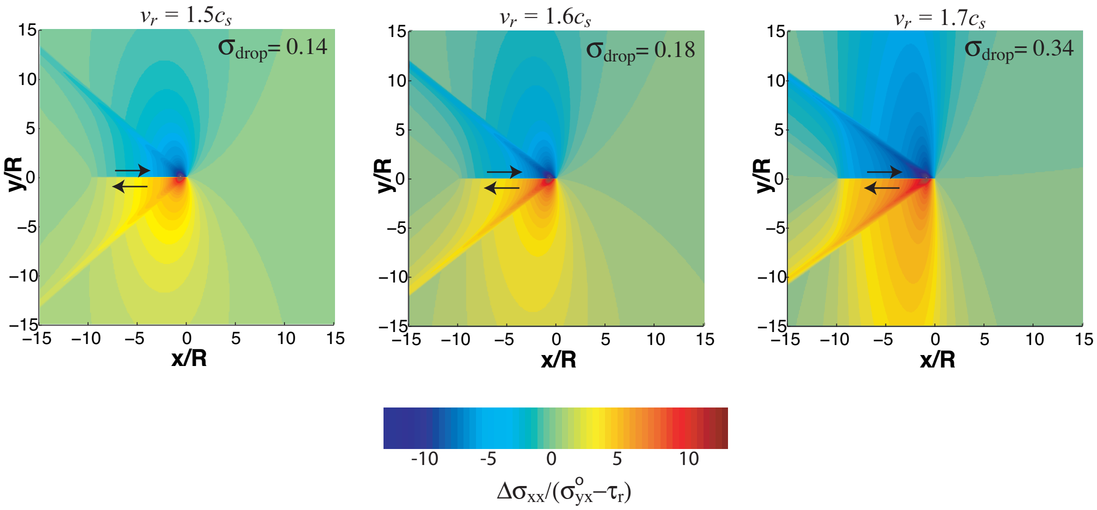

Figure 5.3: Perturbation in fault parallel stress, $\Delta\sigma_{xx}/(\sigma^0_{yx} - \tau_r)$ normalized by dynamic stress drop due to a supershear slip pulse propagating steadily at various rupture speeds, v_r. All results are for $R/L = 0.1$ where R and L are the size of the slip weakening zone and the length of the slip pulse respectively and $\sigma_{drop} = (\sigma^0_{yx} - \tau_r)/(\tau_p - \tau_r)$.

of the P wave stressing region in the medium hosting the slip pulse. Once again we notice a greater spatial influence by supershear ruptures compared to sub-Rayleigh ruptures. Figure 5.3 showing the perturbation in $\Delta\sigma_{xx}$ illustrates the non-attenuating and Lorentz-like contraction features of supershear ruptures.

To characterize the off-fault stressing induced by a supershear slip pulse, we look at the change of Coulomb stress on fault structures with assumed orientations, and also on structures which are optimally oriented for Coulomb failure based on the total stress tensor. Note that in calculating dynamic Coulomb stress changes on optimally oriented structures and in the evaluation of off-fault failure, all the six non-dimensional parameters are to be specified. However, when evaluating the change in the dynamic Coulomb stress on fault structures with assumed orientations, only three non-dimensional parameters need to be specified (if stresses are normalized by the dynamic stress drop) *a priori*, namely, v_r/c_s,

R/L and f_s.

We evaluate the change in the Coulomb Stress $\Delta CS = \Delta\tau + f_s\Delta\sigma$ (here $\Delta\tau > 0$ in the direction of possible slip and $\Delta\sigma > 0$ for tension) on faults, both optimally oriented and the ones with assumed orientations, at each grid point and only the region where failure is encouraged is contoured, i.e. the region where $\Delta CS > 0$. The optimal orientation was determined from the final stress state. We also evaluate Coulomb stress changes for structures slipping out of the plane, i.e., normal and reverse faults. Refer to Appendix C for more details.

5.6 The 2001 M_w 8.1 Kokoxili (Kunlun) earthquake

The Kokoxili surface rupture (Figure 5.4) has been studied by a number of workers, *Xu et al.* [2002], *Lin et al.* [2002, 2003], *Lasserre et al.* [2005] and *Klinger et al.* [2006] among others, and mapped in detail using Ikonos satellite images and supporting fieldwork by *Klinger et al.* [2005]. Particular attention was paid to the slip-partitioned section, which is also discussed by *King et al.* [2005]. *Kikuchi and Yamanaka* [2001], *Lin et al.* [2003], *Bouchon and Vallee* [2003], *Antolik et al.* [2004] , *Tocheport et al.* [2006] and *Robinson et al.* [2006] did seismological studies of the rupture process associated with the Kokoxili event. The field team noted other interesting features, but unfortunately could not study them in detail so that we do not have careful field documentation. Thus although the observations may be consistent with rupture propagation at supershear speeds the correlation should be treated with caution.

North of the fault, bridge abutments crossing minor drainages on the Kunlun Pass to Golmud road were damaged. Since fragile walls and poorly constructed buildings were

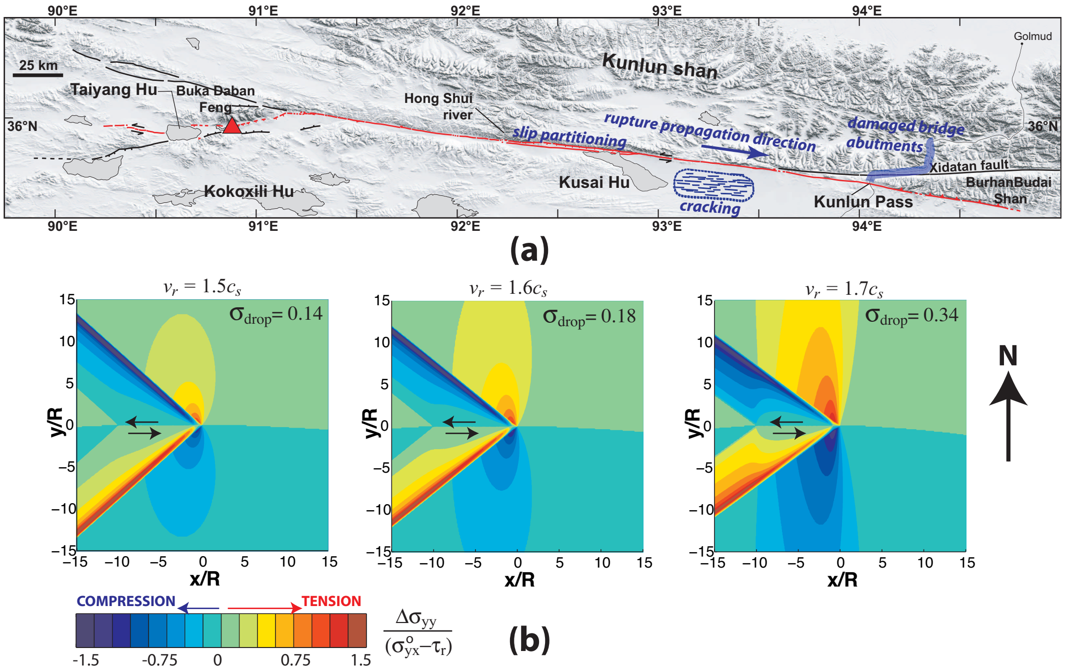

Figure 5.4: (a) Simplified map of the surface rupture (red line) for the 2002 Kokoxili earthquake (adapted from *Klinger et al.* [2005]). The epicentre is indicated by a red triangle so that rupture propagated mainly to the east. The slip-partitioned section extends from the Hong Shui river to north of the middle of Kusai Hu (lake). Extensive cracking was observed (with approximate crack orientations drawn by authors) from east of the Kusai Hu to about halfway to the Kunlun Pass. North of the pass (where the road to golmud is outlined in blue) bridge abutments were damaged. The extent of the region of cracking parallel to the strike of the fault is likely to be correct, but the extent perpendicular to it is simply not determined, and it is only sure that the cracking extended to the horizon on both sides of the road. (b)Perturbation in fault normal stress, $\Delta\sigma_{yy}/(\sigma^0_{yx} - \tau_r)$ normalized by dynamic stress drop due to a 'left-lateral' supershear slip pulse propagating steadily at various rupture speeds, v_r (all other figures in this paper are drawn for right lateral slip). The results are for $R/L = 0.1$ where R and L are the size of the slip weakening zone and the length of the slip pulse respectively and $\sigma_{drop} = (\sigma^0_{yx} - \tau_r)/(\tau_p - \tau_r)$.

undamaged even closer to the fault and such bridges are not normally sensitive to shaking, a likely explanation is that the damage resulted from large ground strains probably in extension. The damage did not appear to be due to compression although, without more careful examination, it cannot be excluded.

South of the fault, on the road between the Kunlun Pass and Kusai Hu, extensive ground cracking occurred (Figure 5.5) oriented at approximately fault parallel as shown in Figure 5.4a. The cracking was not mapped since the cracks were too small to appear on Ikonos images. Direct mapping of a large region would have required an extended period at an altitude of nearly 4000 meters which was not possible. The extent of the region of cracking (shown in Figure 5.4) parallel to the strike of the fault is likely to be correct, but the extent perpendicular to it is simply not determined, and it is only sure that the cracking extended to the horizon on both sides of the road. Whether or not the map is accurate, the cracks were substantial distributed features that did not have the character of primary fault ruptures. The field team did not constrain the orientation of these features relative to the main Kokoxili rupture trace. However, the road track shown in Figure 5.5 is roughly oriented in the West-North-West direction (the absence of the Kunlunshan mountain range at the horizon of Figure 5.5 supports this conclusion). That means that the cracks are oriented at shallow angles to the main rupture trace. Our estimates of the far-field stresses (Appendix D) show that, for a left-lateral supershear rupture as the Kokoxili event, the region where the cracks were observed suffered from large fault normal extensional stress perturbation ($\Delta\sigma_{yy} \approx 5 - 15$ MPa for a 3 MPa dynamic stress drop, on the pulse, consistent with the average stress drop inferred by *Rice et al.* [2005] for other large, sub-Rayleigh ruptures) leading to the formation of tensile cracks oriented roughly parallel to the main rupture trace [Figure

5.4b].

Figure 5.5: Cracks along the road from Kusai Hai to the Kunlun pass. At this point the road is several kilometers from the fault. The cracks were not mapped and their orientation was not specifically measured, but was close to the orientation shown in Figure 5.4. The cracking is consistent either with extension, or with compression and inelastic yielding followed by tensional failure when the compression was relaxed.

Because there is only the limited constraint mentioned of the cracking direction, it is instructive to examine other possibilities. If these extensional features were oriented at some near-perpendicular angle to the main rupture trace then this could mean that the extensional features observed were created by the unloading phase following the traversal of a large compressional loading pulse. For such orientation, it would bepossible that the brittle near-surface material (frozen soil sediments) could yield in compaction when the Mach front traversed through the material, and then unloaded as tensile cracks when the compressional strain was removed in the wake of the Mach front. Our estimates of far-field stresses (see Appendix D) show that at Kunlun rupture speeds the fault parallel stress perturbation ($\Delta\sigma_{xx}$), is compressional and quite large ($\approx 5-15$ MPa) for a 3 MPa dynamic stress drop on the pulse [Figures 5.3 and 5.6]. Thus there is a plausible mechanism for any angle of the tensile cracks with respect to the main fault trace, except for angles in the

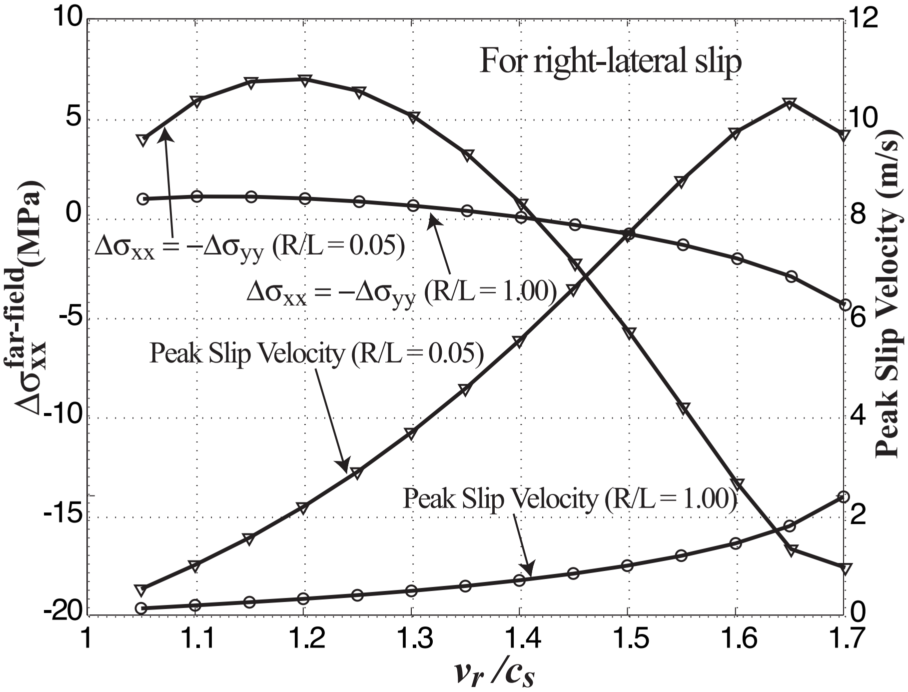

Figure 5.6: Far field perturbation in fault parallel stress, $\Delta\sigma_{xx}$ as a function of rupture velocity calculated using the maximum slip velocities at the corresponding rupture velocities and for different values of R/L. We assume dynamic stress drop to be 3MPa, shear modulus to be 30 GPa and S-wave speed of $3km/s$ in these calculations.

vicinity of $\pm45^0$, in which case the normal stress on these features (whether tensile or compressive) is small in magnitude.

We also checked for the possibility of normal and thrust structures, striking perpendicular to the slip pulse, being activated due to the supershear slip pulse. Figure 5.7 shows the change in the dynamic Coulomb stress on such structures. Note that the southern side of Kunlun (left-lateral) is the $y > 0$ domain in our model (right-lateral). (Also, in the interpretation for left-lateral faulting, in our figures, we are not looking down onto earth's surface from space, but rather up to the surface from the interior.) The figure clearly shows that thrust faulting structures (striking perpendicular to the slip pulse) could be activated in the southern side of Kunlun at large distances. In fact the region of highest positive change in the dynamic Coulomb stress lies along the leading Mach front which extends to distances comparable to the seismogenic depths in our two dimensional model.

At sub-Rayleigh speeds ($0.7 - 0.9c_s$) at a distance of 5km (using *Rice et al.* [2005] estimates of R_0^* (size of the slip weakening zone for a static semi-infinite crack), an average value of 30m used here, and factoring in the Lorentz-like contraction of R this would correspond to approximately 250-1000R) the stresses are quite negligible, at around 0.1% of dynamic stress drop. Thus a sub-Rayleigh rupture could not have created features discussed above.

Klinger et al. [2005] have mapped in detail that a normal fault strand, about 70km long, striking parallel to the Kunlun fault at a distance of approximately 1-2.5km to the north of Kunlun slipped during the 2001 event (see the slip partitioned section in Figure 5.4). The rupture speed is constrained by the inversion studies of *Bouchon and Vallee* [2003] to be between 1.5 and $1.6c_s$. *King et al.* [2005] have related the activation of this normal strand during the event to slip-partitioning at depth where the normal and strike-slip structures are connected. We look for direct Coulomb stress changes on the normal fault strand due to a supershear rupture on an adjacent fault, to see if supershear ruptures could activate such features and possibly provide a complementary mechanism. Figure 5.8 shows this change in Coulomb stress for normal faulting structures striking parallel to the main slip pulse and dipping at 60^0. Since Kunlun is a left-laterally slipping fault and our calculations are for a slip pulse slipping right laterally, the northern side of Kunlun represents $y < 0$ domain in our figure (looking towards the earth's surface from beneath). Normal faulting, in the $y < 0$ domain, is discouraged (negative change in Coulomb stress) in the non-attenuating

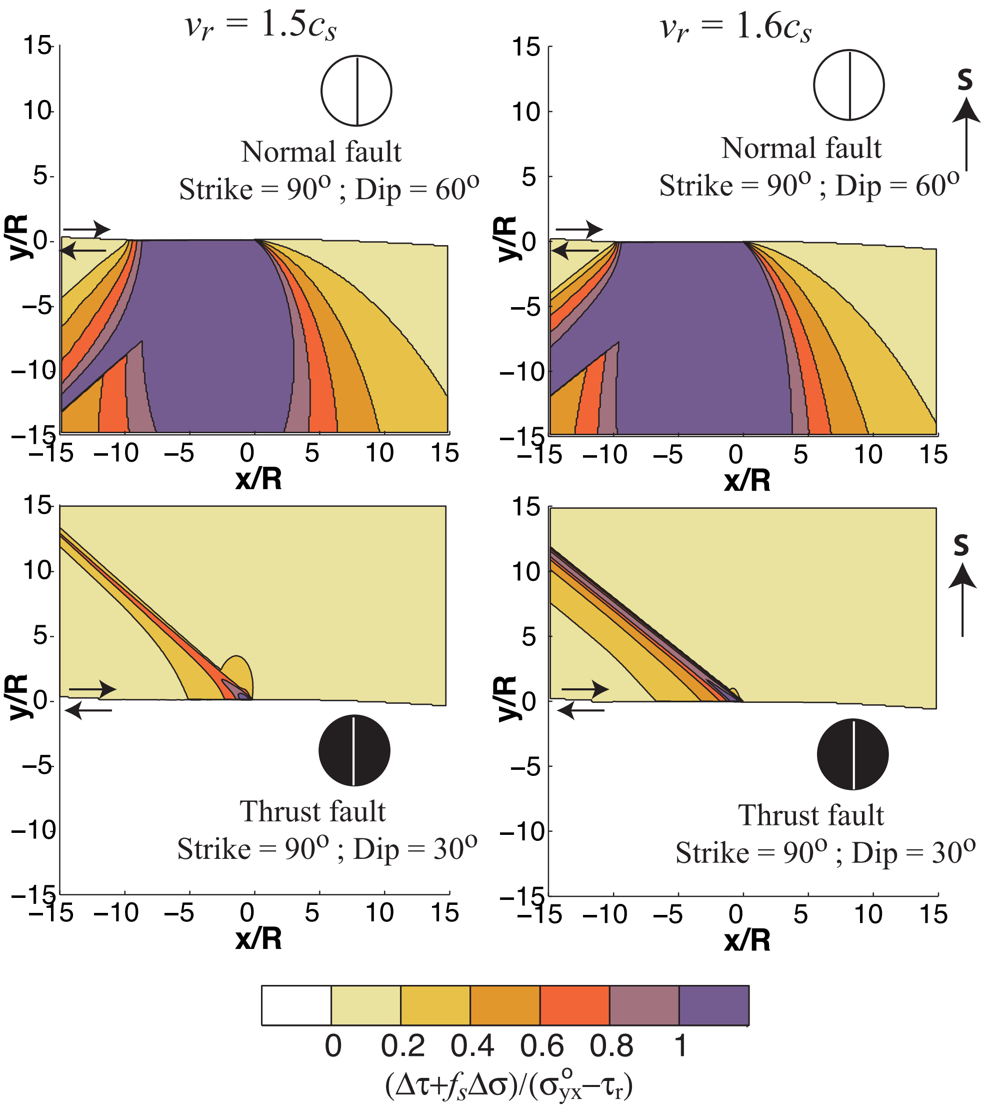

Figure 5.7: Contours of positive change in Coulomb stress (scaled by dynamic stress drop), due to a supershear rupture, on Normal and thrust faults striking perpendicular to the slip pulse and dipping at 60^0 and 30^0 respectively. Open circle represents normal faults and shaded circle represents thrust faults with their strike shown by the bisecting line.

part of the field when a supershear slip pulse propagates on the main fault at speeds like those inferred, $v_r > \sqrt{2}c_s$.

Though normal faulting is favored in the attenuating part of the stress field (corresponding to the P wave field) at higher speeds, the extent of this field, corresponding to 20% of dynamic stress drop, is only up to 200-300m (taking R_0^* =30m and referring to figure 5.15). There is a positive change at speeds $v_r < \sqrt{2}c_s$, but these speeds, especially in the range $1.2c_s$ to $1.3c_s$ at which the effects become numerically significant are thought unlikely.

Since Coulomb stress changes are significant at short distances for all rupture velocities considered here, a supershear slip pulse might have nucleated the normal faulting event at, or near, its junction with the strike-slip strand.

We note that the above mentioned mechanism of nucleating normal faulting event is, however, not unique to the supershear regime as discussed below. Similar calculation in the sub-Rayleigh speed regime shows that the positive change in the Coulomb stress is quite low (around 1% of the dynamic stress drop) at a distance of about $20R$ from the main fault. Using *Rice et al.* [2005] data on R_0^* and factoring in the Lorentz-like contraction of R, the above distance would be roughly between 100 and 400m.

Thus it seems most unlikely that a sub-Rayleigh rupture could have activated the normal fault structure. We thus find that at the rupture speeds for the Kunlun event normal fault activation by positive changes in Coulomb stress on the same is unlikely to happen,

and no viable alternative is provided to the hypothesis that the normal faulting resulted from slip-partitioning at depth [*King et al.*, 2005].

The value of Ψ (defined earlier [Figure 5.1] and bearing in mind that the fault is left-lateral) about 200 km to the east of the Kunlun-Xidatan junction was estimated to be be-

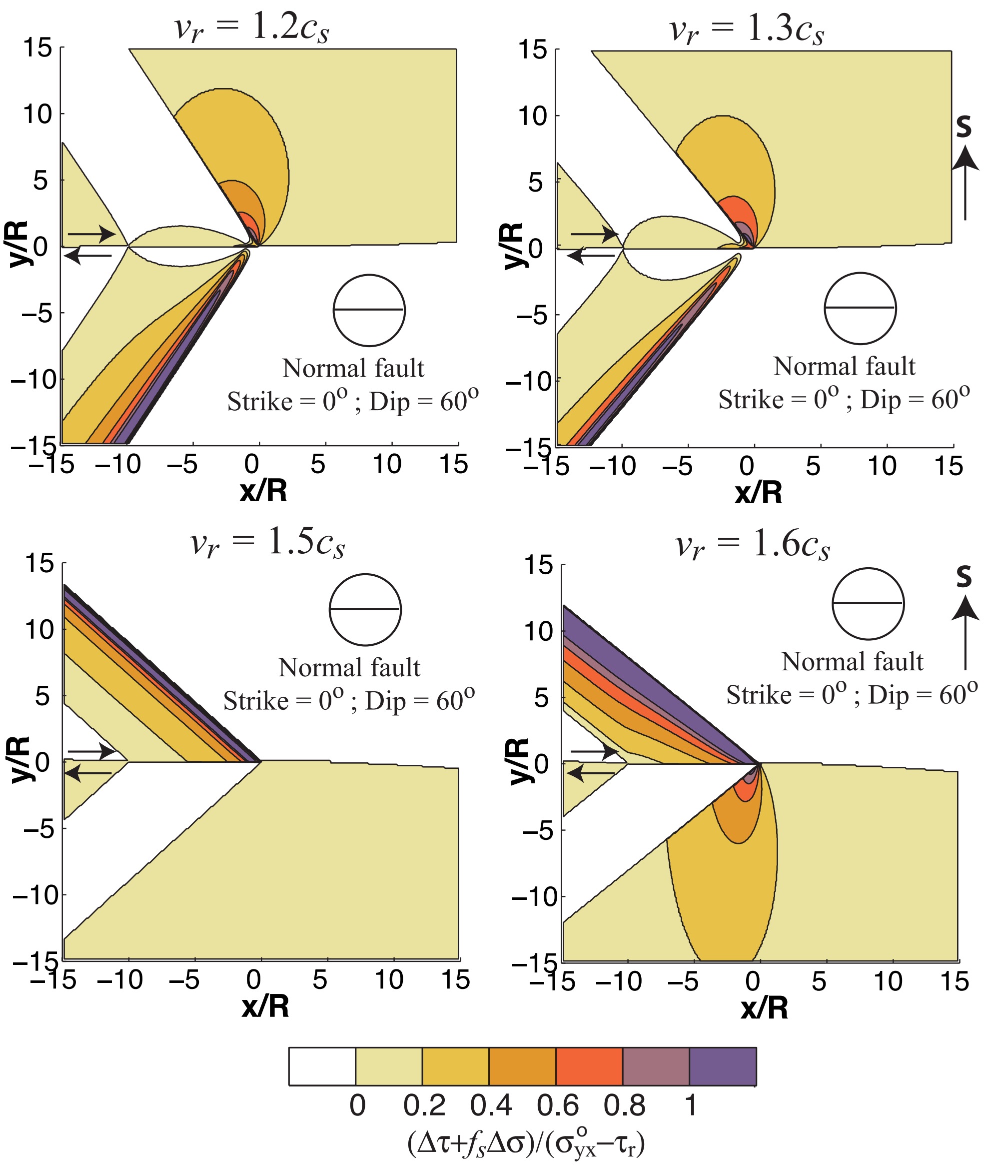

Figure 5.8: Contours of positive change in Coulomb stress (scaled by dynamic stress drop), due to a supershear rupture, on Normal faults striking parallel to the slip pulse and dipping at 60^0. Open circle represents normal faults with their strike shown by the bisecting line.

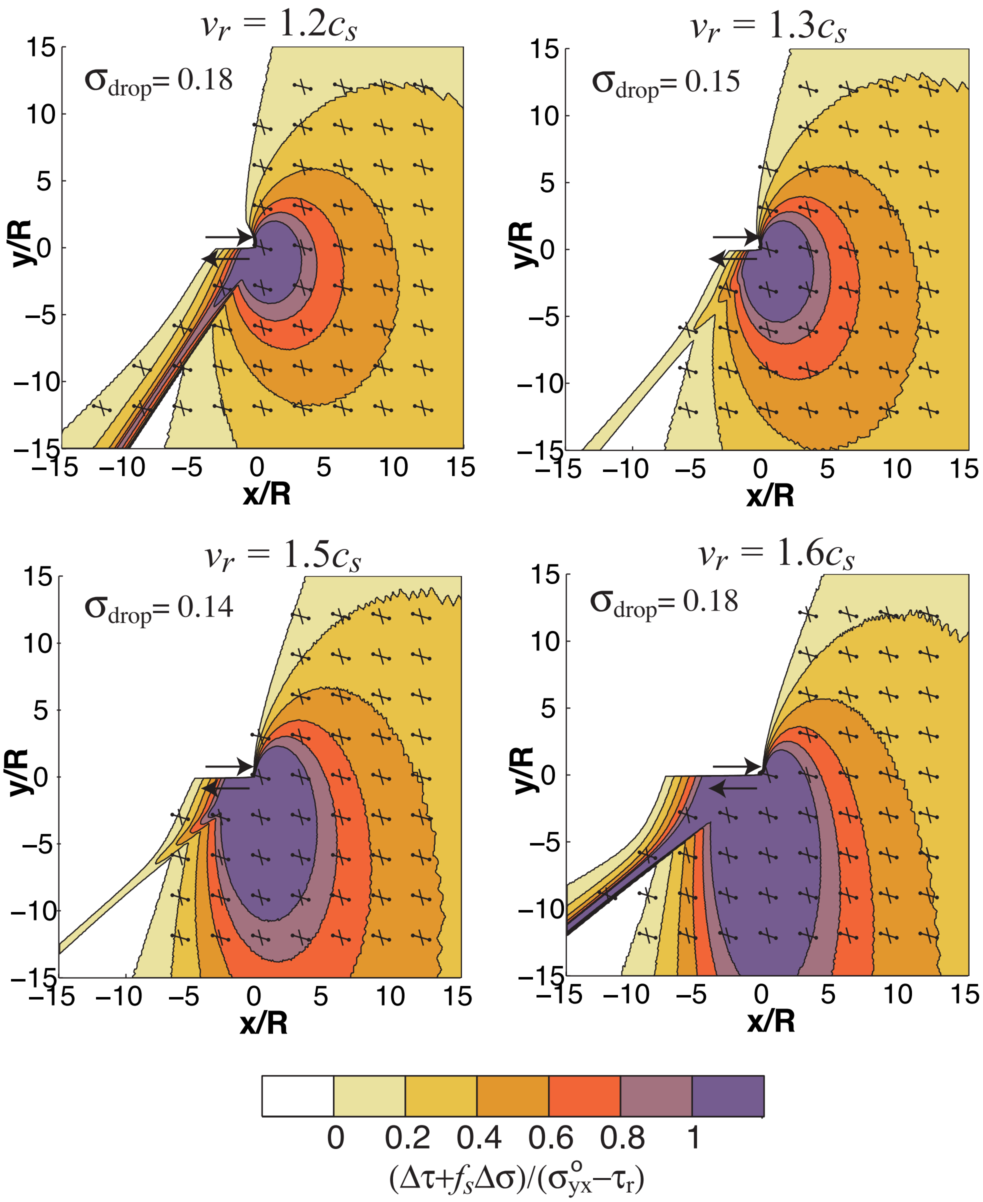

Figure 5.9: Effect of rupture velocity on positive Coulomb stress changes (maximum of the two on optimally oriented structures) induced by an intersonic slip pulse on optimally oriented structures. Here $\Psi = 45^0$ and $\sigma_{drop} = (\sigma^0_{yx} - \tau_r)/(\tau_p - \tau_r)$. σ^0_{zz} is chosen such that the pre-stress field favors pure strike-slip faulting. Dumb-bell shaped lines represent optimal right-lateral strike-slip structures and simple lines represent left-lateral strike-slip structures.

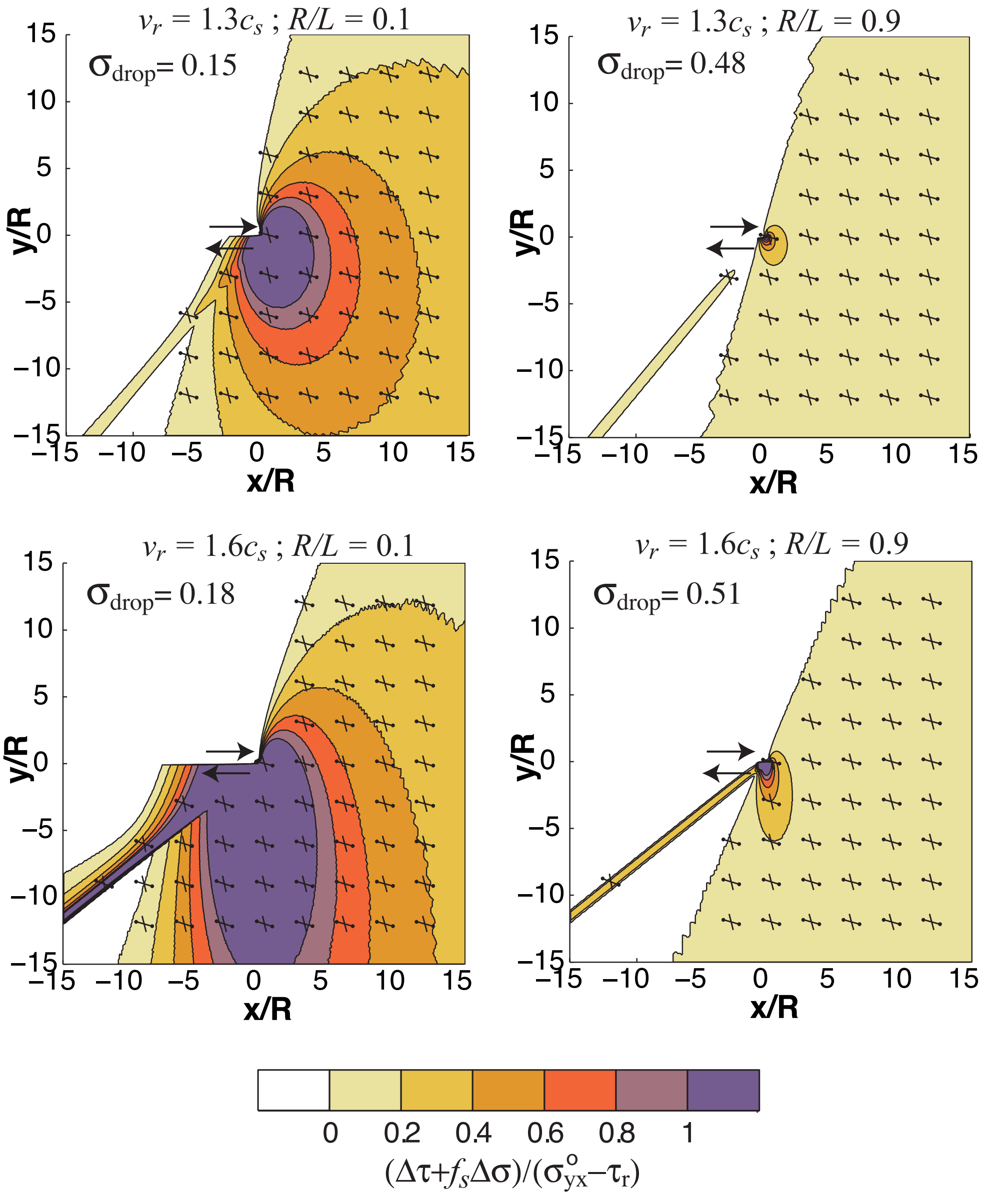

Figure 5.10: Effect of the size of the slip weakening zone relative (R) to the length of the slip pulse (L) on Coulomb stress changes (maximum of the two on optimally oriented structures) induced by an intersonic slip pulse on optimally oriented structures. Here $\Psi = 45^0$. σ^0_{zz} is chosen such that the pre-stress field favors pure strike-slip faulting. Refer to figure 5.8 for explanation of symbols.

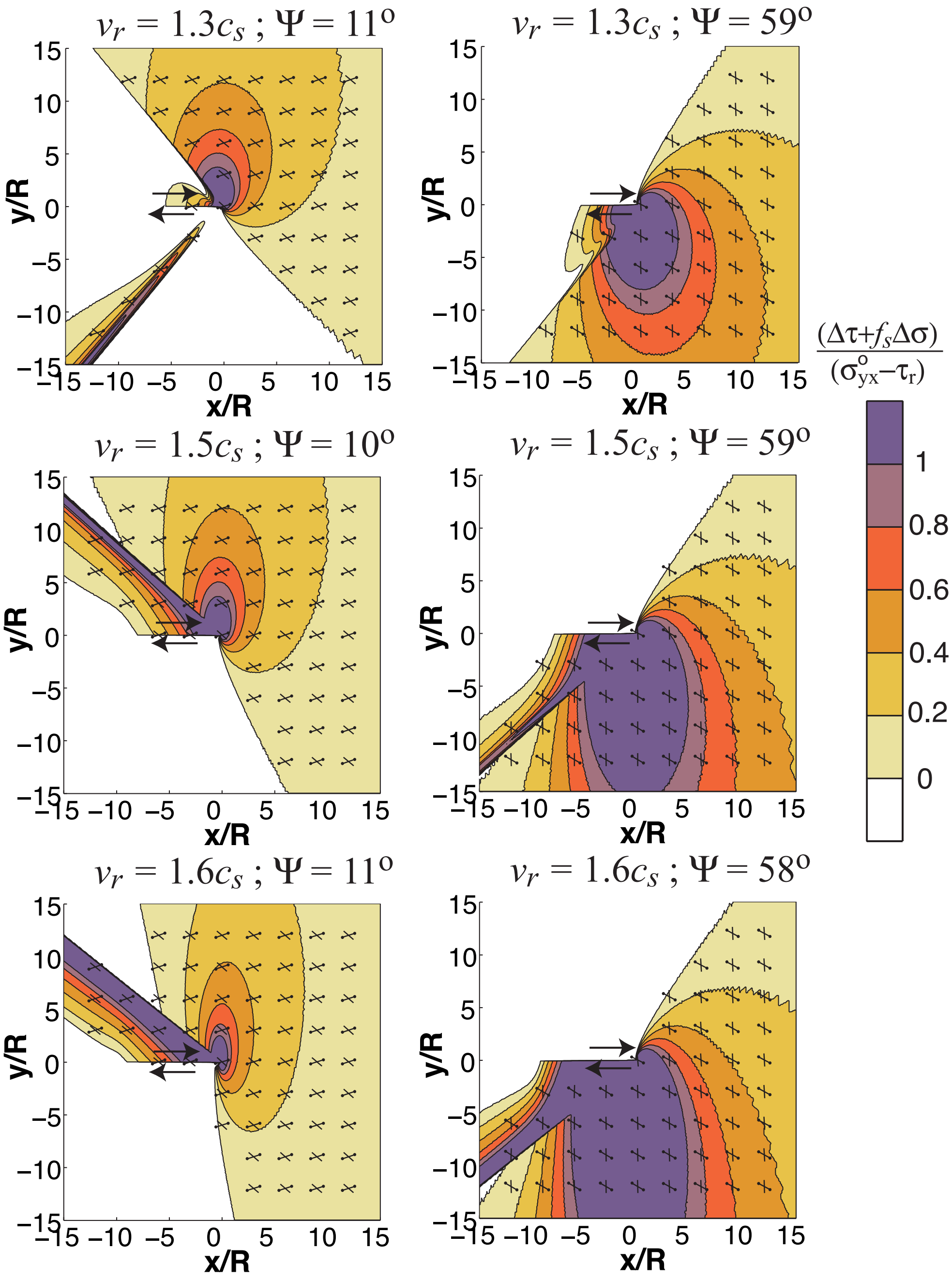

Figure 5.11: Effect of Ψ on positive Coulomb stress changes (maximum of the two on optimally oriented structures) induced by an intersonic slip pulse on optimally oriented structures. σ^0_{zz} is chosen such that the pre-stress field favors pure strike-slip faulting. Refer to figure 5.8 for explanation of symbols.

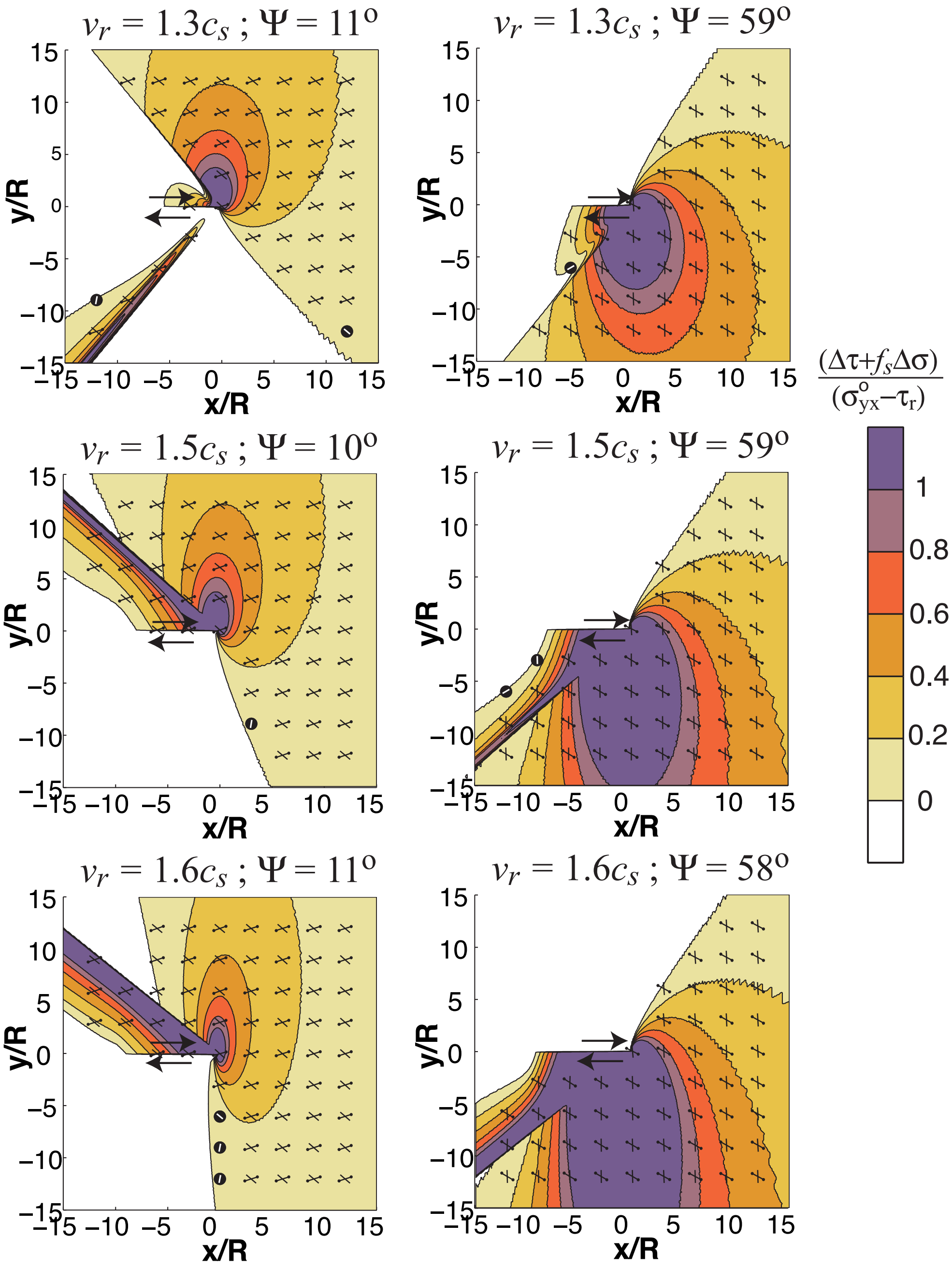

Figure 5.12: Same as Figure 5.11 except σ^0_{zz} is chosen such that the pre-stress field favors equally both strike-slip and thrust faulting. Refer to figure 5.8 for explanation of symbols.

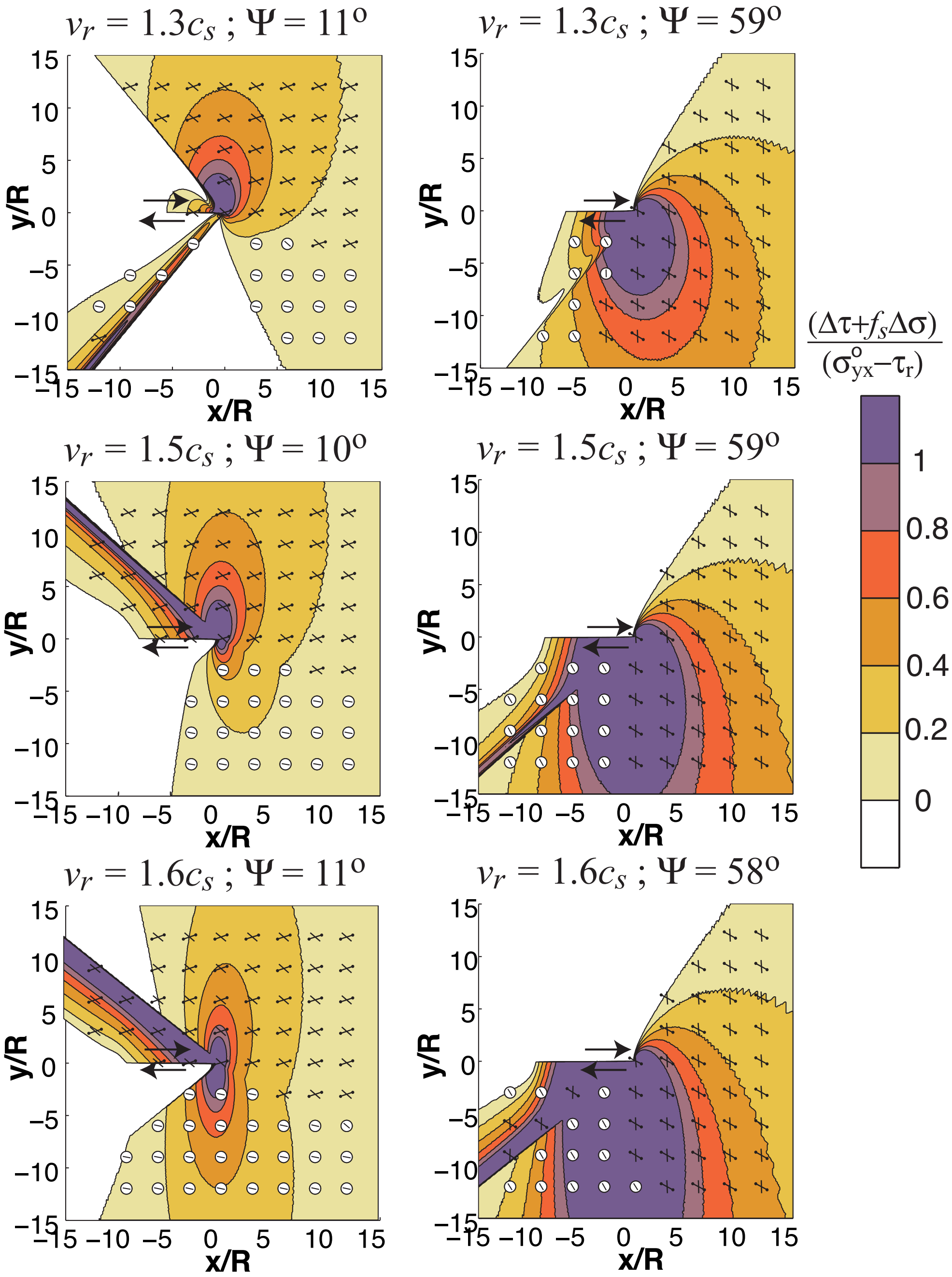

Figure 5.13: Same as Figure 5.11 except σ^0_{zz} is chosen such that the pre-stress field favors equally both strike-slip and normal faulting. Refer to figure 5.8 for explanation of symbols.

tween 30 and 45 degrees from orientations of active faults in the region. It was noted for Denali fault in Alaska, which has similar tectonic features as Kunlun, by *Ratchkovski* [2003], that the orientation of the maximum principal stress rotated about the normal to the strike as one traversed along the strike of the fault. This might be the case with Kokoxili but no similar stress direction estimate exists for the region to the east as of now. The orientation of the cracks and the existence of both normal and strike-slip structures gives us an additional constraint on Ψ. Firstly, if the cracks were created by the unloading phase following the traversal of a large compressional loading pulse then the orientation of the cracks might give us some constraint on the direction of the maximum in-plane compressive stress, Ψ. The average orientation of the cracks seem to be between 50 and 55 degrees (no precise measurements were made in the field) with respect to the fault and these features are expected to form perpendicular to the maximum in-plane compressive stress direction, provided that the stress perturbation added to that compression. This suggests that Ψ should be roughly between 35 and 40 degrees. The simultaneous existence of normal and strike-slip faulting, if interpreted (too strictly) to mean that the τ/σ were the same on both the structures, that σ_{zz}, the maximum principal compressive stress, and the remaining principal stresses be compressive and not greater than σ_{zz}, puts Ψ in the range of 16 to 27 degrees (for τ/σ between 0.3 and 0.6). The direction $\Psi_{\Delta\sigma}$ of the principal compression in the perturbation far-field lies between 0 and 10 degrees when $v_r > \sqrt{2}c_s$, specifically between 3 and 6 degrees when $1.5c_s < v_r < 1.6c_s$. In fact, in the far-field $\Psi_{\Delta\sigma} = 0.5\tan^{-1}(-\cot 2\beta)$ where $\sin\beta = c_s/v_r$. For the far-field compressive stress along the principal direction to become yet more compressive we must have $\Psi - \Psi_{\Delta\sigma} < \pi/4$ which implies that $\Psi < \pi/4 - 0.5\tan^{-1}(\cot 2\beta) = 39^0$ to 42^0 when $1.5c_s < v_r < 1.6c_s$. Thus the above constraints on pre-stress direction make it plausible that stresses in the far-field caused the ground cracking.

5.7 Effect of various model parameters on the change in dynamic Coulomb Stress

Since the perturbation in the elastic field due to S-wave radiation from a supershear slip pulse extends to infinity in our 2-D model (practically this would be limited to the depth of the seismogenic zone) we expect significant effects at larger distances from the supershear slip pulse than its sub-Rayleigh analogue. Below we will explore the influence of various non-dimensional model parameters, outlined earlier, on off-fault damage. This is done generically without specific application to the Kokoxili event. All the figures have the maximum positive change in Coulomb stress, due to a supershear pulse, contoured for an optimally oriented structure at each grid point.

5.7.1 Effects of v_r and R/L

The effects of rupture velocity and R/L on the off-fault stress field (for optimally oriented structures) are shown in Figures 5.9 and 5.10. These results were obtained for $\sigma^0_{xx}/\sigma^0_{yy} = 1.0$ $(\Psi = 45^0)$, $R/L = 0.1$ and σ^0_{zz} chosen such that pre-stress favors strike-slip faulting i.e $\sigma^0_{zz} = 0.5(\sigma_1 + \sigma_3)$. With increasing rupture velocity and decreasing R/L, the off-fault stressing, in a medium hosting a supershear slip pulse, increases. Both cases show significant far-field effects on the extensional side of the fault and increasing near field effects (outside the Mach front) with increasing rupture velocity. Increasing R/L results in a reduction in the stress concentration ahead of the rupture tip resulting in reduced off-fault stressing.

5.7.2 Effect of Ψ

Pre-Stress favors pure strike-slip faulting ($\sigma^0_{zz} = 0.5(\sigma_1 + \sigma_3)$)

We consider two different $\sigma^0_{xx}/\sigma^0_{yy}$ ratios, 2.0 and 0.8, for which $\Psi = 10^0 - 11^0$ and $58^0 - 59^0$ respectively. The slight variation in Ψ is due to the fact that σ^0_{xy} varies with rupture velocity. We consider the effects of the above parameters for $v_r = 1.3, 1.5$ and $1.6c_s$. As seen in Figure 5.11 switching from low value of Ψ to a higher value results in the shift of the domain of positive Coulomb stress change from mainly on the compressional side to mainly on the extensional side.

Pre-stress equally favors both thrust and strike-slip faulting ($\sigma^0_{zz} = \sigma_1$)

As in the previous sub-section the region where there is a positive change in Coulomb stress switches from being predominantly on the compressional side to the extensional side as Ψ is increased. The region of maximum increase Coulomb stress change also increases with rupture velocity. [Figure 12].

Pre-stress equally favors both normal and strike-slip faulting ($\sigma^0_{zz} = \sigma_3$)

Referring to Figure 5.13 we see the same general features outlined earlier stand out. The main difference between the three cases discussed is the nature of faulting which follows again the choice of pre-stress parameters.

5.8 Energy balance and estimates

As explained in *Dunham and Archuleta* [2005], the proper energy balance for a supershear slip pulse is given by $\sigma_{yx}^0\delta = \tau_r\delta + G_{frac} + G_{rad}$, where σ_{yx}^0 is the far field shear stress, τ_r is the residual strength of the fault, δ is the locked-in slip left in the wake of the slip pulse. Here $\tau_r\delta$ is the dissipation at the residual strength level, G_{frac} is the dissipation at stresses excess of the residual which defines the fracture energy, and G_{rad} is the energy flow away from the slip pulse associated with the S waves.

The locked-in slip δ is given by the expression,

$$\frac{\delta}{R} = \frac{1}{v_r}\int_0^{L/R} V(\xi)d\xi \tag{5.9}$$

where V is the slip velocity distribution which depends on R/L and v_r/c_s and is given by $V(\xi) = -2v_r[(\hat{\alpha}_s^2+1)/4\mu\alpha_d]\Im S(\xi)$ when approaching the fault from $y > 0$ and ξ denotes x/R. G_{frac} is given by

$$\frac{\mu G_{frac}}{(\tau_p-\tau_r)^2 R} = \int_0^1 V^*(\xi)(1-\xi)d\xi \tag{5.10}$$

where $V^*(\xi) = \mu V(\xi)/[(\tau_p-\tau_r)v_r] = -2\{(\hat{\alpha}_s^2+1)/[4\alpha_d(\tau_p-\tau_r)]\}\Im S(\xi)$. G_{rad} is then evaluated from the energy balance equation. The energy flux associated with G_{rad} extends all the way to infinity and vanishes when the rupture velocity is $\sqrt{2}c_s$. We non-dimensionalize energy in our model, following *Rice et al.* [2005], with seismically observable parameters, as $\hat{G} = \pi LG/\mu\delta^2 = F(v_r/c_s, R/L)$ where μ is the shear modulus of the medium hosting the slip pulse. The non-dimensional function, F cannot be reduced to a simple analytical expression, as in the sub-Rayleigh case, but has to be numerically determined. Also, unlike the sub-Rayleigh case, the dependence of F on rupture speed and R/L

are no longer separable. Figure 5.14 shows the variation of G_{frac} and G_{rad} with rupture velocity for a fixed ratio of dynamic stress drop to strength drop, $(\sigma_{yx}^0 - \tau_r)/(\tau_p - \tau_r)$ = 0.3. The total energy, $G_{frac} + G_{rad}$, decreases monotonically with increasing fracture energy. Since this ratio is dependent on both the rupture speed and the size of the process zone with respect to the length of the slip pulse we have to vary R/L with rupture velocity to obtain the energy values at fixed stress drop.

One can also use the energy balance equation to evaluate how the size of the slip-weakening zone, R, varies with R/L and v_r/c_s. We scale this value of R with the size of the process zone at static limit for a semi-infinite crack, R_0^* as in ***Rice et al.*** [2005] where

$$R_0^* = \frac{9\pi}{16(1-\nu)} \frac{\mu G_{frac}}{(\tau_p - \tau_r)^2} \tag{5.11}$$

Here ν is the Poisson ratio of the medium, set at 0.25 in our model, and G_{frac} is the fracture energy release rate. Using this with equation 5.11 we get R/R_0^*.

Figure 5.15 shows the variation of R/R_0^* for the complete range of admissible speeds for a dynamic shear crack. The expression for R/R_0^* for the sub-Rayleigh range was obtained from ***Rice et al.*** [2005] equation 14. R/R_0^* undergoes Lorentz-like contraction in the sub- Rayleigh regime, diminishing to zero at the Rayleigh wave speed, c_R. The speed range between c_R and c_s, the S wave speed, is inadmissible on energetic grounds for a steady shear crack. Beyond c_s, R/R_0^* monotonically diminishes to zero again as the rupture speed approaches the P wave speed. For the supershear speed range inferred from various earthquakes, between 1.5-1.7c_s, R/R_0^* lies between 0.3 and 0.6. Estimates of R_0^* by ***Rice et al.*** [2005], for the ***Heaton*** [1990] event set, varies between 1.3-36 m (with an uncertainty of factor of two since this value depended on R/L). This was obtained under the

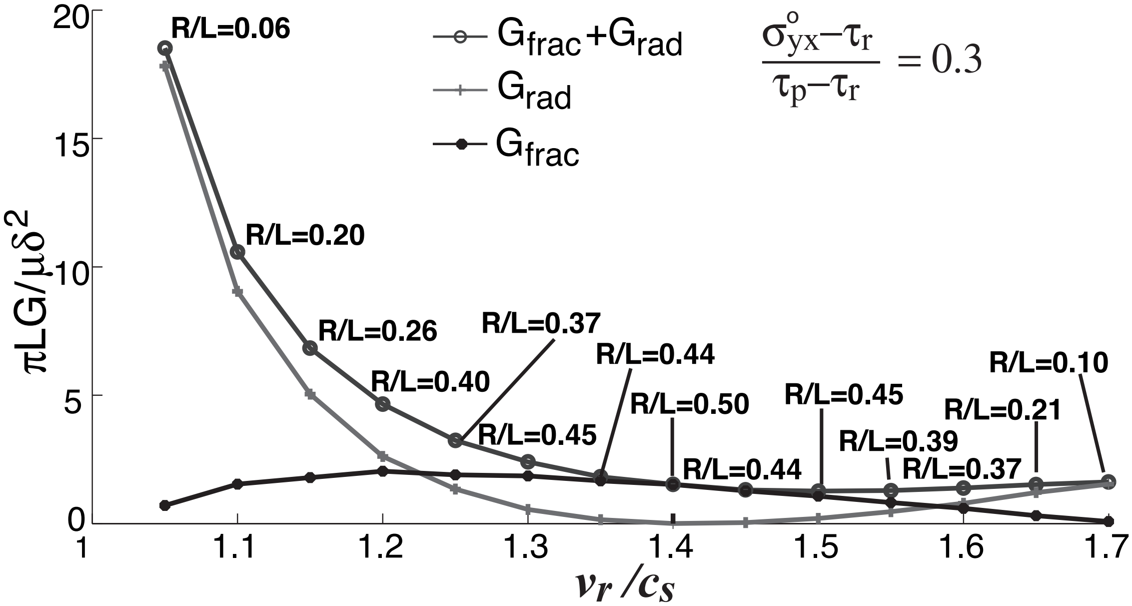

Figure 5.14: Scaled fracture energy release rate, G_{frac}, energy radiated by S-wave, G_{rad} and the total energy as a function of rupture speed, v_r for $(\sigma_{yx}^0 - \tau_r)/(\tau_p - \tau_r) = 0.3$.

assumption of high peak strength and low residual strength implying $(\tau_p - \tau_r) \approx \tau_p = f_s\bar{\sigma}_n$ where $f_s = 0.6$ and $\bar{\sigma}_n$ is the effective normal pressure

calculated at median depth for each of the earthquakes in the set. For low strength drop case, their estimates of R_0^* varied between 73m to 3.3 km.

We evaluate the spatial slip distribution, $\Delta u(x)$, on the fault by numerically integrating the expression for slip velocity, $V = \partial\Delta u/\partial t = -v_r\partial\Delta u/\partial x$. This spatial distribution of slip is then used along with the spatially linear failure criterion used in our model to determine the slip weakening law implied by our model. Figure 5.16 shows this slip-weakening behavior. There is little deviation from the linear slip-weakening law, that is often (but somewhat arbitrarily) assumed in numerical simulations of dynamic shear ruptures, regardless of the choice of R/L. There is also some sensitivity to rupture velocity in the slip-weakening curves unlike the sub-Rayleigh case but that too is modest.

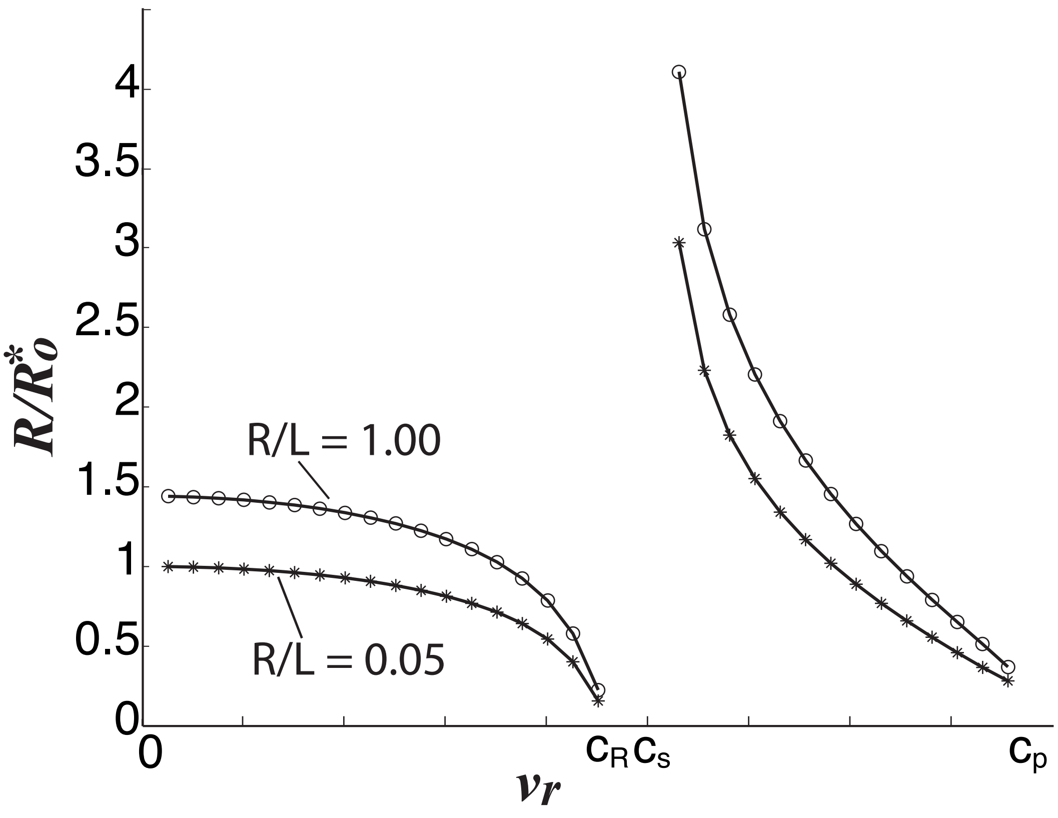

Figure 5.15: Variation in the scaled size of the process zone, R/R_0^*, with rupture velocity, v_r. R_0^* is the size of the process zone at static limit for a semi-infinite shear crack. c_R, c_s and c_p are the Rayleigh, S and P wave speeds of the medium respectively.

5.9 Summary and conclusions

We have studied here the off-fault stressing induced by a 2-D steady slip pulse propagating at supershear speeds in a homogeneous isotropic elastic medium with a linear strength degradation boundary condition like in Figure 5.1. This work is an extension of the *Rice et al.* [2005] model which looked at the sub-Rayleigh speed regime. Unlike its sub-Rayleigh analogue the dependence on rupture velocity, as v_r/c_s, and the relative size of the slip-weakening zone, as R/L, for the elastic field of a supershear slip pulse are inseparable.

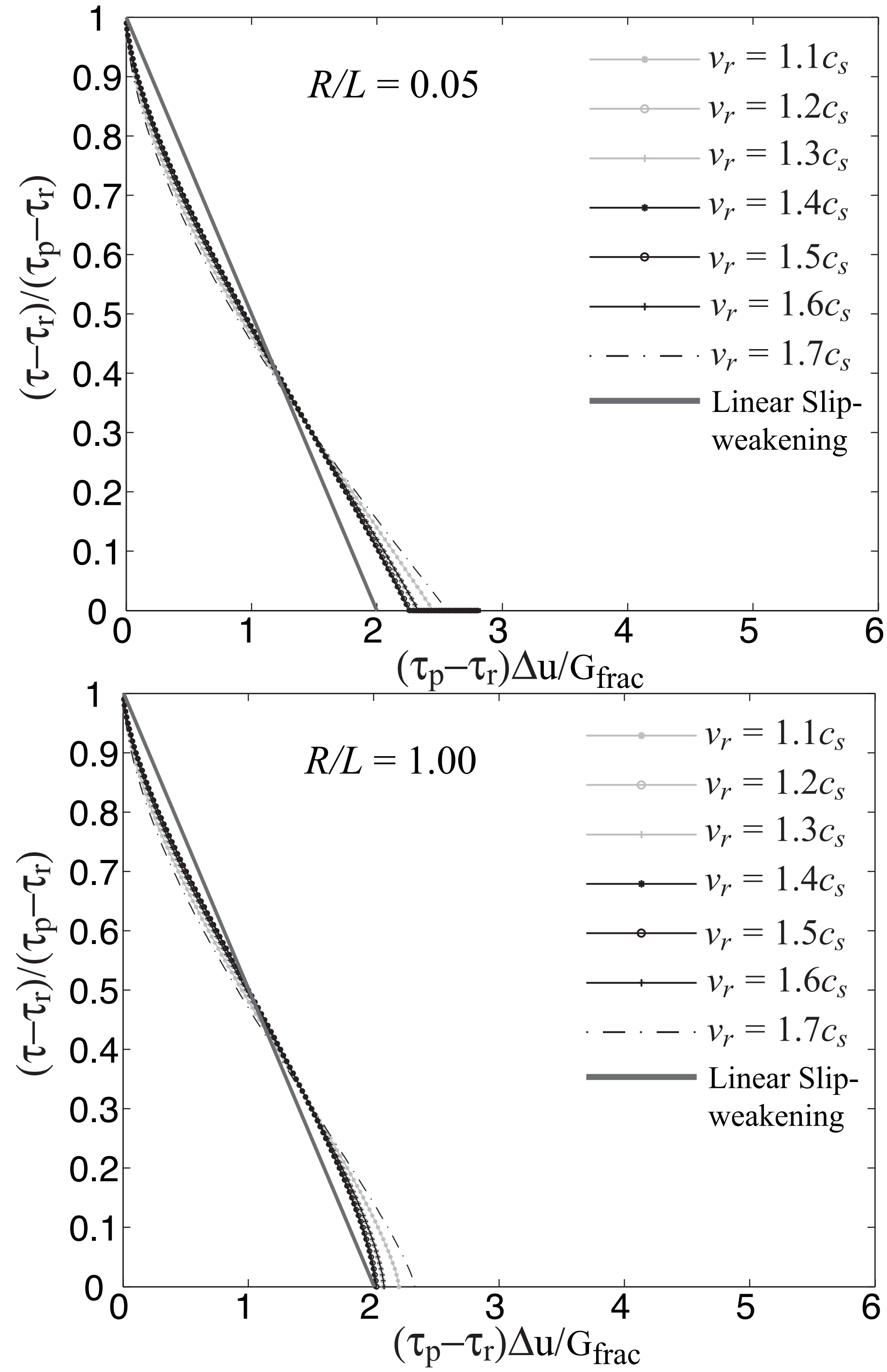

Figure 5.16: Slip weakening law implied by our analysis compared with the linear slip weakening law for $R/L = 0.05$ and 1.00.

Because of the supershear nature of the pulse, Mach fronts develop at the two ends of the slip pulse and, because our model is 2D and steady state, the elastic field within this band of Mach fronts does not attenuate with distance (practically up to distances comparable to the seismogenic zone depth) leading to a unique feature of the supershear slip pulse. We expect significant effects of the supershear slip pulse to be observed as damage at large distances. *Bernard and Baumont* [2005] also show, in their analytic and numerical model for kinematic ruptures, that the ground acceleration due to a supershear rupture is unusually high at distances of the order of few tens of kilometers. We observe that this feature is consistent with extension-like failure features observed a few kilometers away from the Kunlun fault during the 2001 Kokoxili event, thus lending support to the suggestion that its rupture speed was supershear in that region. We used our slip pulse model to also examine the simultaneous normal faulting observed during the 2001 Kokoxili event. However that strand, lying parallel to the main strike-slip fault on the extensional side, does not experience positive change in Coulomb stress, so the specific features of supershear rupture do not provide an alternative to the slip partitioning explanation of that feature [*King et al.*, 2005].

We also evaluated the change in Coulomb stress, in the medium hosting the slip pulse, on optimally oriented structures allowing for out-of-plane failure too. Failure is encouraged ($\Delta CS > 0$) mainly on the extensional side of the fault and increases in extent with increasing rupture velocity (v_r) and decreasing R/L. Increasing angle of orientation of the maximum in-plane principal compressive stress (Ψ) with the slip pulse results in the switching of the zone of $\Delta CS > 0$ from the compressional to the extensional side of the slip pulse.

We also evaluated the radiated seismic energy and fracture energy due to a supershear slip pulse for a fixed dynamic stress drop (scaled by the strength drop), $(\sigma^0_{yx} - \tau_r)/(\tau_p - \tau_r)$ = 0.3, and showed that the total of radiated and fracture energy decreases monotonically with increasing rupture velocity. Using those results we also showed that the size of the slip-weakining zone decreases monotonically too with increasing rupture velocity in the supershear regime. We also showed that our spatially linear failure criterion deviates very little from the linear slip weakening behavior regardless of the choice of R/L.

Chapter 6

Attenuation of Radiated Ground Motion and Stresses from 3D Supershear Ruptures

6.1 Abstract

Radiating shear and Rayleigh waves from supershear ruptures form Mach waves that transmit large-amplitude ground motion and stresses to locations far from the fault. We simulate bilateral ruptures on a finite-width vertical strike-slip fault (of width W and half-length L with $W << L$) breaking the surface of an elastic half-space, and focus on the wavefield in the near-source region (i.e., at distances much less than L). In the immediate vicinity of the fault (at distances much smaller than W), two-dimensional slip-pulse models (i.e., models in which the lateral extent of the slip zone is unbounded) [*Dunham and Archuleta*, 2005; *Bhat et al.*, 2007a] accurately predict the wavefield at sub-surface locations, although Rayleigh wave Mach fronts will always exist at the surface. Amplitudes associated with the Mach wedge in these models are undiminished with distance from the fault, but at these close distances, dilatational field components have equally large amplitudes. When viewed from distances far greater than W, the fault is accurately modeled as a line source that produces a Mach cone. Geometrical spreading of the Mach cone occurs radially and amplitudes for the shear Mach cone there decrease with the inverse square-root of distance [*Ben-Menahem and Singh*, 1987]. The amplitudes for the Rayleigh Mach cone should not attenuate with distance for the ideally elastic material considered here. The transition between these two asymptotic limits occurs at a distance comparable to W. The rate at which the fault weakens at the rupture front exerts a strong influence on the off-fault fields only in the immediate vicinity of the fault for both sub-Rayleigh ruptures, but also at the Mach fronts of supershear ruptures. Rapid weakening, which is known to produce larger slip velocities on the fault, also generates larger amplitudes at the Mach front. We thus conclude that radiating Mach waves of three-dimensional supershear rup-

tures do transmit large-amplitude ground motions and stresses far from the fault, but with amplitudes moderated at distances greater than the fault width by decay with distance due to geometrical spreading.

6.2 Introduction

The velocity at which a rupture propagates influences the amplitude and character of the radiated ground motion and stresses. A distinct manifestation of this occurs when ruptures exceed the S-wave speed and generate shear Mach waves that efficiently transmit ground motion and stresses away from the fault. When a supershear rupture propagates in an elastic half space Rayleigh Mach fronts are to be expected too. Near the rupture front, at the surface, the rupture would have a tendency to perturb the out-of-plane stress component. To satisfy the traction free surface criteria Rayleigh waves have to be emitted from the crack front. Since the rupture velocity is greater than the Rayleigh wave speed Rayleigh Mach fronts would thus be generated from the rupture front. The Rayleigh Mach front originates from the rupture tip but, since the Rayleigh wave speed is less than the S-wave speed of the medium, lags behind the shear Mach front as one moves along the two Mach fronts. The objective of the current work is to quantify how the amplitude of radiated waves, specifically of those associated with the Mach wave, diminishes with distance from the fault. We further compare fields from supershear ruptures to those produced by sub-Rayleigh ruptures with the aim of contrasting the rate at which amplitudes decay with distance from the fault for both classes of ruptures.

Supershear propagation, first suggested by analytical [*Burridge*, 1973] and numerical [*Andrews*, 1976; *Das and Aki*, 1977] studies, has since been confirmed in laboratory experiments [*Rosakis et al.*, 1999; *Xia et al.*, 2004]. Supershear speeds have been reported for a number of earthquakes, primarily from analyses of near-source records of the 1979 Imperial Valley [*Archuleta*, 1984; *Spudich and Frazer*, 1984], 1999 Izmit and Düzce [*Bouchon et al.*, 2001, 2002], and 2002 Denali fault [*Ellsworth et al.*, 2004; *Dunham and Archuleta*, 2004] events. As *Savage* [1971] and *Ben-Menahem and Singh* [1981] have shown, there are also distinctive features of supershear ruptures at regional and teleseismic distances (e.g., changes in the radiation pattern), and an inversion of the 2001 Kokoxili (Kunlun) event [*Bouchon and Vallee*, 2003] using regional Love waves suggests supershear propagation. The unique characteristics of near-source records from supershear events, particularly of records at Pump Station 10 (located only 3 km from fault) in the 2002 Denali fault event, prompted a closer look at characteristics of radiated ground motion from supershear ruptures.

We build on a number of previous studies that have examined the influence of rupture speed on near-source ground motion. *Ben-Menahem and Singh* [1987] studied the acceleration field generated by a point velocity dislocation (a singularity moving along a line in a full space and leaving in its wake a fixed moment per unit length) that travels a finite distance at a supershear speed before stopping. In addition to starting and stopping phases, shear Mach waves were implicated as carriers of large-amplitude accelerations. Their results further demonstrate how the Mach wave only passes through a particular region surrounding the fault. By considering propagation only along a line, their analysis applies only to observation points sufficiently removed from the fault (i.e., at distances much greater than the fault width). A number of other researchers have focused primarily on the wavefield in the immediate vicinity of the fault (extending out to distances comparable to the fault width, but not much beyond that). By examining a sequence of kinematics models with various rupture speeds, *Aagaard and Heaton* [2004] demonstrated how the well-known two-sided fault-normal velocity waveform of sub-Rayleigh ruptures (the so-called "directivity pulse" that has been of primary concern in seismic hazard [*Somerville et al.*, 1997]) vanishes when ruptures exceed the S-wave speed. Instead, the largest amplitudes now occur at the Mach front. *Bernard and Baumont* [2005] combined kinematic models of supershear ruptures with an asymptotic isochrone-based analysis of fields near the Mach front to explore features of the Mach wave from supershear ruptures. Their asymptotic analysis, which did not include any corrections for a finite fault width, showed that for straight ruptures fronts, field amplitudes at the Mach front remain undiminished with distance from the fault; rupture-front curvature leads to an inverse square-root decay of amplitudes with distance due to a loss of coherence at the Mach front.

The starting point for our analysis is the two-dimensional steady-state slip-pulse model developed by *Rice et al.* [2005] to examine stress fields near the rupture front of sub-Rayleigh ruptures. This model was extended to supershear speeds by *Dunham and Archuleta* [2005] and *Bhat et al.* [2007a]. *Dunham and Archuleta* [2005] focused on ground motion (specifically, velocity records) from slip pulses in the context of models of the Denali fault event [*Ellsworth et al.*, 2004; *Dunham and Archuleta*, 2004]. *Bhat et al.* [2007a] studied the off-fault damage pattern due to supershear ruptures and hypothesized that anomalous ground cracking observed at a few tens of kilometers from the fault during the 2001 Kokoxili (Kunlun) event resulted from the high stresses at the Mach front emanating from a supershear rupture. This observation raises the possibility that radiated stresses from a large supershear event might trigger slip on adjacent faults of the proper orientation. One

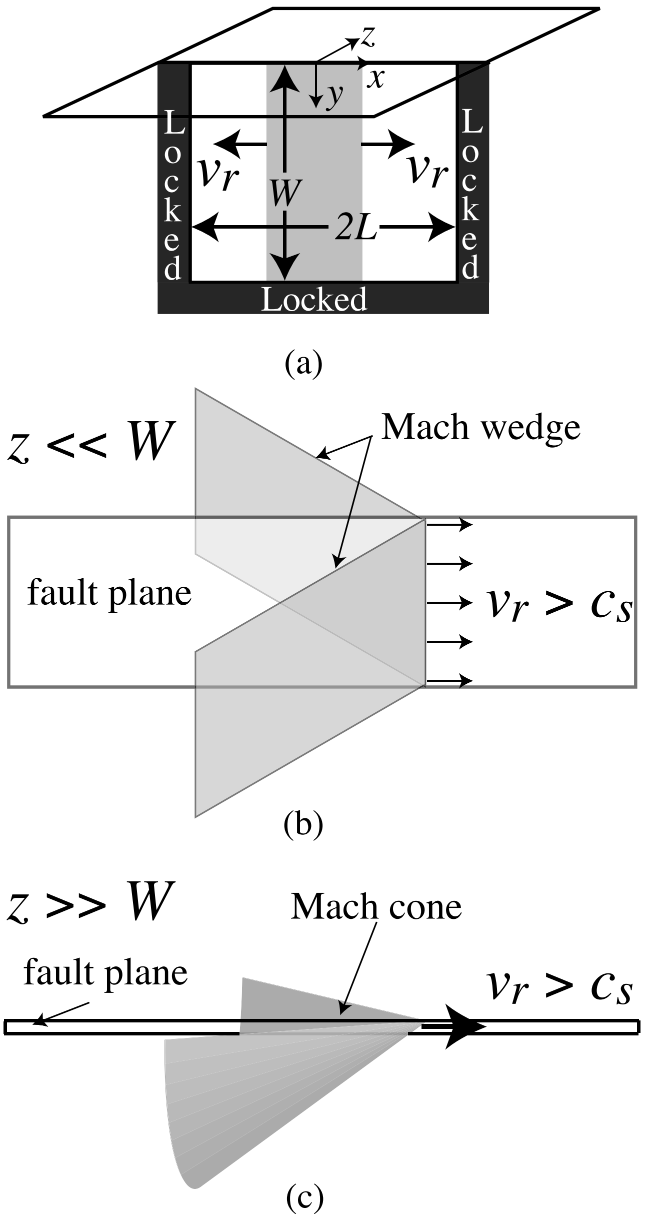

Figure 6.1: (a) Rupture on a fault of width W and half-length L that expands bilaterially at speed v_r. (b) Mach wedge from a steady-state supershear rupture in 2D, which approximates S-wave radiation from slip on a finite-width fault at locations close to the fault ($z \ll W$) and away from the fault edges. (c) Mach cone emitted by supershear line source, which approximates radiation from slip on a finite-width fault when viewed from afar ($z \gg W$).

objective of the current work is to quantify how the amplitude of Coulomb stresses on pre-existing structures is influenced by rupture speed and the finite fault width, and whether or not these amplitudes are sufficient to activate secondary faulting.

The most distinctive feature of the 2D supershear slip-pulse models is the shear Mach wave. In addition to the shear Mach waves found in two-dimensional models, we also expect Rayleigh Mach waves emanating from the rupture front out along the free surface. The two-dimensional plane-strain models feature large changes in the normal stress parallel to the rupture front. These changes appear only in the vicinity of the fault and not further away at the shear Mach front since fields there are nondilational. When considering rupture in a half-space, the component of normal stress parallel to the rupture front is also normal to the free surface, and must be negated there to satisfy the traction-free boundary condition. This can be accomplished by the superposition of normal loads on the free surface that negate the moving vertical normal stress pattern. These moving loads, which propagate at a super-Rayleigh speed, will then excite Rayleigh Mach waves [*Lansing*, 1966; *Georgiadis and Lykotrafitis*, 2001]. The combined assumptions of two dimensions (i.e., an infinite extent of the slipping region parallel to the rupture front), steady-state propagation, and a homogeneous linear elastic medium cause the shear Mach waves to extend infinitely far from the fault and for the amplitude of fields associated with the Mach wave to remain undiminished with distance from the fault. This study addresses the first of these assumptions by considering ruptures in three dimensions, specifically right-lateral strike-slip ruptures on a finite-width vertical fault breaking the surface of an elastic half-space. The focus in on the wavefield after the rupture has propagated many times further than the fault width.

To understand the effect of bounding the vertical extent of the slipping region, consider two limiting cases of a rupture on a vertical surface-breaking fault of width W and half-length L (Fig. 6.1a). At locations close to the fault and away from its edges (specifically, at locations much closer that W), the fault width is unimportant and two-dimensional models provide an accurate description of the fields, at least if the slip-weakening zone length R is much less than W. In this extremely near-source region, the Mach front assumes the form of a wedge (Fig. 6.1b) and Mach-wave amplitudes will not diminish with distance from the fault. Of course, this region is further complicated by the presence of dilatational fields of comparable amplitude. At the opposite extreme, consider points far removed from the fault (specifically, at distances greatly exceeding W). From these distant points, the fault appears as a line source, and S-wave radiation now forms a Mach cone (Fig. 6.1c). Since the cross-section of the cone is a circle, geometrical spreading dictates that shear Mach-wave amplitudes will decrease with the inverse square-root of radial distance from the fault. It is not clear that the Rayleigh Mach-wave amplitudes would attenuate at all, in the ideally elastic material considered. It is of critical importance to hazard calculations to understand exactly how the transition between these two extremes occurs. Specifically, to what distances are large ground motion and stresses transported for realistic fault geometries? *Bhat et al.* [2007a] hypothesized that the transition between the two limits occurs at distances comparable to W, and our results confirm this hypothesis, although the Rayleigh Mach fronts also contribute to the fields and, in the ideally elastic uniform material, they would not decay at all with distance.

6.3 Model Geometry

We model ruptures on a vertical right-lateral strike-slip fault that intersects the free surface (Fig. 6.1a). W is the fault width, and v_r is the rupture velocity; we study three representative values of v_r: $0.8c_s$, $1.3c_s$, and $1.6c_s$, where c_s is the S-wave speed. The sub-Rayleigh speed, $0.8c_s$, was chosen as mid-range of typical $0.7 - 0.9c_s$ speed range inferred for various earthquakes. *Bouchon and Vallee* [2003] suggest a speed of around $1.6c_s$ for the 2001 Kokoxili (Kunlun) event and hence that speed was considered in our simulations. The value of $1.3c_s$ was chosen to see the effect of transitioning from the Eshelby speed of $\sqrt{2}c_s$ at which the shear Mach front is not generated at the rupture front [*Eshelby*, 1949]. For simplicity, we keep v_r fixed (rather than considering a more natural transition from sub-Rayleigh to supershear speeds, which would generate a more complicated set of waveforms) and consider symmetrically expanding bilateral ruptures that propagate a distance L in each direction. We also wish to work in the context of a dynamic model, in the sense that we specify a constant stress drop, $\Delta\sigma$, within the rupture. In this sense, our models are closely related to self-similar singular crack models in 2D. In our work, we prevent a stress singularity at the rupture front by employing a cohesive zone model that can be interpreted in the context of the commonly used slip-weakening friction law. The parameters of this model are the peak and residual strengths, τ_p and τ_r, and the distance, R, over which strength drops from τ_p to τ_r. As discussed by *Dunham and Archuleta* [2005] and *Bhat et al.* [2007a], the extent of the cohesive zone (relative to the length of the rupture) plays a large role in determining the maximum amplitude of fields at the Mach front.

The specific, simplified, procedure we use to force ruptures with the desired properties was originally employed by *Andrews* [1985]. The shear strength of the fault, τ_{str}, weakens linearly with distance (with weakening rate A) behind the rupture front:

$$\tau_{str}(x,t) = \max\{\tau_r, \tau_r + A(|x| - v_r t)\}. \tag{6.1}$$

The fault is locked until stress reaches the fault strength, τ_p (which is not specified *a priori* in this approach, but depends on τ_r and A, and varies moderately with the position of the rupture tip), at which time slip commences and weakening occurs in such a way as to ensure that stress always equals strength during sliding. This is illustrated in Fig. 6.2. In this model, both τ_p and R evolve as the rupture expands in order to provide a solution with non-singular and continuous stress at the tip. An associated energy release rate, or fracture energy G, can then be inferred as the area under the resulting plot of $\tau - \tau_r$ vs. slip. In 2D self-similar crack models, the energy release rate increases linearly with propagation distance; the procedure we use, if applied in this context, results in an increase of both τ_p and R to accomodate the increasing energy flux into the cohesive zone. Thus the shear and Rayleigh Mach waves would be distinct, non-overlapping phases at distances well less than a kilometer from the fault if R is indeed on the order of a few 10's of meters.

We note several other important quantities that will be of interest to us. The first is the seismic S ratio [$S = (\tau_p - \sigma^0_{zx})/(\sigma^0_{zx} - \tau_r)$], a measure of the initial load, σ^0_{zx}, relative to the peak and residual strengths. The stress drop is $\Delta\sigma = \sigma^0_{zx} - \tau_r$ and the strength drop is $\tau_p - \tau_r$. The fracture energy, G, may be calculated for each point on the fault as

$$G = \int [\tau(t) - \tau_r] V(t) dt = \int [\tau(\delta) - \tau_r] d\delta, \tag{6.2}$$

in which V is the slip velocity and the integrals are taken over all time t or all slip δ. Finally, we define an equivalent slip-weakening distance D_c via the relation

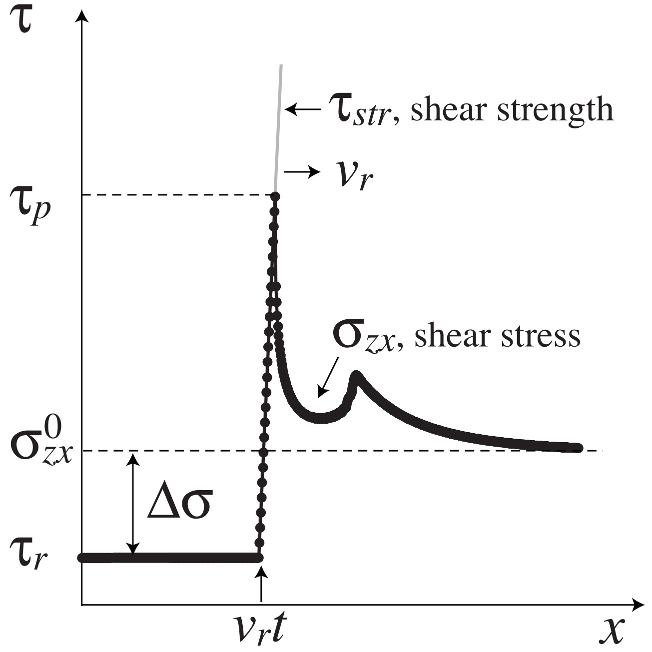

Figure 6.2: Fracture criterion used to force a rupture at speed v_r with stress drop $\Delta\sigma$. Fault strength increases linearly from $|x| = v_r t$ (grey line). When shear stress on the fault (black line and points from numerical model for sub-Rayleigh rupture at $0.8c_s$) reaches the strength, slip commences.

$$G = \frac{1}{2}(\tau_p - \tau_r)D_c, \tag{6.3}$$

which proves useful when interpreting our results in the context of the commonly used linear slip-weakening law [*Andrews*, 1976].

We next non-dimensionalize the model by scaling all distances by W and time by W/c_s. Stress is scaled with $\Delta\sigma$, particle and slip velocities by $\Delta\sigma c_s/\mu$ where μ is the shear modulus. Displacements and slip scale with $\Delta\sigma W/\mu$. When considering physical values of these parameters, we take $\mu = 30$ GPa, $c_s = 3$ km/s, and $W = 10$ km. We consider a Poisson material (i.e., one for which the P-wave speed is given by $c_p = \sqrt{3}c_s$), and choose

		stress drop	
field, scale (units)	low	moderate	large
stress, $\Delta\sigma$ (MPa)	0.3	3	30
velocity, $\Delta\sigma c_s/\mu$ (m/s)	0.03	0.3	3
displacement, $\Delta\sigma W/\mu$ (m)	0.1	1	10
fracture energy, $\Delta\sigma^2 W/\mu$ (MJ/m^2)	0.03	3	300

Table 6.1: Representative dimensionalizing factors by which non-dimensional values reported in this study may be converted to physical values; a range exists due to uncertaintly in $\Delta\sigma$. Other parameters employed in these relations are $\mu = 30$ GPa, $c_s = 3$ km/s, and $W = 10$ km.

τ_r to yield a dynamic coefficient of friction of 0.2 (but note that the actual value of normal stress, σ^0_{zz}, is unimportant since normal stress on the fault remains unaltered by slip on vertical strike-slip faults in a homogeneous medium). Estimates of stress drop vary widely, and to encompass this range we consider three respresentative values of $\Delta\sigma$: 0.3 MPa, 3 MPa, and 30 MPa. We report non-dimensional values (denoted by a superscript $*$) in our figures, and these may easily converted to physical values by the scaling factors decribed above and summarized for reference in Table 6.1.

We numerically solve our problem with a staggered-grid finite-difference code [*Favreau et al.*, 2002] with fault boundary conditions implemented with the staggered-grid split-node (SGSN) method of *Dalguer and Day* [2007]. Rake rotation is permitted, in that the slip vector rotates so as to be aligned with the shear traction vector. The degree of rake rotation depends on the change in stress relative to the initial level of stress in the medium. In our simulations, $\sigma^0_{zx}/(\sigma^0_{zx} - \tau_r) = 1.2$ and we have no transverse shear load (i.e., $\sigma^0_{zy} = 0$). The method is fourth order in space and second order in time for wave propagation in the body, but the spatial order is reduced to second order at the fault. We implement the free-surface boundary condition using the fourth-order W-AFDA scheme proposed by *Kristek et al.*

[2002], and place perfectly matching layer (PML) absorbing boundaries on the remaining sides [*Marcinkovich and Olsen*, 2003]. Ruptures propagate for $15W$ in each direction before reaching the end of the fault (we lock the fault beyond this), but the computational domain extends in this direction out to $\pm 20W$ to permit an examination of stopping phases. The fault-normal extent of the computational domain is $15W$. We run each simulation for a duration that permits the S-wave stopping phase from the fault ends to reach $15W$ in the fault-normal direction. We discretize the medium with a uniform grid spacing of $h^* = 0.02$ (i.e., a grid spacing of $h = 200$ m for $W = 10$ km, which is far larger than desired if the *Rice et al.* [2005] estimates of slip-weakening zone sizes R of a few tens of meters at mid-seismogenic depths are accurate). Numerical resolution is discussed below, but we note here that the resolution is determined by the choice of the cohesive-zone parameter A^*; larger A^* implies smaller R.

The two-dimensional case provides a convenient starting point to calibrate the numerical method, and it further provides reference solutions to which we can compare our 3D results to isolate the effects of the finite fault width. The immediately arising question is which parameters should be held fixed when comparing sub-Rayleigh and supershear ruptures. For expanding ruptures on homogeneous faults, the seismic S ratio determines whether or not ruptures will achieve supershear speeds [*Andrews*, 1976]. While this parameter has less importance in the context of our constant-speed models, this knowledge motivates our method of comparing sub-Rayleigh and supershear ruptures.

Consider the case that both G and $\tau_p - \tau_r$ are intrinsic properties of the fault (which immediately implies a particular D_c as defined above). Then what determines whether or not a rupture propagates at a supershear speed is the stress drop $\Delta\sigma$, relative to $\tau_p - \tau_r$.

From this perspective, we wish to hold G, $\tau_p - \tau_r$, and D_c fixed while varying v_r and $\Delta\sigma$. However, the former quantities all vary with propagation distance in our model. In the two-dimensional self-similar case, G increases linearly with distance [*Freund*, 1990; *Broberg*, 1989]. Upon introducing a cohesive zone with characteristic size $\Delta\sigma/A$, self-similarity is lost and both $\tau_p - \tau_r$ and D_c become increasing functions of distance. A strictly self-similar model—which would feature a constant $\tau_p - \tau_r$ and a D_c that increased linearly with time or propagation distance—could be achieved by making A inversely proportional to time, but we do not follow this approach. Instead, we simply select a distance $x^* = 8$ and match G and $\tau_p - \tau_r$ at this location. Matching G at any location suffices to match G for all locations, but this is unfortunately not the case for $\tau_p - \tau_r$ and D_c as discussed above.

The single tunable parameter in our models is A^*, and we first examined the sub-Rayleigh case ($v_r = 0.8c_s$) with an eye on numerical resolution. Choosing $A^* = 7.00$ places a minimum of $(\Delta\sigma^*/A^*)/h^* \approx 7$ grid points within the cohesive zone; this number increases as the rupture expands (see Fig. 6.2 for an example of our resolution). By gathering data from ruptures with various A^* at the two supershear values of v_r, we identified the model parameters listed in Table 6.2.

We further need to explore how the particular choice of A (and hence $\tau_p - \tau_r$ and D_c) influences field amplitudes. There is considerable uncertaintly in the appropriate values of $\tau_p - \tau_r$ and D_c. From the perspective of seismic inversions, here are two primary reasons for this. First, slip inversions are limited in bandwidth, and *Guatteri and Spudich* [2000] and *Spudich and Guatteri* [2004] have shown that a strong trade-off exists between strength drop and slip-weakening distance for sub-Rayleigh ruptures. Second, *Dunham and Archuleta* [2005] have pointed out that, at least for two-dimensional steady-state ruptures,

v_r/c_s	S	A^*	G^*	D_c^*	$\Delta\sigma$ (MPa)	A (MPa/km)	R (km)	D_c (m)
0.8	2.03	7.00	3.19	2.10	3.00	2.10	4.33	2.10
1.3	1.28	2.71	1.80	1.58	3.99	1.08	8.43	2.10
1.6	0.53	3.72	0.82	1.06	5.92	1.93	4.72	2.09

Table 6.2: Model parameters, reported as both non-dimensional values and when dimensionalized in the case that $\Delta\sigma = 3$ MPa for $v_r = 0.8c_s$ (see Table 6.1 and text for further discussion of the dimensionalization method). The dimensional values of G and $\tau_p - \tau_r$ are $9.57\ \mathrm{MJ/m^2}$ and $9.09\ \mathrm{MPa}$ respectively. Note that G, $\tau_p - \tau_r$, D_c, and S increase with propagation distance in our model; the values reported here are measured at $x = 8W$ in the 2D geometry.

the wavefield of sub-Rayleigh ruptures consists entirely of evanescent waves. This implies that a given frequency component of the wavefield decays exponentially with distance from the fault over a scale that is inversely proportional to the frequency. This also occurs for the dilatational component of fields from supershear ruptures. In contrast to this, the frequency content of the shear component of the wavefield (appearing as the Mach waves) is preserved with increasing distance from the fault. To explore this issue in the context of our three-dimensional rupture model, we conduct an additional two runs for $v_r = 1.6c_s$, increasing A first by a factor of two and then by a factor of four.

6.4 Results

We proceed by propagating ruptures using the model parameters listed in Table 6.2 for both the 2D and 3D geometries. Prior to examining the off-fault fields, it is appropriate to examine the pattern of wavefronts generated by a bilaterally expanding supershear rupture that stops (discussed here in the 2D context, although a similar pattern appears in 3D as well). Only a certain region—a trapezoid on each side of the fault for each Mach front—

experiences the passage of the Mach waves (Fig. 6.3), and it is within this region that the largest amplitudes are expected. In the 2D case, after the rupture has stopped, amplitudes at the planar edge of the Mach wave remain undiminished as it radiates from the fault.

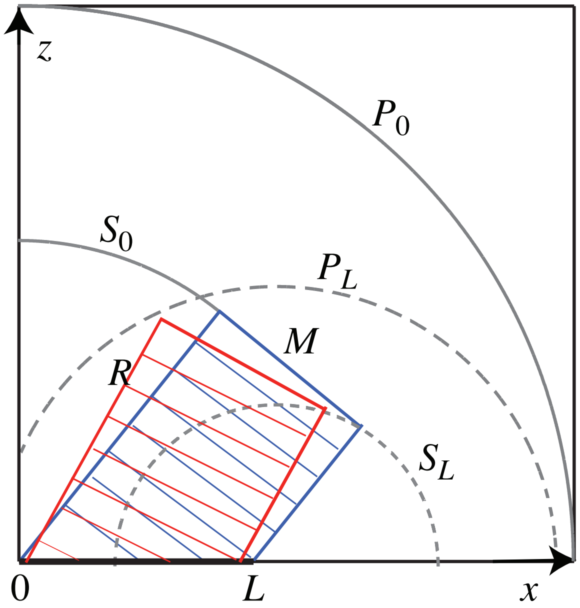

Figure 6.3: Wavefronts from a bilaterially expanding supershear rupture (in 2D) that stops after propagating a distance L. The starting phases are marked as P_0 and S_0, the stopping phases as P_L and S_L, and the Mach front as M. Points within the hatched blue trapezoid (marked by M) have experienced the passage of the shear Mach wave. The points in the hatched red trapezoid (marked by R) have experienced the passage of the Rayleigh Mach wave. A number of other wavefronts—such as head waves, Rayleigh waves, and Rayleigh-wave diffractions—are not shown.

Fig. 6.4 show snapshots of particle velocities from our 3D ruptures. The wavefronts illustrated in Fig. 6.3 are clearly seen. As previous studies have revealed, the dominant component of motion changes from the fault-normal to the fault-parallel direction as the rupture exceeds the S-wave speed [*Aagaard and Heaton*, 2004; *Dunham and Archuleta*, 2005]. The two-sided fault-normal pulse dominates the ground motion from sub-Rayleigh ruptures, but the largest amplitudes are concentrated within a distance $\sim W$ from the fault.

Large amplitudes are also present in the region beyond the end of the fault; these are carried by S-wave stopping phases. For supershear ruptures, the largest amplitudes, aside from those in the immediate vicinity of the rupture front, occur along the (closely coincident) Rayleigh and shear Mach fronts, which extend from the fault out to a distance determined by how far the rupture has propagated.

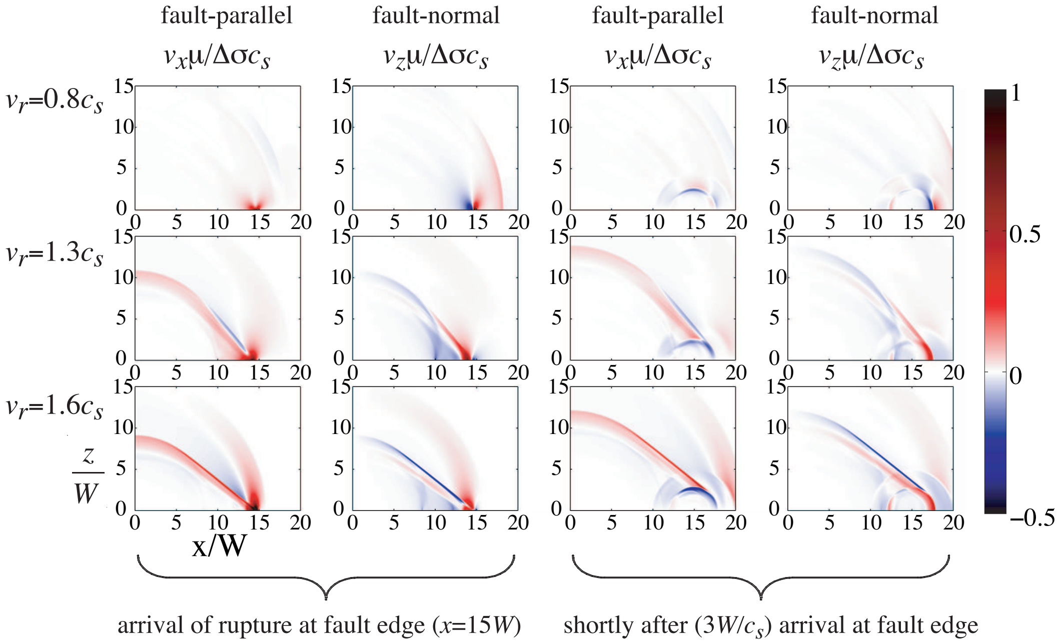

Figure 6.4: Snapshots of the free-surface velocity field for various ruptures speeds at two times: just as the rupture arrives the edge of the fault and at a slightly later time (an additional $3W/c_s$ after the arrival) to emphasize the stopping phases. Ruptures have identical G, $\tau_p - \tau_r$, and D_c but different $\Delta\sigma$. Note that the value of $\Delta\sigma$ used to non-dimensionalize the velocities is different for each rupture speed (see Table 6.1). The color scale is saturated for positive values to emphasize field amplitudes away from the rupture front. The closely coincident shear and Rayleigh Mach fronts can be seen in the fault-normal component since its sign are opposite for the the two fronts.

To further explore the ground motion histories, we plot seismograms at $x = 10W$ for various distances from the fault (Fig. 6.5). The location $x = 10W$ is chosen because the rupture is well-developed at this point (in the sense that the effects of the fault width are established), but the effects of the stopping phases are relatively minor. In addition to the seismograms, we mark the arrival times of the P- and S-wave starting and stopping phases and, for stations within the Mach beam for supershear ruptures, the Mach fronts. For example, the S-wave stopping phase arrives at

$$t = \frac{L}{v_r} + \frac{\sqrt{(L-x)^2 + z^2}}{c_s}. \tag{6.4}$$

Within the Mach beam, the shear Mach front arrives at

$$t = \frac{x + z\sqrt{v_r^2/c_s^2 - 1}}{v_r}. \tag{6.5}$$

and the Rayleigh Mach front arrives at

$$t = \frac{x + z\sqrt{v_r^2/(0.9194c_s)^2 - 1}}{v_r}. \tag{6.6}$$

Using these seismograms as a reference, we are now in a position to determine the influence of the cohesive-zone size on ground-motion amplitudes. To illustrate the main result, we compare velocity seismograms from supershear ruptures with three values of A (Fig. 6.6). As A is increased (corresponding to more rapid weakening with a larger $\tau_p - \tau_r$ and smaller D_c but fixed G), amplitudes at the Mach fronts rise accordingly. This occurs only at the Mach fronts. This is clearly evident when comparing the amplitudes of the dilatational waveform that preceeds the Mach fronts; these amplitudes are completely insensitive to how rapidly the fault weakens. It further follows that the entire wavefield (both dilatational and shear components) of sub-Rayleigh ruptures will be rather insensitive to details of the weakening process at the rupture front. A possible exception to this might occur when the rupture process is highly unsteady. If this is the case, then the wavefield

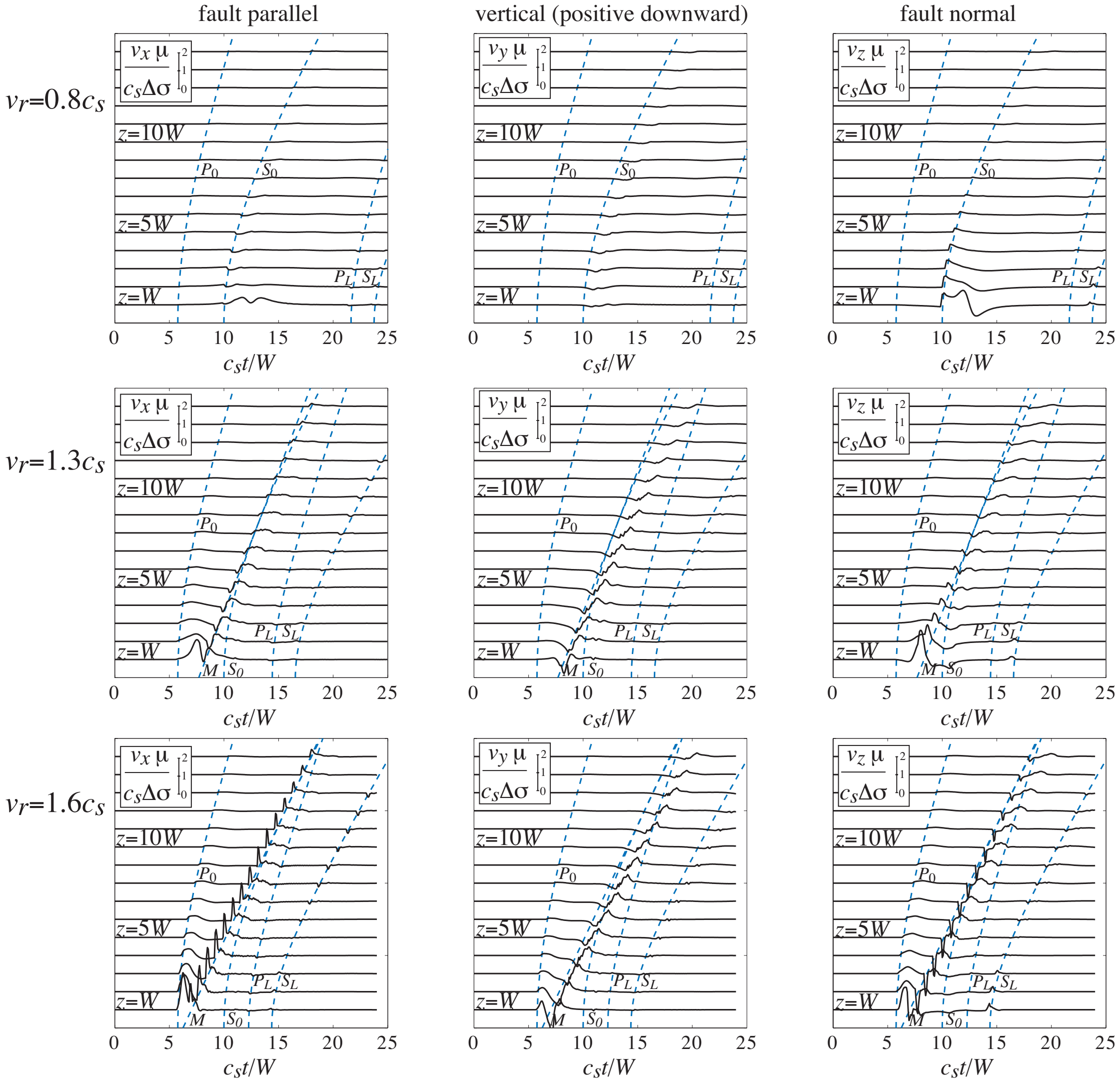

Figure 6.5: Velocity seismograms at $x = 10W$ for various distances from the fault. Major wavefront arrivals are marked. Ruptures have identical G, $\tau_p - \tau_r$, and D_c but different $\Delta\sigma$. Note that the value of $\Delta\sigma$ used to non-dimensionalize the velocities is different for each rupture speed (see Table 6.1).

consists of both evanescent and radiating waves; these radiating waves will transport high-frequency signals away from the fault.

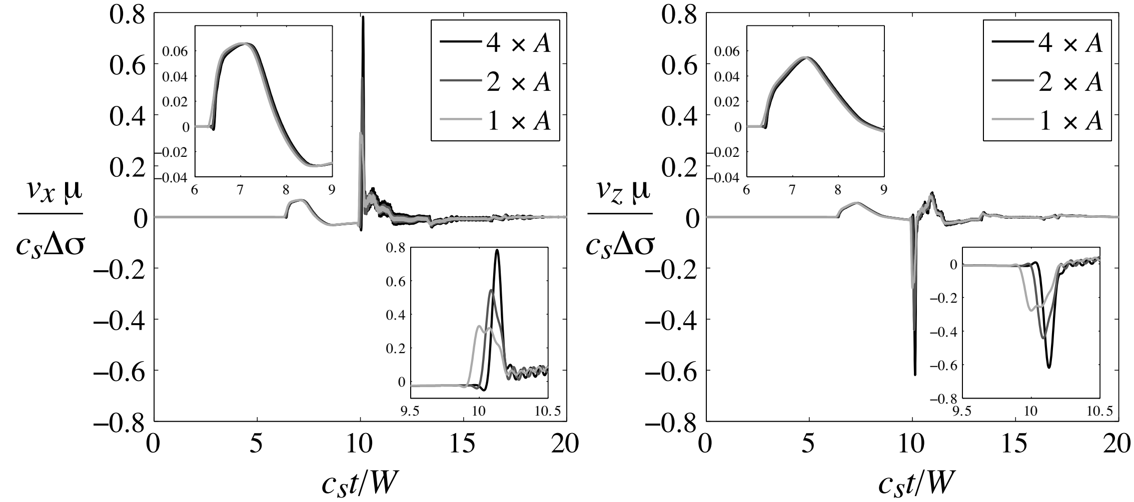

Figure 6.6: Velocity seismograms at $x = 10W$ and $z = 5W$ for a supershear rupture ($v_r = 1.6c_s$) illustrating the effect of decreasing the cohesive-zone size, which is inversely proportional to A, the rate of weakening with distance from the rupture front. The two insets show close-up views of the dilatational waveform, which is insensitive to A, and the Mach fronts, which is highly sensitive to A. Due to low numerical resolution in our simulations we are unable to use realistic values of R, as predicted by *Rice et al.* [2005], and hence unable to separate out the effects of the shear and Rayleigh Mach fronts. A precise definition of A is given in (6.1).

Our next step is to quantify the ground motion in our simulations by plotting the maximum peak-to-peak velocity amplitude experienced at each point on the free surface (Fig. 6.7). In all cases, the largest ground motion occurs in the immediate vicinity of the fault. For sub-Rayleigh ruptures, the region beyond the fault end in the propagation direction also experiences strong shaking; this is carried by the S-wave stopping phase. For supershear ruptures, locations within the Mach beam also experience large amplitudes; this is most evident for $v_r = 1.6c_s$. As discussed above, the peak amplitudes transmitted along the Mach front are quite sensitive to the particular details of the weakening process at the rupture front. As A is increased, the amplitudes within the Mach beam also increase and eventually dominate any peak-to-peak motion generated by stopping phases.

The final step in our analysis is to plot of maximum peak-to-peak amplitudes on the free surface along a line normal to the fault at $x = 10W$ (Fig. 6.8). Amplitudes from the supershear rupture at $v_r = 1.6c_s$ are almost always the largest, except that fault-normal motion close to the fault is largest from sub-Rayleigh ruptures. The contrast between supershear and sub-Rayleigh ruptures is quite prominant at distances exceeding W. The non-monotonic decrease of amplitude with increasing distance that appears for supershear ruptures (e.g., around $x = 2W$ for $v_r = 1.6c_s$ on the fault-parallel component) stems from the fact that close to the fault, peak amplitudes occur not at the Mach front but within the dilatational waveform preceeding it. At a distance of about $2W$, the Mach front, which decays at a more gradual rate than dilatational field components, becomes the carrier of the peak amplitudes. This can be seen by examining the seismograms in Fig. 6.5.

We also show a similar plot for supershear ruptures ($v_r = 1.6c_s$) with larger values of A (corresponding to larger $\tau_p - \tau_r$ and smaller D_c) in Fig. 6.9. As A is increased, the Mach front becomes more concentrated and exhibits larger amplitudes. As discussed previously, fields from sub-Rayleigh ruptures become increasingly insensitive to A away from the fault. This means that larger values of A will result in an increase in peak-to-peak amplitudes far from the fault for supershear rupture (as evidenced by Fig. 6.9). On the other hand, sub-Rayleigh ruptures will have amplitudes only as large as those shown in Fig. 6.8 regardless of the extent of the cohesive zone.

As stated earlier, one objective of this project is to evaluate the validity of using the two-dimensional steady-state slip-pulse model of *Dunham and Archuleta* [2005] and *Bhat*

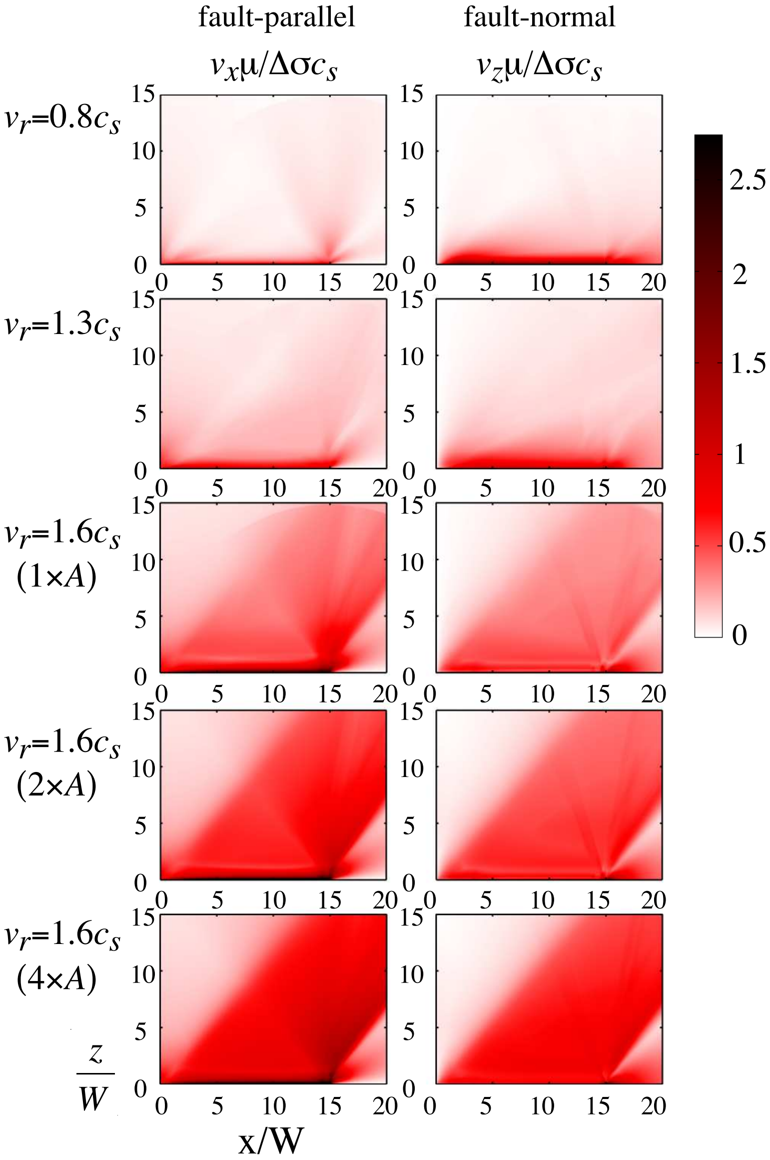

Figure 6.7: Maximum peak-to-peak amplitude of the free-surface velocity field. The top three rows compare ruptures with different speeds; these ruptures have identical G, $\tau_p - \tau_r$, and D_c but different $\Delta\sigma$. The bottom two rows illustrate the effect of increasing the weakening rate, A, at the rupture front. Fracture energy is preserved, so increasing A increases $\tau_p - \tau_r$ and decreases D_c. For a precise definition of A in our model, see equation (6.1). Note that the value of $\Delta\sigma$ used to non-dimensionalize the velocities is different for each rupture speed (see Table 6.1). The color scale covers the entire range of amplitudes for the top three rows, but is saturated for the bottom two rows.

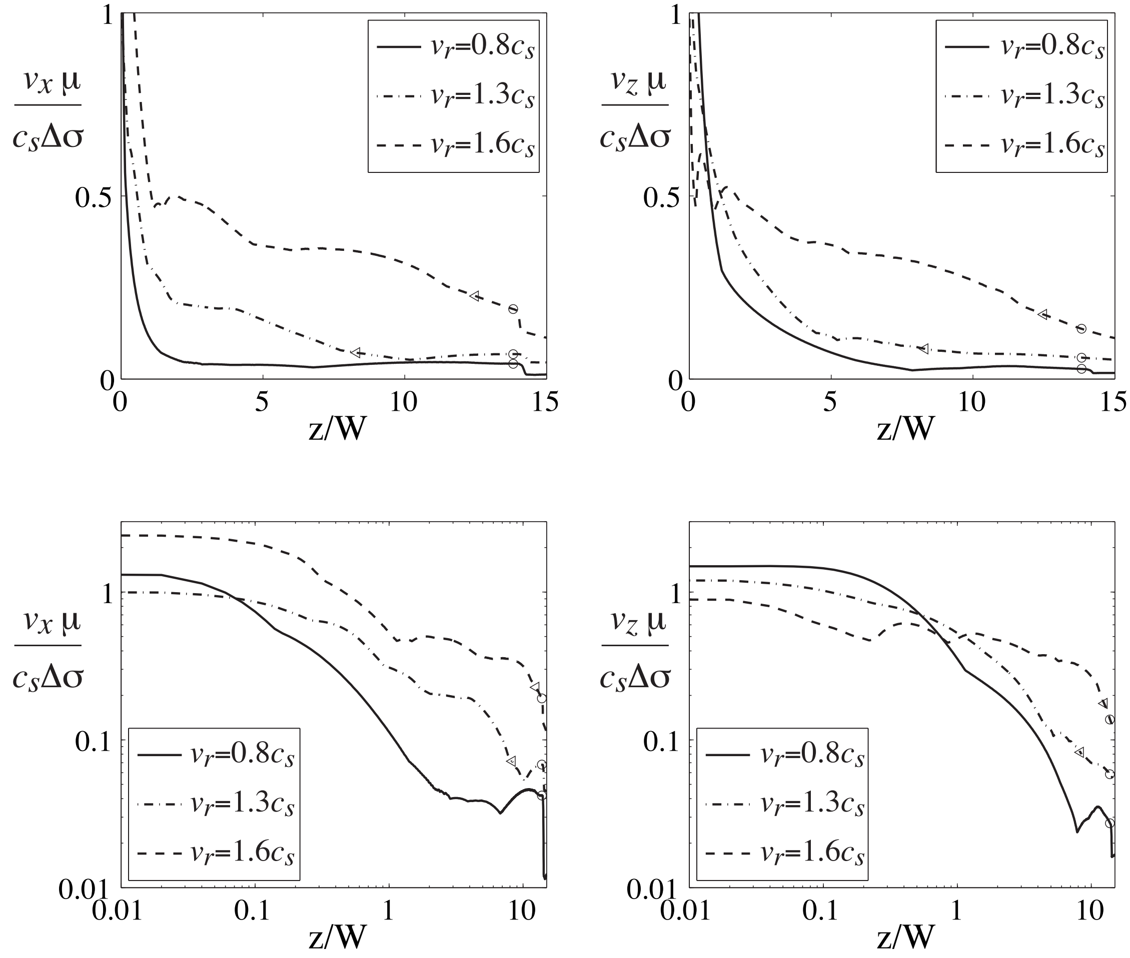

Figure 6.8: Maximum peak-to-peak amplitude of fields at $x = 10W$ as a function of fault-normal distance (shown on both linear and log-log scales). Ruptures have identical G, $\tau_p - \tau_r$, and D_c, but different $\Delta\sigma$. Note that the value of $\Delta\sigma$ used to non-dimensionalize the velocities is different for each rupture speed (see Table 6.1).

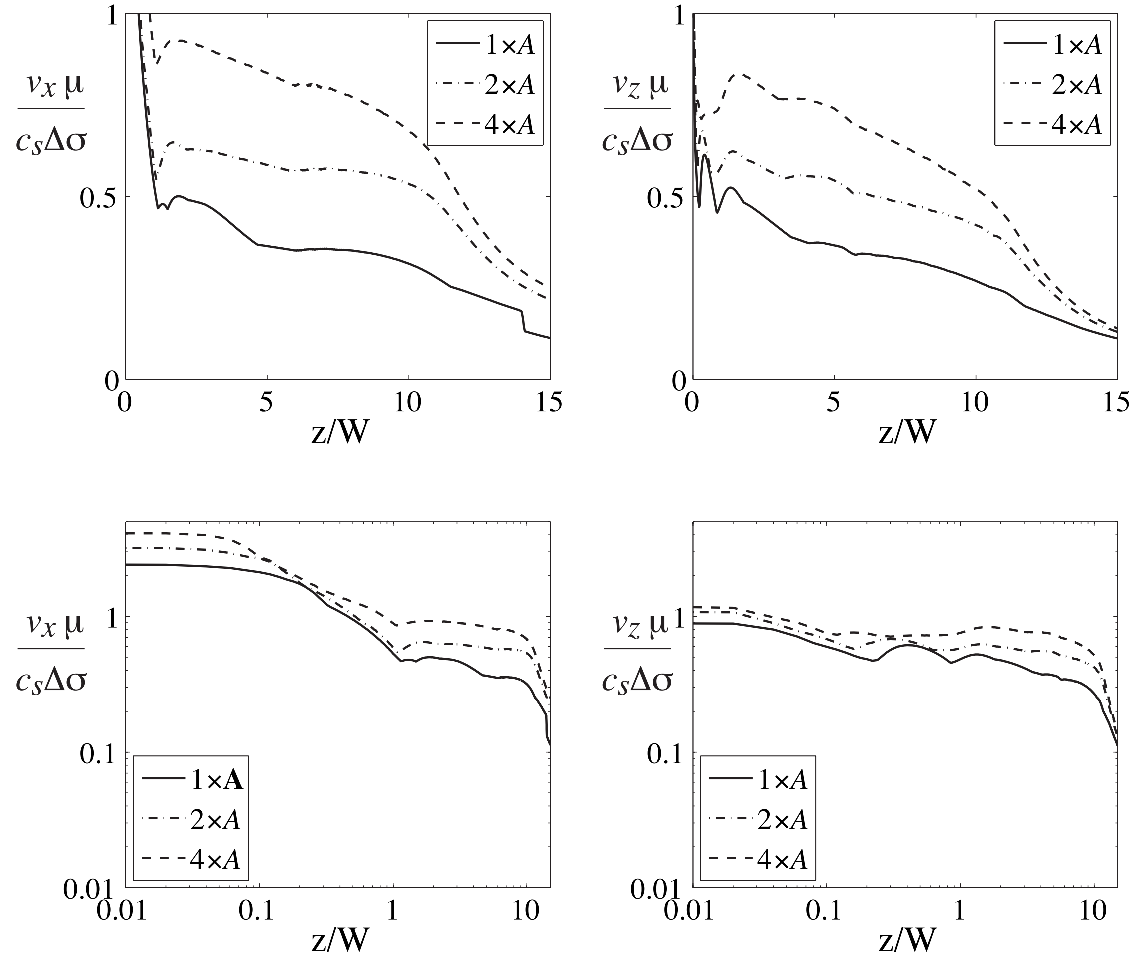

Figure 6.9: Maximum peak-to-peak amplitude of fields from a supershear rupture ($v_r = 1.6c_s$) at $x = 10W$ as a function of fault-normal distance (shown on both linear and log-log scales). The weakening rate at the rupture front, A, is increased by a factor of two and then by a factor of four. Fracture energy is preserved, so increasing A increases $\tau_p - \tau_r$ and decreases D_c. For a precise definition of A in our model, see equation (6.1).

et al. [2007a] to predict fields around propagating ruptures. We consider only the case of $v_r = 1.6c_s$, since we are primarily interested in how rapidly amplitudes at the Mach front decay with distance from the fault (which we expect to be influenced by the finite fault width). The parameters of the slip-pulse model are the rupture speed v_r, the strength drop $\tau_p - \tau_r$, the extent of the cohesive zone, and the length of the slip pulse. We assign these parameters by matching our 3D results at the free surface when the rupture front reaches $x = 10W$. This is shown in Fig. 6.10. Then, by evaluating the expressions given in *Dunham and Archuleta* [2005], we obtain plots of the maximum peak-to-peak amplitudes in the two-dimensional model as a function of distance from the fault; these are compared to our three-dimensional results, calculated not over all time as before, but now from the wavefield present at the time that the rupture front reaches $x = 10W$, in Fig. 6.11. As expected, the two-dimensional model provides an accurate prediction of the fields in the immediate vicinity of the fault. This approximation breaks down at distances much larger than W, where an inverse square-root decay of amplitudes of the shear Mach waves diminishes amplitudes below that in the two-dimensional model, and contributions of the Rayleigh Mach waves exist too.

6.5 Numerical Evidence for Rayleigh Wave Mach Fronts

The most distinctive feature of the 2D supershear slip-pulse models is the shear Mach wave. However, in 3D calculations incorporating a free surface, we should also expect Mach fronts from Rayleigh waves that are generated at the rupture front on the surface. In fact our 3D simulations show rupture propagation as a slip pulse leading to a Mach band that is bounded by Mach fronts from the leading and the trailing edge of the slip pulse.

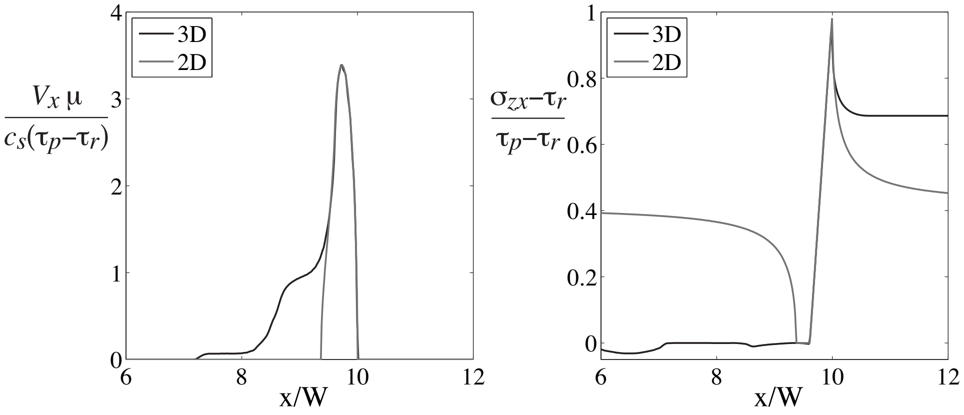

Figure 6.10: Slip velocity and shear stress for a three-dimensional supershear rupture ($v_r = 1.6c_s$) and its approximation by a two-dimensional steady-state slip pulse. Parameters are matched to the solution on the fault at the free surface when the rupture reaches $x = 10W$.

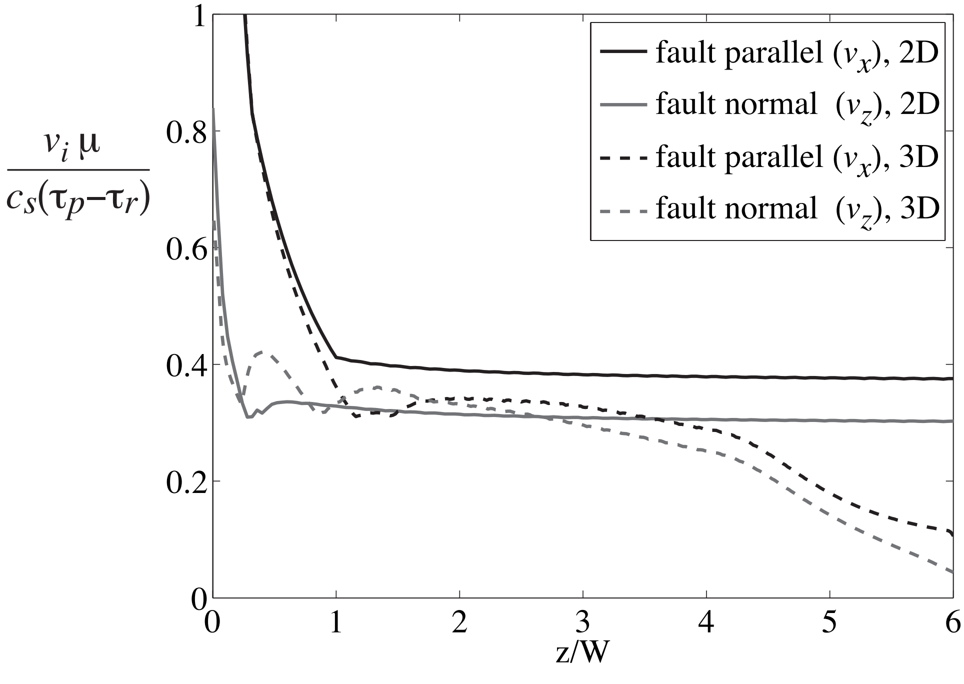

Figure 6.11: Maximum peak-to-peak amplitude of fields at in the medium when the rupture reaches $x = 10W$ as a function of fault-normal distance. The curves labeled "3D" are from our numerical simulations; these are compared with the fields from a two-dimensional steady-state slip-pulse model (labeled "2D").

From each edge of the slip pulse we expect shear and Rayleigh Mach fronts to emanate into the medium. Since the Rayleigh wave speed is less than the S-wave speed of the medium the Mach band should be bounded at the leading edge by the shear Mach front and at the trailing edge by the Rayleigh Mach front.

As a rupture propagates through an elastic half space it would, if constraints of plane strain in the $x - z$ plane were imposed, perturb the out-of-plane stress component, σ_{yy}, near the surface. However, since there is nothing to supply such constraint, stress σ_{yy}, must be zero. This means that the rupture tip near the surface would tend to bulge up the medium, near the crack tip, on the compressional side and similarly bulge down on the extensional side of the fault. However, since the traction free surface boundary condition also has to be satisfied, inevitably, Rayleigh waves have to be generated at the rupture front. As the rupture moves at supershear speeds and since the Rayleigh wave speed is less than the shear wave speed ($c_R = 0.9194c_s$ for a Poisson material) we should also expect the generation and propagation of Mach fronts due to Rayleigh waves.

The difficulty in clearly distinguishing this feature arises from the fact that the Rayleigh wave Mach front orientations is only slightly smaller than the shear wave Mach front orientation. The orientation of the Rayleigh wave Mach front with respect to $-x$ axis (or the half-angle of the Mach cone) is given by $\beta_R = \sin^{-1}(c_R/v_r) = \sin^{-1}(0.9194c_s/v_r)$ (for Poisson material) where c_R is the Rayleigh wave speed of the medium. Similarly the orientation of the shear Mach front is given by $\beta_s = \sin^{-1} c_s/v_r$. For $v_r = 1.6c_s$, $\beta_s - \beta_R \approx 3.6°$. This makes it hard to visually distinguish the two Mach fronts.

To identify the Rayleigh wave Mach front we exploit the fact that it has some characteristic effect on particle velocities and surface stresses. First we separate the dilatational

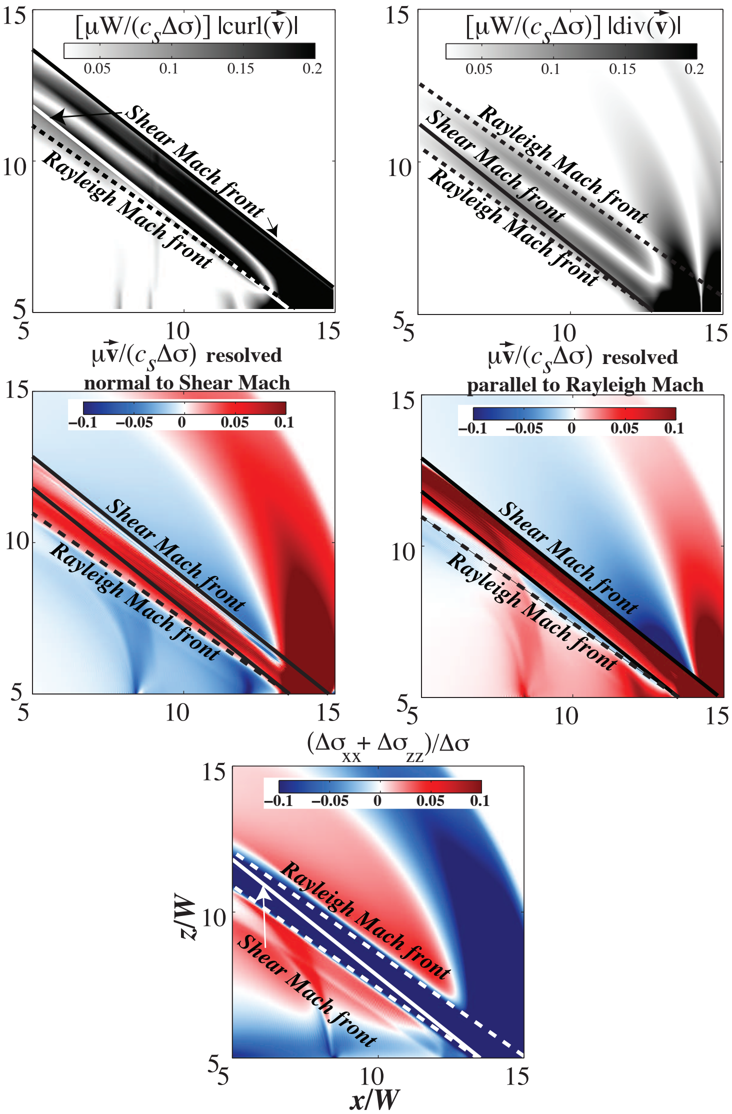

Figure 6.12: Various filtering techniques adopted to separate the Rayleigh wave and S-wave Mach fronts. The solid lines represent shear Mach front and the dashed lines represent Rayleigh Mach front. $\Delta\sigma$, $c_s$andμ are the stress drop, S-wave speed and the shear modulus of the medium respectively. The results above are for earth's surface (i.e. $y = 0W$). We expect $\mathrm{div}(\vec{v})$ to filter out shear wave contributions, $\mathrm{curl}(\vec{v})$ to filter out primary contribution (note that Rayleigh wave is the sum of shear and primary contributions). $\vec{v}$ resolved normal to shear Mach should isolate Rayleigh Mach contribution and $\vec{v}$ resolved parallel to Rayleigh Mach should isolate shear Mach contribution. $\Delta\sigma_{xx} + \Delta\sigma_{zz}$ is zero in the shear Mach band and should be non-zero within Rayleigh Mach band only.

and the rotational component of the fault-parallel and fault-normal velocities. To isolate the dilatational field we take the divergence of the velocity vector. This field should filter out, approximately, the shear component of the velocity (approximately in the sense that shear waves impinging on a free surface may generate P- and Rayleigh waves) and the resulting Mach band should be parallel to the expected orientation of the Rayleigh wave Mach front. We indeed see this feature in Fig. 6.12.

To isolate the rotational component of the velocity field we take its curl and hence approximately filter out the P-wave and some of the Rayleigh wave contributions. The resulting Mach band then shows up parallel to the shear Mach front orientation Fig. 6.12.

Secondly, the direction of motion of surface velocity vector contributed within the shear Mach front should be parallel to it while the same within the Rayleigh Mach front should be perpendicular to it. Thus the component of velocity parallel to the Rayleigh Mach front should isolate S-wave related motion within the shear Mach band. Similarly the component of velocity normal to the shear Mach front should isolate Rayleigh wave related motion within the Mach band. Fig. 6.12 shows this filtering effect quite clearly. In general we notice that the Rayleigh Mach front effect dominates the trailing edge of the Mach band and the shear Mach front effect dominates the leading edge.

A more convincing way to diagnose for the existence of Rayleigh Mach front is to look at various stress components. For a 2D plane strain supershear rupture the dominant field within the Mach front is due to the S-waves. This means that the volumetric part of the stress tensor should vanish within the Mach front. Thus for 2D plane strain supershear ruptures, $\Delta\sigma_{ii} = 0, i = x, y, z$. In 3D, if the only dominant field in the Mach front is due to S-waves then the same condition should be valid within the Mach band. We check for this feature in our 3D results, at the surface ($\Delta\sigma_{yy} = 0$), and we see in Fig. 6.12 that this is not the case. That is $\Delta\sigma_{xx} \neq -\Delta\sigma_{zz}$ within the Mach band. In fact we see large compressive stressing in the Mach band and this is consistent with the expected sense of stressing due to a Rayleigh wave which exerts compressional stresses in both the fault-parallel and fault-normal directions on the compressional side of the fault. Further, the Mach band should be parallel to the Rayleigh Mach fronts which is clearly seen in Fig. 6.12.

We have thus shown that, unlike the 2D supershear slip pulse models of *Dunham and Archuleta* [2005] and *Bhat et al.* [2007a] where the Mach front was solely due to the S-waves, supershear ruptures in a 3D elastic half space also lead to the generation of Mach fronts from Rayleigh waves. We see that this leads to a more complex stress and velocity field within a Mach band. Also, since the Rayleigh waves are not subject to geometrical attenuation, they attenuate a lot slower that the S-waves (and not at all in an ideally elastic medium), significant ground motion and off-fault stressing can be experienced at large distances.

The Rayleigh and shear Mach bands have substantial overlap over the entire range of Fig. 6.12, but they may be an artifact of the the extremely large slip-weakening zones, R, (4.72 km for $v_r = 1.6c_s$ compared to the few tens of meters estimated by *Rice et al.* [2005]) that we had to assume to make our simulations feasible. In fact the fronts may separate over distances away from the rupture front that are much smaller than W. If we assume that $\tilde{R}$ is the part of the slip weakening zone R over which large gradients in the stress and velocity fields are generated then the distance over which the Rayleigh and shear Mach fronts would separate is given by

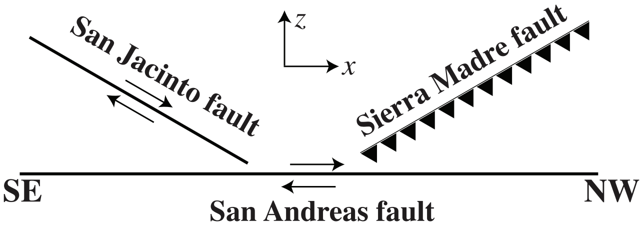

Figure 6.13: Geometry of faults on which Coulomb stress change, ΔCS, is calculated. The right-lateral vertical strike-slip San Jacinto-like and Sierra Madre-like thrust faults strike at $150°$ and $30°$ with respect to the main, San Andreas-like fault, respectively. The Sierra Madre-like fault dips at $30°$. Note that only the fault plane orientations are required to calculate ΔCS; hence, the location and dimensions of the faults are for illustrative purposes only.

$$z_{sep} = \frac{\tilde{R}}{(\cot\beta_R - \cot\beta_s)} \tag{6.7}$$

where $\beta_R = \sin^{-1}(0.9194c_s/v_r)$ and $\beta_s = \sin^{-1}(c_s/v_r)$. $z_{sep} = 5.7\tilde{R}$ for $v_r = 1.6c_s$.

6.6 Off-fault Stressing and Activation of Secondary Faults by Supershear Ruptures

We next turn our attention to the off-fault stress fields, in particular to explore the hypothesis that the large stresses carried by the Mach waves (both shear Mach and Rayleigh Mach) of supershear ruptures could activate secondary faulting on nearby faults. To characterize the stress field, we look at Coulomb stress changes, ΔCS, on pre-existing fault structures of a given orientation (Fig. 6.13). These are surely affected by our large slip-weakening zone sizes, which cause the high-stress shear and Rayleigh Mach fronts to remain overlapped in the regions contoured (they do not seem to have reinforcing effects on

Coulomb stress in general, but rather to have somewhat opposing effects). We specifically focus on two fault orientations, motivated by potential rupture of the southern San Andreas fault. The first is a thrust fault with a dip of 30° that strikes at 30° with respect to the main fault, which provides a rough approximation to thrust features like the Sierra Madre fault north of the Los Angeles basin. The second is a vertical strike-slip fault that also strikes at 150° with respect to the main fault. This orientation is based on the San Jacinto fault, and like the main fault is right-lateral. Note that we do not specify any spatial dimensions of the faults as we are only interested in resolving shear and normal stresses onto structures of a particular orientation.

6.6.1 Coulomb Stress on a fault plane of known orientation

Consider a fault plane Σ lying in a 3D space (Fig. C.1). Let **x, y** and **z** form a right-handed co-ordinate system where the surface of the earth is in the **x-z** plane and the **y** axis points vertically downwards from the earth's surface. The strike direction, $\vec{s}$, is chosen along the surface trace of the fault plane such that the dip, defined below, is $\leq 90^0$. Let $\vec{s}$ make an angle of ϕ with the **x** axis (measured positive for left-handed rotation about **y**) and let γ be the dip of the faulting plane, measured positive for right-handed rotation about the strike direction (i. e., angle from earth's surface at right of the strike direction to the fault plane). The positive strike direction is always chosen such that $0 < \gamma \leq 90^0$. Let Σ^+ and Σ^- to be the positive and the negative side of the fault plane respectively (Fig. C.1a); Σ^- is the footwall (or is assigned arbitrarily if $\gamma = 90^0$).

Let $\vec{n}$ be the unit normal to the fault plane directed from Σ^- to Σ^+. This will imply that any traction calculated with respect to this vector represents the action on the Σ^- plane due

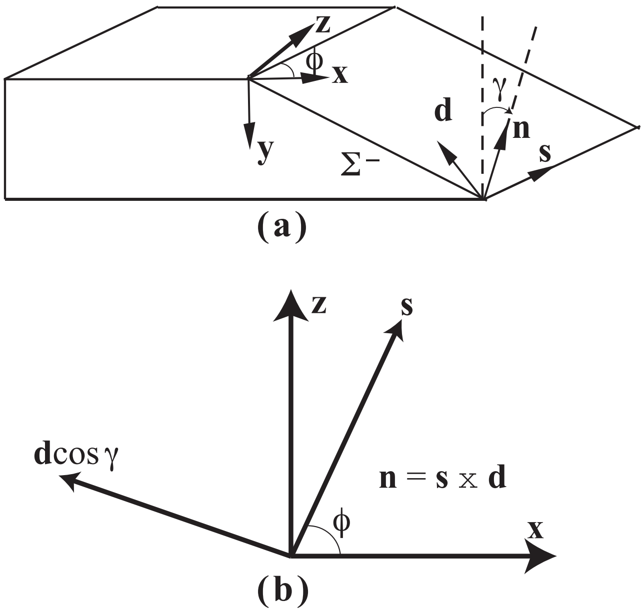

Figure 6.14: a) Σ^- side of the fault plane, taken as the footwall for the dipping fault, and chosen arbitrarily if the fault is vertical. ϕ is the angle measured from the **x**-axis to the surface trace of the fault corresponding with strike direction $\vec{s}$, counter-clockwise about **y**. γ is the angle from the **x-z** plane, at the right of the strike direction, to the fault plane. **s, d** and **n** are the strike, updip and outward normal vectors respectively to the Σ^- surface. b) Projections of **s** and **d** on the **(x-z)** plane.

to the Σ^+ plane.

Looking at Fig. C.1b the component of $\vec{d}$ on the **x-z** plane is then $\vec{d}\cos\gamma$. Since this component is perpendicular to $\vec{s}$, the strike vector, the projections of $\vec{d}$ on the **x** and **z** axes are $-\sin\phi\cos\gamma$ and $\cos\phi\cos\gamma$ respectively. Thus

$$\vec{d} = (-\sin\phi\cos\gamma)\hat{i} + (-\sin\gamma)\hat{j} + (\cos\phi\cos\gamma)\hat{k} \tag{6.8}$$

The unit vector acting along the strike direction is then given by [Fig. C.1b]

$$\vec{s} = (\cos\phi)\hat{i} + (0)\hat{j} + (\sin\phi)\hat{k} \tag{6.9}$$

Then the vector acting along the updip direction is simply given by $\vec{n} = \vec{s} \times \vec{d}$ which is

$$\vec{n} = (\sin\phi \sin\gamma)\hat{i} + (-\cos\gamma)\hat{j} + (-\cos\phi \sin\gamma)\hat{k} \tag{6.10}$$

The traction acting on the fault plane is then given by $T_i = \sigma_{ji} n_j$ where σ_{ij} are the components of the stress tensor (tensile positive) in the original **x-y-z** coordinate system. The normal stress on the fault plane is then given by $\sigma_n = T_i n_i$.

Define rake angle (λ) as the angle between the unit slip vector, $\vec{\xi}$, (slip vector $\Delta\vec{u}$ is defined = $\vec{u}^+ - \vec{u}^-$ where $\vec{u}$ is the displacement vector and $\vec{\xi} = \Delta\vec{u}/|\Delta\vec{u}|$) and $\vec{s}$, measured positive from the strike direction to that of $\vec{\xi}$ for counterclockwise rotation about the $\vec{n}$ direction. In terms of the rake angle (λ) the unit slip vector $\vec{\xi}$ is given by

$$\vec{\xi} = \vec{s}\cos\lambda + \vec{d}\sin\lambda \tag{6.11}$$

It is then clear that a rake angle of 0 or π would result in pure left or right-lateral faulting respectively and a rake angle of $-\pi/2$ or $\pi/2$ would result in pure normal or thrust faulting respectively.

The shear stress in the slip direction is now given by $\tau = \sigma_{ij}\xi_i n_j$ and the normal stress acting on the fault plane is given by $\sigma_n = \sigma_{ij} n_i n_j$ where σ_{ij} are the components of the stress tensor. τ is positive when slip occurs in the direction of the unit slip vector. That direction is surface parallel for strike-slip faults and in the direction of the dip for dip-slip faults. σ_n is positive when the fault is unclamped.

The Coulomb stress, CS, is then given by $CS = \tau + f_s\sigma_n$ where f_s is the static co-efficient of friction. We emphasize that this is the CS component associated with an assumed slip direction, $\vec{\xi}$.

6.6.2 Coulomb stress changes on San Jacinto and Sierra Madre-like faults due to supershear ruptures

Figs. 6.15 and 6.16 show snapshots from our 3D simulations of ΔCS, evaluated at the surface ($y = 0W$) at two times: just as the rupture arrives the edge of the fault and at a slightly later time (an additional $3W/c_s$ after the arrival) to emphasize the stopping phases. Stress fields are evaluated at every point on the free surface, and only the regions of positive Coulomb stress change ($\Delta CS > 0$) are shown. It is well to note that the figures would likely look notably different if calculations could be done with small enough slip-weakening zone size that the shear and the Rayleigh Mach fronts did not overlap so substantially as in the present work.

We evaluate the temporal evolution of Coulomb stress change, akin to the synthetic seismogram plots in Fig. 6.5, on the above structures, along a line extending perpendicularly away from the fault at $x = 10W$ and at mid-seismogenic depth ($y = 0.5W$). This is shown in Figs. 6.17 and 6.18. We also calculate the maximum positive Coulomb stress change, ΔCS_{max}, and study how this quantity decreases with distance from the fault in Fig. 6.19.

Since the calculations for Coulomb stress changes in Figs. 6.15 and 6.16 were made at the surface we expect significant contributions to this stress change from the shear and Rayleigh Mach fronts.

While *Bhat et al.* [2007a] have obtained simple expressions for the far-field stress perturbation along a Mach front due to a 2D supershear slip pulse, any comparison of their results with the 3D calculations would be invalid as the dilatational part of the stress field in the Mach front is non-negligible except at distances away from the fault at which the

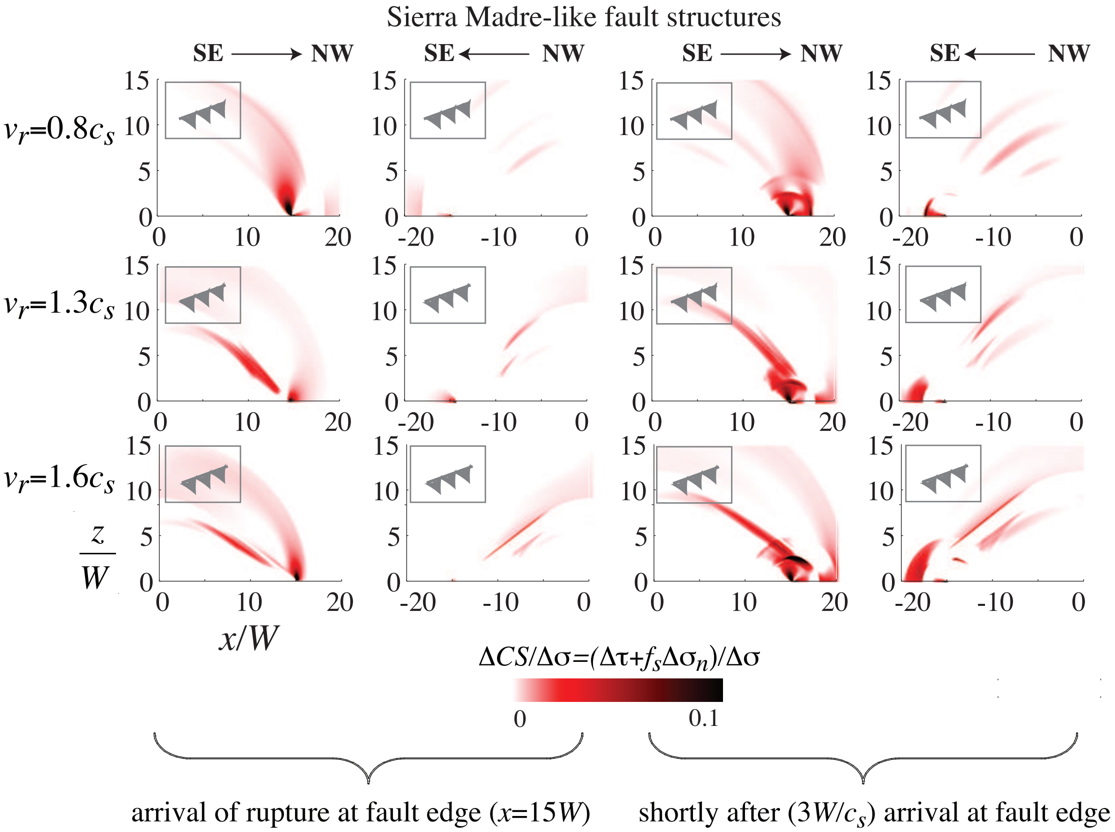

Figure 6.15: Snapshots of Coulomb stress change, ΔCS, on Sierra Madre-like thrust structures for various ruptures speeds at two times: just as the rupture arrives the edge of the fault and at a slightly later time (an additional $3W/c_s$ after the arrival) to emphasize the stopping phases. Ruptures have identical G, $\tau_p - \tau_r$, and D_c but different $\Delta\sigma$. Note that the value of $\Delta\sigma$ used to non-dimensionalize the velocities is different for each rupture speed (see Table 6.1). Contours are evaluated on the earth's surface ($y = 0W$).

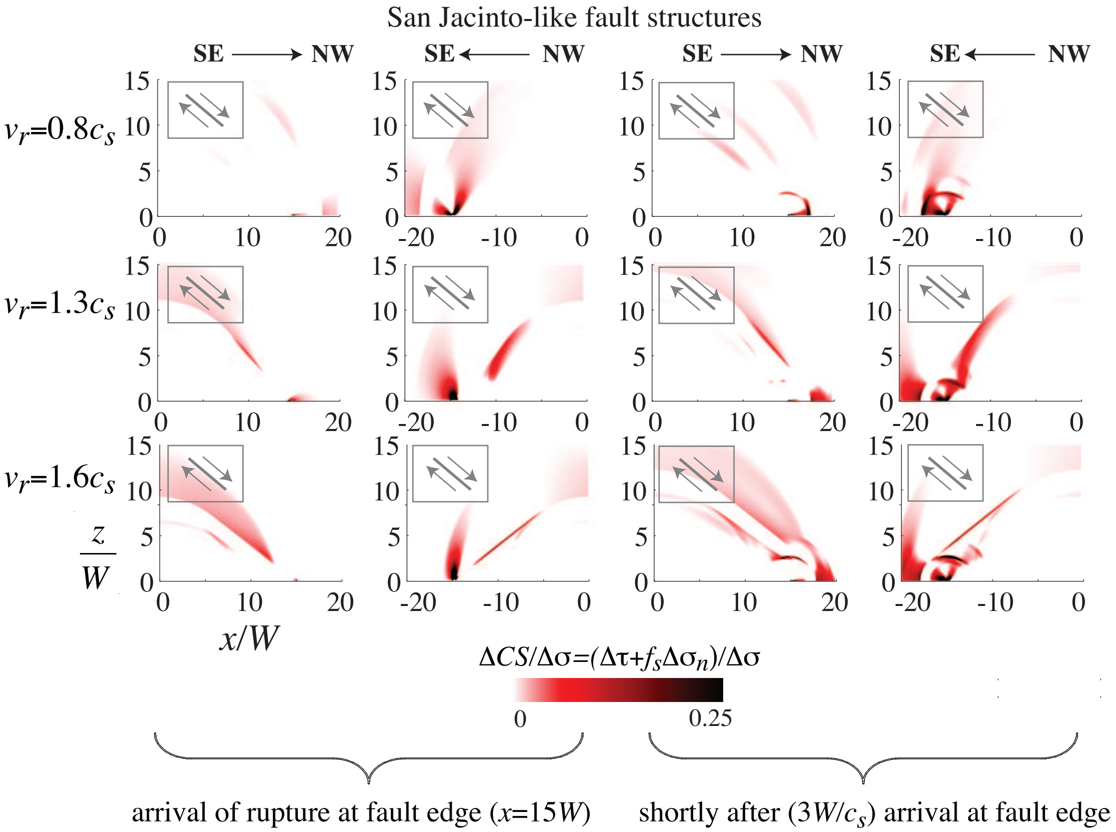

Figure 6.16: Same as Fig. 6.15 but for San Jacinto-like strike-slip structures. Contours are evaluated on the earth's surface ($y = 0W$).

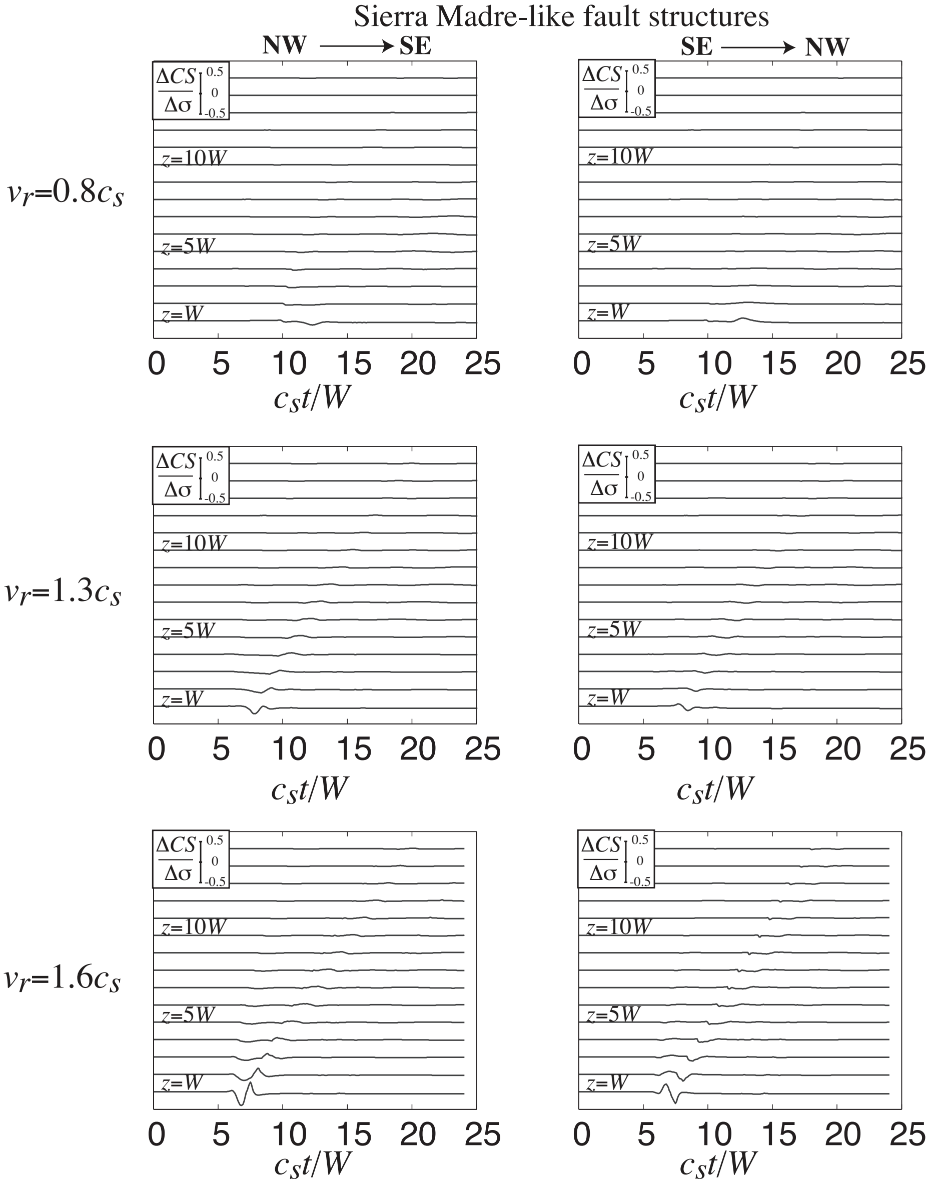

Figure 6.17: Temporal evolution of ΔCS on Sierra Madre-like fault structures at various fault-normal distances at mid-seismogenic depth ($y = 0.5W$).

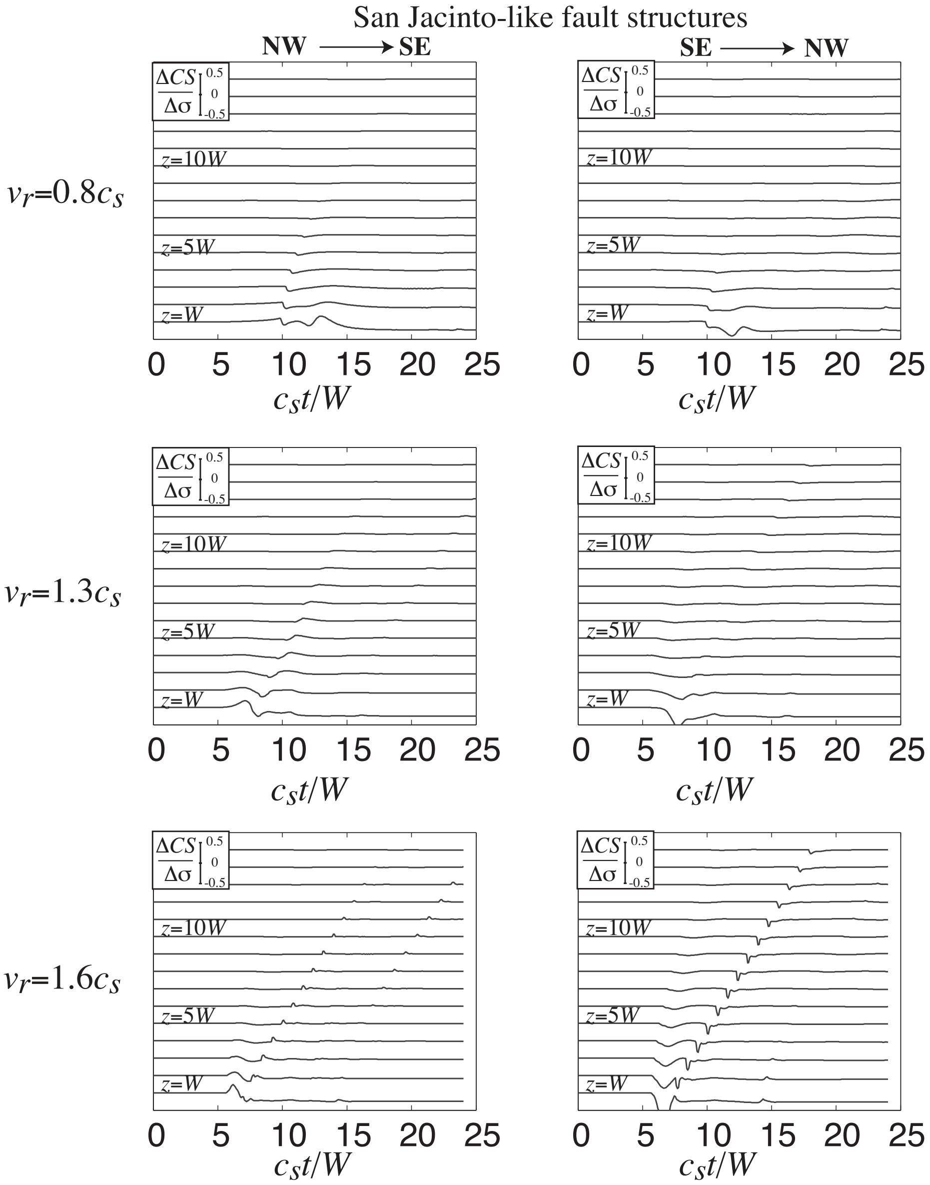

Figure 6.18: Temporal evolution of ΔCS on San Jacinto-like fault structures at various fault-normal distances at mid-seismogenic depth ($y = 0.5W$).

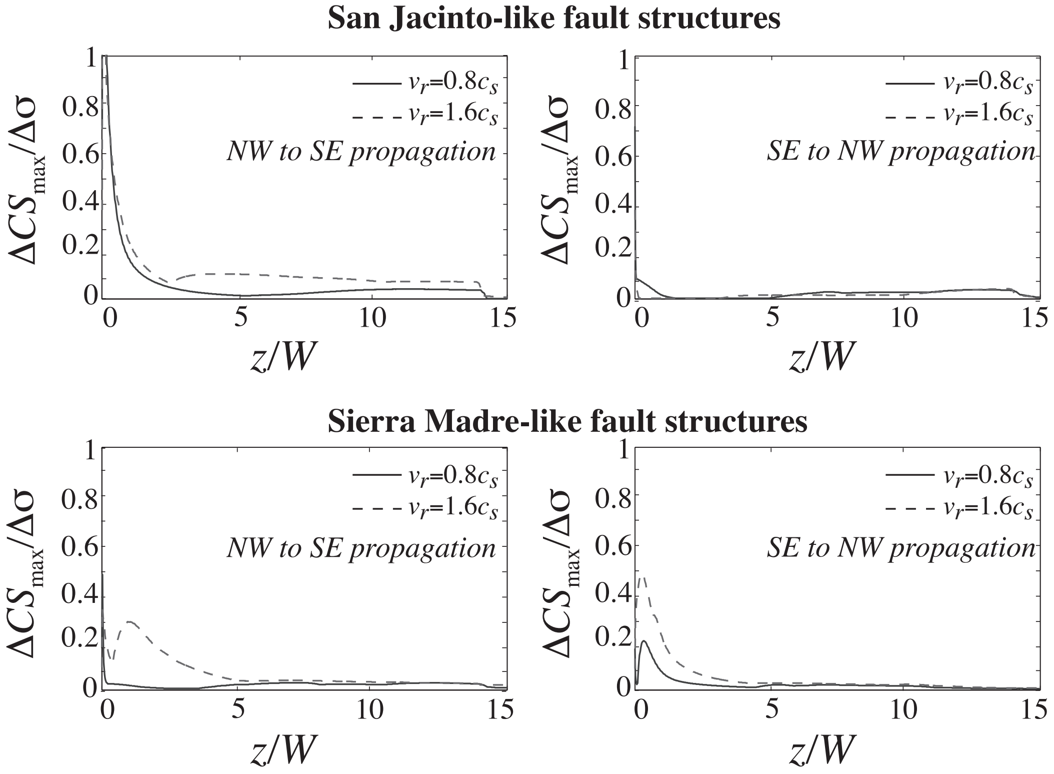

Figure 6.19: Evolution of maximum positive Coulomb stress change $\Delta CS_{\max}$ on San Jacinto-like and Sierra Madre-like fault structures with fault-normal distance. $\Delta CS_{\max}$ is evaluated at $x = 10W$ at mid-seismogenic depth ($y = 0.5W$).

shear and Rayleigh Mach bands are non-overlapping (such distances are probably unrealistically large in our simulations). The vanishing dilatational contribution to the stresses, within the Mach band was an essential ingredient in the 2D approximations.

Fig. 6.15 shows ΔCS for Sierra Madre-like structures due to a rupture propagating at various speeds and opposite directions of propagation on the San Andreas fault. We see that in general these structures are favorably oriented for activation at distances upto $5W$ when the supershear rupture is propagating from SE to NW on San Andreas. The fault structures strike almost perpendicular to the Mach fronts for this direction of propagation. We do see Mach front stressing of Sierra Madre-like structures for NW to SE propagation of supershear rupture on San Andreas, at $v_r = 1.6c_s$, but these stress changes are still smaller compared to a SE to NW propagation direction.

Fig. 6.16 shows ΔCS for San Jacinto-like structures due to a rupture propagating at various speeds and opposite directions of propagation on the San Andreas fault. We see that in general these structures are favorably oriented for activation at distances upto $5W$ when the supershear rupture is now propagating from NW to SE on San Andreas. The fault structures once again strike almost perpendicular to the Mach fronts for this direction of propagation. SE to NW propagation of rupture on the San Andreas fault is highly discouraged for activation of such structures by Mach front stressing.

It is interesting to note that the radiated stress field from stopping a supershear rupture at $v_r = 1.6c_s$ is only slightly larger compared to the stress field from a stopping sub-Rayleigh rupture. This is due to the fact that the rupture is approaching the P-wave speed of the medium ($c_p = \sqrt{3}c_s$), resulting in a significant contribution from the dilatational field (due to a Lorentz-like contraction of the stress fields in the fault parallel direction [and corresponding extension in the fault normal direction) at fault-normal distances up to approximately 2 to $4W$. Furthermore, we see that the amplitude of Coulomb stress changes at the Mach front is generally comparable to the stress changes in the immediate vicinity of the fault from a stopping sub-Rayleigh rupture. For a stress drop of 3 MPa, the Coulomb stress perturbation carried by the Mach front for $v_r = 1.6c_s$ is about 0.1 MPa at a distance of $5W$.

Harris et al. [1991]; *Harris and Day* [1993] and *Fliss et al.* [2005] suggest that such stopping-phase stress fields might activate slip on adjacent, but unconnected, fault segments. However, while the large stress perturbation experienced in the near-fault-end region (for both sub-Rayleigh and supershear ruptures) is a permanent feature (at least until the next earthquake), the Mach-front stress perturbations are transient. The duration of these features can be seen in the Coulomb stress "seismograms" in Figs. 6.17 and 6.18. The typical duration of these features (for the probably too large slip-weakening zone sizes in our simulations) at a distance of $5W$ is $0.5W/c_s$ or about 1.67 seconds for representative values of W and c_s. It is not yet established whether or not such stress perturbations of such short duration (but large amplitude) can nucleate ruptures on secondary faults.

Fig. 6.19 shows the maximum positive Coulomb stress change, $\Delta CS_{\max}$, experienced at locations along a line extending from the fault at $x = 10W$ and $y = 0.5W$. The direction of propagation for sub-Rayleigh ruptures barely changes $\Delta CS_{\max}$ in the far field ($z >> W$) experienced by our two secondary fault orientations. For supershear ruptures, the propagation direction that favors activation of San Jacinto-like and Sierra Madre-like ruptures is clear. A NW to SE supershear rupture moving at on the San Andreas fault transmits stresses along the Mach front out to large distances, $10W$, that might activate San Jacinto-like faults. $\Delta CS_{\max}$ at such a distance is about 0.3 MPa for $\Delta\sigma = 3$ MPa and $v_r = 1.6c_s$. For activation of Sierra Madre-like thrust features, due to Mach front stresses, at distances (up to $3W$) the most favorable direction of propagation of supershear rupture on the San Andreas fault is now from SE to NW. In this case, too, thrust structures at a distance of $3W$ experience $\Delta CS_{\max} \approx 0.3$ MPa for $\Delta\sigma = 3$ MPa and $v_r = 1.6c_s$. Finally, these stress changes from supershear ruptures are sensitive to details of the weakening process at the rupture front, as discussed earlier in the context of the velocity field. The estimates given here should be interpreted as a lower bound, since we are constrained to the most gradual of physically likely weakening rates by numerical constraints. When parameterized by the slip-weakening distance, a reduction of D_c from about 2 m (as used in the calculations shown here) to 0.5 m (with a corresponding increase in the strength drop) would increase amplitudes at the Mach front by a factor of four. Also, the overlapping Mach bands are sometimes partly self-cancelling as regards contributions to ΔCS, a feature that would not be present when they do not overlap.

6.7 Discussion

We have explored the influence of rupture speed on the character and amplitude of ground motion and radiated stresses from ruptures on a finite-width surface-beraking fault in a half-space. This extends our previous work on supershear dynamic ruptures in two dimensions [*Dunham and Archuleta*, 2005; *Bhat et al.*, 2007a]. In those two-dimensional steady-state models, the Mach wave transports velocities and stress comparable to those experienced on the fault out to infinity. Without a source of waves below the bottom edge of the fault, field amplitudes in our three-dimensional model must diminish beyond a distance that scales with the fault width, W. As *Ben-Menahem and Singh* [1987] pointed out, the decay rate will be governed by the geometrical spreading of the Mach cone, causing shear wave amplitudes to decrease with the inverse square-root of distance from the fault. The same consideration suggest no attenuation of Rayleigh waves.

We have not modeled two important factors that will influence field amplitudes: incoherence of the rupture process, and scattering and attenuation along the path of radiating waves. The former has been examined by *Bernard and Baumont* [2005] in the context of rupture-front curvature. At distances much closer than W, an extra factor proportional the inverse square-root of distance to the fault must be added. *Ben-Menahem and Singh* [1987] accounted for attenuation in the form of a constant quality factor in their study of propagating supershear point dislocations, finding the precise manner in which attenuation bounds otherwise infinite accelerations (from their delta-function source time function).

Unlike the 2D supershear slip pulse models of *Dunham and Archuleta* [2005] and *Bhat et al.* [2007a] where the Mach front was solely due to the S-waves, supershear ruptures in 3D elastic half space also lead to the generation of Mach fronts from Rayleigh waves. This leads to a more complex stress and velocity field within a Mach band. Also, since the Rayleigh waves attenuate a lot slower that the S-waves we see significant ground motion and off-fault stressing at large distances.

As our two-dimensional models suggested, there are significant differences between the radiated wavefields of sub-Rayleigh and supershear ruptures. Off-fault fields not in the immediate vicinity of the fault are only sensitive to details of the weakening process at the rupture front within the Mach beams of supershear ruptures. Decreasing the extent of the cohesive zone while simultaneously increasing the strength drop (e.g. to hold fracture energy fixed) increases the amplitudes of the Mach waves and makes their region of non-overlap move closer to the fault. In general, we find larger amplitudes of velocities and stresses far from faults for supershear ruptures that for sub-Rayleigh ruptures. For $W = 10$ km, a stress drop of 3 MPa, and a slip-weakening distance of about 2 m, peak velocities of 0.1 m/s are expected at 10 km. Coulomb stress changes (on favorably oriented faults) at these distances are about 0.3 MPa. Both velocity and stress amplitudes scale linearly with stress drop and, quite importantly, depend also on the extent of the cohesive zone. The estimates given above lie at the least conservative end of physically likely values, since much smaller slip-weakening distances, corresponding to higher velocities and stresses, have been suggested from a combination of laboratory constraints and seismic observations. When decreasing the cohesive-zone size by a factor of two and four, the peak velocities and stresses at the Mach front are increased by approximately the same factor.

Our results raise the possibility that stresses from a supershear rupture might initiate slip on faults adjacent to the one hosting the supershear rupture. As a hypothetical example, we consider what might occur if the southern San Andreas fault fails at supershear speeds. Activation of San Jacinto-like structures is favored if the rupture propagates from the NW to SE direction while Sierra Madre-like structures are activated if the rupture propagates from SE to NW. Our least conservative, but computationally most feasible, parameter choice involves overlap of the two Mach bands at all distances shown, a condition which usually leads to some partial cancellation of Coulomb stress changes that would not be present for more conservative choices when the bands do not overlap except quite near the fault.

Chapter 7

Conclusion

As discussed in the introduction the role of fault geometric complexity in dynamic earthquake rupture propagation and off-fault damage is very pertinent one both from a fundamental and practical aspects. Some of these issues that are still not fully resolved in earthquake source physics are

1. How do earthquakes navigate through a geometrically complex fault system?
2. How do earthquakes stop and what determines the size of an earthquake or how do faults host earthquakes of various rupture lengths?
3. What are the sources of complexities in the stress and strength distribution on the fault?
4. What is the extent and distribution of off-fault damage due to an earthquake rupture and does it strongly depend on the rupture speed?
5. Are supershear ruptures more harmful from a seismic hazard point of view since they manifest homogeneous shear wave Mach fronts (and newly identified Rayleigh wave Mach fronts)?

We address each of the above questions in this work. We first address the question of dynamic rupture propagation through a branched fault system. The theory of fault branching developed by *Poliakov et al.* [2002] and *Kame et al.* [2003] was tested on the recent Denali fault earthquake using the numerical method developed by *Kame et al.* [2003]. In brief, their results showed that a shallow branching angle ($\varphi = \pm 15^o$) and a pre-stress state conducive for branching ($\Psi = 13^o$ for $\varphi = 15^o$ and $\Psi = 56^o, 70^o$ for $\varphi = -15^o$) resulted in rupture termination on the main fault for all rupture velocities, when approaching the branch junction, except high valued ones ($v_r = 0.90c_s$) because of reduced interaction between the main and the branched faults. However, when the orientation of the principal maximum compressive stress, Ψ, approached its extremum, $\Psi = 0^o$ or 90^o, even the high rupture velocity cases led to exclusive branching.

We numerically simulated the observed slip transfer from the Denali to Totschunda faults by the methodology of *Kame et al.* [2003] which uses a 2D elastodynamic boundary integral equation model of mode II rupture with self-chosen path along a branched fault system. The strength of the faults was assumed to follow a Coulomb law with a friction coefficient that slip-weakens from its static to dynamic value. All but one of our simulations for incoming sub-Rayleigh rupture velocities predict that the rupture path will branch off along the Totschunda fault without continuation along the Denali fault. The exception is the case when the prestress inclination is 70^o, a lower limit to the plausible range, and incoming rupture speed at the branching point is $0.90c_s$. In this case rupture follows the branch but there is also a continuation of rupture along the Denali fault beyond the branching location, at a lower speed than that along the Totschunda fault. However when the prestress inclination is steeper, at 80^o, the rupture chooses Totschunda exclusively when its velocity near the branching location is around $0.90c_s$. We also see exclusive continuation of rupture on the Totschunda fault when the rupture is supershear, $1.40c_s$. We thus add one more field case, to the five other discussed in *Kame et al.* [2003] showing that a relatively simple 2D theory of fault branching developed by *Poliakov et al.* [2002] and *Kame et al.* [2003] sufficiently explains/predicts the general direction of rupture propagation.

The above theory of fault branching focussed on the role of pre-stress state, rupture velocity at the branching junction, and the branch angle in controlling rupture path selection on branched fault systems, without terminating the rupture on the branch (referred here as "infinite" branches). We extend this theory to incorporate the role of fault branch lengths in dynamic rupture propagation on a main fault. We studied the cases by *Kame et al.* [2003] and *Bhat et al.* [2004] where branching was observed and terminated rupture on the branched fault at various distances from the branching junction. A dynamically propagating rupture when stopped radiates stress perturbations as it tries to establish a static stress field. The zone of influence of this static-like field depends on many parameters including the length of the rupture. *Harris and Day* [1993]; *Harris et al.* [2002] and *Fliss et al.* [2005] have studied the phenomenon of rupture jumping to an adjacent fault due to stoppage on the main fault. In our studies, with finite branched systems, we thus expect some complexity in the rupture propagation process due to the stoppage of rupture on the branch in comparison with the previous studies on "infinite" branches done by *Kame et al.* [2003].

We have noticed that for branches on the compressional side termination of rupture on the same barely affects the rupture on the main fault except for the case when $\Psi = 13^o, v_r = 0.80c_s, \varphi = 30^o$ and $L_{br} = 30R_0$. For the above case we pointed out that a propitious combination of parameters led to the direct interaction between the rupture front on the main fault and the large stress perturbation from the branch end led to the termination of rupture on the main fault. A short or an infinite branch would have allowed for the rupture to continue on the main fault [Figure 3.10].

For branches on the extensional side, while an infinite branch would have allowed continuation of rupture on the main fault for high incoming rupture velocity and shallow branch angle, termination of rupture on the branch led to its continuation on the main fault for and $\Psi = 70^o, L_{br} = 6, 20R_0$. We also showed that, for the above cases, when v_r was reduced to

$0.80c_s$ terminating the rupture on the branch closer to the main fault led to re-nucleation of rupture on the main fault [*Bhat et al.*, 2007b]. We, however, still lack good field examples to validate the results obtained in our numerical simulations.

We also addressed the relation between fault branches left after a large, complex earthquake and rupture directivity in the event. For that we investigated a new dynamic mechanism which leaves behind a feature that looks like a backward fault branch, that is, a branch directed opposite to the primary direction of rupture propagation. The mechanism consists of the stopping of the rupture on one fault strand and jumping to a neighboring strand, by stress radiation to it and nucleation of rupture on it which propagates bilaterally. Rare as such a feature might be, it could mislead observers attempting to understand the directivity of a past complex earthquake, contrary to the simplifications assumed by *Nakata et al.* [1998]. We conclude that it is difficult to judge the directivity of the main event from the pattern of branches it left, and that additional understanding of the structure near the fault junction is needed to reach definitive conclusions [*Fliss et al.*, 2005].

We analyze a field example of a backward fault branch formed during the Landers 1992 earthquake, when rupture propagating along the Kickapoo fault stopped at the end of that strand and then jumped to the Homestead Valley fault, where it developed bilaterally. The southern end (4 km) of the Homestead Valley rupture formed a backward branch, while the main rupture continued NNW. We conclude that what we describe is definitely possible mechanically, that it very plausibly was the rupture mechanism in the Kickapoo to Homestead Valley transition, and that it could act more generally in other large earthquakes, as well as at the northern segements of the 1992 Landers earthquake, which rupture through complex fault systems. This means that caution is needed when relating fault branches of past earthquakes with their directivity. Simple forward branching, even if probably most common, is certainly not the only branching mechanism.

Our work has broadened the mechanical analysis of fault jumping, the basis of which is due to *Harris et al.* [1991], *Harris and Day* [1993] and*Harris and Day* [1999] who numerically analyzed ruptures jumping between parallel faults. Here we analyzed ruptures jumping onto possibly non-parallel faults, and subsequent propagation along gradually curving faults, using the elastodynamic boundary equation (BIE) method with a Coulomb type of slip-weakening. A fully systematic analysis of such jumps has to be left for future work.

A phenomenon revealed in our simulations is how adverse curvature of a fault, like for the southern Homestead Valley fault in this modeling, can slow (and surely, sometimes stop) rupture propagation. By adverse curvature, we mean curvature towards the compressional side of a fault. With such curvature, nonuniform slip like that occurring near the rupture tip induces locally increased normal stress, and assuming as we have here that friction strength is proportional to effective normal compression, that locally increases the resistance to slip-weakening failure compared to that which coud be estimated based on the fault-normal component of the pre-stress field. While the curvature significantly slowed, but did not stop, the rupture propagation in our simulations it is clear that stronger curvature could stop propagation.

To address the issue of the role of supershear ruptures in the generation/re-activation of off-fault damage we studied here the off-fault stressing induced by a 2D steady slip pulse propagating at supershear speeds in a homogeneous isotropic elastic medium with a linear strength degradation boundary condition like in Figure 5.1. This work is an extension of the *Rice et al.* [2005] model which looked at the sub-Rayleigh speed regime.

Because of the supershear nature of the pulse, Mach fronts develop at the two ends of the slip pulse and, because our model is 2D and steady state, the elastic field within this band of Mach fronts does not attenuate with distance leading to a unique feature of the supershear slip pulse. We expect significant effects of the supershear slip pulse to be observed as damage at large distances. *Bernard and Baumont* [2005] also show, in their analytic and numerical model for kinematic ruptures, that the ground acceleration due to a supershear rupture is unusually high at distances of the order of few tens of kilometers, for an assumed rupture depth extent of 17 km. We observe that this feature is consistent with extension-like failure features observed a few kilometers away from the Kunlun fault during the 2001 Kokoxili event, thus lending support to the suggestion that its rupture speed was supershear in that region.

We also evaluated the change in Coulomb stress (ΔCS), in the medium hosting the slip pulse, on optimally oriented structures allowing for out-of-plane failure too. Failure is encouraged ($\Delta CS > 0$) mainly on the extensional side of the fault and increases in extent with increasing rupture velocity (v_r) and decreasing size of the process zone, R, with respect to the slip pulse length, L. Increasing angle of orientation of the maximum in-plane principal compressive stress (Ψ) with the slip pulse results in the switching of the zone of $\Delta CS > 0$ from the compressional to the extensional side of the slip pulse.

We also evaluated the radiated seismic energy and fracture energy due to a supershear slip pulse for a fixed dynamic stress drop (scaled by the strength drop), $(\sigma^0_{yx} - \tau_r)/(\tau_p - \tau_r)$ = 0.3, and showed that the total of radiated and fracture energy decreases monotonically with increasing rupture velocity. Using those results we also showed that the size of the slip-weakining zone decreases monotonically too with increasing rupture velocity in the supershear regime.

To quantify the character and amplitude of radiated ground motion and stresses in a 3D medium we have explored the influence of rupture speed on a finite-width fault. This extends the previous work on supershear dynamic ruptures in 2D [*Dunham and Archuleta*, 2005; *Bhat et al.*, 2007a]. Without a source of waves below the bottom edge of the fault, field amplitudes in our 3D model must diminish at a distance that scales with the fault width, W. For $W = 10$ km, a stress drop of 3 MPa, and a slip-weakening distance of 2.1 m, peak velocities of about 0.3 m/s are expected at 30 km. The (dynamic) stress changes, on faults oriented favorably at these distances are about 0.3 MPa. Both velocity and stress amplitudes scale linearly with stress drop and depend also on the extent of the cohesive zone. The estimates given above are least conservative in that the cohesive zones in our models extend over a few kilometers; much smaller distances have been suggested from a combination of laboratory constraints and seismic observations [*Rice et al.*, 2005]. Our results raise the possibility that stresses from a supershear rupture might initiate slip on faults adjacent to the one hosting the supershear rupture. As a hypothetical example, we consider what might occur if the southern San Andreas fault fails at supershear speeds. While activation of San Jacinto-like structures is favored if the rupture propagates from the NW to SE direction Sierra Madre-like thrust structures get activated when the rupture propagates SE to NW along the San Andreas.

We have also newly identified Mach fronts due to Rayleigh waves propagating from the rupture front of a supershear rupture in a 3D elastic half-space. These Mach fronts manifest from the rupture front to satisfy the plane strain like conditions on the earth's surface. In an ideally elastic material these Mach fronts will not geometrically attenuate with distance from the fault resulting in larger ground motions and stresses than from a pure shear Mach front. However, since our slip-weakening zone size is substantially larger (4.72 km for $v_r = 1.6c_s$ compared to the few tens of meters estimated by *Rice et al.* [2005]) we expect the Rayleigh and shear Mach fronts to overlap over a substantial distance. The resulting overlap will lead to partial cancellation of stresses that would not be present for more conservative choices of model parameters.

Bhat et al. [2007a] have speculated that the distance at which supershear ruptures significantly perturb stresses and particle velocity in the medium should be of the order of the width of the seismogenic zone. We have now shown, in our numerical simulations of supershear ruptures in a 3D elastic half space, that this distance is atleast a few times the width of the seismogenic zone.

Bibliography

Aagaard, B. T., and T. H. Heaton, Near-source ground motions from simulations of sustained intersonic and supersonic fault ruptures, *Bull. Seismol. Soc. Amer.*, *94*, 2064–2078, 2004.

Andrews, D. J., Rupture velocity of plane strain shear cracks, *J. Geophys. Res.*, *81*(B32), 5679–5689, 1976.

Andrews, D. J., Dynamic plane-strain shear rupture with a slip-weakening friction law calculated by a boundary integral method, *Bull. Seismol. Soc. Amer.*, *75*, 1–21, 1985.

Antolik, M., R. E. Abercrombie, and G. Ekstrom, The 14 November 2001 Kokoxili (Kunlunshan), Tibet, earthquake: Rupture transfer through a large extensional step-over, *Bull. Seismol. Soc. Amer.*, *94*, 1173–1194, 2004.

Aochi, H., and E. Fukuyama, Three-dimensional nonplanar simulation of the 1992 Landers earthquake, *J. Geophys. Res.*, *107*(B2), doi:10.1029/2000JB000061, 2002.

Aochi, H., E. Fukuyama, and M. Matsu'ura, Spontaneous rupture propagation on a nonplanar fault in 3D elastic medium, *Pure. Appl. Geophys.*, *157*, 2003–2027, 2000a.

Aochi, H., E. Fukuyama, and M. Matsu'ura, Selectivity of spontaneous rupture propagation on a branched fault, *Geophys. Res. Lett.*, *27*, 3635–3638, 2000b.

Aochi, H., R. Madariaga, and E. Fukuyama, Effect of normal stress during rupture propagation along non-planar faults, *J. Geophys. Res.*, *107*(B2), doi:10.1029/2001JB000500, 2002.

Aochi, H., O. Scotti, and C. Berge-Thierry, Dynamic transfer of rupture across differently oriented segments in a complex 3D fault system, *Geophys. Res. Lett.*, *32*(21), doi:10.1029/2005GL024158, 2005.

Archuleta, R. J., A faulting model for the 1979 Imperial Valley earthquake, *J. Geophys. Res.*, *89*(B6), 4559–4586, 1984.

Aydin, A., and R. A. Schultz, Effect of mechanical interaction on the development of strike-slip faults with echelon patterns, *J. Struct. Geol.*, *12*(1), 123–129, 1990.

Ben-Menahem, A., and S. J. Singh, *Seismic waves and sources*, Springer Verlag, 1981.

Ben-Menahem, A., and S. J. Singh, Supershear accelerations and Mach-waves from a rupturing front:I-Theoretical-model and implications, *J. Phys. Earth*, *35*, 347–365, 1987.

Bernard, P., and D. Baumont, Shear Mach wave characterization for kinematic fault rupture models with constant supershear rupture velocity, *Geophys. J. Int.*, *162*, 431–447, 2005.

Bhat, H. S., R. Dmowska, J. R. Rice, and N. Kame, Testing theory for fault branching: Denali to Totschunda, Alaska, November 3, 2002, *Trans. Am. Geophys. U., EOS*, *83*, 2002.

Bhat, H. S., R. Dmowska, J. R. Rice, and N. Kame, Dynamic slip transfer from the Denali to Totschunda faults, Alaska: Testing theory for fault branching, *Bull. Seismol. Soc. Amer.*, *94*, S202–S213, 2004.

Bhat, H. S., R. Dmowska, G. C. P. King, Y. Klinger, and J. R. Rice, Off-fault damage patterns due to supershear ruptures with application to the 2001 M w 8.1 Kokoxili (Kunlun) Tibet earthquake, *J. Geophys. Res., in press*, 2007a.

Bhat, H. S., M. Olives, R. Dmowska, and J. R. Rice, Role of fault branches in earthquake rupture dynamics, *submitted to J. Geophys. Res.*, 2007b.

Bouchon, M., and D. Streiff, Propagation of a shear crack on a nonplanar fault: A method of calculation, *Bull. Seismol. Soc. Amer.*, *87*(1), 61–66, 1997.

Bouchon, M., and M. Vallee, Observation of long supershear rupture during the magnitude 8.1 Kunlunshan earthquake, *Science*, *301*, 824–826, 2003.

Bouchon, M., N. Toksoz, H. Karabulut, M. P. Bouin, M. Dietrich, M. Aktar, and M. Edie, Seismic imaging of the 1999 Izmit (Turkey) rupture inferred from the near-fault recordings, *Geophys. Res. Lett.*, *27*, 3013–3016, 2000.

Bouchon, M., M. P. Bouin, H. Karabulut, M. N. Toksoz, M. Dietrich, and A. J. Rosakis, How fast is rupture during an earthquake? New insights from the 1999 Turkey earthquakes, *Geophys. Res. Lett.*, *28*, 2723–2726, 2001.

Bouchon, M., M. N. Toksoz, H. Karabulut, M. P. Bouin, M. Dietrich, M. Aktar, and M. Edie, Space and time evolution of rupture and faulting during the 1999 Izmit (Turkey) earthquake, *Bull. Seismol. Soc. Amer.*, *92*, 256–266, 2002.

Brankman, C. M., and A. Aydin, Uplift and contractional deformation along a segmented strike-slip fault system: the Gargano Promontory, southern Italy, *J. Struct. Geol.*, *26*(5), 2004.

Broberg, K. B., On transient sliding motion, *Geophys. J. Roy. Astr. Soc*, *52*, 397–432, 1978.

Broberg, K. B., The near-tip field at high crack velocities, *Int. J. Fract.*, *39*(1), 1–13, 1989.

Broberg, K. B., *Cracks and Fracture*, Academic Press, 1999.

Burridge, R., Admissible speeds for plane-strain self-similar shear cracks with friction but lacking cohesion, *Geophys. J. Roy. Astron. Soc*, *35*, 439–455, 1973.

Burridge, R., G. Conn, and L. B. Freund, Stability Of A Rapid Mode-II Shear Crack With Finite Cohesive Traction, *J. Geophys. Res*, *84*, 2210–2222, 1979.

Cleveland, W. S., Robust locally weighted regression and smoothing scatterplots, *J. Amer. Statist. Assoc.*, *74*(368), 829–836, 1979.

Cochard, A., and R. Madariaga, Dynamic faulting under rate-dependent friction, *Pure. Appl. Geophys.*, *142*, 419–445, 1994.

Dalguer, L. A., and S. Day, Staggered-Grid Split-Node method for spontaneous rupture simulation, *J. Geophys. Res.*, *112, B02302*, doi:10.1029/2006JB004467, 2007.

Das, S., and K. Aki, A numerical study of two-dimensional spontaneous rupture propagation, *Geophys. J. Roy. Astron. Soc*, *50*, 643–668, 1977.

Das, S., and B. V. Kostrov, On the numerical boundary integral equation method for three-dimensional dynamic shear crack problems, *J. Appl. Mech*, *54*(1), 99–104, 1987.

Dmowska, R., J. Rice, and N. Kame, Fault branching and rupture directivity, *Trans. Am. Geophys. U., EOS*, *83(47)*, Abstract NG21B–0939, 2002.

Dreger, D. S., D. D. Oglesby, R. Harris, N. Ratchkovski, and R. Hansen, Kinematic and dynamic rupture models of the November 3, 2002 M_w 7.9 Denali, Alaska, earthquake, *Geophys. Res. Lett.*, *31*, doi:10.1029/2003GL018333, 2004.

Duan, B., and D. D. Oglesby, Multicycle dynamics of nonplanar strike-slip faults, *J. Geophys. Res*, *110*, doi:10.1029/2004JB003298, 2005.

Dunham, E. M., and R. J. Archuleta, Evidence for a supershear transient during the 2002 Denali fault earthquake, *Bull. Seismol. Soc. Amer.*, *94*, S256–S268, 2004.

Dunham, E. M., and R. J. Archuleta, Near-source ground motion from steady state dynamic rupture pulses, *Geophys. Res. Lett.*, *32*, 2005.

Eberhart-Phillips, D., et al., The 2002 Denali fault earthquake, Alaska: A large magnitude, slip-partitioned event, *Science*, *300*, 1113–1118, 2003.

Ellsworth, W. L., M. Celebi, J. R. Evans, E. G. Jensen, D. J. Nyman, and P. Spudich, Processing and modeling of the pump station 10 record from the November 3, 2002, Denali fault, Alaska earthquake, *Proceedings, 11th Intern. Conf. Soil Dynam. Earthq. Eng*, *1*, 471–477, 2004.

Eshelby, J. D., Uniformly moving dislocations, *Proc. Phys. Soc. Lond. A*, *62*, 307–314, 1949.

Eshelby, J. D., The elastic field of a crack extending non-uniformly under general anti-plane loading, *J. Mech. Phys. Solids*, *17*(3), 177–199, 1969.

Estabrook, C. H., and K. H. Jacob, *Stress indicators in Alaska*, chap. Neotectonics of North America, D. B. Slemmons, E. R. Engdahl, M. D. Zoback, and D. D. Blackwell (Editors), Geological Society of America, Boulder, Colorado, Decade Map vol. 1, 387-399, 1991.

Estabrook, C. H., D. B. Stone, and J. N. Davies, Seismotectonics Of northern Alaska, *J. Geophys. Res*, *93*(B10), 12,026–12,040, 1988.

Favreau, P., M. Campillo, and I. R. Ionescu, Initiation of shear instability in three-dimensional elastodynamics, *J. Geophys. Res.*, *107*, 2147–2164, 2002.

Felzer, K. R., and G. C. Beroza, Deep structure of a fault discontinuity, *Geophys. Res. Lett.*, *26*(14), 2121–2124, 1999.

Fliss, S., H. S. Bhat, R. Dmowska, and J. R. Rice, Fault branching and rupture directivity, *J. Geophys. Res.*, *110*, doi:10.1029/2004JB003368, 2005.

Fossum, A. F., and L. B. Freund, Nonuniformly moving shear crack model of a shallow focus earthquake mechanism, *J. Geophys. Res.*, *80*(B23), 3343–3347, 1975.

Freund, L. B., Mechanics of dynamic shear crack-propagation, *J. Geophys. Res*, *84*, 2199–2209, 1979.

Freund, L. B., *Dynamic Fracture Mechanics*, Cambridge University Press, Cambridge, 1990.

Georgiadis, H. G., and G. Lykotrafitis, A method based on the radon transform for three-dimensional elastodynamic problems of moving loads, *J. Elast.*, *65*, 87–129, doi:10.1023/A:1016135605598, 2001.

Guatteri, M., and P. Spudich, What can strong-motion data tell us about slip-weakening fault-friction laws, *Bull. Seismol. Soc. Amer.*, *90*(1), 98–116, doi:10.1785/0119990053, 2000.

Guebelle, P. H., and J. R. Rice, A spectral method for three-dimensional elastodynamic fracture problems, *J. Mech. Phys. Solids*, *43*(11), 1791–1824, 1995.

Hardebeck, J. L., and E. Hauksson, Crustal stress field in southern California and its implications for fault mechanics, *J. Geophys. Res.*, *106*(B10), 21,859–21,882, 2001.

Harris, R. A., and S. M. Day, Dynamics of fault interaction-Parallel strike-slip faults, *J. Geophys. Res.*, *98*(B3), 4461–4472, 1993.

Harris, R. A., and S. M. Day, Dynamic 3D simulations of earthquakes on en echelon faults, *Geophys. Res. Lett.*, *26*(14), 2089–2092, 1999.

Harris, R. A., R. J. Archuleta, and S. M. Day, Fault steps and the dynamic rupture process: 2D numerical simulations of a spontaneously propagating shear fracture, *Geophys. Res. Lett*, *18*(5), 893–896, 1991.

Harris, R. A., J. F. Dolan, R. Hartleb, and S. M. Day, The 1999 Izmit, Turkey, Earthquake: A 3D Dynamic Stress Transfer Model of Intraearthquake Triggering, *Bull. Seismol. Soc. Amer.*, *92*(1), 245–255, 2002.

Hauksson, E., L. M. Jones, and K. Hutton, The 1999 M_w 7.1 Hector Mine, California, earthquake sequence: Complex conjugate strike-slip faulting, *Bull. Seismol. Soc. Amer.*, *92*(4), 1154–1170, 2002.

Heaton, T. H., Evidence for and implications of self-healing pulses of slip in earthquake rupture, *Phys. Earth Planet. Int.*, *64*(1), 1–20, 1990.

Ida, Y., Cohesive force across tip of a longitudinal-shear crack and Griffiths specific surface-energy, *J. Geophys. Res*, *77*, 3796–3805, 1972.

Kame, N., and T. Yamashita, Simulation of the spontaneous growth of a dynamic crack without constraints on the crack tip path, *Geophys. J. Int.*, *139*, 345–358, 1999a.

Kame, N., J. R. Rice, and R. Dmowska, Effects of prestress state and rupture velocity on dynamic fault branching, *J. Geophys. Res.*, *108*(B5), doi:10.1029/2002JB002189, 2003.

Kase, Y., and K. Kuge, Numerical simulation of spontaneous rupture processes on two non-coplanar faults: The effect of geometry on fault interaction, *Geophys. J. Int.*, *135*(3), 911–922, 1998.

Kase, Y., and K. Kuge, Rupture propagation beyond fault discontinuities: Significance of fault strike and location, *Geophys. J. Int.*, *147*(2), 330–342, 2001.

Kikuchi, M., and Y. Yamanaka, *Special Event Page, 2001/11/14 Qinghai Xinjiang Border, China*, wwweic.eri.u-tokyo.ac.jp/topics/ 200111140926, *Earthquake Information Center, ERI, Univ. Tokyo, Japan*, 2001.

Kikuchi, M., and Y. Yamanaka, Source rupture processes of the central Alaska earthquake of Nov. 3, 2002, inferred from teleseismic body waves (the 10/23 M_w 6.7 event), *EIC Seismological Note No. 129, revised 5 November 2002*, 2002.

King, G., Y. Klinger, D. Bowman, and P. Tapponnier, Slip partitioned surface breaks for the 2001 Kokoxili earthquake, China (M_w 7.8), *Bull. Seismol. Soc. Am*, *95*(2), 731–738, 2005.

King, G. C. P., Speculations on the geometry of the initiation and termination processes of earthquake rupture and its relation to morphology and geological structure, *Pure. Appl. Geophys.*, *124*(3), 567–585, 1986.

King, G. C. P., and J. Nabelek, The role of bends in faults in the initiation and termination of earthquake rupture, *Science*, *228*, 984–987, 1985.

Klinger, Y., X. Xu, P. Tapponnier, J. Van der Woerd, C. Lasserre, and G. King, High-resolution satellite imagery mapping of the surface rupture and slip distribution of the $M_w \sim 7.8$, 14 November 2001 Kokoxili earthquake, Kunlun fault, northern Tibet, China, *Bull. Seismol. Soc. Amer.*, *95*(5), 1970–1987, 2005.

Klinger, Y., M. R., and G. C. P. King, Evidence for an earthquake barrier model from Mw $\sim$ 7.8 Kokoxili (Tibet) earthquake slip-distribution, *Earth Planet. Sc. Lett.*, *242*, 354–364, 2006.

Knuepfer, P. L. K., Implications of the characteristics of end-points of historical surface fault ruptures for the nature of fault segmentation, *U. S. Geol. Surv. Open File Rep.*, *89–315*, 193–228, 1989.

Koller, M. G., M. Bonnet, and R. Madariaga, Modelling of dynamical crack propagation using time-domain boundary integral equations, *Wave Motion*, *16*(4), 339–366, 1992.

Kristek, J., P. Moczo, and R. J. Archuleta, Efficient methods to simulate planar free surface in the 3d 4th-order staggered-grid finite-difference schemes, *Stud. Geophys. Geod.*, *46*, 355–381, 2002.

Lansing, D. L., The displacements in an elastic half-space due to a moving concentrated normal load, *Tech. Rep. R-238*, NASA, 1966.

Lapusta, N., and J. R. Rice, Nucleation and early seismic propagation of small and large events in a crustal earthquake model, *J. Geophys. Res*, *108*(B4), doi:10.1029/2001JB000793, 2003.

Lapusta, N., J. R. Rice, Y. Ben-Zion, and G. Zheng, Elastodynamic analysis for slow tectonic loading with spontaneous rupture episodes on faults with rate-and-state-dependent friction, *J. Geophys. Res*, *105*(B10), 23,675–23,789, 2000.

Lasserre, C., G. Peltzer, F. Crampé, Y. Klinger, J. Van der Woerd, and P. Tapponnier, Coseismic deformation of the 2001 M_w= 7.8 Kokoxili earthquake in Tibet, measured by synthetic aperture radar interferometry, *J. Geophys. Res*, *110*(B12), doi:10.1029/2004JB003500, 2005.

Lawn, B. R., and T. R. Wilshaw, *Fracture of Brittle Solids*, Cambridge University Press, New York, 1993.

Li, Y. G., K. Aki, D. Adams, A. Hasemi, and W. H. K. Lee, Seismic guided waves trapped in the fault zone of the Landers, California, earthquake of 1992, *J. Geophys. Res.*, *99*(B6), 11,705–11,722, 1994.

Li, Y. G., J. E. Vidale, S. M. Day, and D. D. Oglesby, Study of the 1999 M_w 7.1 Hector Mine, California, earthquake fault plane by trapped waves, *Bull. Seismol. Soc. Amer.*, *92*(4), 1318–1332, 2002.

Lin, A., B. Fu, J. Guo, Q. Zeng, G. Dang, W. He, and Y. Zhao, Co-seismic strike-slip and rupture length produced by the 2001 M_s 8.1 central Kunlun earthquake, *Science*, *296*(5575), 2015–2016, 2002.

Lin, A., M. Kikuchi, and B. Fu, Rupture segmentation and process of the 2001 M_w 7.8 central Kunlun, China, earthquake, *Bull. Seismol. Soc. Amer.*, *93*(6), 2477–2492, 2003.

Liu, Y., and J. R. Rice, Aseismic slip transients emerge spontaneously in 3D rate and state modeling of subduction earthquake sequences, *J. Geophys. Res*, *110*(B8), doi:10.1029/2004JB003424, 2005.

Marcinkovich, C., and K. B. Olsen, On the implementation of perfectly matched layers in a three-dimensional fourth-order velocity-stress finite difference scheme, *J. Geophys. Res.*, *108*(B5), 2276, doi:10.1029/2002JB002235, 2003.

Muskhelishvili, N. I., *Singular integral equations: Boundary problems of function theory and their application to mathematical physics. Translation from Russian edited by J. R. M. Radok*, P. Nordoff, Groningen, 1953.

Nakamura, K., G. Plafker, K. H. Jacob, and J. N. Davies, A tectonic stress trajectory map of Alaska using information from volcanoes and faults, *Bull. Earthq. Res. Inst.*, *55*, 89–100, 1980.

Nakata, T., K. Shimazaki, Y. Suzuki, and E. Tsukuda, Fault branching and directivity of rupture propagation (in Japanese), *J. Geogr.*, *107*, 512–528, 1998.

Oglesby, D. D., The dynamics of strike-slip step-overs with linking dip-slip faults, *Bull. Seismol. Soc. Amer.*, *95*(5), 1604–1622, 2005.

Oglesby, D. D., and S. M. Day, The effect of fault geometry on the 1999 Chi-Chi(Taiwan) earthquake, *Geophys. Res. Lett.*, *28*, 1831–1834, 2001.

Oglesby, D. D., R. J. Archuleta, and S. B. Nielsen, The three-dimensional dynamics of dipping faults, *Bull. Seismol. Soc. Amer.*, *90*, 616–628, 2000a.

Oglesby, D. D., R. J. Archuleta, and S. B. Nielsen, Dynamics of dip-slip faulting: Explorations in two dimensions, *J. Geophys. Res.*, *105*(B6), 13,643–13,653, 2000b.

Oglesby, D. D., S. M. Day, Y. G. Li, and J. E. Vidale, The 1999 Hector Mine earthquake: The dynamics of a branched fault system, *Bull. Seismol. Soc. Amer.*, *93*(6), 2459–2476, 2003a.

Oglesby, D. D., S. M. Day, and D. R. H. O'Connell, Dynamic and static interaction of two thrust faults: A case study with general implications, *J. Geophys. Res*, *108*(B10), 2489, doi:10.1029/2002JB002228, 2003b.

Olsen, K. B., R. Madariaga, and R. J. Archuleta, Three-dimensional dynamic simulation of the 1992 Landers earthquake, *Science*, *278*(5339), 834–838, 1997.

Palmer, A. C., and J. R. Rice, Growth of slip surfaces in progressive failure of overconsolidated clay, *Proc. R. Soc. London. Ser. A-Math. Phys. Eng. Sci.*, *332*, 527–548, 1973.

Peyrat, S., K. Olsen, and R. Madariaga, Dynamic modeling of the 1992 Landers earthquake, *J. Geophys. Res.*, *106*(B11), 26,467–26,482, 2001.

Poliakov, A. N. B., R. Dmowska, and J. R. Rice, Dynamic shear rupture interactions with fault bends and off-axis secondary faulting, *J. Geophys. Res.*, *107*(B11), doi:10.1029/2001JB000572, 2002.

Ratchkovski, N. A., Change in stress directions along the central Denali fault, Alaska after the 2002 earthquake sequence, *Geophys. Res. Lett.*, *30*, 2003.

Ratchkovski, N. A., and R. A. Hansen, New constraints on tectonics of interior Alaska: Earthquake locations, source mechanisms and stress regime, *Bull. Seismol. Soc. Amer.*, *92*, 998–1014, 2002.

Rempel, A. W., and J. R. Rice, Thermal pressurization and onset of melting in fault zones, *J. Geophys. Res*, *111*(B9), doi:10.1029/2006JB004314, 2006.

Rice, J., Mathematical analysis in the mechanics of fracture, in, *Fracture: An Advanced Treatise*, *Vol. II, edited by H. Liebowitz*, pp. 191–311, Elsevier, 1968.

Rice, J. R., *The mechanics of earthquake rupture*, chap. Physics of the earth's interior (Proc. Intn'l. School of Physics 'Enrico Fermi', Course 78, pp. 555-649, 1979), A. M. Dziewonski, and E. Boschi (Editors), Italian Physical Society and North-Holland Publishing Co., Amsterdam, 1980.

Rice, J. R., Heating and weakening of faults during earthquake slip, *J. Geophys. Res*, *111*(B5), doi:10.1029/2005JB004006, 2006.

Rice, J. R., C. G. Sammis, and R. Parsons, Off-fault secondary failure induced by a dynamic slip pulse, *Bull. Seismol. Soc. Amer.*, *95*(1), 109–134, 2005.

Robinson, D. P., C. Brough, and S. Das, The M_w 7.8, 2001 Kunlunshan earthquake: Extreme rupture speed variability and effect of fault geometry, *J. Geophys. Res.*, *111*(B8), 2006.

Rockwell, T. K., S. Lindvall, M. Herzberg, D. Murbach, T. Dawson, and G. Berger, Paleoseismology of the Johnson Valley, Kickapoo and Homestead Valley Faults: Clustering of earthquakes in the eastern California shear zone, *Bull. Seismol. Soc. Amer.*, *90*(5), 1200–1236, 2000.

Rosakis, A. J., O. Samudrala, and D. Coker, Cracks faster than the shear wave speed, *Science*, *284*, 1337–1340, 1999.

Rousseau, C. E., and A. J. Rosakis, On the influence of fault bends on the growth of sub-Rayleigh and intersonic dynamic shear ruptures, *J. Geophys. Res.*, *108*(B9), doi:10.1029/2002JB002310, 2003.

Savage, J. C., Radiation from supersonic faulting, *Bull. Seismol. Soc. Amer.*, *61*(4), 1009–1012, 1971.

Savage, J. C., and M. Lisowski, Strain accumulation along the Denali fault at the Nenana river and Delta river crossings, Alaska, *J. Geophys. Res*, *96*(B9), 14,481–14,492, 1991.

Segall, P., and J. R. Rice, Does shear heating of pore fluid contribute to earthquake nucleation?, *J. Geophys. Res*, *111*(B9), doi:10.1029/2005JB004129, 2006.

Sibson, R. H., Stopping of earthquake ruptures at dilational fault jogs, *Nature*, *316*(6025), 248–251, 1985.

Somerville, P. G., N. F. Smith, R. W. Graves, and N. A. Abrahamson, Modification of empirical strong ground motion attenuation relations to include the amplitude and duration effects of rupture directivity, *Seismol. Res. Lett.*, *68*, 199–222, 1997.

Sowers, J. M., J. R. Unruh, W. R. Lettis, and T. D. Rubin, Relationship of the Kickapoo fault to the Johnson Valley and Homestead Valley faults, San Bernardino county, California, *Bull. Seismol. Soc. Amer.*, *84*(3), 528–536, 1994.

Spotila, J., and K. Sieh, Geologic investigations of a “slip gap” in the surficial ruptures of the 1992 Landers earthquake, southern California, *J. Geophys. Res*, *100*, 543–559, 1995.

Spudich, P., and L. N. Frazer, Use of ray theory to calculate high-frequency radiation from earthquake sources having spatially variable rupture velocity and stress drop, *Bull. Seismol. Soc. Amer.*, *74*, 2061–2081, 1984.

Spudich, P., and M. Guatteri, The effect of bandwidth limitations on the inference of earthquake slip-weakening distance from seismograms, *Bull. Seismol. Soc. Amer.*, *94*(6), 2028–2036, doi:10.1785/0120030104, 2004.

Tada, T., and T. Yamashita, Non hypersingular boundary integral equations for two dimensional non-planar crack analysis, *Geophys. J. Int.*, *130*(2), 269–282, 1997.

Tocheport, A., L. Rivera, and J. Van der Woerd, A Study of the 14 November 2001 Kokoxili earthquake: History and geometry of the rupture from teleseismic data and field observations, *Bull. Seismol. Soc. Amer.*, *96*(5), 1729–1741, 2006.

Wallace, W. K., B. L. Sherrod, and T. E. Dawson, Character and significance of surface rupture near the intersection of the Denali and Totschunda faults, M_w 7.9 Denali fault earthquake, Alaska, November 3, 2002, *Trans. Am. Geophys. U., EOS*, *S72F-1335*, 2002.

Wesnousky, S. G., Seismological and structural evolution of strike-slip faults, *Nature*, *335*(6188), 340–343, 1988.

Wesnousky, S. G., Predicting the endpoints of earthquake ruptures, *Nature*, *444*(7117), 358–360, 2006.

Xia, K. W., A. J. Rosakis, and H. Kanamori, Laboratory earthquakes: The sub-rayleigh-to-supershear rupture transition, *Science*, *303*, 1859–1861, 2004.

Xu, X., W. Chen, W. Ma, G. Yu, and G. Chen, Surface rupture of the Kunlunshan earthquake (M_s 8.1), northern Tibetan plateau, China, *Seism. Res. Lett*, *73*, 884–892, 2002.

Yamashita, T., and E. Fukuyama, Apparent critical slip displacement caused by the existence of a fault zone, *Geophys. J. Int.*, *125*(2), 459–472, 1996.

Yamashita, T., and Y. Umeda, Earthquake rupture complexity due to dynamic nucleation and interaction of subsidiary faults, *Pure. Appl. Geophys.*, *143*(1), 89–116, 1994.

Yoffe, E. H., The moving Griffith crack, *Phil. Mag*, *42*(2), 739–750, 1951.

Yule, D., and K. Sieh, Complexities of the San Andreas fault near San Gorgonio Pass: Implications for large earthquakes, *J. Geophys. Res*, *108*(10.1029), 2003.

Zachariasen, J., and K. Sieh, The transfer of slip between two en echelon strike-slip faults: A case study from the 1992 Landers earthquake, southern California, *J. Geophys. Res.*, *100*(B8), 15,281–15,302, 1995.

Appendix A

Boundary Integral Equation (BIE) method

Numerical implementation of the dynamic rupture propagation scheme was done using the 2D Boundary Integral Equation (BIE) method as described in [*Kame et al.*, 2003, and references therein]. Boundary integral equation methods are very efficient for the study of cracks in homogeneous media, in that the calculations are done only along the crack trace which therefore allows the study of complex crack geometries.

This method derives from the basic integral representation theorem in dynamic elasticity, (e.g., *Aki and Richards* [1980]). *Tada* [1995] has calculated the change in tangential and normal stresses due to a mode II rupture along an arbitrarily shaped crack/fault. To numerically calculate the stresses for such arbitrarily shaped fault, represented by Γ in figure A.1, it is approximated by a polygon consisting of elements of constant length Δs. The time is also discretized by a set of equally spaced time steps with an interval of Δt. In applications (*Koller et al.* [1992]; *Kame and Yamashita* [1999a], among others) the ratio $c_p \Delta t/\Delta s$ has been chosen equal to $1/2$ where c_p is the P-wave speed of the medium. This ensures that the dynamical procedure is explicit (true for all $c_p \Delta t/\Delta s < 1$). This value in practice should be smaller than $1/\sqrt{2}$, to respect the stability conditions of corresponding two-dimensional finite difference methods, as explained by *Koller et al.* [1992].

Following earlier works by, e.g.,*Andrews* [1985], *Das and Kostrov* [1987], *Koller et al.* [1992], *Cochard and Madariaga* [1994], *Tada and Yamashita* [1997], *Kame and Yamashita* [1999a], and *Kame et al.* [2003], the displacement discontinuities along the fault are represented in the BIE using a piecewise constant interpolation. A constant slip velocity $V^{i,k}$, to be determined, is assumed within each spatial element (cell i of length Δs) and during each time step k, which runs from $(k-1)\Delta t$ to $k\Delta t$; here $k = 1...n$. A discretized version of stresses were then calculated in earlier works by *Koller et al.* [1992], *Cochard and*

Madariaga [1994], *Kame and Yamashita* [1999a, 1999b, 2003], *Kame et al.* [2003], and *Fliss et al.* [2004] using piecewise constant interpolation cells.

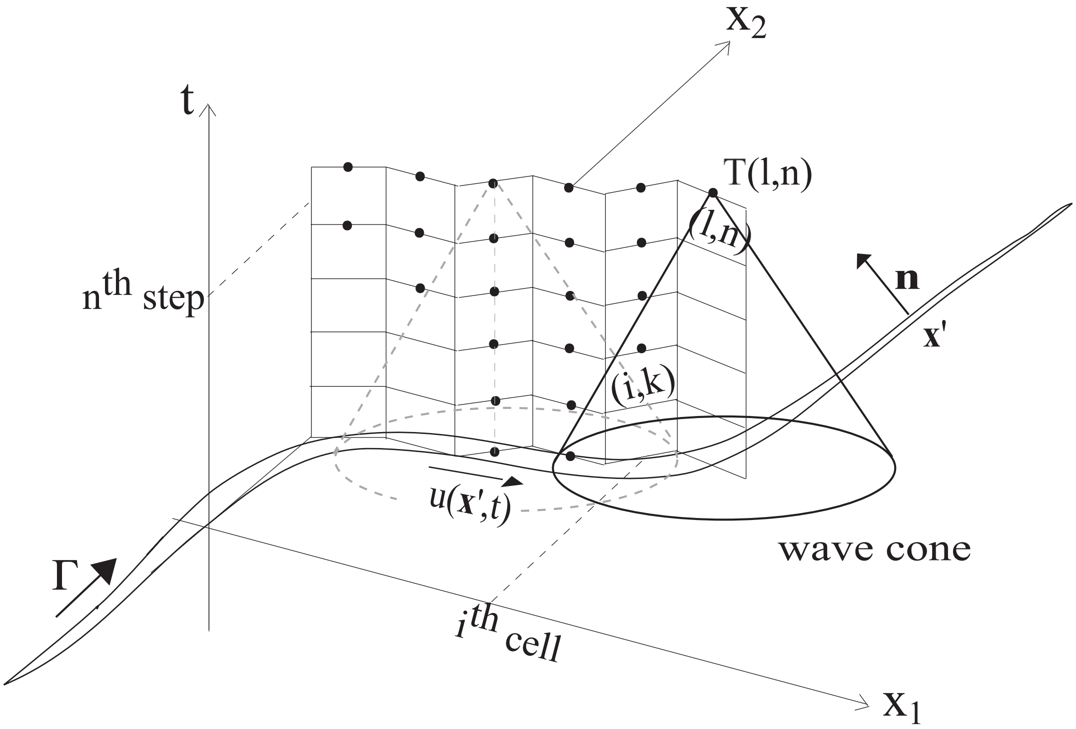

Figure A.1: Nomenclature used and schematic diagram of the discretized BIE method. The points represent the cells with non-zero slip velocity [*Fliss et al.* 2004].

The resulting expressions for $\sigma_{21}^{l,n}$ and $\sigma_{22}^{l,n}$, at the center of cell l at the end of time step n, are

$$\sigma_{21}^{l,n} = -\frac{\mu}{2c_s}V^{l,n} + \sum_{k=0}^{n-1}\sum_{i} V^{i,k}K_t^{l,i,n-k} + \sigma_{21}^{l,0}, \qquad \text{(A.1)}$$

$$\sigma_{22}^{l,n} = \sum_{k=0}^{n-1}\sum_{i} V^{i,k}K_n^{l,i,n-k} + \sigma_{22}^{l,0} \qquad \text{(A.2)}$$

for n = 1, 2, ... Here $K^{l,i,n-k}$ represents the stress at the center of cell l, at the end of time step n due to a unit slip velocity within cell i during time step k. These kernels can be calculated analytically in 2D by appropriate integrations of the stress field in response to impulsive point double-couples. Also, $K_t^{l,i,0} = -\mu/(2c_s)$ when $i = l$ and is 0 otherwise, given that our Δt is less than a P-wave travel time over a cell; $\mu/(2c_s)$ is the radiation damping factor or fault impedance [*Cochard and Madariaga*, 1994; *Guebelle and Rice*, 1995] and represents the instantaneous contribution of the current slip velocity to the shear stress at the same position. $K_n^{l,i,0} = 0$ is zero because we consider no opening along the fault. Also, $\sigma_{21}^{l,0}$ and $\sigma_{22}^{l,0}$ are the tractions in the static initial state at $t = 0$.

Because of the proprieties of wave propagation, the convolution sums have to be done only for those cells i and prior time steps k that fall inside the P-wave cone of l, n, as illustrated in Figure A.1.

Nucleation of the rupture

In order to nucleate dynamic rupture, we first assume [*Kame et al.*, 2003] a nucleation zone in a static equilibrium state (corresponding to the state at $t = 0$ discussed above). We allow slip in a region of length L_{nucl} slightly larger than the minimum nucleation size L_c given by equation 4.15, but prevent slip outside this region until $t > 0$, so that a dynamic rupture begins with non-negligible slip rate at the crack tip at time step $n = 1$. The static equilibrium is found when the slip and the stress field due to the initial stress and the slip in the nucleation region satisfies the slip-weakening law.

If the nucleation zone consists of N cells, then their N unknown pre-slips D^l (the notation D is synonymous with Δu) alter the tectonic prestress $\sigma_{21}^{l,0}$ at the center of cell l to a new static stress

$$\sigma_{21}^{l} = \sum_{i} D^{i} K_{t,static}^{l,i} + \sigma_{21}^{l,0} \tag{A.3}$$

Here $K_{t,static}^{l,i}$ is the corresponding static stress kernel. Because we nucleate here along a straight segment of the fault, that kernel depends there only on $l-i$. Also, sliding gives no change in the normal stress on that same planar segment from its value $\sigma_{22}^{l,0})$ due to the prestress field.

We must choose the D^{l} for the N cells of the nucleation zone so that stresses at each cell are consistent with the slip-weakening strength of equations 4.13 and 4.14. That is, if the law is represented as $\tau = -\sigma_n F(\Delta u)$, then we require that the σ_{21}^{l} for the N cells also satisfy

$$\sigma_{21}^{l} = -\sigma_{22}^{l,0} F(D^{l}) \tag{A.4}$$

The solution of that and equation A.3 is numerically determined using the Newton-Raphson method. The resulting slips D^{l} are identified as $D^{l,0}$, i.e., at time 0, for the dynamic analysis.

The distribution of slip along this initial nucleation region causes an initial stress concentration which is slightly larger than the peak strength at the both tips of the zone and so enables propagation of the rupture at the first dynamic time steps.

Rupture dynamics procedures

At time 0^{+}, we begin the dynamic analysis. For $n = 1, 2, ...$, stresses at the end of the nth time step are determined in terms of slip rates $V^{i,k}$ by

$$\sigma_{21}^{l,n} = -\frac{\mu}{2c_s}V^{l,n} + (\sigma_{21}^{l,n})_{past}, \tag{A.5}$$

$$(\sigma_{21}^{l,n})_{past} = \sum_{k=0}^{n-1}\sum_{i} V^{i,k}K_t^{l,i,n-k} + \sum_i D^{i,0}K_{t,static}^{l,i} + \sigma_{21}^{l,0}, \tag{A.6}$$

$$\sigma_{22}^{l,n} = \sum_{k=0}^{n-1}\sum_{i} V^{i,k}K_n^{l,i,n-k} + \sum_i D^{i,0}K_{n,static}^{l,i} + \sigma_{22}^{l,0} \tag{A.7}$$

and, of course, slips are updated to the end of the step by $D^{l,n} = D^{l,n-1} + \Delta t V^{l,n}$. Here $(\sigma_{21}^{l,n})_{past}$ is the stress at time $n\Delta t$ due to the history of slip everywhere up to time $(n-1)\Delta t$; it is equal to $\sigma_{21}^{l,n}$ for cells which do not slip in that nth time step.

To solve for the slip rate in each time step, we assure that the stresses and slip at the end of that step precisely satisfy the slip-weakening constitutive law. Thus, as above, let $\tau = -\sigma_n F(\Delta u)$ represent the strength. Then if

$$(\sigma_{21}^{l,n})_{past} < -\sigma_{22}^{l,n}F(D^{l,n-1}) \tag{A.8}$$

we must set $V^{l,n} = 0$, which is consistent with $D^{l,n} = D^{l,n-1}$ and $\sigma_{21}^{l,n} = (\sigma_{21}^{l,n})_{past}$. For the cells at each rupture tip, that test becomes $(\sigma_{21}^{l,n})_{past} < -\sigma_{22}^{l,n}F(0) = -\mu_s\sigma_{22}^{l,n}$ and, if met, it means that the rupture front does not advance in that time step.

On the other hand, for all cells satisfying

$$(\sigma_{21}^{l,n})_{past} \geq -\sigma_{22}^{l,n}F(D^{l,n-1}) \tag{A.9}$$

we must choose $V^{l,n}$ to satisfy

$$(\sigma_{21}^{l,n})_{past} - \frac{\mu}{2c_s}V^{l,n} = -\sigma_{22}^{l,n}F(D^{l,n-1} + \Delta t V^{l,n}) \tag{A.10}$$

Kame et al. [2003] stated conditions on the Δt to ensure that there exists a unique solution of equation A.10 satisfying $V^{l,n} \geq 0$. For the linear slip-weakening law adopted here, that reduces to

$$\frac{\mu}{2c_s} > -\sigma_{22}^{l,n}(\mu_s - \mu_d)\frac{\Delta t}{D_c} \tag{A.11}$$

(It assures, e.g., that if there is equality in A.9, then the obvious solution $V^{l,n} = 0$ is the only possible one.) For the linear law the solution is readily written out explicitly, with different forms depending on whether $D^{l,n-1} < D_c$ or $D^{l,n-1} \geq D_c$. In the latter case the result is just $V^{l,n} = (2c_s/\mu)[(\sigma_{21}^{l,n})_{past} + \mu_d\sigma_{22}^{l,n}]$. Thus, we determine the slip velocity on each fracturing element.

If we use the definition of the different parameters given earlier, the above inequality assuring a unique nonnegative slip velocity becomes [*Kame et al.*, 2003]:

$$\Delta s/R_0 < 8/(\sqrt{3}\pi) \quad \text{that is} \quad \Delta s/R_0 < 1.47. \tag{A.12}$$

Here, however, it is important to understand that the R_0, which scales inversely with $\tau_p - \tau_r$ $[= (\mu_s - \mu_d)(-\sigma_n)]$ as in equation 4.16, must be evaluated with σ_n equated to the momentary normal stress $\sigma_{22}^{l,n}$. That is not constant in time for propagation along branched or curved faults, and the criterion, which must be satisfied all along the rupturing zone(s) considered, can only be tested for certain during the solution itself (which may then have to be redone with a more refined Δs, and hence Δt). This is important in propagation along faults which curve towards the compressional side of the advancing rupture, because that locally increases the fault-normal compression and can invalidate the choice of a Δs that seemed acceptable in terms of the prestress field.

Regularization; smoothing the slip rate distribution

Following *Yamashita and Fukuyama* [1996], we introduce what they call "artificial attenuation" to eliminate short-wavelength oscillations which appear in slip velocity, due to the abrupt progress of the fracture front along the discretized fault trace. The oscillations only gradually become evident for large numbers time steps but then they grow rapidly, and invalidate the results [*Yamashita and Fukuyama*, 1996; *Kame and Yamashita*, 1999a; *Kame et al.*, 2003]. We likewise try to eliminate the oscillations by their regularization procedure. Thus, after calculating the slip velocity V over the ruptured region, at each time step, n, we transform it to a smoothed one by

$$V_{\mathrm{sm}}^{i,n} = V^{i,n} + \alpha \left(V_{\mathrm{sm}}^{i-1,n} + V_{\mathrm{sm}}^{i+1,n} - 2V_{\mathrm{sm}}^{i,n} \right) \tag{A.13}$$

The unknown $V_{\mathrm{sm}}^{i,n}$ is then solved for numerically, along the currently ruptured zone where $V^{i,n} \geq 0$ (but with $V_{\mathrm{sm}}^{i,n}$ set to 0 for all cells where $V^{i,n} = 0$), using a matrix inversion. The $V_{\mathrm{sm}}^{i,n}$ are then used to redefine $V^{i,n}$ for updating the slip and doing future convolution sums.

The choice of the smoothing factor α is delicate: stronger smoothing suppresses not only the oscillations but the amount of slip. A compromise has to be made between stability and plausibility of the solution. Comparing their numerical results using this procedure with an analytical solution, *Yamashita and Fukuyama* [1996] have shown that the value $\alpha = 1/2$ gives stable and reasonably accurate results. This value is chosen for our simulations.

Appendix B

Evaluating rupture velocity in numerical procedures

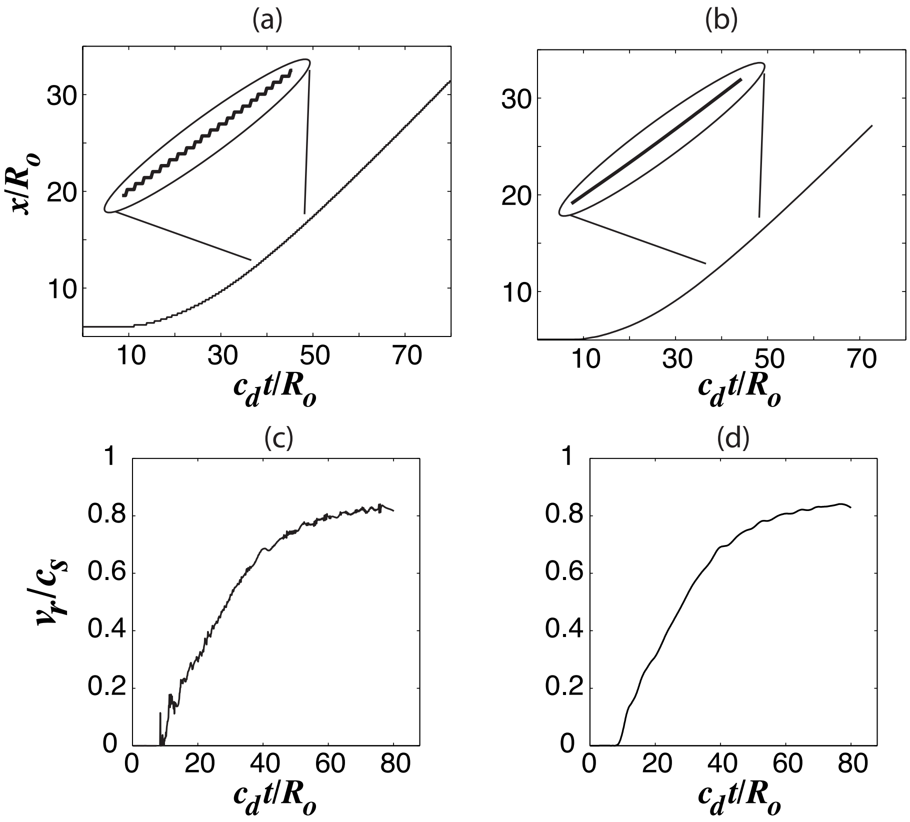

Figure B.1: Data smoothing for rupture tip position and rupture velocity data. (a) Rupture tip position versus time before smoothing (Oval inset shows zoomed in plot). (b) Rupture tip position versus time after locally weighted polynomial regression smoothing (Oval inset shows zoomed in plot). (c) Rupture velocity evolution obtained by numerically differentiating A1(b). (d) Rupture velocity after after locally weighted polynomial regression smoothing.

Due to the discretized (spatial and temporal) nature of the numerical procedure the rupture tip progress is quantized. In other words the incremental rupture tip advance is through a distance equal to the length of the spatial cell over a variable, but necessarily integer, number of time steps. This leads to a staircase like data-set [Figure B.1(a)] for rupture tip advance over time. Direct numerical differentiation of this data to obtain rupture velocity evolution with time is hence not recommended.

In earlier work *Bhat et al.* [2004] the above mentioned issue with numerical differentiation was partially overcome by evaluating the rupture velocity in the following way. They calculated the average time (Δt_{avg}) taken for the rupture tip to advance by three spatial cells ($3\Delta s$). The rupture velocity, v_r, is then simply given by $v_r = 3\Delta s/\Delta t_{avg}$. The procedure is robust enough for calculations where there are no abrupt changes in the crack-tip advance history and produces a relatively good rupture velocity evolution data. In the current work we noticed several abrupt transitions in the rupture tip history data and the above mentioned algorithm would fail to capture such transitions.

We instead use locally weighted quadratic polynomial regression [*Cleveland*, 1979] to smooth the rupture tip position versus time data [Figure B.1(b)]. At each point in the data set a quadratic polynomial is fit to a subset of the data using weighted least squares method, giving more weight to points near the point whose response is being estimated and less weight to points further away. The value of the regression function for the point is then obtained by evaluating the local polynomial. The resulting data-set was then numerically differentiated using a forward difference scheme to calculate the rupture velocity evolution data [Figure B.1(c)]. This data was further smoothed using the locally weighted quadratic polynomial regression method to produce the rupture velocity evolution plot [Figure B.1(d)].

We also used the above algorithm to verify the results obtained by *Bhat et al.* [2004], Figure 12 (see Figure 2.14 for the updated version). While the resulting rupture velocity curve was significantly smoother the general conclusions obtained by *Bhat et al.* [2004] agrees with the smoothed data.

Appendix C

Determination of Coulomb Stress changes on faults

Coulomb Stress on a fault plane of known orientation

Consider a fault plane Σ lying in a 3D space (Figure C.1). Let **x, y** and **z** form a right-handed co-ordinate system where the surface of the earth is in the **x-y** plane and the **z** axis points vertically upwards from the earth's surface. The strike direction, $\vec{s}$, is chosen along the surface trace of the fault plane such that the dip, defined below, is $\leq 90^0$. Let $\vec{s}$ make an angle of ϕ with the **x** axis (measured positive for counterclockwise rotation about **z**) and let γ be the dip of the faulting plane, measured positive for right-handed rotation about the strike direction (i. e., angle from earth's surface at right of the strike direction to the fault plane). The positive strike direction is always chosen such that $0 < \gamma \leq 90^0$. Let Σ^+ and Σ^- to be the positive and the negative side of the fault plane respectively [Figure C.1a]; Σ^- is the footwall (or is assigned arbitrarily if $\gamma = 90^0$).

Let $\vec{n}$ be the unit normal to the fault plane directed from Σ^- to Σ^+. This will imply that any traction calculated with respect to this vector represents the action on the Σ^- plane due to the Σ^+ plane.

Looking at Figure C.1b the **z** axis component of $\vec{n}$ is $\cos\gamma$. The component of $\vec{n}$ on the **x-y** plane is then $\sin\gamma$. Since this component is perpendicular to $\vec{s}$, the strike vector, the projections of $\vec{n}$ on the **x** and **y** axes are $\sin\phi\sin\gamma$ and $-\cos\phi\sin\gamma$ respectively. Thus

$$\vec{n} = (\sin\phi\sin\gamma)\hat{i} + (-\cos\phi\sin\gamma)\hat{j} + (\cos\gamma)\hat{k} \tag{C.1}$$

The unit vector acting along the strike direction is then given by [Figure C.1b]

$$\vec{s} = (\cos\phi)\hat{i} + (\sin\phi)\hat{j} + (0)\hat{k} \tag{C.2}$$

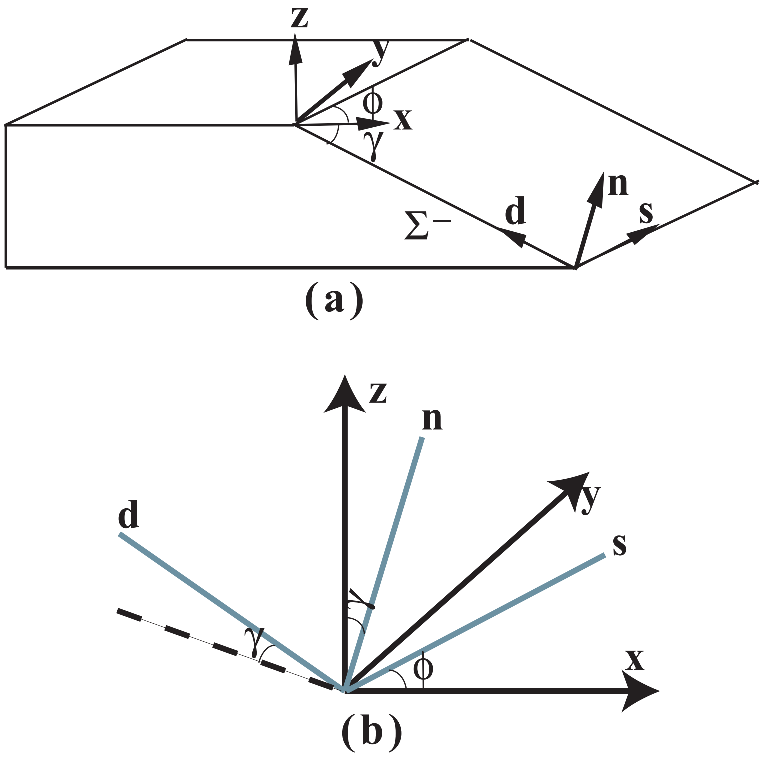

Figure C.1: a) Σ^- side of the fault plane, taken as the footwall for the dipping fault, and chosen arbitrarily if the fault is vertical. ϕ is the angle measured from the **x**-axis to the surface trace of the fault corresponding with strike direction $\vec{s}$, counter-clockwise about **z**. γ is the angle from the **x-y** plane, at the right of the strike direction, to the fault plane. **s, d** and **n** are the strike, updip and outward normal vectors respectively to the Σ^- surface. b) Various angles between the **(s, d, n)** and **(x, y, z)** coordinate systems.

Then the vector acting along the updip direction is simply given by $\vec{d} = \vec{n} \times \vec{s}$ which is

$$\vec{d} = (-\sin\phi\cos\gamma)\hat{i} + (\cos\phi\cos\gamma)\hat{j} + (\sin\gamma)\hat{k} \tag{C.3}$$

The traction acting on the fault plane is then given by $T_i = \sigma_{ji}n_j$ where σ_{ij} are the components of the stress tensor (tensile positive) in the original **x-y-z** coordinate system. The normal stress on the fault plane is then given by $\sigma = T_i n_i$.

The maximum shear stress acting on the plane is given by $\tau_{max} = \sqrt{\tau_s^2 + \tau_d^2}$ where $\tau_s(= T_i s_i)$ and $\tau_d(= T_i d_i)$ are the shear stresses acting along the strike and the updip directions respectively. Define rake angle (λ) as the angle between the unit slip vector, $\vec{\xi}$, (slip vector $\Delta\vec{u}$ is defined = $\vec{u}^+ - \vec{u}^-$ where $\vec{u}$ is the displacement vector) and $\vec{s}$, measured positive from the strike direction to that of $\vec{\xi}$ for counterclockwise rotation about the $\vec{n}$ direction.

In terms of the rake angle (λ) the unit slip vector $\vec{\xi}$ is given by $\vec{\xi} = \vec{s}\cos\lambda + \vec{d}\sin\lambda$ and the shear stress in the slip direction is given by $\tau = T_i\xi_i$.

It is then clear that a rake angle of 0 or π would result in pure left or right lateral faulting respectively and a rake angle of $-\pi/2$ or $\pi/2$ would result in pure normal or thrust faulting respectively.

The Coulomb Stress (CS) is now given by $CS = \tau + f_s\sigma$ where f_s is the static friction coefficient of the fault plane. τ is positive when slip occurs in the direction of the unit slip vector and σ is positive when the fault is unclamped.

The above methodology may be used In circumstances for which the fault plane is given and the geological sense of motion along it is known and is assumed to be active after stress change.

Coulomb Stress on optimal Mohr-Coulomb planes

From Mohr-Coulomb failure theory it is known that for optimally oriented planes for failure (planeson which CS is maximum) the unit normals make angles of $\beta = \pm(\pi/4 + \varphi/2)$ (where $\tan\varphi = f_s$) with the maximum compressive stress direction, and their line of intersection aligns with the intermediate principal stress direction. The slip vectors of the conjugate planes are in the plane comprising the maximum and minimum compressive stress directions. [Figure C.2]

The shear and normal stresses on these planes are then given by

$$\begin{aligned}\tau &= \frac{(\sigma_1 - \sigma_3)}{2}\sin 2\beta \\ \sigma &= \frac{(\sigma_1 + \sigma_3)}{2} + \frac{(\sigma_1 - \sigma_3)}{2}\cos 2\beta\end{aligned} \tag{C.4}$$

where $\sigma_1 \geq \sigma_2 \geq \sigma_3$ are the principal stresses, and (like σ) are positive if tensile.

Application to plane strain in the x-y plane aligned with the earth's surface

Case 1. $\sigma_1 = \sigma_{zz}$ (least compressive stress normal to the surface). This case results in pure thrust faulting and both the conjugate planes are thrust faults. The strike of the two planes are along $\pm\vec{\nu_2}$ where $\vec{\nu_2}$ is the eigen-vector corresponding to the intermediate principal stress, σ_2. The dip is $\pi/4 - \varphi/2$.

Case 2. $\sigma_2 = \sigma_{zz}$. This case results in strike-slip faulting and the conjugate planes strike left laterally and right laterally. The strike of the two planes makes an angle of $\pm(\pi/4 - \varphi/2)$ with the maximum compressive stress (σ_3) direction. The dip is $\pi/2$.

Case 3. $\sigma_3 = \sigma_{zz}$ (most compressive stress normal to the surface). This case results in pure normal faulting and both the conjugate planes are normal faults. The strike of the two planes are given by $\pm\vec{\nu_2}$ where $\vec{\nu_2}$ is the eigen-vector corresponding to the intermediate principal stress, σ_2. The dip is $\pi/4 + \varphi/2$.

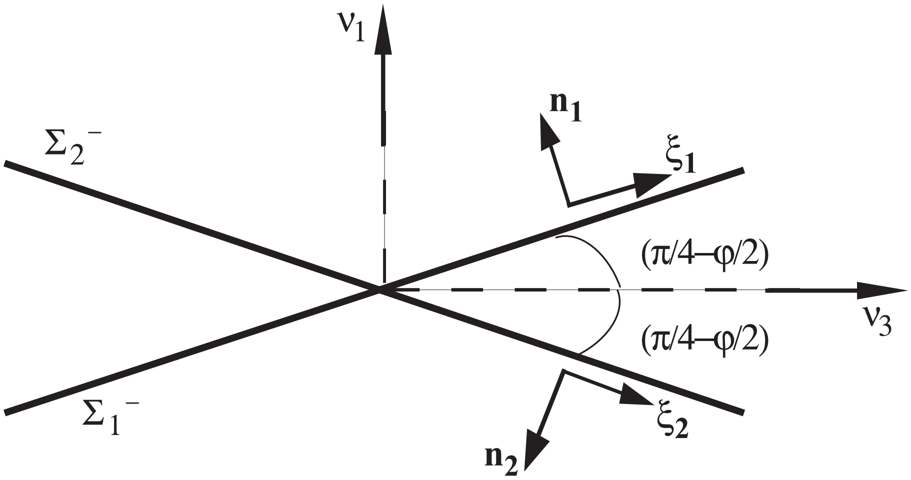

Figure C.2: Optimally oriented conjugate planes (Σ_1 and Σ_2) for failure. $\vec{\nu_1}, \vec{\nu_3}$ are the eigen-vectors corresponding to the minimum and maximum principal compressive stresses respectively. $\vec{n_1}, \vec{\xi_1}$ and $\vec{n_2}, \vec{\xi_2}$ are the unit normal and unit slip vectors respectively to the conjugate planes. $\tan\varphi = f_s$ where f_s is the coefficient of friction for the planes.

Determination of the change in Coulomb Stress (ΔCS) due to an earthquake rupture

Case when fault plane and candidate direction of slip is known: Let σ_{ij}^0 be the initial stress state (in the **x-y-z** system) and $\Delta\sigma_{ij}$ be the perturbation to the stress-field due to an earthquake rupture. Then ΔCS is given by $\Delta CS = \Delta\tau + f_s\Delta\sigma$ where $\Delta\tau$ and $\Delta\sigma$ are given by $\Delta\tau = \Delta\sigma_{ij}n_i\xi_j$ and $\Delta\sigma = \Delta\sigma_{ij}n_in_j$. The vectors $\vec{n}$ and $\vec{\xi}$ are defined in the first section.

Case when fault planes are optimally oriented: We first begin by determining the conjugate failure planes for the total stress state i.e. for $\sigma_{ij} = \sigma_{ij}^0 + \Delta\sigma_{ij}$. Let $\vec{\nu_1}$ and $\vec{\nu_3}$ be the eigen-vectors associated with the minimum and maximum principal stresses respectively of the total stress state. The failure plane normals are then obtained by rotating $\vec{\nu_3}$ about $\vec{\nu_2}$ by an angle of $\pm(\pi/4 + \varphi/2)$. Let $\vec{n_1}$ and $\vec{n_2}$ be the outward unit normals to the conjugate planes and $\vec{\xi_1}$ and $\vec{\xi_2}$ be the unit vectors in the direction of slip on the $\Sigma^{+}_{1/2}$ planes respectively [Figure C.2]. Then

$$\vec{\xi_1} = \vec{\nu_3}\cos(\pi/4 - \varphi/2) + \vec{\nu_1}\sin(\pi/4 - \varphi/2) \qquad \text{(C.5)}$$

$$\vec{n_1} = -\vec{\nu_3}\cos(\pi/4 + \varphi/2) + \vec{\nu_1}\sin(\pi/4 + \varphi/2) \qquad \text{(C.6)}$$

$$\vec{\xi_2} = \vec{\nu_3}\cos(\pi/4 - \varphi/2) - \vec{\nu_1}\sin(\pi/4 - \varphi/2) \qquad \text{(C.7)}$$

$$\vec{n_2} = -\vec{\nu_3}\cos(\pi/4 + \varphi/2) - \vec{\nu_1}\sin(\pi/4 + \varphi/2) \qquad \text{(C.8)}$$

ΔCS is then calculated for each of the optimal planes by $\Delta CS = \Delta\tau + f_s\Delta\sigma$ where $\Delta\tau$ and $\Delta\sigma$ are given by $\Delta\tau = \Delta\sigma_{ij}n_i\xi_j$ and $\Delta\sigma = \Delta\sigma_{ij}n_in_j$. n_i, ξ_i are the components of the unit normal and unit slip vectors respectively for each of the optimal planes. The maximum of the two ΔCS values is then sometimes identified as the plane more likely to slip due to an earthquake rupture, although we see no firm basis for that. However, this is not the only way the change in Coulomb stress on optimal planes be identified. The different conjugate fault plane orientations can be determined for stress states both before (σ^0_{ij}) and after the rupture (σ_{ij}) and then the Coulomb stress changes can be evaluated as $\Delta CS = (CS)^{\sigma^0+\Delta\sigma}_{optimal} - (CS)^{\sigma^0}_{optimal}$. This would give a unique value of ΔCS regardless of the optimal plane chosen in each of the stress states. Our contour plots here use the first method.

Appendix D

Non attenuating part of far field stresses in Mach band

In their study of an supershear slip pulse, propagating at steady state in a two dimensional homogeneous isotropic medium under plane strain conditions, *Dunham and Archuleta* [2005] have shown that the off-fault velocity fields trace out the exact slip velocity during the passsage of the S-wave front. This means that a non-attenuating field, caused by the passage of the S-wave front, is traced out in the medium, through which the slip pulse passes, and extends, theoreticaly, to infinity. Nevertheless this observation points out that siginificant effects of the supershear slip pulse can be observed at large distances away from it unlike its sub-Rayleigh analogue where both the P wave and the S wave stress fields attenuate as $1/r$ with distance from the source, r. In the following section we re-express the far field stress distribution in terms of the slip velocity distribution on the fault. Let $V(x)$ be the slip rate along the rupture and Δu the slip, i.e.,

$$\begin{aligned} V(x) &= (\partial u_x/\partial t)^+ - (\partial u_x/\partial t)^- \\ &= -v_r[(\partial u_x/\partial x)^+ - (\partial u_x/\partial x)^-] \\ &= -2v_r(\partial u_x/\partial x)^+ = -2v_r\epsilon_{xx}^{fault} \\ &= -2v_r[\frac{1-\nu}{2\mu}\sigma_{xx}^{fault}] \\ &= -[v_r(\hat{\alpha}_s^2+1)/(2\mu\alpha_d)]\Im S(z_s) \end{aligned} \tag{D.1}$$

using $\nu = 0.25$ and equation 5.1. $S(z_s)$ is given by equation 5.2, and $z_s = x + i0^+$, the limit as we approach the fault from $y > 0$, in order to get the sign of $\Im S(z_s)$ correct. Solving for $\Im S(z_s)$ and using this in equation 5.1 (ignoring the P wave contribution) with $z_s = x + \hat{\alpha}_s|y|$, the far field stress changes are

$$\begin{aligned}
\Delta\sigma_{xx}^{far} &= -\mu(v_r^2 - 2c_s^2)V(z_s)sign(y)/v_r^3 \\
\Delta\sigma_{yx}^{far} &= -\mu(v_r^2 - 2c_s^2)^2 V(z_s)/(2v_r^3 c_s^2 \hat{\alpha}_s) \\
\Delta\sigma_{yy}^{far} &= -\Delta\sigma_{xx} \\
\Delta\sigma_{zz}^{far} &= 0 \qquad \text{(D.2)}
\end{aligned}$$

Because $V(x)$ is always positive in our cases, $\Delta\sigma_{xx}^{far}$ and $\Delta\sigma_{yy}^{far}$ change signs as v_r increases past $\sqrt{2}c_s$, but $\Delta\sigma_{yx}^{far}$ is negative for all v_r, except for $\sqrt{2}c_s$ at which all the $\Delta\sigma_{kl}^{far}$ vanish. The expressions predict that when $v_r > \sqrt{2}c_s$, the sign of the far-field $\Delta\sigma_{xx}^{far}$ is the same as that along the rupture surface on the corresponding side of the fault, but that the sign is reversed when $v_r < \sqrt{2}c_s$. It can also be quite easily shown that the far-field stress perturbation, $\Delta\sigma_{xx}^{far} = 0.75(1 - 2\sin^2\beta)\Delta\sigma_{xx}^{on-fault}$ where β is the Mach angle, $\sin\beta = c_s/v_r$. Thus at velocities close to $\sqrt{2}c_s$ the far-field stress perturbation is still a significant percentage of the same on the fault.

We note that an alternative way to derive the ratio of far-field shear to normal stresses is to employ Mohr's circle concepts. We know that for an element of material, in the medium in which a steady state supershear rupture is propagating, one of whose faces is aligned with the Mach front (in $y > 0$ say), the stress component that jumps in value as the Mach front is crossed is the shear stress acting on it. The shear and normal stresses in the cartesian coordinate system for this element is then obtained by rotating it about the center by an angle β. This translates to a rotation in the Mohr's circle plane by an angle of 2β. Thus, if $\Delta\tau$ is the shear stress acting on the element aligned with the Mach front then $\Delta\sigma_{yy}^{far} = \Delta\tau\sin(2\beta)$ and $\Delta\sigma_{yx}^{far} = -\Delta\tau\cos(2\beta)$. Thus $\Delta\sigma_{yx}^{far}/\Delta\sigma_{yy}^{far} = -\cot(2\beta)$ [Figure D.1]. Using the results above we can now make some estimates on far field stress perturbations

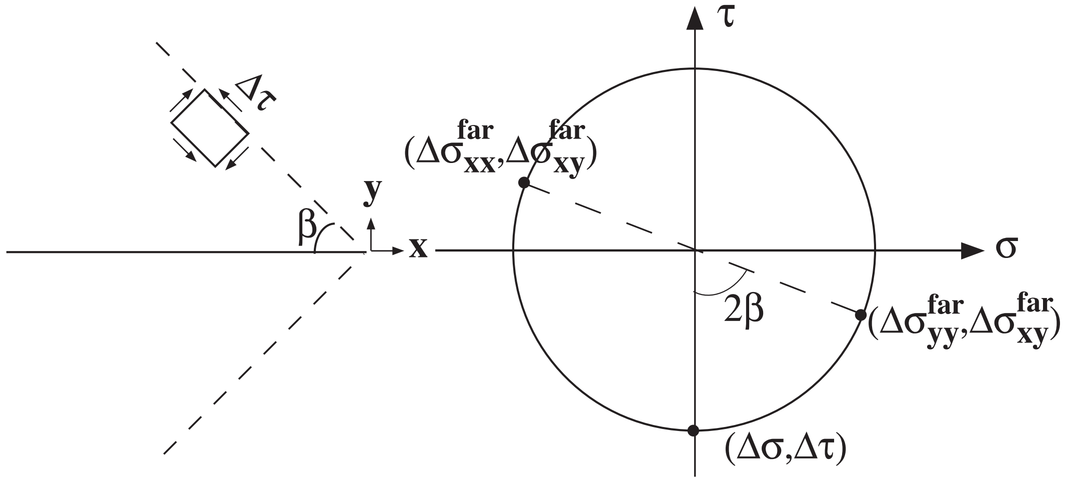

Figure D.1: Stresses acting on an element aligned with the Mach-fronts and in the cartesian system. $\Delta\tau$ is the shear stress acting on the element in that orientation and $\Delta\sigma$ is the normal stress ($= 0$). β is the inclination of the Mach-front with respect to the slip pulse. $\Delta\sigma_{xy}^{far}$ and $\Delta\sigma_{yy}^{far}$ are the shear and normal stress in the far-field measured with respect to the **x**-**y** co-ordinates. For the Mohr's circle we use tensile positive convention. Note that $\Delta\tau > 0$ when $v_r < \sqrt{2}c_s$ and changes sign at higher speeds crossing zero at $v_r = \sqrt{2}c_s$.

left in the wake of an supershear slip pulse. Some assumptions need to be made before making estimates of the far field stress values. Firstly, we shall use the maximum slip velocities obtained from our model for small ($R/L = 0.05$) and large ($R/L = 1.0$) values of the process zone (R) with respect to the length of the slip pulse (L) [Figure 5.6]. Slip velocity, V, in our model is non-dimensionalized as $\mu V/[(\sigma_{yx}^0 - \tau_r)c_s]$, where μ is the shear modulus of the medium, $(\sigma_{yx}^0 - \tau_r)$ is the dynamic stress drop and c_s is the shear wave speed of the medium. We assume that $\mu =$ 30GPa, $(\sigma_{yx}^0 - \tau_r) =$ 3MPa and $c_s =$ 3km/s. This gives us maximum slip velocity values varying from 0.5m/s to 10.5m/s and increasing with increasing rupture velocity.

Using the above values of slip velocity one can now make reasonable estimates of far field stresses [Figure 5.6]. This provides some interesting results. Firstly, the perturbation in the shear stress field $\Delta\sigma_{xy}^{far}$ is always negative in the far field as expected earlier. $\Delta\sigma_{xx}^{far}$ changes sign from being extensional ($\Delta\sigma_{xx}^{far} > 0$) to compressional as one crosses the $\sqrt{2}c_s$ rupture velocity value. The magnitude of the stress perturbation is also quite high, varying between -17MPa and 8MPa (using the maximum value of slip velocity). Also, the changes in the far field stresses seem to be very sensitive to the rupture velocity. For example, $\Delta\sigma_{xx}^{far}$ increases from 1MPa to 3MPa as the rupture velocity changes from $1.45c_s$ to $1.5c_s$. Ofcourse, the slip velocity also changes here as the rupture velocity changes. Hence it is useful to know the change in the stress field for fixed value of peak slip velocity and slightly different values of rupture velocity. Taking V = 5m/s as representative of the faster slip velocities we get the rough estimates for $v_r = 1.51c_s$ to $1.61c_s$ (on the compressional side of the fault),

$$\begin{aligned}
\Delta\sigma_{xx}^{far} &= -(4.0 \text{ to } 7.0 \text{ MPa })sign(y) \\
\Delta\sigma_{yx}^{far} &= -(0.4 \text{ to } 1.5 \text{ MPa }) \\
\Delta\sigma_{yy}^{far} &= +(4.0 \text{ to } 7.0 \text{ MPa })sign(y) \qquad \text{(D.3)}
\end{aligned}$$

Those are large normal stress changes, 40 bars at $1.51c_s$, 70 bars at $1.61c_s$, especially given that they do not attenuate with distance until 3D effects enter the model. For $v_r = 1.21$ to $1.31c_s$, the normal stress changes have the same magnitude range but reverse sign from those above. The estimtes are peak stress values; average stress changes, if $V_{average}$ is about 1m/s, would be a fifth as large, but still significant at about 10 bars.